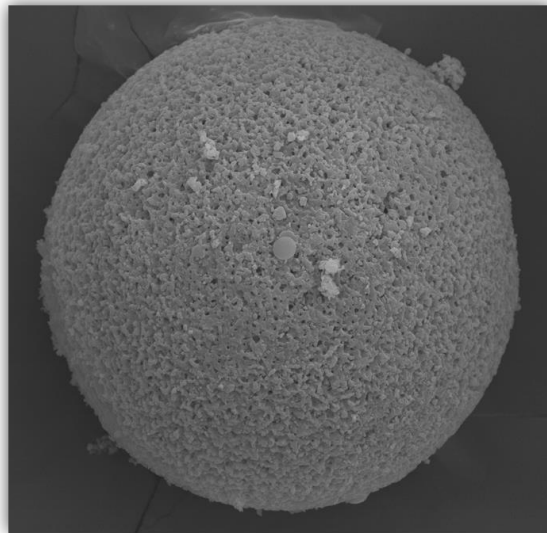


UNIVERSIDADE DE LISBOA
INSTITUTO SUPERIOR TÉCNICO



**Silica-based single and multicomponent oxide microspheres
with interconnected macroporosity: MICROSCAFS[®]**

Mário Filipe Lima do Vale

Supervisor: Doctor Ana Clara Lopes Marques

Thesis approved in public session to obtain the PhD Degree in Chemical Engineering

Jury final classification: Pass with Distinction

2024



UNIVERSIDADE DE LISBOA
INSTITUTO SUPERIOR TÉCNICO

**Silica-based single and multicomponent oxide microspheres
with interconnected macroporosity: MICROSCAFS®**

Mário Filipe Lima do Vale

Supervisor: Doctor Ana Clara Lopes Marques

Thesis approved in public session to obtain the PhD Degree in Chemical Engineering

Jury final classification: Pass with Distinction

Jury

Chairperson: Doutor Henrique Aníbal Santos de Matos, Instituto Superior Técnico, Universidade de Lisboa

Members of the Committee:

Doutor Sidney José Lima Ribeiro, Instituto de Química, Universidade Estadual Paulista (UNESP);

Doutora Verónica Cortés de Zea Bermudez, Escola de Ciências da Vida e do Ambiente, Universidade de Trás-os-Montes e Alto Douro;

Doutor José Paulo Sequeira Farinha, Instituto Superior Técnico, Universidade de Lisboa

Doutor José Manuel Félix Madeira Lopes, Instituto Superior Técnico, Universidade de Lisboa

Doutora Ana Clara Lopes Marques, Instituto Superior Técnico, Universidade de Lisboa

Funding Institution

Fundação para a Ciência e a Tecnologia (FCT)

2024



This work was financially supported by Fundação para a Ciência e a Tecnologia with Ph.D. grants SFRH/BD/138717/2018 and COVID/BD/152946/2022 and the FCT project <http://doi.org/10.54499/PTDC/EQU-EQU/1056/202> (SOLAR2CLEAN—Engineered solar light driven photocatalytic systems for wastewater purification) <https://solar2clean.tecnico.ulisboa.pt>

Abstract

The aim of this thesis is to apply and study a modified sol-gel method that integrates polymerization-induced phase separation, by spinodal decomposition, and sol-gel chemistry to create microspheres with tailored interconnected macroporosity, registered under the name MICROSCAFS[®]. First, SiO₂ (S) MICROSCAFS[®] were created by progressively raising the temperature of the synthesis, promoting the sol-gel transition and phase separation between siloxane-rich domains and water-rich domains, within the droplets of a water-in-oil emulsion. Besides tetraethoxysilane, a silica precursor with inherent gelation/phase separation capability was used, namely (3-glycidyloxypropyl)trimethoxysilane, so no specific gelation additives, nor porogens were needed. This innovative method was then adapted, to create SiO₂-TiO₂ (ST) and SiO₂-TiO₂-HfO₂ (STH) MICROSCAFS[®] for the first time. The introduction of titania and hafnia precursors with higher reactivities allowed to use constant and lower temperature, yielding MICROSCAFS[®] with diameters mode ranging from 69 to 105 μm and pore size mode as high as 1.9 μm in a faster and reproducible way. Optimization studies were carried out by systematically varying several synthesis parameters and a correlation between the size and amount of macropores and the mechanical properties of the MICROSCAFS[®] was established.

As a proof of concept, engineered photocatalytic ST MICROSCAFS[®] were developed, by loading ST MICROSCAFS[®] with a commercial TiO₂ photocatalyst, without modification tuned for visible light harvesting. Photocatalytic degradation of methyl orange dye of 87% (in 2 h) in a batch reactor and 29% (in 6 h) in a flow reactor was achieved, using a calibrated solar light simulator (1 sun) and a photocatalyst/pollutant mass ratio of 23. This thesis introduces a novel flow kinetic model for simulating the photocatalytic MICROSCAFS[®] performance, being the degradation by-products elucidated by high-resolution mass spectrometry. MICROSCAFS[®] are shown to be recyclable and a promising solution for environmental remediation, using straightforward flow conditions, and no need for expensive separation steps.

Keywords sol-gel, phase separation, interconnected macroporosity, microspheres, heterogeneous photocatalysis

Resumo

O objetivo desta tese é aplicar e estudar um método baseado em sol-gel, mas modificado de forma a integrar a separação de fases por decomposição espinodal e a química sol-gel para criar, de forma customizada, microesferas com macroporos interconectados, registadas como MICROSCAFS®. Inicialmente, foram criados MICROSCAFS® de SiO₂ através da elevação progressiva da temperatura da síntese, promovendo a transição sol-gel e a separação de fases entre domínios ricos em siloxano e domínios ricos em água, dentro das gotículas de uma emulsão água-em-óleo. Além do tetraetoxisilano, foi utilizado um precursor de sílica com capacidade inerente de gelificação/separação de fases, nomeadamente (3-glicidiloxipropil)trimetoxi silano. Este método inovador foi então adaptado para criar MICROSCAFS® de SiO₂-TiO₂ e SiO₂-TiO₂-HfO₂ pela primeira vez. A introdução de precursores de titânia e hafnia com reatividades mais elevadas permitiu o uso de uma temperatura constante e mais baixa, resultando em MICROSCAFS® com diâmetros até 105 µm e tamanho de poro até 1.9 µm de maneira mais rápida e reproduzível. Os parâmetros de síntese foram sistematicamente alterados e estabeleceu-se correlações entre o tamanho e a quantidade de macroporos e as propriedades mecânicas dos MICROSCAFS®.

Como prova de conceito, os MICROSCAFS® foram impregnados com nanopartículas de TiO₂ comerciais e utilizados na degradação fotocatalítica de uma solução aquosa de alaranjado de metilo utilizando luz solar simulada (1 sol). Foi alcançada uma degradação de 87% (em 2 horas) em um reator descontínuo e 29% (em 6 horas) em um reator contínuo, utilizando uma razão mássica fotocatalisador/poluinte de 23. Esta tese introduz um novo modelo cinético de fluxo para simular o desempenho fotocatalítico dos MICROSCAFS®, sendo os subprodutos de degradação elucidados por espectrometria de massa de alta resolução. Demonstrou-se que os MICROSCAFS® são recicláveis e uma solução promissora para remediação ambiental, utilizando fluxo contínuo de forma simples e evitando etapas de separação dispendiosas.

Palavras-chave sol-gel, separação de fases, macroporosidade interconectada, microesferas, fotocatalise heterogénea

Acknowledgements

I want to express my most profound appreciation to my supervisor, Professor Ana Clara Marques, for all the support and patience she has given me since the conception of my Ph.D. Without her invaluable feedback and effort, I wouldn't have grown as a researcher and accomplished my scientific achievements. I am also thankful to my co-authors António Mariquito, Sofia Moreira Fernandes, Mónica Loureiro, Rita Serôdio, Doctor Beatriz Barrocas, Doctor Maria João Ferreira, Professor José Madeira Lopes, Professor Luís Reis, Professor Maria Conceição Oliveira, and Professor Moisés Pinto for the all the help provided to my research and writing. I also want to thank Professor Ana Paula Serro for providing the assets needed to perform the rheological studies.

I am grateful for the financial support provided by Fundação para a Ciência e Tecnologia through the SFRH/BD/138717/2018 and COVID/BD/152946/2022 grants, as well as funding provided by the BL43/2023_IST-ID grant through the SOLAR2CLEAN project (PTDC/EQU EQU/1056/2020, <http://doi.org/10.54499/PTDC/EQU-EQU/1056/2020>). I sincerely thank my R&D unit, CERENA- Centro de Recursos Naturais e Ambiente, for accepting me and providing all the necessary work conditions.

Special thanks to all my lab colleagues and to my friends Mónica Loureiro, António Mariquito and David Duarte, for all the good talks and moments.

Finally, I want to thank my life partner, Inês Antunes, and my parents, Conceição and Mário Vale, for their love and unconditional support. Without them, this journey would have been impossible.

Table of Contents

Chapter 1 - Introduction	1
1.1. Problem statement	2
1.2. Thesis specific objectives and outline	3
1.3. Outputs	6
Chapter 2 – Literature review: Macroporosity control by phase separation in sol-gel derived monoliths and microspheres	9
2.1. Background on Sol-gel and Phase Separation	10
2.1. Macroporous silica (SiO ₂) monoliths	16
2.1.1. Pioneering works	16
2.1.2. Further developments on inorganic and inorganic-organic SiO ₂ monoliths	26
2.2. Macroporous SiO ₂ based multicomponent oxide monoliths	32
2.3. Macroporous non-siliceous single and multi-oxide, and non-oxide monoliths	39
2.3.1. Titania (TiO ₂) macroporous monoliths	40
2.3.1.1. Formamide systems	40
2.3.1.2. Chelated systems	42
2.3.2. Zirconia and alumina macroporous monoliths	43
2.3.3. Other non-siliceous macroporous monolithic systems	46
2.4. Macroporous microspheres	57
2.5. Macroporous microspheres by sol-gel/phase separation	61
2.5.1. Multicavities / incontinuous inner macroporosity	61
2.5.2. Interconnected macroporosity	63
2.6. Final Remarks	71
Chapter 3 - Silica-based MICROSCAFS®	73
3.1. Introduction	74
3.1.1. Synthesis of the silica (S) MICROSCAFS®	74
3.1.2. Characterization	76
3.2. Results and discussion	77
3.2.1. Evolution of the reaction medium during the synthesis	77
3.2.2. Microspheres size and characteristic size	78
3.2.3. Chemical structure of the dried and heat-treated microspheres	88
3.3. Conclusion	95

Chapter 4 – Multicomponent Oxide MICROSCAFS®	97
4.1. Study on the effect of the ST and STH MICROSCAFS® synthesis' parameters	98
4.1.1. Introduction	98
4.1.2. Experimental	98
4.1.2.1. Synthesis of the ST and STH MICROSCAFS®	98
4.1.2.2. Characterization	100
4.1.2.3. Rheological characterization	101
4.1.2.4. X-ray computed tomography	102
4.1.2.5. MICROSCAFS® mechanical properties analysis	102
4.1.3. Results and discussion	103
4.1.3.1. MICROSCAFS® formation mechanism and other features	103
4.1.3.2. Effect of synthesis temperature on the ST MICROSCAFS® morphology	111
4.1.3.3. Effect of the Si alkoxide type on the ST MICROSCAFS® morphology	115
4.1.3.4. Effect of the Ti precursor's chelating agent and emulsion characteristics on the ST MICROSCAFS® morphology	122
4.1.3.5. Development of multicomponent oxide SiO ₂ -TiO ₂ -HfO ₂ (STH) MICROSCAFS®	127
4.1.3.6. MICROSCAFS® mechanical properties	129
4.1.4. Conclusion	138
4.2. Mechanistic study of the formation of multicomponent oxide MICROSCAFS® by cryo-SEM	140
4.2.1. Introduction	140
4.2.2. Experimental	140
4.2.2.1. Cryo-Scanning Electron Microscopy	140
4.2.2.2. Further Characterization	140
4.2.3. Results and Discussion	141
4.2.4. Conclusion	148
Chapter 5 - Solar light-driven photocatalytic water purification using multicomponent oxide MICROSCAFS®	149
5.1. Introduction	150
5.2. Experimental	152
5.2.1. Preparation of the photocatalytic MICROSCAFS®	152
5.2.2. Characterization	153
5.2.3. Photocatalytic tests	154

5.2.4. Kinetics modeling of the photocatalytic performance	156
5.2.5. Analytical methods for photocatalysis by-products determination	159
5.3. Results and discussion	159
5.3.1. Characterization of the MICROSCAFS® before and after heat treatment and photocatalyst (P25 TiO ₂ NPs) loading	159
5.3.2. Photocatalytic studies on the TiO ₂ NPs loaded MICROSCAFS®	169
5.3.3. Kinetic studies	175
5.3.4. Study of the by-products from photocatalytic MO degradation	182
5.3.5. Scavenger's study on the photocatalytic MICROSCAFS® and photocatalysis mechanistic study	185
5.4. Conclusion	188
Chapter 6 - Conclusions and Future Work	189
6.1. Conclusions	190
6.2. Future Work	193
Chapter 7 - References	195

List of Figures

- Figure 2.1. Sol-gel hydrolysis and condensation reactions in alkoxides.....11
- Figure 2.2. Illustrative phase diagram of a binary system showing UCST behavior. Φ_C is the volume fraction of the critical composition where spinodal decomposition occurs at temperature T_1 . Φ_N is the volume fraction of composition where nucleation-growth occurs at temperature T_1 . Adapted from [57]......14
- Figure 2.3. Illustrative phase diagrams of systems with immiscibility window for comparison of physical and chemical cooling phenomena. Reprinted, with adaptations, by permission from Springer Nature Customer Service Centre GmbH: Springer, J. Sol-Gel Sci. Technology, Polymerization-induced phase separation in silica sol-gel systems containing formamide, Kaji H, Nakanishi K, Soga N, © Kluwer Academic Publishers. Manufactured in The Netherlands (2013) [19]......16
- Figure 2.4. Variations in gel morphology with increasing NaPSS concentration (C , in mol mol⁻¹), at 60 °C for NaPSS Mw between 50000 and 100000: (a) $C = 0.179$, scale bar=2 μm , (b) $C = 0.187$, scale bar=2 μm , (c) $C = 0.194$, scale bar=5 μm , (d) $C = 0.201$, scale bar=5 μm , (e) $C = 0.208$, scale bar=20 μm , (f) $C = 0.215$, scale bar=50 μm . Reprinted with permission from K. Nakanishi and N. Soga, *J. Am. Ceram. Soc. Copyright © 1991 WILEY-VCH Verlag GmbH & Co. KGaA, Weinheim* [16].18
- Figure 2.5. Possible structures at various coarsening stages of spinodal decomposition. Reprinted (and adapted) with permission from K. Nakanishi and N. Soga, *J. Am. Ceram. Soc. Copyright © 1991 WILEY-VCH Verlag GmbH & Co. KGaA, Weinheim* [16].19
- Figure 2.6. Effect on the gel morphologies with the type of organic solvent, for the system TEOS-HPAA (of Mw 250000) and reaction temperature 80 °C. Solubility parameter, δ_s ((cal cm⁻³)^{1/2}): formamide (FA) – 19.2, N-methylformamide (NMF) – 16.1, N,N-dimethylformamide (DMF) – 12.1, glycerol (Gly) – 16.5, ethylene glycol (EG) – 14.6 and propylene glycol (PG) – 12.6. Reprinted from J. Non. Cryst. Solids, Vol. 142, N. Soga, K. Nakanishi, Phase separation in silica sol-gel system containing polyacrylic acid. IV. Effect of chemical additives, Pages 45-54, Copyright (1992), with permission from Elsevier [63]......21
- Figure 2.7. Schematic phase diagrams for the formamide system (a), and for an organic polymer containing system (b). ϕ_C, i and ϕ_C, f are critical compositions just after all the constituents are mixed and during phase separation, respectively. The value of ϕ_C, f in formamide system is much smaller (more silica-poor), and binodal and spinodal lines are more asymmetric than those in HPAA system. Reprinted, with adaptations, by permission from Springer Nature Customer Service Centre GmbH: Springer, J. Sol-Gel Sci. Technology, Polymerization-induced phase separation in silica sol-gel systems containing formamide, Kaji H, Nakanishi K, Soga N, © Kluwer Academic Publishers. Manufactured in The Netherlands (2013) [19]......23
- Figure 2.8. Scanning electron images of dried gel morphology for increasing quantities of PEO (100000 Mw), in a synthesis that involves 6.51 g of TEOS, 0.81 g f 60% aq. HNO₃ and 8 g of H₂O: a) 0.30 g PEO; b) 0.40 g PEO; c) 0.50 g PEO; d) 0.60 g

PEO. Reprinted by permission from Springer Nature Customer Service Centre GmbH: Springer, J. Sol-Gel Sci. Technology, Phase separation kinetics in silica sol-gel system containing polyethylene oxide. I. Initial stage, Nakanishi K, Yamasaki Y, Kaji H, Soga N, Inoue T, Nemoto N, © 1994 Kluwer Academic Publishers, Boston. Manufactured in The Netherlands (1994) [66].....25

Figure 2.9. Differential pore size distribution of PMSQ monoliths achieved by using different durations of the acidic step, from 10 minutes to 5 h (dried at 300 °C). Measurements carried out by MIP. Reprinted (and adapted) with permission from Dong H, Brennan JD (2006) Controlling the morphology of methylsilsesquioxane monoliths using a two-step processing method. Chem Mater 18:541–546 . <https://doi.org/10.1021/cm051900n> [75]. Copyright 2006 American Chemical Society.....29

Figure 2.10. Increasing magnification, from right to left, of a silica monolith prepared from glycol-modified silane in the presence of P123 at pH=1. Republished with permission of Royal Society of Chemistry (Great Britain), from Sol-gel synthesis of monolithic materials with hierarchical porosity, A. Feinle, MS. Elsaesser, N. Hüsing, 45, 12, 2015 [20]; permission conveyed through Copyright Clearance Center, Inc..31

Figure 2.11. SEM images of heat-treated monoliths of composition 70%SiO₂–30%CaO (mol%), prepared by (a) the sol-gel technique without addition of PEO; (b) the sol-gel/phase separation technique with addition of PEO. Reprinted by permission from Springer: Springer Nature, Journal of Materials Research, Sol-gel-derived glass scaffold with high pore interconnectivity and enhanced bioactivity, A.C. Marques, R.M. Almeida, A. Thiema, S. Wang, M.M. Falk and H. Jain [3]. Copyright Springer Nature 2009.....37

Figure 2.12. SEM images of a heat-treated monolith of composition 70%SiO₂–30%CaO (mol%), prepared by the sol-gel/phase separation technique with addition of PEO: (a) magnification of 300x; (b) magnification of 120,000x. Reprinted by permission from Springer:Springer Nature, Journal of Materials Research, Sol-gel-derived glass scaffold with high pore interconnectivity and enhanced bioactivity, A.C. Marques, R.M. Almeida, A. Thiema, S. Wang, M.M. Falk and H. Jain [3]. Copyright Springer Nature 2009.....37

Figure 2.13. (a) Interconnected pore size distributions for SiO₂-CaO heat treated monoliths, determined by MIP. The samples analyzed were prepared both with and without PEO, as well as with and without solvent exchange. Reprinted by permission from Springer:Springer Nature, Journal of Materials Research, Sol-gel-derived glass scaffold with high pore interconnectivity and enhanced bioactivity, A.C. Marques, R.M. Almeida, A. Thiema, S. Wang, M.M. Falk and H. Jain [3]. Copyright Springer Nature 2009; (b) Bright field TEM image of the monolith prepared with PEO and solvent exchange procedure. Reprinted by permission from Springer Nature:Springer Nature, Journal of Sol-Gel Science and Technology, Nano/macroporous monolithic scaffolds prepared by the sol-gel method, A.C. Marques, H. Jain, C. Kiely, K. Song, C.J. Kiely and R.M. Almeida [4]. Copyright Springer Nature 2009.38

Figure 2.14. SEM images of the dried TiO₂ gels prepared with different PVP contents (x): (a) 50 mg; (b) 70 mg, (c) 90 mg; (d) 100 mg; (e) 110 mg; (f) 115 mg (quantities used in the formulation: 0.5g TiOSO₄.xH₂O: 1ml H₂O: 0.3ml EG: 0.248 ml formamide: x mg PVP). Reprinted by permission from Springer Nature Customer Service Centre GmbH: Springer, J. Sol-Gel Sci. Technology, Sol-gel synthesis of macroporous TiO₂ from ionic precursors via phase separation route, Li W, Guo X, Zhu Y, Hui Y, Kanamori K, Nakanishi K, © Kluwer Academic Publishers. Manufactured in The Netherlands (2013) [106].42

Figure 2.15. SEM images of Al₂O₃ dried monoliths prepared with different amounts of phase separation inducer additive, PEO (1000000Mw). Reprinted (and adapted) with permission from Tokudome Y, Fujita K, Nakanishi K, Miura K, Hirao K (2007) Synthesis of monolithic Al₂O₃ with well-defined macropores and mesostructured skeletons via the sol-gel process accompanied by phase separation. Chem Mater 19:3393–3398. <https://doi.org/10.1021/cm063051p> [110]. Copyright 2007 American Chemical Society.45

Figure 2.16. Representative synthesis schemes, employing metal alkoxides, for macroporous monoliths of non-siliceous oxide composition, based on the sol-gel/phase separation method.46

Figure 2.17. Representative synthesis schemes, employing metal salts (ionic precursors) for macroporous monoliths of non-siliceous single and multi-oxide compositions, based on the epoxide mediated sol-gel/phase separation method. .47

Figure 2.18. (a) Appearance of typical xerogel transition metal hydroxide monoliths; (b) Corresponding SEM images exhibiting the monoliths' microstructure, derived from precursors of following low-valence elements: (b) Mn²⁺, (c) Fe²⁺, (d) Co²⁺, (e) Ni²⁺ and (f) Zn²⁺, respectively. Reprinted from the open access paper by F. Liu, D. Feng, H. Yang, X. Guo, "Preparation of macroporous transition metal hydroxide monoliths via a sol-gel process accompanied by phase separation.", Sci. Rep. 10 (2020) [129]. <http://creativecommons.org/licenses/by/4.0/>52

Figure 2.19. SEM images of C/TiO₂ with increasing amounts of TiO₂ (Ti precursor EGMT). Reprinted with permission from J. Schoiber, C. Koczwar, S. Rumswinkel, L. Whitmore, C. Prehal, F. Putz, M. S. Elsaesser, O. Paris, N. Hüsing, Chempluschem, Copyright © 2021 WILEY-VCH Verlag GmbH & Co. KGaA, Weinheim [137].56

Figure 2.20. Morphology of TiO₂ thin films prepared with increasing amounts of phase separation inducer, PEO (1800-2200 Mw), and obtained by dip-coating at 100 mm/min withdrawal speed: (a) 0 g; (b) 0.5 g; (c) 1 g; (d) 2 g PEO. Reprinted by permission from Springer Nature Customer Service Centre GmbH: Springer, J. Mat. Sci., Morphology of thin anatase coatings prepared from alkoxide solutions containing organic polymer, affecting the photocatalytic decomposition of aqueous acetic acid, Kato K, Tsuzuki A, Torii Y, Taoda H, Kato T, Butsugan Y, ©1995 Chapman & Hall [139].58

Figure 2.21. SEM images of TiO₂ microspheres exhibiting inner incontinuous macroporosity, prepared by O/W emulsion method combined with sol-gel transition and phase separation. The larger the amount of phase separation inducer

(PVP), the larger the pore volume and size. (a and b) 0 g PVP; (c and d) 0.190 g PVP; (e and f) 0.571 g PVP; (h and i) 1.142 g PVP; (j and k) 1.903 g PVP. Reprinted from Chinese Chem. Lett., Vol. 25, W. W. Cai, H. Yang, X. Z. Guo, A facile one-step route to synthesize titania hollow microspheres with incontinuous multicavities, Pages 441-446, , Copyright (2014), with permission from Elsevier [22].62

Figure 2.22 – Representative synthesis flowchart, employing O/W emulsification as soft template, and sol-gel/phase separation, for the achievement of metal oxide microspheres with incontinuous inner macroporosity.....63

Figure 2.23. Representative synthesis flowcharts, employing W/O emulsification as soft template, for the achievement of sol-gel derived macro/mesoporous SiO₂ microspheres: a) method developed by Yang et al. [23]; b) method developed by Shi et al. [26]. The O phase is composed by paraffin oil and Span®80.64

Figure 2.24. SEM images for the SiO₂ microspheres prepared by the W/O emulsion method combined with sol-gel transition and phase separation, using TEOS as Si precursor and PEO as phase separation inducer additive. Their narrow size distribution is due to liquid elutriation techniques, which allowed to select microspheres of diameter ranging from 6 to 10 μm. Reprinted from Microporous Mesoporous Mater., Vol. 116, Z. G. Shi, Y.Q. Feng, Synthesis, and characterization of hierarchically porous silica microspheres with penetrable macropores and tunable mesopores, Pages 701-704, Copyright (2008), with permission from Elsevier [24].65

Figure 2.25. a) Preparation schemes for the sol-gel derived macro/mesoporous SiO₂ microspheres (MICROSCAFS®), synthesized from TEOS and GPTMS, obtained by W/O emulsion combined with sol-gel transition and phase separation, in the absence of any gelation or phase separation inducer additive: a) Representative synthesis flowchart; b) drawing scheme. The O phase is composed by decahydronaphthalene (decalin) and Span®80.....68

Figure 2.26. Optical microscopy photographs of reaction medium aliquots taken at different stages of the MICROSCAFS®' synthesis. (a) emulsion, (b) emulsion after addition of the hydrolysate, 1h at 65 °C, (c) after 1h at 80 °C, (d) epoxy functionalized silica based porous microspheres dried at 40 °C. Bar scale = 300 μm (a-d). Photos acquired in transmission mode (a-c). Photos acquired in reflection mode (d).68

Figure 2.27. Macro/mesoporous epoxy-functionalized silica microspheres (MICROSCAFS®), synthesized from TEOS and GPTMS, obtained by emulsion combined with sol-gel transition and phase separation, in the absence of any gelation or phase separation inducer additive. Reprinted from Microporous Mesoporous Mater., Vol. 261, M.V. Loureiro, M. Vale, A. De Schrijver, J.C. Bordado, E. Silva, A.C. Marques, Hybrid custom-tailored sol-gel derived microsccaffold for biocides immobilization, Pages 252-258, Copyright (2018), with permission from Elsevier [41].69

Figure 3.1. Schematic of the S MICROSCAFS® synthesis.....75

Figure 3.2. Optical microscopy photographs of reaction medium aliquots taken at different stages of the S MICROSCAFS [®] synthesis (2S-REF). Bar scale = 300 μm (i-viii). Photos acquired in transmission mode (i-iv). Photos acquired in reflection mode (v-viii). The photo on the right side was taken by a camera machine. Bar scale = 1 cm.	77
Figure 3.3. SEM images of the produced particles. The inset shows a magnified image of one microsphere for each case.	79
Figure 3.4. SEM images of the internal structure of the produced particles.....	79
Figure 3.5. Size distributions of the S MICROSCAFS [®]	80
Figure 3.6. Evolution of the silica hydrolysate viscosity with the HCl/silanes molar ratio.....	81
Figure 3.7. Evolution of the S MICROSCAFS [®] ' characteristic size with their diameter (size), for the syntheses where the pre-hydrolysis time is 1 h. The inset shows the values for the surfactant amount employed in the corresponding synthesis, and the value for the MICROSCAFS [®] ' size and characteristic size.	82
Figure 3.8. Pore size distribution curves of the S MICROSCAFS [®]	86
Figure 3.9. N ₂ adsorption-desorption isotherms of the S MICROSCAFS [®]	87
Figure 3.10. ²⁹ Si MAS spectrum of microspheres 2S-REF.....	88
Figure 3.11. ²⁹ Si CP/MAS spectrum of microspheres 2S-REF. *spinning side bands	89
Figure 3.12. ¹³ C CP/MASS TOSS of microspheres 2S-REF.	90
Figure 3.13. Possible structures of unreacted and reacted epoxy group in GPTMS.	90
Figure 3.14. FTIR-ATR spectra of the porous microspheres, heat-treated for 1 h at 150 °C (a) and 700 °C (b). The inset shows the magnified region of the spectra, from 1300 to 700 cm^{-1}	92
Figure 3.15. FTIR-ATR spectra of the pure compounds.....	93
Figure 4.1. General scheme of ST MICROSCAFS [®] preparation, exhibiting the different main stages and associated optical microscopy images (scale bar = 400 μm).	104
Figure 4.2. ATR-FTIR spectra of MICROSCAFS [®] ST/50C, dried at 40 °C, and heat treated for 1h at 150 °C and 700 °C.....	105
Figure 4.3. Thermogram of ST/50C MICROSCAFS [®] dried at 45 °C (red) and heat treated for 1 h at 700 °C (black).....	106
Figure 4.4. SEM images of MICROSCAFS [®] ST/85C: without LiOH treatment (a) scale bar: 10 μm , (c) scale bar: 100 nm; with LiOH treatment (b) scale bar: 10 μm , (d) scale bar: 100 nm.	107

Figure 4.5. Evidence for synthesis reproducibility: (a, b, c) Optical microscopy images of three different batches of the same synthesis of MICROSCAFS® ST/85C; (d, g) SEM images (scale bar: 200 µm) of two different batches of the synthesis of MICROSCAFS® ST/50C/GPTMS+; (e,h) same as (d, g) with scale bar = 50 µm; (f, i) same as (d, g) with scale bar = 5 µm. Note: d, e and f were acquired with a higher voltage (15 kV) than g, h and i (10 kV).....	108
Figure 4.6. SEM images of the MICROSCAFS® ST/85C, at different magnifications, obtained using different quantities of surfactant SPAN®80: 2, 4, 6, 8 and 10 g. Scale bar (from top to bottom): 100 µm, 10 µm, 1 µm, 1 µm, 100 nm.....	109
Figure 4.7. Optical microscopy images of the MICROSCAFS® ST/85C synthesized using different combinations of surfactants (from left to right): Span® 80 (HLB=4.3), Span® 80+Tween® 80 (HLB=5.2) and Span® 80 + Pluronic® P123 (HLB=5.2). Scale bar: 500 µm.....	110
Figure 4.8. Optical microscopy images of the MICROSCAFS® ST/RT and ST/50C obtained using different quantities of surfactant Span® 80: 2, 6 and 10 g.....	110
Figure 4.9. Morphology of ST MICROSCAFS® synthesized at room temperature (ST/RT), 50°C (ST/50C), and 85°C (ST/85C). Top left: Optical microscopy photographs (scale bar = 600 µm); Top right: SEM images (scale bar = 8 µm) of a particle cross-section; Bottom left: particle size distributions; Bottom right: MIP pore size distribution curves.....	113
Figure 4.10. N ₂ adsorption isotherm and DFT pore size distribution (inset) of MICROSCAFS® synthesized at room temperature (ST/RT), 50 °C (ST/50C), and 85 °C (ST/85C).....	114
Figure 4.11. Complex viscosity evolution over time for the hydrolysates at (a) room temperature, (b) 50 °C, and (c) 85 °C.....	115
Figure 4.12. Morphology of ST MICROSCAFS® synthesized using 0.65 (ST/50C/GPTMS-), 0.86 (ST/50C), and 1.08 (ST/50C/GPTMS+) GPTMS/TEOS molar ratios. Top left: Optical microscopy photographs (scale bar = 600 µm); Top right: SEM images (scale bar = 8 µm) of a particle cross-section; Bottom left: particle size distributions; Bottom right: MIP pore size distribution curves.....	117
Figure 4.13. Top: Cross-section images obtained by CT from MICROSCAFS® ST/50C/GPTMS- and ST/50C/GPTMS+ obtained with the CCD detector when placed, without pressing, inside a cylindrical container. Scale bar = 700 µm; Middle: Pore and skeleton size distributions, calculated from CT images; Bottom: open and total porosity calculated from CT images.	118
Figure 4.14. Complex viscosity evolution over time of the hydrolysates with (a) 0.65, (b) 0.86, and (c) 1.08 GPTMS/TEOS molar ratio.	119
Figure 4.15. BET adsorption isotherm and DFT pore size distribution (inset) of MICROSCAFS® synthesized using 0.65 (ST/50C/GPTMS-), 0.86 (ST/50C), and 1.08 (ST/50C/GPTMS+), GPTMS/TEOS molar ratio.	120

Figure 4.16. ATR-FTIR spectra of MICROSCAFS® ST/50C and ST/50C/GPTMS+, with heat treatment for 1h at 700°C.....	122
Figure 4.17. Morphology of ST MICROSCAFS® synthesized using 1:4 (ST/50C) and 1:6 (ST/50C/AA+) TiPOT/CH ₃ COOH molar ratios, and 0.45 (ST/50C) and 0.68 (ST/50C/W+) W/O mass ratios. Top left: Optical microscopy photographs (scale bar = 600 μm); Top right: SEM images (scale bar = 8 μm) of a particle cross-section; Bottom left: particle size distributions; Bottom right: MIP pore size distribution curves.	123
Figure 4.18. Flow test curves of three groups of emulsion each belonging to different W/O ratios.	124
Figure 4.19. Complex viscosity evolution over time of the hydrolysates with (a) 1:4 TiPOT:CH ₃ COOH molar ratio (sample ST/50C), (b) 1:6 TiPOT:CH ₃ COOH molar ratio (sample ST/50C/AA+), and (c) 1:4 TiPOT:CH ₃ COOH molar ratio, diluted with an equivalent amount of the excess of emulsion water.....	125
Figure 4.20. N ₂ adsorption isotherm and DFT pore size distribution (inset) of MICROSCAFS® synthesized at 0.45:1 (ST/50C) and 0.68:1 (ST/50C/W+) W/O mass ratios.....	126
Figure 4.21. Optical microscopy photograph of STH MICROSCAFS® made using 13.7 g of hafnium dichloride oxide octahydrate salt.....	127
Figure 4.22. Morphology of double (ST/50C/GPTMS+) and triple (STH/50C/GPTMS+) oxide MICROSCAFS®. Top left: Optical microscopy photographs (scale bar = 600 μm); Top right: SEM images (scale bar = 8 μm) of a particle cross-section; Bottom left: particle size distributions; Bottom right: MIP pore size distribution curves.	128
Figure 4.23. ATR-FTIR spectra of MICROSCAFS® ST/50C/GPTMS+ and STH/50C/GPTMS+, with heat treatment for 1h at 700 °C.....	129
Figure 4.24. Effect of (a) reaction temperature, (b) GPTMS/TEOS molar ratio, (c) TiPOT/CH ₃ COOH molar ratio and W/O mass ratio, and (d) addition of Hafnium dichloride oxide salt (STH multicomponent oxides) in the MICROSCAFS®' mechanical properties.	131
Figure 4.25. Cross-sectional 3D CT image of the powder (top line) and a single microsphere (bottom line) of the ST/50C/GPTMS- and ST/50C/GPTMS+ MICROSCAFS® (scale, distance between points: top left = 250 μm, top right = 250 μm, bottom left = 5 μm, bottom right = 10 μm).....	132
Figure 4.26. Effect of MICROSCAFS®' cumulative pore volume in (a) compressibility, (b) relaxation, (c) elastic recovery, and (d) stiffness.....	133
Figure 4.27. Effect of MICROSCAFS®' pore size mode in (a) compressibility, (b) relaxation, (c) elastic recovery, and (d) stiffness.....	133

Figure 4.28. Effect of MICROSCAFS® particle size mode in (a) compressibility, (b) relaxation, (c) elastic recovery, and (d) stiffness.	134
Figure 4.29. Compression and relaxation tests of (a, b) ST/RT, (c, d) ST/50C, and (e, f) ST/85C dried MICROSCAFS®	136
Figure 4.30. Compression and relaxation tests of (a, b) ST/50C/GPTMS-, (c, d) ST/50C/GPTMS+ dried MICROSCAFS®	137
Figure 4.31. Compression and relaxation tests of STH/50C/GPTMS+ dried MICROSCAFS®	137
Figure 4.32. Compression and relaxation tests of (a, b) ST/50C/AA+, (c, d) ST/50C/W+ dried MICROSCAFS®	138
Figure 4.33. Different stages of the MICROSCAFS® synthesis process, observed by optical microscopy. Scale bar = 400 µm.	141
Figure 4.34. Cryo-SEM images of (a) W/O emulsion and (b) ST pre-hydrolysate (Stage 1).	142
Figure 4.35. Cryo-SEM images of (a) ST oligomer clusters in the water phase, (b) STH MICROSCAFS® (cross-section) in the embryonic stage (BE mode), (c) STH MICROSCAFS® in the embryonic stage (BE mode), (d) ST MICROSCAFS® (cross-section) in the embryonic stage (SE mode) (Stage 2).....	144
Figure 4.36. Example of a MICROSCAFS® final morphology.	145
Figure 4.37. Cryo-SEM images of (a) ST and (b) STH MICROSCAFS® after the addition of ammonia (Stage 3).	146
Figure 4.38. Formation mechanism of the multi-oxide MICROSCAFS®	147
Figure 5.1. Continuous flow reactor with total recirculation to a tank. 1 – Solar simulator; 2 – Sample chamber (solar reactor); 3 – Peristaltic pump; 4 – MO solution stirred tank.....	155
Figure 5.2. Process flow diagram of the flow reactor. (1) Peristaltic pump; (2) continuous flow chamber (solar reactor, side view) containing the photocatalytic MICROSCAFS®; (3) solar simulator (Xe lamp), and (4) stirred tank.....	157
Figure 5.3. Particle size distributions of the ST MICROSCAFS® before and after HT (calcination) at 900 °C during 30 min.	160
Figure 5.4. SEM images of the MICROSCAFS® used for the particle size distributions, before (left column) and after (right column) being heat treated at 900 °C for 30 minutes.	161
Figure 5.5. Optical microscopy photographs of the MICROSCAFS® in three subsequent stages: 1 (first column) – dried MICROSCAFS®; 2 - (second column)	

MICROSCAFS® after being heat treated at 900 °C for 30 minutes; 3 (third column) – MICROSCAFS® after being loaded with the P25 TiO₂ NPs. 163

Figure 5.6. SEM images of the internal porosity (left), and corresponding MIP pore size distributions (right) of the MICROSCAFS® (a) dried at 45 °C, (b) heat-treated at 900 °C and (c) loaded with P25 TiO₂ NPs and heat-treated at 500 °C. 164

Figure 5.7. N₂ adsorption-desorption isotherms of the MICROSCAFS® (a) dried at 45 °C, (b) heat-treated at 900 °C and (c) loaded with P25 TiO₂ NPs. 165

Figure 5.8. TEM image of the P25 TiO₂ NPs (b) and their respective particle size distribution (b). 166

Figure 5.9. ATR-FTIR spectra of all the MICROSCAFS® (a, c and e) and it's respective zoom between 1500 and 400 cm⁻¹ (b, d and f). 168

Figure 5.10. (a) Plots of C/C_0 versus time of the heat-treated unloaded MICROSCAFS®, i.e. without photocatalyst (P-/HT, P0/HT and P+/HT), P25 TiO₂ NPs and photolysis of the MO dye; (b) Plots of C/C_0 versus time of the photocatalytic P25 TiO₂ NPs loaded MICROSCAFS®; (c) UV-vis spectra of MO solution aliquots taken during the light phase of a P+/HT/P25 experiment; (d) Photos of MO solution aliquots at the starting of the illumination and after 120 minutes when using the P+/HT/P25. Experiments done in batch conditions at 19 °C, pH = 7, mass(TiO₂ NPs)/mass(MO) = 23, 50 mL of 10 mg/L MO aq. solution, 50 mg of P25 TiO₂ NPs loaded MICROSCAFS® (11 – 12.5 mg TiO₂), irradiance = 1000 W m⁻² (1 sun)..... 170

Figure 5.11. Spectral output of LCS-100 Solar Simulator with standard AM1.5G filter. 170

Figure 5.12. Kubelka-Munk transformed UV-Vis DRS absorption spectra of the P25 TiO₂ NPs loaded MICROSCAFS® and P25 TiO₂ NPs. 171

Figure 5.13. (a) Plots of C/C_0 versus time of the P25 TiO₂ NPs loaded MICROSCAFS® using a continuous flow set-up; (b) MO degradation evolution achieved for 6 consecutive cycles with solar light irradiation for 6 hours using sample P+/HT/P25; (c) UV-Vis spectra of the final MO solution after each cycle in the range of 190 to 600 nm; (d) UV-Vis spectra of the final MO solution after each cycle in the range of 230 to 300 nm. Experiments done in flow conditions at 19 °C, pH = 7, mass (P25 TiO₂ NPs)/mass (MO) = 23, 200 mL of 10 mg/L MO aq. solution, 200 mg of P25 TiO₂ NPs loaded MICROSCAFS® (46-50 mg TiO₂), volumetric flow = 10 mL min⁻¹, irradiance = 1000 W m⁻² (1 sun)..... 172

Figure 5.14. Side and top views of the continuous flow reactor's sample chamber. The arrows indicate the direction of the flow of the MO solution and the color it's concentration. 173

Figure 5.15. SEM images of the P-/HT/P25 (left column) and P+/HT/P25 (right column) photocatalytic MICROSCAFS® after one cycle in batch and in flow. 174

Figure 5.16. Adjusted kinetic models in batch using the photocatalytic MICROSCAFS® with different porosities and size. Kinetic rate constant values (k) are indicated for each case.....	176
Figure 5.17. Adjusted kinetic models of the flow reactor using the photocatalytic MICROSCAFS® with different porosities, and a constant tank volume of 200 mL. Apparent flow (adjusted) kinetic rate constant values (k_{app}) are indicated for each case.....	177
Figure 5.18. Adjusted kinetic model of a complete MO degradation using the continuous flow reactor.....	179
Figure 5.19. TPs identification of MO photocatalytic degradation, during 120 and 360 min using P0/HT/P25 MICROSCAFS® on the (a) batch and (b) flow reactor, respectively. MO degradation values (%) were obtained by UV-Vis spectroscopy.	184
Figure 5.20. MO degradation evolution after 120 min. of irradiation using P+/HT/P25 as catalyst, when in the presence of selected scavengers: EtOH, BQ and EDTA to quench $\cdot\text{OH}$, $\text{O}_2^{\cdot-}$, and h^+ , respectively.	186
Figure 5.21. Photoactivation mechanism proposed for P+/HT/P25 MICROSCAFS® used as catalyst for the photodegradation of MO under solar light irradiation.	187

List of Tables

Table 2.1. Overview of some of the latest developments on SiO ₂ macro and mesoporous hierarchically structured monoliths (inorganic and hybrid composition) prepared via sol-gel/phase separation processing.	32
Table 2.2. Varied synthetic strategies for the achievement of SiO ₂ -based multicomponent oxide monoliths, prepared via sol-gel/phase separation processing.....	35
Table 2.3. Specific examples of synthetic strategies for the achievement of non-siliceous single and multi-oxide porous monoliths, prepared via sol-gel/phase separation processing.	49
Table 2.4. Specific examples of synthetic strategies for the achievement of non-siliceous multi-oxide and non-oxide porous monoliths, prepared via sol-gel/phase separation processing.	53
Table 2.5. Compilation of specific examples of macroporous microspheres and their synthesis strategies based on the emulsion method combined with sol-gel transition and phase separation.	70
Table 3.1. S MICROSCAFS® steps' temperature and times.....	75
Table 3.2. Synthesis reaction parameters and relevant characterization results, such as hydrolysate viscosity, microspheres' diameter, and average characteristic size.	78
Table 3.3. MIP results, upon elimination of the porosity data above 10 µm.....	85
Table 3.4. N ₂ adsorption/desorption data of the S MICROSCAFS®.....	87
Table 4.1. ST and STH MICROSCAFS®' synthesis parameters.....	99
Table 4.2. Particle size distribution data.....	111
Table 4.3. Average hydrolysate viscosity and MICROSCAFS®' synthesis pH.....	112
Table 4.4. EDS relative atomic concentrations of the dried MICROSCAFS®.....	121
Table 4.5. Mechanical parameters of the dried MICROSCAFS®.....	135
Table 4.6. EDS atomic concentrations of the different regions of the sample by cryo-SEM.....	142
Table 5.1. MICROSCAFS®' synthesis parameters, which suffered variation.....	152
Table 5.2. Particle size distribution data of the treated and non-heat-treated MICROSCAFS®.....	162
Table 5.3. EDS atomic concentration data of the MICROSCAFS®. Ti/Si is the atomic % ratio.....	167

Table 5.4. FTIR band intensity ratio $ITi - O - TiSi - O - Si$	169
Table 5.5. Average kinetic rate constants and apparent flow reactor rate constants of the photocatalytic MICROSCAFS®.....	178
Table 5.6. Experimental conditions, MO degradation and kinetic rate constants (k or k_{app}) of supported TiO_2 photocatalyst - comparison of the present study with the literature.....	180
Table 5.7. LC-HRMS/MS identification of MO and their degradation by-products.	185

Abbreviations and Acronyms

ATC	Automatic Temperature Compensation
ATR	Attenuated total reflectance
BDC	2-aminoterephthalic acid
BET	Brunauer, Emmett, Teller
BJH	Barrett-Joyner-Halenda
BQ	p-benzoquinone
BTME	Bis(trimethoxysilyl)ethane
BTMH	Bis(trimethoxysilyl)hexane
CCD	Charge-coupled device
CNF	Cellulose nanofibrils
CP	Cross-polarization
CT	Computed tomography
CTAB	Hexadecyltrimethylammonium bromide
CTAC	Hexadecyltrimethylammonium chloride
DEG	Diethylene glycol
DFT	Density functional theory
DMDMS	Dimethoxydimethylsilane
DRS	Diffuse reflectance spectroscopy
DMF	N,N-dimethylformamide
DSP	Differential scanning porosimetry
DTA	Differential Thermal Analysis
EDA	Ethylenediamine
EDS	Energy dispersive X-ray spectroscopy
EDTA	Ethylenediaminetetraacetic acid disodium salt dihydrate
EG	Ethylene glycol
EGDMA	Ethylene glycol dimethacrylate
EGMT	Ethylene glycol modified titanate
EO	Ethylene oxide
EtOH	Ethanol
FA	Formamide
FEG	Field emission gun
FTIR	Fourier-transform infrared spectroscopy
FWHM	Full width at half maximum
GMA	Glycidyl methacrylate
GPTMS	(3-glycidyloxypropyl)trimethoxysilane
HDTMS	Hexadecyltrimethoxysilane
HLB	Hydrophilic-lipophilic balance
HPAA	Poly(acrylic acid)
HPLC	High performance liquid chromatography
IR	Infra-red
IUPAC	International Union of Pure and Applied Chemistry

LC-HRMS/MS	Liquid chromatography–high resolution mass spectrometry/mass spectrometry
LCST	Lower critical solution temperature
MAS	Magic angle spinning
MIP	Mercury intrusion porosimetry
MO	Methyl orange
MOF	Metal organic framework
MTES	Methyltriethoxysilane
MTMS	Methyltrimethoxysilane
NaPSS	Poly(sodium-4-styrene sulfonate)
NMF	N-methylformamide
NMR	Nuclear magnetic resonance
nOTES	n-Octyltriethoxysilane
NPs	Nanoparticles
PAAm	Poly(acrylamide)
PEG	Polyethylene glycol
PEO	Poly(ethylene oxide)
PG	Propylene glycol
PhTMS	Phenyltrimethoxysilane
PMMA	Poly(methyl methacrylate)
PMSQ	Polymethylsilsesquioxane
PO	Propylene oxide
PPG	Polypropylene glycol
PPO	Poly(propylene oxide)
PS	Polystyrene
PVA	Polyvinyl alcohol
PVP	Poly(vinylpyrrolidone)
REF	Reference
RF	Resorcinol formaldehyde
RT	Room temperature
S	Silica
SAXS	Small angle x-ray scattering
SDS	Sodium dodecyl sulfate
SEM	Scanning electron microscopy
ST	Silica-titania
STA	Simultaneous Thermal Analyzer
STH	Silica-titania-hafnia
TBOT	Titanium tetrabutoxide
TEA	Triethylamine
TEG	Triethylene glycol
TEM	Transmission electron microscopy
TEOS	Tetraethyl orthosilicate
TG	Thermogravimetry
TGA	Thermogravimetric analysis

TMB	Trimethyl benzene
TMOS	Tetramethoxysilane
TOA	Trioctylamine
TOSS	Total Suppression of Spinning Sidebands
TPMI	Technology Platform on Microencapsulation and Immobilization
TPZR	Zirconium tetra-2-propoxide
UCST	Upper critical solution temperature
UHPLC	Ultra High Performance Liquid Chromatograph
UV	Ultra-violet
VTMS	Vinyltrimethoxysilane
XRD	X-ray diffraction
YAG	Yttrium aluminum garnet
YZA	Yttria-stabilized zirconia

This page was purposely left in blank.

Chapter

Introduction

1

1.1. Problem statement

Tailored porous materials with controlled pore size, shape, and morphology (interconnectivity) are a relevant research topic in the materials and chemistry domains, due to their high potential for sustainable and innovative applications in the fields of catalysis, chromatography, controlled release, scaffolds for biomedical applications, sensing, energy storage and conversion, sorption, and separation [1–4].

Varied methods for developing porous materials have been reported, such as sacrificial templating [5–7], direct foaming [8–10], and freeze casting technique [11–14]. In the past decades, an alternative method for the development of silica monoliths, with complex and often hierarchically organized porosity, through phase separation and sol–gel reaction has gained increasing importance [2,3,15–20], being the spinodal decomposition process, the main driver for obtaining monolithic gels with well-defined interconnected macropores [21]. Porous materials with monolithic shape are indeed the most explored, however porous microspheres may be preferred for specific applications since they can be easily packed into existing reactors, columns, or other containers.

The present thesis targets the synthesis and development of porous microspheres with a particular application in the photocatalytic purification of water (driven by the United Nations Sustainable Development Goals), which is an example of the immense applications of porous microspheres as support materials. In this case, porosity directly influences the photocatalytic activity, since macropores (>50 nm) facilitate the mass transport of liquids to the active sites, avoiding concentration gradients, and giving better performance in flow-through catalytic systems; mesopores (2–50 nm) are responsible for the high surface area of these materials, as well as for the size and shape selectivity. Moreover, the employment of porous microspheres as support materials for photocatalytic nanoparticles (NPs) prevents their aggregation and facilitates the easy recovery of the catalysts from polluted water and their reuse.

Despite the successful development of macroporous spheres by combining acid or alkaline catalysts with porogen and phase separation agents [22–37], the

Technological Platform on Microencapsulation and Immobilization (TPMI) group created a more straightforward approach for silica microspheres with interconnected macroporosity, registered under the name MICROSCAFS[®], which dispenses the need for such additives [38–41]. Instead, a specific silane combination (tetraethoxysilane, TEOS, and (3-glycidyloxypropyl)trimethoxysilane, GPTMS) has been used to provide inherent gelation/phase separation capability. This method involves shorter production times and lower temperatures, since there is no need for calcination to get rid of polymeric additives to achieve the porous structure. A simple drying of the MICROSCAFS[®] is enough to eliminate the solvent remaining within their 3D interconnected network. The current state of the art demands comprehensive research on porous microspheres in what regards the tailoring of their pore morphology and composition using this innovative synthesis methodology.

The main goal of this Ph.D. project is to reach a breakthrough in advanced wet-chemistry processing for porous material tailoring, develop reproducible and customized multicomponent oxide MICROSCAFS[®] and apply them in the development of an efficient and sustainable photocatalysis solution. In this approach, the obtained porous microspheres (MICROSCAFS[®]) will act as a support material to photocatalytic NPs, preventing aggregation, boosting their performance, and enabling recyclability of the photocatalytic system.

1.2. Thesis specific objectives and outline

This work has the following objectives:

1. Explore innovative strategies to create multicomponent oxide microspheres with tailored, interconnected porosity from nano to micron scale (MICROSCAFS[®]), and optimize them by systematic variation of the synthesis parameters;
2. Get an insight into the MICROSCAFS[®] formation mechanism using cutting-edge cryogenic scanning electron microscopy (SEM) together with energy dispersive X-ray spectroscopy (EDS) techniques;

3. Comprehensively assess the MICROSCAFS[®] pore morphology complementing electron microscopy, MIP and N₂ adsorption/desorption techniques with X-ray computed tomography;
4. Correlate morphological features with mechanical properties of the MICROSCAFS[®];
5. Develop photocatalytic MICROSCAFS[®], by TiO₂ NPs immobilization, and investigate the influence of their size and pore size distribution on the solar light-driven photocatalytic degradation of methyl orange (MO) organic dye in aqueous solution (including the implementation of the photocatalysis system at IST);
6. Compare the photocatalytic behavior of the developed new materials using a batch reactor and a continuous flow reactor with recirculation to a tank and perform a modeling study of the photocatalytic MICROSCAFS[®] performance on the latter one.

This thesis comprises seven chapters, with the initial chapter (Chapter 1) introducing the work, stating the research problem, its relevance, and the need to solve it. Following a concise contextualization, this chapter defines the thesis objectives, its outline and presents a list of publications and communications derived from the present research. Additionally, references to extra publications and outputs produced during the Ph.D. period are included.

Chapter 2 consists of a comprehensive review of macroporosity control by phase separation in sol-gel-derived monoliths and microspheres, based on the review article by Ana C. Marques and Mário Vale [40]. A detailed scientific background on phase separation is first provided focusing on thermodynamics aspects. Then, a detailed literature review on the development of macroporous monoliths is given, starting with pioneering works from Nakanishi *et al.* within the silica monoliths topic and evolving to silica multicomponent oxide monoliths, non-siliceous single, multi, and non-oxide monoliths. This chapter ends with a literature review on macroporous spheres created by polymerization-induced phase separation, which is directly linked with the topic of this thesis.

Chapter 3 consists of the first systematic study of the synthesis parameters effect on the porosity of S MICROSCAFS[®]. This is based on the original article by Mário Vale *et*

al. [39]. It leverages on the work (S MICROSCAFS®) previously developed by o team (Technology Platform on Microencapsulation and Immobilization). The effect of a greater amount of pre-hydrolysis catalyst, greater pre-hydrolysis time, and greater quantity of surfactant was studied, in terms of pore morphology, characterized through mercury intrusion porosimetry (MIP), N₂ adsorption desorption and SEM images. A new explanation for the phase separation mechanism is provided, using, and adding to the scientific background provided in Chapter 2. Finally, solid-state ²⁹Si and ¹³C nuclear magnetic resonance (NMR) and a detailed Fourier-transform infrared spectroscopy (FTIR) spectroscopy analysis were applied to these microspheres, elucidating on their chemical composition.

Chapter 4 introduces the creation of multicomponent silica-titania (ST) and silica-titania-hafnia (STH) MICROSCAFS® using an adapted method from that developed for S MICROSCAFS® (Chapter 3). It is based on the original articles by Mário Vale *et al.* [42] and Mário Vale and Ana C. Marques [43]. Besides leading to multi-oxide compositions, it has the benefit of using constant synthesis temperature (as low as room temperature) and a reduced synthesis duration (from ~6 h to 1 h 30 min) together with higher reproducibility of the obtained MICROSCAFS® features.

Chapter 4.1 studies the effect of varied synthesis parameters, namely synthesis temperature, GPTMS/TEOS molar ratio, Ti precursor/chelating agent molar ratio and emulsion water(W)/oil(O) mass ratio on the architecture, pore size and morphology, of the MICROSCAFS®, including a critical discussion around phase separation thermodynamics and sol-gel kinetics phenomena. Optical microscopy photos, SEM images, energy-dispersive X-ray spectroscopy (EDS), FTIR spectroscopy, thermogravimetric analysis (TGA), MIP, and N₂ adsorption isotherms are used to study the morphology and atomic composition of the different MICROSCAFS®. Rheological studies of the different precursor solutions were made to monitor the gelation and crosslinking over time in the first stages of the sol-gel reaction. X-ray computed tomography was applied to get a broader, more accurate picture of the morphology of the MICROSCAFS® by observing cross-sectional cuts, which is only possible through this technique. Finally, the mechanical properties of the MICROSCAFS® were assessed through compression tests in a Instron 5566 universal testing machine. Chapter 4.2 reports on cryo-SEM simultaneously

combined with EDS to visualize phase separation phenomena and study the chemical elemental composition at specific regions of the samples and reaction times, elucidating the first stages of the MICROSCAFS® formation process. It includes a graphical representation of the formation mechanism of the multi-oxide MICROSCAFS®.

The ST MICROSCAFS® produced in the previous chapter are then applied to photocatalysis in Chapter 5. ST MICROSCAFS® with different porosities and sizes were used as support materials to photocatalytic NPs and were tested in batch and flow for the photocatalytic degradation of MO dye. The MICROSCAFS® were loaded with commercial P25 Degussa TiO₂ NPs using a wet impregnation method. SEM images, EDS, and FTIR spectroscopy were used as usual to study the internal and external morphology and the chemical composition of the photocatalytic MICROSCAFS®. A new kinetic model for the continuous flow reactor was developed to yield the simulation of the process, and the transformation products were analyzed by liquid chromatography-tandem high resolution mass spectrometry (LC-HRMS/MS) over time, shedding light on the extent of the pollutant degradation.

Chapter 6 recontextualizes the objective of this thesis and describes the most relevant findings and conclusions from the previous chapters (3 to 5), emphasizing the primary accomplishments and contributions of this study. Furthermore, it also leaves some suggestions for future works to promote a leverage from this work.

1.3. Outputs

Papers

1. M. Vale, M. V. Loureiro, M.J. Ferreira, A.C. Marques, Silica-based microspheres with interconnected macroporosity by phase separation, *J Solgel Sci Technol* 95 (2020) 746–759. <https://doi.org/10.1007/s10971-020-05257-4>
2. A.C. Marques, M. Vale, Macroporosity Control by Phase Separation in Sol-Gel Derived Monoliths and Microspheres, *Materials* 14 (2021) 4247. <https://doi.org/10.3390/ma14154247>
3. M. Vale, S. Orišková, A. Mariquito, L. Reis, M. Pinto, A.C. Marques, Multicomponent oxide microspheres with designed macroporosity

(MICROSCAFS®): a customized platform for chemicals immobilization, RSC Adv 13 (2023) 12951–12965. <https://doi.org/10.1039/D3RA00895A>

4. M. Vale, A.C. Marques, Mechanistic Study of the Formation of Multicomponent Oxide Porous Microspheres (MICROSCAFS®) by Cryo-Scanning Electron Microscopy, Gels 9 (2023) 704. <https://doi.org/10.3390/gels9090704>
5. M. Vale, B.T. Barrocas, R.M.N. Serôdio, M.C. Oliveira, J.M. Lopes, A.C. Marques, Robust Photocatalytic MICROSCAFS® with Interconnected Macropores for Sustainable Solar-Driven Water Purification, Int J Mol Sci 25 (2024) 5958. <https://doi.org/10.3390/ijms25115958>

Oral presentations

1. Invited oral presentation “Fundamentals on porous particles for chemicals immobilization”, at the Workshop TPMI2023 (8-12 May 2023) organized by the Technological Platform on Microencapsulation and Immobilization (TPMI) group at Instituto Superior Técnico, Lisbon, Portugal.
2. Invited oral presentation “Immobilization on tailored porous microspheres (MICROSCAFS®) and its applications”, at the Workshop TPMI2023 (8-12 May 2023) organized by the Technological Platform on Microencapsulation and Immobilization (TPMI) group at Instituto Superior Técnico, Lisbon, Portugal.

Poster presentations

3. Encontro Ciência 2022 (May 2022) – Lisbon, “Engineered photocatalytic porous microspheres for water purification”, contributors: Mário Vale, Ana C. Marques
4. SolGel 2022 (July 2022) – Lyon, “Enlightenment of multicomponent oxide porous microspheres generation”, contributors: Mário Vale, Ana C. Marques
5. PhD Open Days (November 2022) – Lisbon, IST, “Enlightenment of multicomponent oxide porous microspheres (MICROSCAFS®) generation”, contributors: Mário Vale

Workshop participation

1. Escola Ibero-Americana de Catálise (EICAT) (September 2018) organized by Federação Ibero-Americana de Sociedades de Catálise (FISoCat) and Sociedade Portuguesa de Química (SPQ) at Instituto Superior Técnico, Lisbon, Portugal.

2. Photonic glasses by sol-gel (July 2022) organized by the International Sol-Gel Society (ISGS) and the International Commission on Glass (ICG) during the SOLGEL 2022 conference at Lyon, France.

Event organization

1. Member of the organizing committee of the Workshop TPMI2023 (8-12 May 2023) organized by the Technological Platform on Microencapsulation and Immobilization (TPMI) group at Instituto Superior Técnico, Lisbon, Portugal. Role: member of the organizing committee.

Projects

1. Team member at FCT Project "SOLAR2CLEAN" - Engineered solar light driven photocatalytic systems for wastewater purification (PTDC/EQU/EQU/1056/2020); PI: Professor Ana C. Marques, CoPI: Professor Susete Dias;

Chapter

2

Literature review: Macroporosity control by phase separation in sol-gel derived monoliths and microspheres

The following chapter is based on the peer-reviewed article:

A.C. Marques, M. Vale, Macroporosity Control by Phase Separation in Sol-Gel Derived Monoliths and Microspheres, Materials 14 (2021) 4247.
<https://doi.org/10.3390/ma14154247>

2.1. Background on Sol-gel and Phase Separation

The sol-gel technique represents a wet chemistry approach in chemical synthesis, employed to create glassy or ceramic materials, along with composites, at relatively mild temperatures. This method has demonstrated versatility in generating diverse compositions, primarily oxides, manifesting in various forms such as monoliths, coatings, thin films, composites, porous membranes, powders or particles, and fibers.

The sol-gel technique is a bottom-up process that includes the preparation of a suspension of colloidal particles called “sol” followed by gelation and then the removal of the liquid existing in fine interconnected channels within the wet gel [44]. The liquid sol is composed of suspended nanometric particles that originate from the chemical reaction of molecular precursors like metal alkoxides and/or organometallic compounds (or metal salts or oxides). Simultaneous and competitive hydrolysis and condensation reactions occur during the transition from sol to a three-dimensional network structure called “gel”. Alcohols, which are removed by volatilization, are formed as by-products of the hydrolysis whereas the (poly)condensation leads to the establishment of metal (M)-oxygen-metal bond, or Si-O-Si in the case of silicon, releasing an alcohol (less common) or water in the process (Figure 2.1).

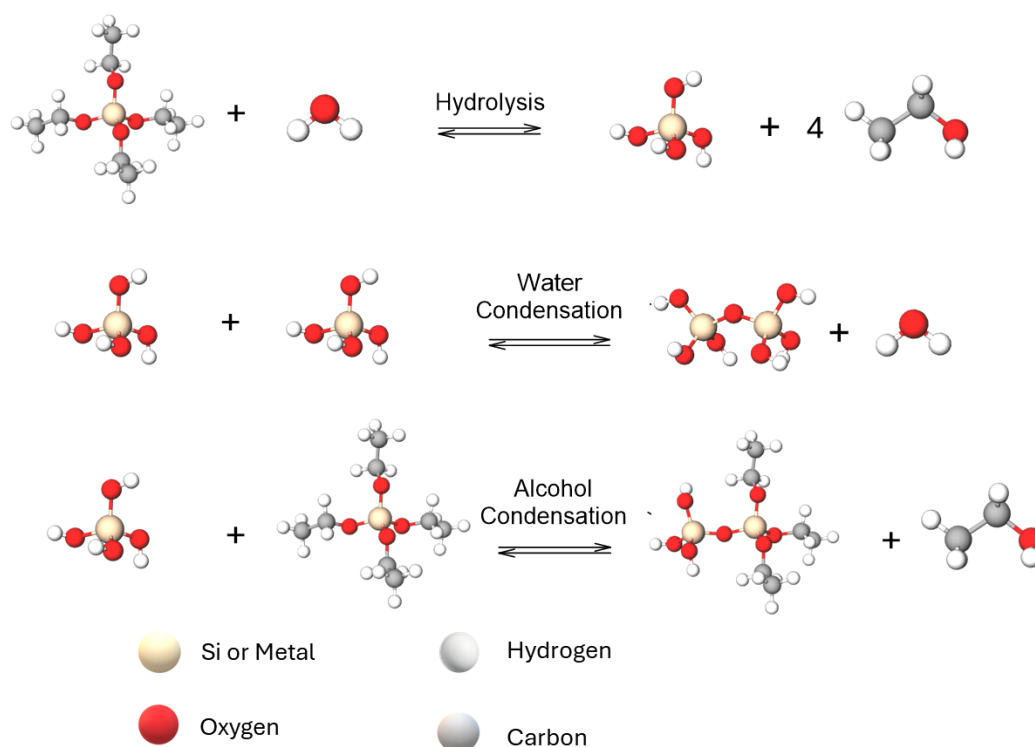


Figure 2.1. Sol-gel hydrolysis and condensation reactions in alkoxides.

The generation of silanols, formed through the hydrolysis reactions of alkoxide (e. g. silanes) or metal precursors, are necessary for condensation to occur in alkoxide-based systems.

The structure of the porous interconnected network of a gel depends mainly on the size and shape of the sol particles and the kinetics of the formation of covalent bonds between these particles. Wet gels can be dried but often shrink by a factor of 5-10 due to capillary forces. The resulting dried gel is called “aerogel” or “xerogel.” Aerogels are formed when the liquid is extracted at a supercritical state, whereas xerogels are formed when the liquid evaporates at room temperature.

Synthesis parameters like the type of precursor, pH, alkoxy group to water ratio (R_w), type of solvent, temperature, and relative and absolute concentration of the components in the precursor mixtures influence the rates of hydrolysis and condensation steps, and thus the final texture and properties of the sol-gel materials [45]. Reaction time and catalyst amount also have a relevant impact in the degree of condensation of the silane network [46]. Metals, such as Ti, Zr, Hf, are more electropositive (Lewis acidic) than Si and thus more susceptible to a nucleophilic

attack, exhibiting faster gelation. Moreover, the preferred coordination number is higher than the valence. Different kinetics must be dealt with using complexation strategies or lower temperatures, for example.

In generic terms, phase separation is a spontaneous thermodynamic phenomenon, which results in the creation of, at least, two distinct phases from a homogeneous mixture. In general, phase separation starts from a molecular length scale and proceeds with the growing of the characteristic size (mean dimension of a set of skeleton and pore) of phase separated domains with time toward a macroscopic length scale. The dynamics of phase separation was studied intensively in the 20th century [47,48], notwithstanding recent studies have been devoted to this topic, namely the coarsening behavior of network-forming phase separation of colloidal suspensions [49,50]. Phase separation by spinodal decomposition occurs when the mixture is plunged into the unstable region of the miscibility window in an equilibrium phase diagram. In this case, the two developed phases, when in comparable volume fractions, form a 3-D interconnected two-phase morphology with a narrow domain size distribution, which is at the basis for interconnected macroporosity generation [51].

The thermodynamic process of mixed solutions containing polymers, adapted to the case of macroporous materials generated by phase separation, is described by the Flory-Huggins theory, which centers on the expression for the free energy of mixing derived from a lattice model [52–55]. The theory is constituted by combinatorial entropy terms associated with polymer chain configurations on the lattice, as well as an enthalpic contribution owing to interactions between the different species.

The Gibbs free energy change of mixing, ΔG_m , is given by Equation 2.1:

$$\Delta G_m = \Delta H_m - T\Delta S_m \propto RT \left(\frac{\phi_1}{P_1} \ln \phi_1 + \frac{\phi_2}{P_2} \ln \phi_2 + \chi_{12} \phi_1 \phi_2 \right) \quad (2.1)$$

where R is the gas constant, T is the temperature, ϕ_i and P_i are the volume fractions and the degrees of polymerization of the two different components (i=1 and i=2),

which can be polymerizable, or not (e.g. in the case of solvents), and χ_{12} is the Flory interaction parameter which describes the compatibility between both components.

The first two terms inside the parenthesis, Equation 2.1, are related to the entropic contribution to ΔG_m , and the last term to the enthalpic contribution of the system. Therefore, an increase of the polymerization/polycondensation degree, i.e. the formation of non-polar gels (e.g., siloxanes) imposes a decrease in the entropy change ΔS_m , but also an increase in the enthalpy change ΔH_m , due to the arising of polarity differences between the gel and solvent (increased χ_{12}), which results on repulsive interactions. Both will contribute to a gradual increase of ΔG_m , according to Equation 2.1, and the driving force for phase separation is therefore generated.

A phase diagram reflecting the phase behavior of any mixture can be made using the Flory-Huggins solution theory (Figure 2.2), where the binodal and spinodal lines will be reached by solving $\left(\frac{d\Delta G_m}{d\phi_1}\right) = 0$ and $\left(\frac{d^2\Delta G_m}{d\phi_1^2}\right) = 0$, respectively, for the interaction parameter χ_{12} , namely χ_b or χ_s . The definition of χ_{12} can be used to establish the temperature dependence of polymer miscibility, and the most common experimentally-derived form to demonstrate such dependence is given by Equation 2.2 [56], which includes temperature-independent terms, i.e. constants A (“entropic part” of χ_{12}) and B, both tabulated for many polymer blends, where $\frac{B}{T}$ is the “enthalpic part” of χ_{12} :

$$\chi_{12} = A + \frac{B}{T} \quad (2.2)$$

The Flory-Huggins theory assumes that the volume per monomer do not change upon mixing, whereas in most real polymer blends it does. Some monomers may pack together better with certain other monomers. The volume change on mixing and local packing effects are represented by the temperature-independent additive constant A.

In the phase diagram, the point where binodal and spinodal phases overlap is the critical point or critical value of the Flory interaction parameter. The lower critical solution temperature (LCST) and the upper critical solution temperature (UCST) are

the maximum or minimum temperature below or above which the components of a mixture are miscible for all compositions, respectively. Depending on the nature of the interaction, the Flory-Huggins theory can predict the phase behavior of mixtures with primarily repulsive (UCST behavior) or attractive (LCST behavior) interactions, namely for a cooling process and for positive values of B . In this case, $B > 0$, χ_{12} increases as temperature is lowered (Equation 2.2), leading to immiscibility in a UCST system. Figure 2.2 shows a schematic phase diagram of a general binary system showing UCST behavior. ϕ_c and ϕ_N are the compositions where spinodal decomposition and nucleation-growth happen, respectively, at temperature T_1 .

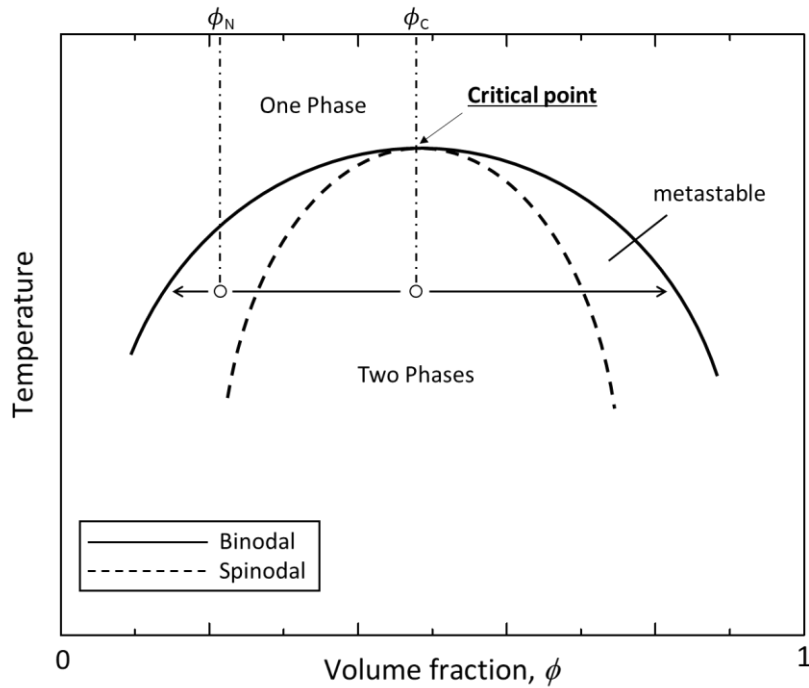


Figure 2.2. Illustrative phase diagram of a binary system showing UCST behavior. ϕ_c is the volume fraction of the critical composition where spinodal decomposition occurs at temperature T_1 . ϕ_N is the volume fraction of composition where nucleation-growth occurs at temperature T_1 . Adapted from [57].

Critical point, or critical composition, ϕ_c , is given by the point where the binodal and spinodal lines coincide, i.e., in a binary blend showing UCST behavior, to the highest point on the spinodal curve, so that it corresponds to $\left(\frac{\partial \chi_s}{\partial \phi}\right) = 0$. The solution of this equation gives ϕ_c (Equation 2.3), which is found to depend on the degree of

polymerization of both components, related with their number of statistical segments, or lattice sites, N_1 and N_2 .

$$\phi_c = \frac{\sqrt{N_1}}{\sqrt{N_1} + \sqrt{N_2}} = \frac{1}{1 + \sqrt{\frac{N_2}{N_1}}} \quad (2.3)$$

Concerning spinodal decomposition, in Figure 2.3a, the arrow pointing down indicates a decrease in the solution temperature and, therefore, a decrease in the degree of freedom between species and subsequently the occurrence of phase-separation - physical cooling or physical quenching. On the other hand, by increasing the number of chemical bonds, such as in a polycondensation process, the degree of freedom also decreases, which makes the mixture to behave as if the physical temperature is decreased by reducing the thermal disturbance of the molecular system. This phenomenon - chemical cooling or chemical quenching - has an analogy with the typical physical cooling that is exhibited by a glass transition [57]. In this sense, Figure 2.3b shows the effect of polymerization–condensation reaction on course, for instance the formation of siloxane oligomers, which increases the polymerization degree and moves the critical point ϕ_c (Equation 2.3) in the diagram, plunging the system into the two-phase region - chemical cooling or chemical quenching. This latter process and how it can be used to create macroporous structures was first studied in sol-gel systems (monoliths) by Nakanishi, *et al.* in the early nineties [16,19,57].

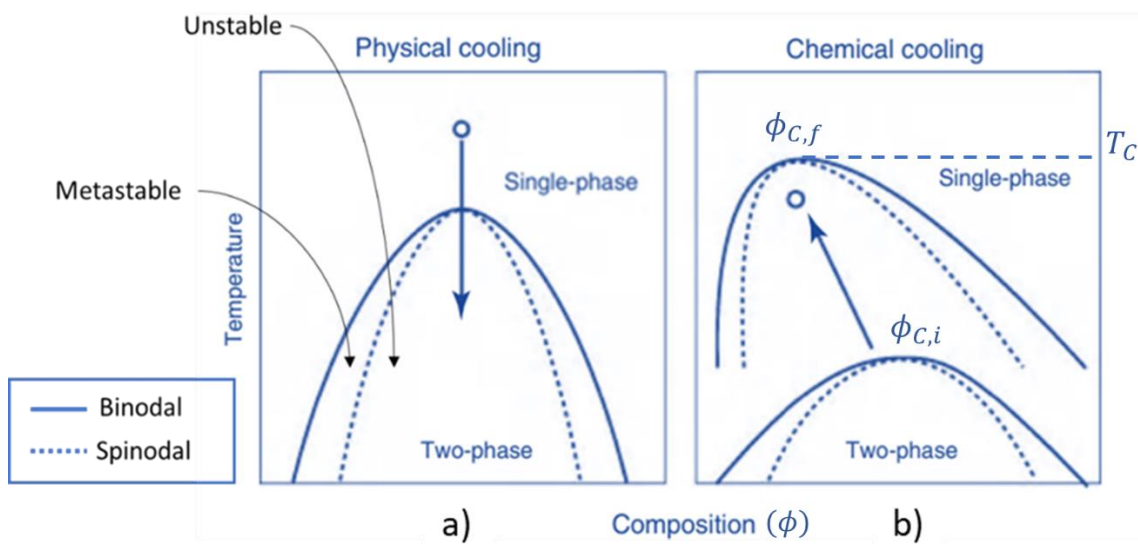


Figure 2.3. Illustrative phase diagrams of systems with immiscibility window for comparison of physical and chemical cooling phenomena. Reprinted, with adaptations, by permission from Springer Nature Customer Service Centre GmbH: Springer, J. Sol-Gel Sci. Technology, Polymerization-induced phase separation in silica sol-gel systems containing formamide, Kaji H, Nakanishi K, Soga N, © Kluwer Academic Publishers. Manufactured in The Netherlands (2013) [19].

2.1. Macroporous silica (SiO₂) monoliths

2.1.1. Pioneering works

The growth and topology of the macromolecules which precede gelation in several sol-gel systems were studied by small angle x-ray scattering (SAXS) and allowed Schaefer and Keefer in 1984 [58] to conclude that the growth and degree of cross-linking of polymer chains, occurring during gelation and under catalytic conditions, may in turn, induce and control phase separation in silicate sol-gel systems. This finding was at the origin of the work by Nakanishi and Soga, in 1991 [59], where for the first time the concept of phase separation in sol-gel systems was applied to the macroporosity control in silica-based monolithic materials.

Their work regarded the formation of micrometer-range porous morphology in silica gels prepared from tetramethoxysilane (TMOS)-methanol solutions that contained poly(sodium-4-styrene sulfonate) (NaPSS) as a porogen agent, under acidic conditions using nitric acid [16,59]. NaPSS is a strongly ionic, water-soluble polymer, which exhibits a limited solubility in alcohols. Different porosity levels were achieved depending on the NaPSS molecular weight (Mw), NaPSS quantity and

temperature employed in the synthesis, explained by spinodal phase separation, which was induced by the chemical cross-linking and diffusional limitation of the reacting TMOS precursor molecules. In this case, a monophasic solution containing one polymeric compound and polymerizable species was found to experience polymerization-induced spinodal phase separation. The term “chemical cooling” was introduced in this paper [16], since chemical reaction drives the change in free energy and is used to denote the “induction of spinodal phase separation by chemical reaction”, including that by polymerization/polycondensation of silicon alkoxides.

NaPSS, is an additive component which has weak interaction with the siloxane network, i.e. hardly establishes hydrogen bonding with the hydroxyl groups on silica surface, and the resulting phase separated system consists of a silica-solvent rich phase and NaPSS-solvent rich phase counterpart. This case is an example of phase separation of the type “**silica versus solvent-polymeric additive**”, involving a **tri-component system “silica-weakly hydrogen bonding polymer-solvent”**. The phase separation in this system is driven by the entropy loss due to the polymerization of silica and thus depends directly on the mutual Mw of the constituents. Other additives that play a similar role are *in situ* esterified poly(acrylic acid) (HPAA) [60–63] and combinations of styrene-divinylbenzene/polydimethylsiloxane), methacrylate/poly(ethylene oxide) (PEO), and acrylamide/PEO [64].

As presented in Figure 2.4, the size of the interconnected structure (characteristic size) increases with the NaPSS concentration, for 60 °C, from ca. 0.2 to 8 μm [16]. The same was also found to happen for 40 °C. The increased temperature promotes the polymerization reactions and improves the mutual solubility of the constituents. Solubility of the NaPSS in the reacting solutions was found to influence the “chemical cooling depth”, i.e. the characteristic size of the porous structure: the higher the solubility, the lower the characteristic size. So, for higher temperatures, more NaPSS is required to achieve the same level of characteristic size.

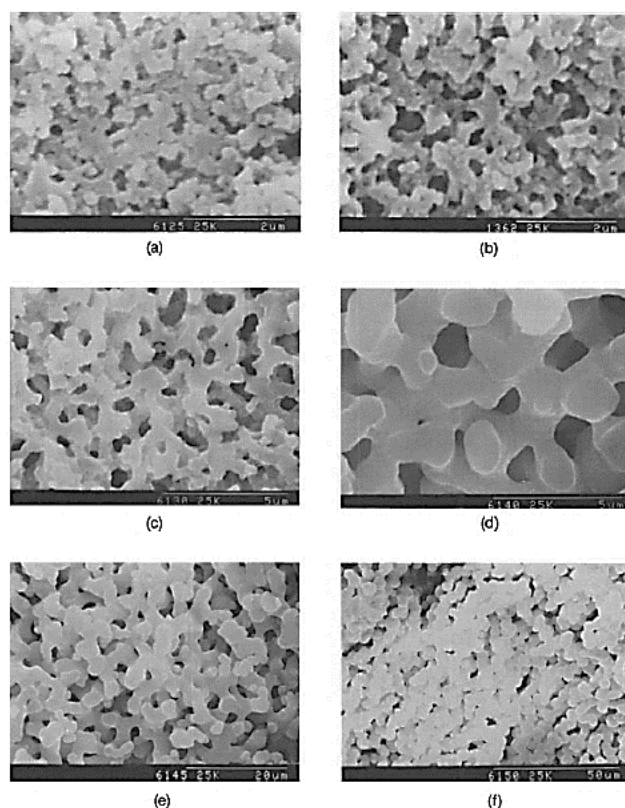


Figure 2.4. Variations in gel morphology with increasing NaPSS concentration (C , in mol mol⁻¹), at 60 °C for NaPSS Mw between 50000 and 100000: (a) $C = 0.179$, scale bar=2 μm , (b) $C = 0.187$, scale bar=2 μm , (c) $C = 0.194$, scale bar=5 μm , (d) $C = 0.201$, scale bar=5 μm , (e) $C = 0.208$, scale bar=5 μm , (f) $C = 0.215$, scale bar=50 μm . Reprinted with permission from K. Nakanishi and N. Soga, *J. Am. Ceram. Soc.* Copyright © 1991 WILEY-VCH Verlag GmbH & Co. KGaA, Weinheim [16].

Nakanishi and Soga, in their pioneering paper [16], introduce the following mechanistic concept: spinodal phase separated structure development (upward movement of the phase diagram, “chemical cooling” of the system), followed by the “freezing” of such structure by the subsequent gelation of silica-rich phase. This results in interconnected morphologies, but various other possible structures, with different characteristic sizes, can be reached in the coarsening stages of spinodal decomposition, as Figure 2.5 represents, depending on how far away it is from the critical composition, when the structure “freezes”. At off-critical compositions (A and C), the break-up of the interconnected structure (percolation-cluster transition) occurs earlier than at near-critical compositions. Composition B (critical composition, ϕ_c) yields an interconnected macroporous structure independently if it is an early, or late freezing. An early freezing of the coarsening structure by gelation results in a finer structure (small characteristic size) with higher connectivity. The larger the time difference between phase separation and gelation (late freezing), the

coarser the structure will become (larger characteristic size), and, in some cases (for off-critical compositions), even breaking up into fragmented particles with no monolithic structure being obtained.

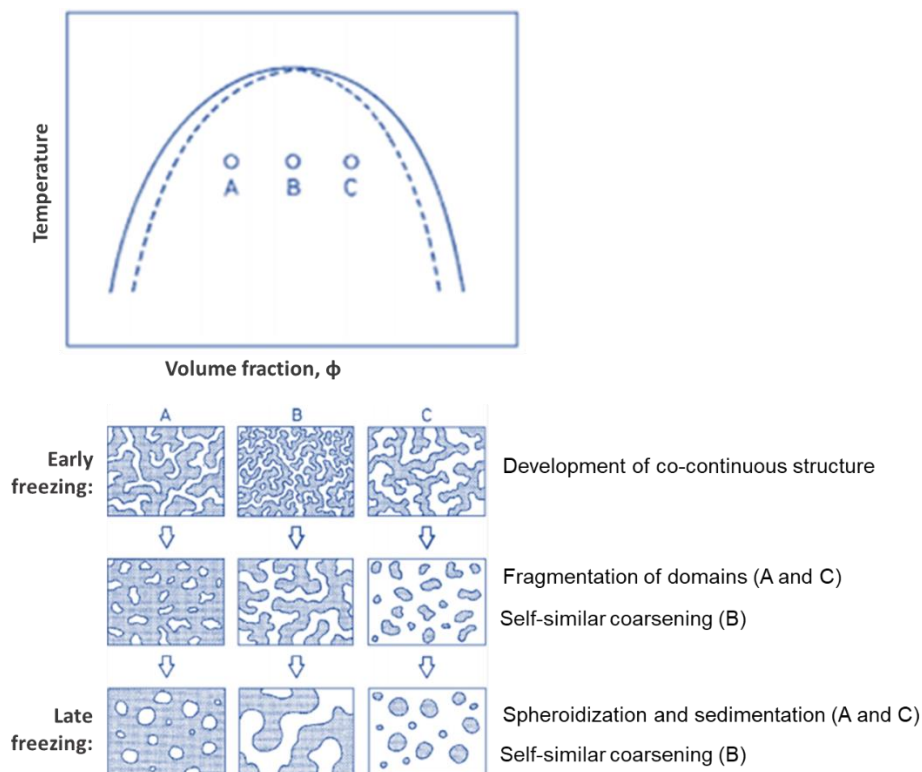


Figure 2.5. Possible structures at various coarsening stages of spinodal decomposition. *Reprinted (and adapted) with permission from K. Nakanishi and N. Soga, J. Am. Ceram. Soc. Copyright © 1991 WILEY-VCH Verlag GmbH & Co. KGaA, Weinheim [16].*

It is, therefore, stated that all parameters affecting the relative rates of phase separation *versus* gelation have a significant influence on the morphology of the final gel, including mesoporosity, degree of macroscopic phase separation, and interconnected macroporosity. Examples of parameters resulting in faster sol-gel transitions are higher temperatures, water/precursor ratio or pH value changes, etc.

The same authors also studied the effects of temperature, M_w , catalytic conditions and concentration of a carboxylic acid, as polymeric additive, on the phase separated morphology in TEOS-HPAA system [60–63]. The polymeric additive in this case displays the same type of weak interaction with the silica oligomers as NaPSS, but more solubility both in water and alcohols, resulting in different phase separation and gelation behaviors, when compared to the strongly ionic, alcohol-insoluble

NaPSS. In the TEOS-HPAA system the interconnected network size was found to depend weakly on the alcohol-water ratio. Experiments where the catalyst (nitric acid):water ratio and reaction temperature were fixed [60], revealed, for increasing quantities of HPAA (with Mw 90000) an early “freezing” (lower gelation time). The lowest values of HPAA concentration yielded microporous monoliths without detectable pores by SEM, while, on the other hand, the highest values of HPAA concentration resulted in a fragmented skeleton with spherical silica particles of a few micrometers. Interconnected macroporosity, characteristic of spinodal decomposition, was achieved for intermediate values of HPAA concentration. In what regards co-solvent (ethanol, or methanol) concentration, the higher its value, the more diluted is the system and the lower the polymerization rate (higher gelation time). Also, segregation strength decreases, which will drive the system to a later phase separation and give fine interconnected domains [60].

A range of average Mw of HPAA, between 10000 to 250000 was studied [61]. Larger HPAA Mw was reported to lead to a general increase in characteristic sizes and decrease in gelation time. Nakanishi and Soga [61] also concluded that the amount of HPAA to obtain interconnected gel morphology decreased proportionately to the inverse square root of Mw. On the other hand, a higher concentration of the catalyst (nitric acid) was found to result in greater characteristic sizes [62], as occurred for NaPSS [16]. To conclude this study with HPAA, different chemical additives, organic solvents, were tested to assess their influence both in the HPAA dissolution, and hydrolysis and gelation process of the alkoxy silane [63]. As it is demonstrated in Figure 2.6, different types of morphologies were obtained depending on the type of solvent used.

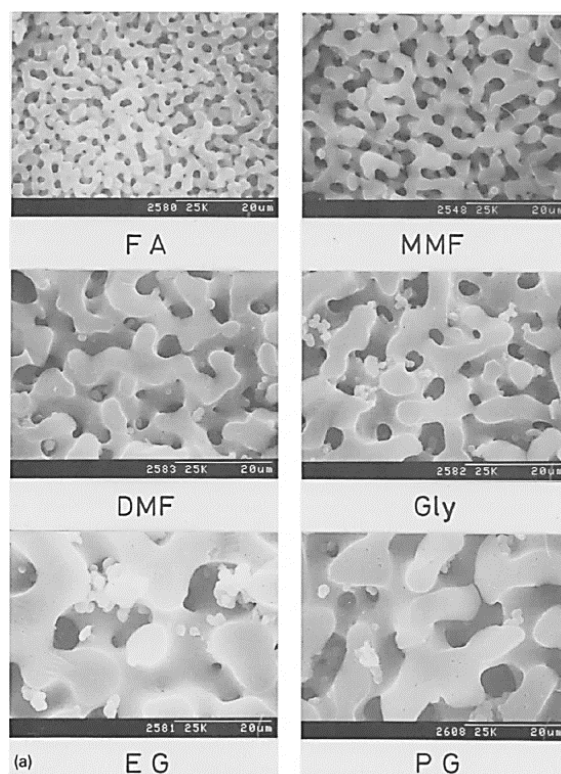


Figure 2.6. Effect on the gel morphologies with the type of organic solvent, for the system TEOS-HPAA (of Mw 250000) and reaction temperature 80 °C. Solubility parameter, δ_s ((cal cm⁻³)^{1/2}): formamide (FA) – 19.2, N-methylformamide (NMF) – 16.1, N,N-dimethylformamide (DMF) – 12.1, glycerol (Gly) – 16.5, ethylene glycol (EG) – 14.6 and propylene glycol (PG) – 12.6. Reprinted from J. Non. Cryst. Solids, Vol. 142, N. Soga, K. Nakanishi, Phase separation in silica sol-gel system containing polyacrylic acid. IV. Effect of chemical additives, Pages 45-54, Copyright (1992), with permission from Elsevier [63].

The authors claimed that solvents which increase the solubility of HPAA (higher solubility parameter) and accelerate the polymerization of silica, e.g., formamide, lead to the formation of fine interconnected structures (smaller characteristic sizes) for a large range of compositions. It was also possible to observe that structures can be divided into two solvent groups: (i) solvents containing an amide group; (ii) solvents with a polyol functional group, with the former ones giving finer structures than solvents that contained alcoholic moieties. Sorbitol, one of the sugar-alcohols with similar molecular structure to glycerol, was also included in this study because of its expected tendency to accelerate polymerization of silica by increasing the activity of the acid catalyst. It was found to be quite effective in promoting fine domains in the present system, due to its ability to reduce the gelation time and high compatibility with the other constituents [63].

Following this previous work, Kaji et al. [19], from the same group, further explored the effect of formamide, but without using any organic polymeric additive. This is an example of phase separation of the type **“silica (hydrophobic) versus poor solvent with common solvent”**, involving a tri-component system **“silica - good solvent - poor solvent”**. This strategy was presented as an alternative to the previous methodology (phase separation between organic polymer-rich and silica-rich domains).

A system consisting of alkoxide (TMOS), a fixed amount of water (H_2O/Si molar ratio <1.5) and formamide, at the molar ratio 1:1.5:2.5, was carried out, under acid-catalyzed condition, where formamide acts as a highly polar solvent, i.e. a poor solvent to the polymerizing silica [19]. Formamide is known to exhibit a hydrogen bonding character and is hydrolyzed to produce ammonia, therefore increasing the pH and polycondensation rate, in the presence of a strong acid [57]. In this case, the gel phase is composed by silica and a good solvent and the fluid phase is formed by both the good solvent and the poor solvent (formamide). There is the formation of silica-rich and solvent-rich phases, and so, Equation 2.3 with $N_{1(\text{solvent})} = 1$ can be used in the formamide system, contrary to the case of HPAAs system, where $N_{1(\text{organic polymer+solvent})}$ is much larger than unity. This results on a $\phi_{C,f}$ shifted to lower silica concentration during phase separation for the formamide system, and more asymmetric binodal and spinodal lines, as shown in Figure 2.7 [19].

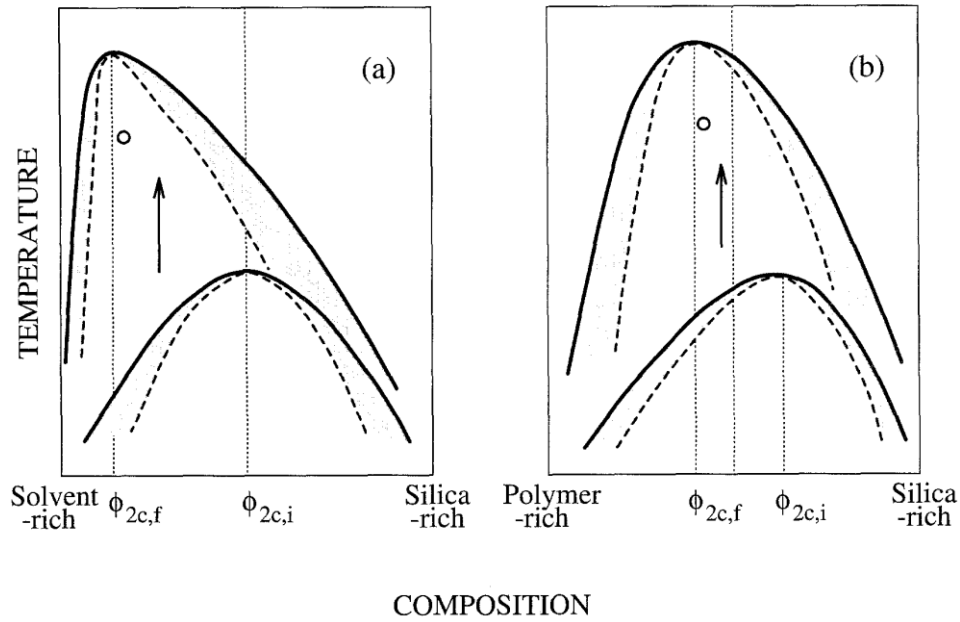


Figure 2.7. Schematic phase diagrams for the formamide system (a), and for an organic polymer containing system (b). $\phi_{c,i}$ and $\phi_{c,f}$ are critical compositions just after all the constituents are mixed and during phase separation, respectively. The value of $\phi_{c,f}$ in formamide system is much smaller (more silica-poor), and binodal and spinodal lines are more asymmetric than those in HPAA system. Reprinted, with adaptations, by permission from Springer Nature Customer Service Centre GmbH: Springer, J. Sol-Gel Sci. Technology, Polymerization-induced phase separation in silica sol-gel systems containing formamide, Kaji H, Nakanishi K, Soga N, © Kluwer Academic Publishers. Manufactured in The Netherlands (2013) [19].

Such qualitative explanation, based on the effect of the polymerization degree on the Flory-Huggins' type ΔG_m leads to observe that the composition region in the formamide system that gives interconnected structures tends to be more silica-poor than that in HPAA system, resulting in the formation of continuous, interconnected, but thinner silica skeletons. In fact, it was also reported [19] that the composition region that gave interconnected structures, in the formamide system, was much more limited and their characteristic sizes were much smaller, typically lower than $10 \mu\text{m}$, than those of the previously reported systems containing an organic polymer [16,19,52,56,57].

Influence of the Si precursor on the gelling process and, therefore, on the gel morphology, was also reported [57]. Methyltrimethoxysilane (MTMS), when compared with TMOS, exhibits reduced functionality, which together with the presence of unhydrolyzable methyl groups attached to silicon, results in slower gelling process, i.e. slower structure formation giving more time for coarsening of the domains. It could lead to a delayed polycondensation *versus* phase separation,

however the dependence of gel morphology on reaction parameters might be easier to control.

These pioneering studies were followed by experiments incorporating additives to induce phase separation on the polymerization of silica, which display a strong interaction with silanols through hydrogen bonding or electrostatic attraction. This type of additive molecules expose their hydrophobic moiety towards surrounding polar solvent and bond with hydroxyl groups of the hydrolyzed silanes, reducing their affinity with the polar solvent. So that, in this case, phase separation takes place between the solvent phase and the Si oligomers covered with the additive molecules. This is an example of phase separation of the type **silica-polymeric additive versus solvent, involving a tri-component system “silica-strongly hydrogen bonding polymer-solvent”**. This category of phase separation, driven by repulsive interaction between the solvent mixture and the polymeric additive adsorbed on the Si oligomers is an enthalpy driven process.

The minimum requirement for the polymeric additive component to induce such kind of phase separation is a strong hydrogen bond with the Si oligomers, which results in a lowered affinity with the polar solvent phase. Studies show that the polymeric additive's M_w does not play a great role in this process, and that polymerizing silica, despite being able to distribute both at the polymeric additive-rich and at the solvent-rich phases, always gels prior at the polymeric additive-rich phase [57]. This indicates that siloxane oligomers present at the polymeric additive-rich phase have higher M_w , or/and are located closer to each other, than those in the solvent-rich phase. A compromise in terms of hydrogen bond strength must be taken into account in order to promote phase separation, without jeopardizing polycondensation reactions between silanols. Examples of polymers, or other compounds fulfilling this requirement are PEO, poly(acrylamide) (PAAm), poly(vinylpyrrolidone) (PVP), nonionic surfactants containing polyoxyethylene units [65], but also ionic surfactants, such as sodium alkylsulfates and alkyltrimethylammonium salts [64].

One of the first polymeric additives to be tested in this type of phase separation systems was PEO, which is a non-ionic polymer that exhibits a LCST type phase diagram with water, i.e. dissolves homogeneously in water at room temperature but phase separates upon heating to near the boiling point of water. PEO molecules interact with silica oligomers via the hydrogen bonding between the ether group in PEO and the silanol group in silica. Phase separation studies in silica sol-gel systems containing PEO, performed by the same research group [17,66,67], showed that the volume fraction of pores mainly depend on the solvent fraction and the domains size decreases with an increase of the PEO/silica ratio, as observed in Figure 2.8.

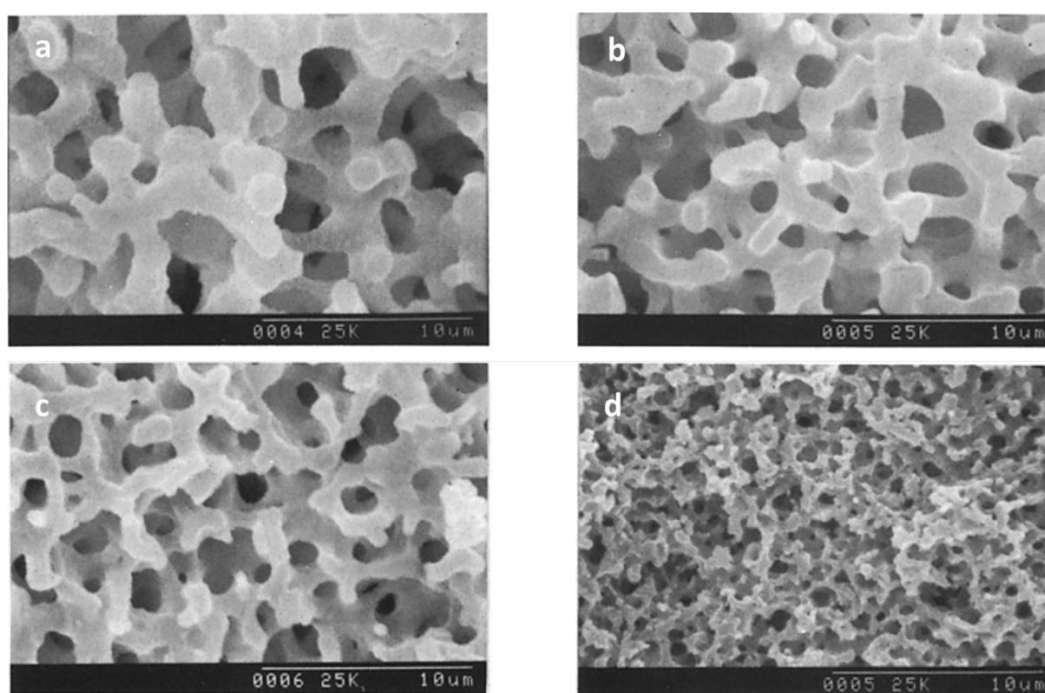


Figure 2.8. Scanning electron images of dried gel morphology for increasing quantities of PEO (100000 Mw), in a synthesis that involves 6.51 g of TEOS, 0.81 g of 60% aq. HNO₃ and 8 g of H₂O: a) 0.30 g PEO; b) 0.40 g PEO; c) 0.50 g PEO; d) 0.60 g PEO. Reprinted by permission from Springer Nature Customer Service Centre GmbH: Springer, J. Sol-Gel Sci. Technology, Phase separation kinetics in silica sol-gel system containing polyethylene oxide. I. Initial stage, Nakanishi K, Yamasaki Y, Kaji H, Soga N, Inoue T, Nemoto N, © 1994 Kluwer Academic Publishers, Boston. Manufactured in The Netherlands (1994) [66].

Gelation becomes slower (longer gelling time, t_g) with greater amounts of PEO, because the strong interaction of silica with PEO reduces the available silanol sites for polycondensation. For instance, t_g increases from 103 to 123 minutes, from a to d, in Figure 2.8 [66]. Moreover, the domain size of the solvent-rich phase generally decreases with the increase of PEO at relatively high concentration range, contrary

to the case of TMOS-NaPSS and TEOS-HPAA systems (entropy driven). The effects of the Mw of PEO and the reaction temperature were also investigated. Nitric acid was employed as catalyst for hydrolysis, and PEO grades of 8300, 10000 and 100000 Mw were used. The overall phase separation tendency of the PEO-silica-solvent system was consistently interpreted by considering the lowered solubility of PEO partly adsorbed onto silica oligomers in an aqueous solvent mixture. Therefore, the higher the Mw of PEO, the lower its concentration at which phase separation was found to occur. The present PEO-silica-solvent ternary system was reported to display a typical UCST behavior: the increased temperature leads to a delay of the onset of phase separation and accelerates the gel formation [67], therefore leading to smaller interconnected domains.

The incorporation of several kinds of nonionic surfactant additives, namely polyoxyethylene nonylphenylethers, at 1.2-2.2 g to 5.15 g of TMOS [65], also resulted in well-defined interconnected macropores, while the mesopores formation was tailored by solvent exchange procedures either in HNO₃ solution, or in NaOH solution. The length of the oxyethylene units in the surfactant molecules was found to play a role in the mesopore characteristics, in the sense that the shorter oxyethylene chains tended to be more incorporated in the gel phase and gave higher mesopore volume.

The selected works, referred in this sub-section, date from the decade of 1990-2000, and are the most representative studies reported on the obtention of silica porous monoliths, involving the three different sol-gel/phase separation systems: a) silica - weakly hydrogen bonding polymer - solvent; b) silica - good solvent - poor solvent; c) silica - strongly hydrogen bonding polymer - solvent.

2.1.2. Further developments on inorganic and inorganic-organic SiO₂ monoliths

Tetra-functional silanes, such as TEOS and TMOS, were the main Si precursors employed in the early works about this topic. Their relatively slow kinetics makes these compounds very easy to handle and thus very attractive. However, silanes with organic functionalities have been used to transfer other functionalities to the resulting inorganic-organic hybrid organosiloxane monoliths. For instance, the presence of alkyl groups covalently attached to Si atom, such as in MTMS,

dimethoxydimethylsilane (DMDMS), n-octyltriethoxysilane (nOTES) or hexadecyltrimethoxysilane (HDTMS) make the siloxane oligomers more hydrophobic and, therefore, more prone to phase separation, when compared to tetra-functional silane systems. It should be noted as well that the presence of specific organic functionalities, such as glycidyl, contributes to polymerization reactions, which also might favor phase separation processes and might avoid the use of phase separation inducer additives, such as those referred in section 3.1 [39]. Also, hybrid compositions, e.g. those resulting from MTMS and DMDMS, result in more flexible xerogels. Moreover, phenyltrimethoxysilane (PhTMS) has been used as a precursor to prepare phenyl-modified macro/mesoporous hybrid silica monoliths, targeting mechanical resistance, better pH stability and resistance to swelling and shrinking in many solvents [68].

Nonionic surfactants have been employed either to suppress excessive phase separation in hybrid compositions, and to tailor mesoporosity giving bimodal hierarchical pore morphologies.

Still on inorganic SiO₂ gels, Nakanishi et al. [65] in 1998 and Sato et al. [69], in 2001, reported the multiscale templating in TMOS derived systems, using nonionic surfactants, polyoxyethylene nonylphenylethers and PEO-b-PPO-b-PEO triblock copolymers, respectively. The latter one was Pluronic P123 having the molecular formula of (EO)₂₀(PO)₇₀(EO)₂₀. Later, P123 and another triblock copolymer, F127 of molecular formula (EO)₁₀₆(PO)₇₀(EO)₁₀₆, were used in combination with trimethyl benzene (TMB) cosolvent or swelling agent [70]. These surfactants functioned as structure-directing agents and phase separation inducers, whereas TMB worked as a pore expander and enhanced the interaction among the hydrophobic moieties of the structure-directing agent. Studying the relationship between the polymerization-induced phase separation, the cooperative assembly of the surfactant micelles and silica oligomers and the sol-gel transition was a central part of the work. Higher amounts of TMB coarsened the initially isotropic macroframeworks, giving a fibrous appearance. The shape of the pores changed from cylindrical to spherical for increasing concentrations of TMB. These nonionic surfactants are known to make hydrogen bonding between the silanol groups (Si-OH) and the ether oxygens of ethylene oxide (EO) units. Cationic surfactants, such as

n-hexadecyltrimethylammonium salts (CTAB for bromide, or CTAC for chloride), on the other hand, have also been used for generating phase separation, and are known to interact with the silica domain by orienting the polar head groups toward silica. The ionic attractive interaction and hydrophobicity of the attached alkyl group were found to cooperatively determine the phase separation tendency [71]. In these former cases, the amphiphilic block copolymer or cationic surfactants were used solely as phase separation inducers and supramolecular templating agents, however the mixture of C₁₄TAB and C₁₈TAB with PEO was also explored by Smått *et al.* [72]. Structures of high order, such as hexagonal or cubic arrays of cylindrical pores, could not be evidenced, however, the use of triblock co-polymers proved to be effective in templating the mesopores in the resulting macroporous silica gels.

Sol-gel/phase separation derived alkylene-bridged silsesquioxanes, with macroporosity, were obtained by Nakanishi *et al.*, from a bis(trimethoxysilyl)hexane (BTMH) - water - methanol system in acidic conditions [73] and compared to a methyltriethoxysilane (MTES) derived monolith. No polymeric phase inducer additive was used in this work, nor formamide, or other gelation promoter. The presence of unhydrolyzable methyl group attached to silicon, in MTES or MTMS silanes, was found to extend the composition region of phase separated morphology even to the water-silane binary compositions [57]. In the case of alkyltrialkoxysilanes, the phase separation tendency increases rapidly with an increase of the length of alkyl chain directly bonded to Si atom. However, in the case BTMH system, the co-continuous macroporous structure was obtained in the composition region containing higher water concentration (Si/water~1/30, molar ratio), than with MTES. Combinations of 4- and 3-functional alkoxysilanes, namely TMOS and vinyltrimethoxysilane (VTMS), and the employment of formamide as an additive polar solvent, resulted in the occurrence of phase separation in extended composition regions with high water concentration, especially at larger amounts of VTMS (e.g. TMOS/VTMS=20/80 molar ratio) [74]. The domain size and pore volume of the macroporous gels could be controlled by the alkoxide:water ratio and total solvent fraction, respectively.

In 2006 Dong *et al.* [75] presented an acid/base two-step method to obtain macroporous polymethylsilsesquioxane (PMSQ) monoliths, from MTMS, without the

use of phase separation inducer additives. In this study, hydrolysis and polycondensation proceed in acidic and basic aqueous media, respectively. Systems in which the gelation time was only slightly longer than the phase separation time (in 4-10 min) showed a significant fraction of macropores. Therefore, it was claimed that increasing the duration of the acid step, the size of polymerized clusters increases and leads to an early onset of phase separation relative to gelation and, therefore to larger macropores size, with narrow distribution [75], as observed in Figure 2.9. The observed shift from mesopores to macropores resulted in a decrease of surface area from 426.4 to 59.3 m²/g.

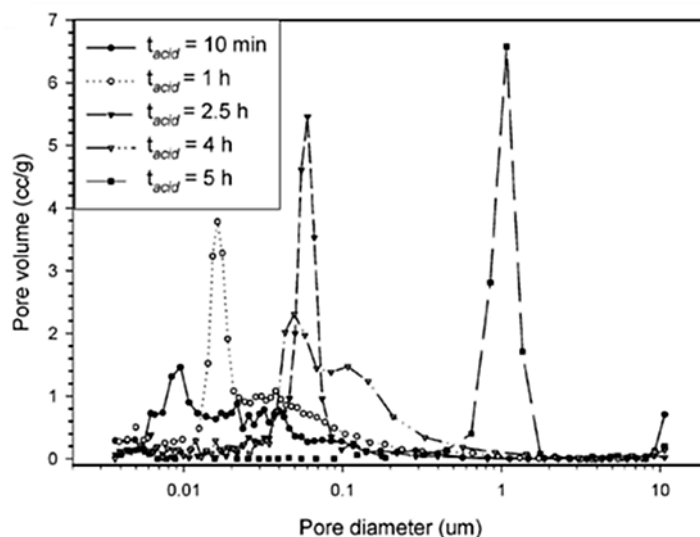


Figure 2.9. Differential pore size distribution of PMSQ monoliths achieved by using different durations of the acidic step, from 10 minutes to 5 h (dried at 300 °C). Measurements carried out by MIP. Reprinted (and adapted) with permission from Dong H, Brennan JD (2006) Controlling the morphology of methylsilsesquioxane monoliths using a two-step processing method. *Chem Mater* 18:541–546. <https://doi.org/10.1021/cm051900n> [75]. Copyright 2006 American Chemical Society.

A few years later, Kanamori et al. [76] studied the transition of mesoporous to hierarchical macro/mesoporous gels in a hybrid PMSQ system derived from MTMS, and Tao *et al.* reported the application of these new hierarchical monoliths to oil removal [77], in 2011. An acid/base two-step method (one pot reaction) was employed, together with the use of a triblock copolymer, F127, which is known to establish weak attractive interactions with methylsiloxane networks. The authors concluded that mesopores are formed through aggregation of PMSQ colloids, while macropores, which result from controlled phase separation by spinodal decomposition, were formed due to the presence of F127 when used at very low

quantities. It should be noted, however, that for larger amounts of F127 (above 0.34 g) macropores were found to decrease in size. Surfactant was extracted by solvent exchange processes.

Kurahashi *et al.* [78] reported the effect of a variety of nonionic PEO-b-PPO-b-PEO triblock copolymers with different Mw and PO/EO ratios (HLB value) on the phase separation behavior of a MTMS based system. Most of the surfactants were found to suppress phase separation, except surfactants L35 (low Mw) and P123 (very high hydrophobicity, high PO/EO ratio) which were the only ones to generate opaque gels, an evidence of successful phase separation, for the range of concentrations studied. Another work suggests that these surfactants, when displaying shorter oxyethylene chains, tend to be incorporated more in the gel phase, giving higher mesopore volume [65].

The hydrolysis of alkoxy silanes lead to the release of low-Mw alcohols, which might negatively impact the supramolecular arrangement of block copolymer surfactants. One solution is their removal by vacuum distillation. Also, Hüsing *et al.* [79], in 2003, created a synthetic route to achieve an alternative silica source, a glycol-based silane, tetrakis(2-hydroxyethyl)orthosilicate, designed to not release those low-Mw alcohols, but instead, ethylene glycol. Monoliths containing pore sizes on different length scales (from micro to macropores) were generated by employing a variety of hydrophilic diol- and polyol-modified silanes [80], and P123 as a template, represented in Figure 2.10, which was posteriorly extracted using supercritical carbon dioxide.

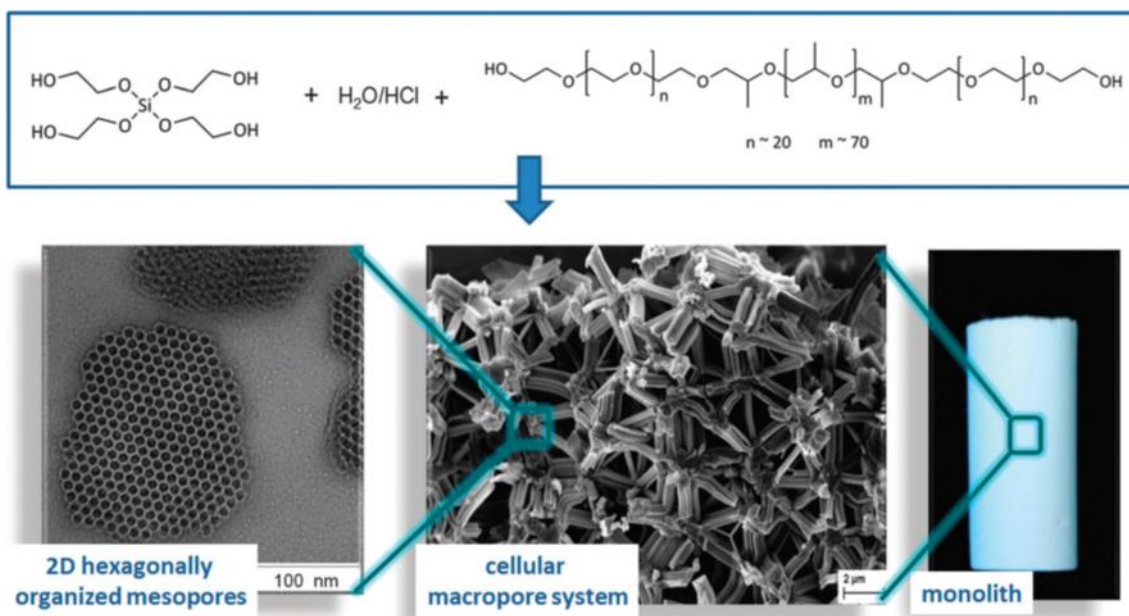


Figure 2.10. Increasing magnification, from right to left, of a silica monolith prepared from glycol-modified silane in the presence of P123 at pH=1. Republished with permission of Royal Society of Chemistry (Great Britain), from Sol-gel synthesis of monolithic materials with hierarchical porosity, A. Feinle, M.S. Elsaesser, N. Hüsing, 45, 12, 2015 [20]; permission conveyed through Copyright Clearance Center, Inc.

Addition of inorganic salts, such as NaCl, NaNO₃ or Na₂SO₄ [81] was another methodology reported to promote the formation of ordered mesostructures in macro/mesoporous hierarchical SiO₂ monoliths, when a weak acidic medium and surfactant P123 are used. The cross-linking degree of the SiO₂ monolith was found to be higher in the presence of these inorganic salts (disappearance of Q^2 site and increased ratio of Q^4/Q^3 in the ²⁹Si MAS NMR spectra), due to the strong ionizing capacity of the anions Cl^- , NO_3^- and SO_4^{2-} that increases the hydrolysis and condensation rate of TMOS.

Table 2.1 lists a series of synthesis strategies to achieve hierarchically structured SiO₂ monoliths with macro and mesopores, via sol-gel/phase separation.

Table 2.1. Overview of some of the latest developments on SiO₂ macro and mesoporous hierarchically structured monoliths (inorganic and hybrid composition) prepared via sol-gel/phase separation processing.

Synthesis strategy	Authors, year reference
Acidic sol-gel synthesis using a nonionic triblock copolymer (P123) as phase separation inducer. Precursor: TMOS	Nakanishi et al., 1998 [65]
Acidic sol-gel synthesis without polymeric phase separation inducer additive, with methanol and water as common solvents. Precursor: bis(trimethoxysilyl)hexane (BTMH)	Nakanishi et al., 2002 [73]
Formamide mediated sol-gel reaction. Acidic sol-gel synthesis without polymeric phase separation inducer additive, with methanol and water as common solvents, and formamide as additive polar solvent to promote gelation and phase separation. Precursor: TMOS and VTMS	Itagaki et al., 2003 [74]
Double-templating synthesis route: PEO as phase separation inducer in combination with an ionic (CTAB) or nonionic surfactant (P123) as structure-directing agents at the nanometer range. Precursor: TEOS	Smatt et al., 2003 [72]
Ethylene glycol-modified silane (precursor) in the presence of P123, for long-range ordering of the mesopores.	Hüsing et al., 2003 [79]
Propane-1,2-diol and glycerol-modified silane (precursor) in the presence of P123, for long-range ordering of the mesopores.	Hüsing et al., 2005 [80]
Acid/base two-step processing method to obtain macroporous PMSQ monoliths. No use of phase separation inducers. Precursor: MTMS	Dong et al., 2006 [75]
Acidic sol-gel synthesis using triblock copolymers (P123 and F127), and TMB as pore expander. Precursor: TMOS or bis(trimethoxysilyl)ethane (BTME)	Nakanishi et al., 2008 [70]
Weak acidic sol-gel synthesis using P123, and inorganic salts (NaCl, NaNO ₃ or Na ₂ SO ₄) for ordered mesostructured and greater silica cross-linking. Precursor: TMOS	Zhong et al., 2009 [81]
Acid/base two-step processing method, using triblock copolymers (F127), to obtain macro/mesoporous PMSQ monoliths. Precursor: MTMS	Kanamori et al., 2011 [76]
Varied nonionic PEO-b-PPO-b-PEO triblock copolymers with different Mw and PO/EO ratios tested as phase separation inducers (PMSQ monoliths). Precursor: MTMS	Kurahashi et al., 2012 [78]

The applications of silica-based monoliths can be extended to non-traditional fields, such as photocatalysis. As an example, SiO₂ porous monoliths prepared in a similar fashion as in [72], have been subjected to vacuum impregnation of sodium tungstate to prepare porous WO₃/SiO₂ monoliths. They exhibited a narrow band gap (2.5 eV) and are suitable for visible light photocatalysis targeting the degradation of toxic-pollutants to reduce water pollution [82].

2.2. Macroporous SiO₂ based multicomponent oxide monoliths

Porous materials with extended chemical compositions are highly desirable, for greater chemical range and variety. The first developments in pure SiO₂ macroporous monoliths were soon followed by the synthesis of multi-oxide silica-based compositions, using the co-gelation method with other metal oxides. However,

the reactivity and stereochemistry of the latter ones is different from those of silicon alkoxides, so that synthesis protocols must be adapted to avoid the precipitation of the highly reactive metal alkoxides. Common strategies include low synthesis temperatures and the employment of chelating ligands.

According to the literature, the first macroporous multi-oxide monolith synthesis using phase separation in sol-gel system was published by Nakanishi *et al.* in 1992 [83]. It involved the hydrolysis and condensation of the TMOS and titanium tetrabutoxide (TBOT) precursors, under strong acidic media, and HPAA as a phase separation inducer, as in previous works for SiO₂ composition [60–63]. Lower hydrolysis temperatures had to be used, in this case, to control the high reactivity of TBOT, which was found to modify the polycondensation mechanism, in a similar fashion as base-catalyzed systems and retard the occurrence of phase separation. Through this method, approximately half amount of the initially added titanium was incorporated in the gel network.

The use of PEO as phase separation inducer has proved to be advantageous for controlling the macroporous morphology. Macroporous SiO₂-TiO₂ monoliths using this strategy (PEO, Mw 20000) were reported in 2012, by Ruzimuradov *et al.* [84] where the influence of various titanium precursors (titanium isopropoxide, TiPOT, TBOT, titanium tetrachloride (TiCl₄), and 30 % titanium sulfate solution (Ti(SO₄)₂)), on phase separation tendency was investigated, for systems containing 5 and 7.6 wt% TiO₂. The authors tested three methods when working with TiPOT precursor: co-gelation, two-step hydrolysis and acac-complexation method. In the co-gelation method the authors added a solution of PEO, water and nitric acid to a mixture of the alkoxide precursors. In the two-step pre-hydrolysis method, TEOS was first partly hydrolyzed under acidic media before the addition of the TiPOT precursor while using a cosolvent and a limiting quantity of water. In this way, TiPOT only condensate with the few available -OH moieties and its reactivity is controlled. In the acetylacetonone acac-complexation route, TEOS, TiPOT and acac were mixed, and then an acidic aqueous solution containing PEO was added.

Titanium alkoxides were found to produce SiO₂-TiO₂ monoliths with high Ti incorporation when acac was used as chelating agent, but largely decreased phase separation tendency. In this case, relatively low reaction temperature (25-30 °C) was

necessary to form macropores. On the other hand, titanium salts (titanium chloride and titanium sulfate) had a small effect on phase separation tendency and yielded, $\text{SiO}_2\text{-TiO}_2$ monoliths with high Ti dispersion, for the studied compositions.

Yang *et al.* [85], in 2013, addressed the challenge to fabricate ordered mesoporous channels in the $\text{SiO}_2\text{-TiO}_2$ bicontinuous macroporous framework walls. They were able to synthesize hierarchical $\text{SiO}_2\text{-TiO}_2$ monoliths with higher Ti contents, by a double-template technique, involving water soluble organic polymers (PEO 10000 Mw) and triblock copolymers. The addition of fluoride (NH_4F) promoted the incorporation of Ti atoms in the silica framework. Table 2.2 compiles different synthesis strategies, based on co-gelation, for a variety of binary and other multicomponent oxide silica-containing hierarchically porous monoliths.

Examples of other binary silicate systems with high SiO_2 content have been already reported such as $\text{SiO}_2\text{-ZrO}_2$ [86–88], with ZrO_2 contents up to 21.3 wt%, and $\text{SiO}_2\text{-Al}_2\text{O}_3$ sol-gel systems [89–91]. An ice bath was used to limit the reactivity of the metal alkoxides. The addition of Zr alkoxide causes the increase of condensation rate and limits the coarsening of domains formed by spinodal decomposition. This effect, however, could be compensated by decreasing the polarity of the solvent, i.e. increasing the length of the alkyl chain of the alcohols (from methanol to 2-propanol) [87]. Incorporation of ZrO_2 into the SiO_2 structure increased thermal resistance, since the $\text{SiO}_2\text{-ZrO}_2$ gel maintained interconnected morphology up to 1200°C , while the pure SiO_2 gel maintained it up to 1000°C [88]. In what regards $\text{SiO}_2\text{-Al}_2\text{O}_3$ monoliths, Takahashi *et al.* [89], and Murai *et al.* [92] reported the synthesis of such monoliths using PEO as template and found that the macropore size could be adjusted by altering the starting compositions. Wu *et al.* [90] and Yang *et al.* [91] further elucidate on the acidic properties and tailored the mesoporous structure of such mixed oxides, by adding, as well, nonionic surfactants, namely polyoxyethylene cetyl ether containing 10 oxyethylene units ($\text{C}_{16}\text{EO}_{10}$) or P123 as structure-directing agents. The Al alkoxide precursor yielded $\text{SiO}_2\text{-Al}_2\text{O}_3$ monoliths with relatively higher Al content than the Al nitrate precursor.

Table 2.2. Varied synthetic strategies for the achievement of SiO₂-based multicomponent oxide monoliths, prepared via sol-gel/phase separation processing.

Composition	Synthetic strategy	Authors, year reference
SiO ₂ -TiO ₂	Acidic sol-gel synthesis using a phase separation inducer (HPAA). Precursors: TMOS and TBOT	Nakanishi et al., 1992 [83]
SiO ₂ -TiO ₂	Acidic sol-gel synthesis using a phase separation inducer (PEG, 20000Mw) and two-step hydrolysis, or acac-complexation route. Precursors: TEOS and Ti salts and alkoxides	Ruzimuradov et al., 2012 [84]
SiO ₂ -TiO ₂	Double-templating synthesis route: phase separation inducer (PEG, 10000Mw), nonionic surfactant (P123), together with NH ₄ F for further Ti incorporation in the framework. Precursors: TMOS and TiPOT	Yang et al., 2013 [85]
SiO ₂ -ZrO ₂	Acidic sol-gel synthesis adding a phase separation inducer (PEO, 100000Mw) and specific alcohols to increase the domain size. Precursors: TMOS and zirconium tetra-2-propoxide (TPZR)	Takahashi et al., 1997 [86]
SiO ₂ -Al ₂ O ₃	Acidic sol-gel synthesis adding a phase separation inducer (PEO, 100000Mw). Precursors: TEOS and aluminum nitrate.	Takahashi et al., 2001 [89]
SiO ₂ -Al ₂ O ₃	Acidic sol-gel synthesis adding a phase separation inducer (PEO, 10000Mw). Precursors: TMOS and aluminium sec-butoxide.	Morai et al., 2004 [92]
SiO ₂ -Al ₂ O ₃	Double-templating synthesis route: phase separation inducer (PEO, 100000Mw) and C ₁₆ EO ₁₀ as the structure-directing agent. Precursors: TMOS and aluminum nitrate, or aluminium isopropoxide.	Wu et al., 2007 [90]
SiO ₂ -Al ₂ O ₃	Double-templating synthesis route: phase separation inducer (PEO, 10000Mw) and P123 as the structure-directing agent. Precursors: TMOS and aluminum nitrate.	Yang et al., 2010 [91]
SiO ₂ -Al ₂ O ₃ (mullite)	Epoxide (propylene oxide, PO) mediated sol-gel reaction + phase separation inducer (PEO, 100000Mw). Precursors: TMOS and aluminum chloride.	Guo et al., 2013 [93]
Ni/SiO ₂	Acidic sol-gel synthesis adding a phase separation inducer (PEO, 100000Mw). Precursors: TEOS and nickel nitrate.	Nakamura et al., 2000 [94]
CuO/SiO ₂ , NiO/SiO ₂	Acidic sol-gel synthesis adding a phase separation inducer (PEO, 10000Mw). Precursors: TMOS and nickel/copper nitrate.	Zheng et al., 2006 [95]
SiO ₂ -CaO	Acidic sol-gel synthesis adding a phase separation inducer (PEO, 100000Mw). Precursors: TMOS and calcium nitrate tetrahydrate (Ca(NO ₃) ₂ ·4H ₂ O).	Marques et al., 2009 [3]
SiO ₂ -CaO-P ₂ O ₅	Acidic sol-gel synthesis, using two strategies: (i) PEO (100000Mw) as phase separation inducer, and urea; (ii) P123 as phase separation inducer and 1,3,5-trimethylbenzene (TMB) as pore expander (micelle-swelling agent). Precursors: TMOS, calcium nitrate tetrahydrate (Ca(NO ₃) ₂ ·4H ₂ O), and triethyl orthophosphate.	Marques et al., 2007 [96]
MgO-Al ₂ O ₃ -SiO ₂ (cordierite)	Epoxide (PO) mediated sol-gel reaction + phase separation inducer (PAAm). Precursors: TMOS, magnesium chloride and aluminum chloride.	Guo et al., 2014 [97]
Al ₂ O ₃ -SiO ₂ -TiO ₂	Formamide mediated sol-gel reaction + phase separation inducer (PEO). Precursors: TEOS, TiPOT, aluminum nitrate nonahydrate,	Sun et al., 2016 [98]

The epoxide-assisted sol-gel processing starting from metal salts has proven to be useful in achieving highly homogeneous binary oxides and was firstly implemented by Guo *et al.* (2013) for SiO₂-Al₂O₃ systems, using PEO as phase separation inducer [93]. The reported homogeneity for the resulting materials, is mainly due to the stable and uniform dispersion of metal cations in the starting solution. Epoxides, such as propylene oxide (PO), are protonated by an acid (H⁺), and an irreversible ring-opening reaction is made to occur by a nucleophilic anionic base. The use of PO enables a uniform and rapid raise of pH, which promotes hydrolysis and polycondensation. In this work [93], formation of a crystalline phase (mullite) occurred, by heat treatment at 1400°C and, despite not impacting the macroporous morphology of the monoliths, the same did not happened to meso, or nanopores, since it led to a drastic decrease of the surface area, from 417 m²/g to 5.4 m²/g.

Experiments involving the addition of nickel into the silica-PEO system [94] showed that its incorporation had a negligible effect on the morphology formation of the porous monoliths, regardless the loading process employed, namely co-gelation, solution exchange or impregnation. However, NiO dispersion varied with the loading procedure. Ni was selectively incorporated into the gel framework, prepared by co-gelation, as fine particles in the system with PEO, probably due to a possible interaction of PEO both with silica and Ni cations, while the latter two methods resulted in Ni aggregation in the macropores. Samarium ions (Sm²⁺) were also incorporated within the silica and silica-alumina matrices of macroporous monoliths, using SmCl₃·6H₂O and thermal reduction of Sm³⁺ to Sm²⁺ [99].

In 2006, the co-gelation method was adapted to produce bimodal porous copper-silica and nickel-silica monoliths by using nitrate precursors, by Zheng *et al.* [95]. Similarly to [94], PEO interacted with both silica and nickel cations, but not significantly with copper cations. These latter ones tended to aggregate as copper salts in the drying step of the wet gel and decomposed into CuO particles by heating.

Marques *et al.* [3,4,96] reported on resorbable glass scaffolds, of molar compositions 70%SiO₂-30%CaO and 77%SiO₂-19%CaO-4%P₂O₅, using several different strategies for the synthesis, as shown in Table 2.2. The obtained monoliths exhibited high pore interconnectivity and enhanced bioactivity and consisted of macropores of ~5 to 300 μm in size within a coral-like gel/glass skeleton, and nanopores ~5-20

nm in size. PEO (PEO/TMOS ~ 10 wt%), or P123 were employed for achieving such macroporosity, by phase separation. Deionized (DI) water and hydrofluoric acid were added before the gelation step. Removal of the solvent-rich phase by evaporation and polymer burn-off introduces macroporosity. Figure 2.11 shows SEM images of heat-treated 70%SiO₂-30%CaO monoliths prepared (a) without addition of PEO and (b) with addition of PEO, revealing an extensive macroporosity in the latter case, also shown in Figure 2.12a, where large pore necks were observed. The size of nanopores was found to increase with the calcium and phosphorous content and with solvent exchange procedures (using DI water and ammonia) as well, whereas macropores remain unaffected [4].

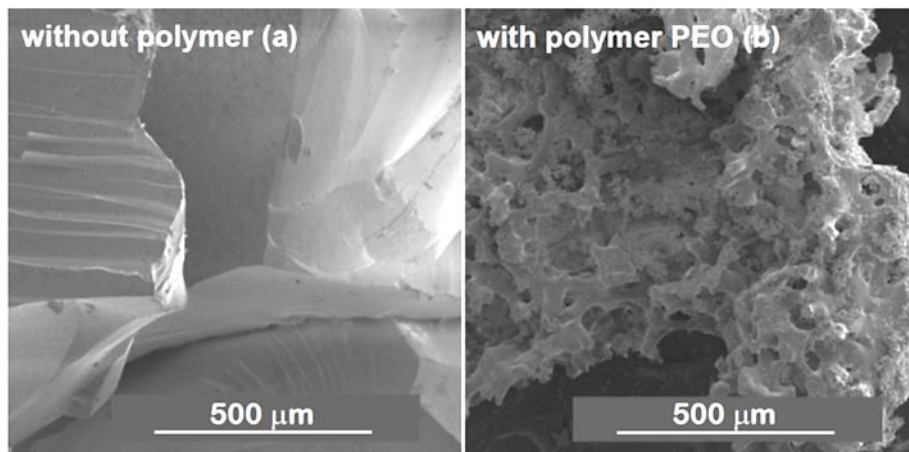


Figure 2.11. SEM images of heat-treated monoliths of composition 70%SiO₂-30%CaO (mol%), prepared by (a) the sol-gel technique without addition of PEO; (b) the sol-gel/phase separation technique with addition of PEO. Reprinted by permission from Springer: Springer Nature, Journal of Materials Research, Sol-gel-derived glass scaffold with high pore interconnectivity and enhanced bioactivity, A.C. Marques, R.M. Almeida, A. Thiema, S. Wang, M.M. Falk and H. Jain [3]. Copyright Springer Nature 2009.

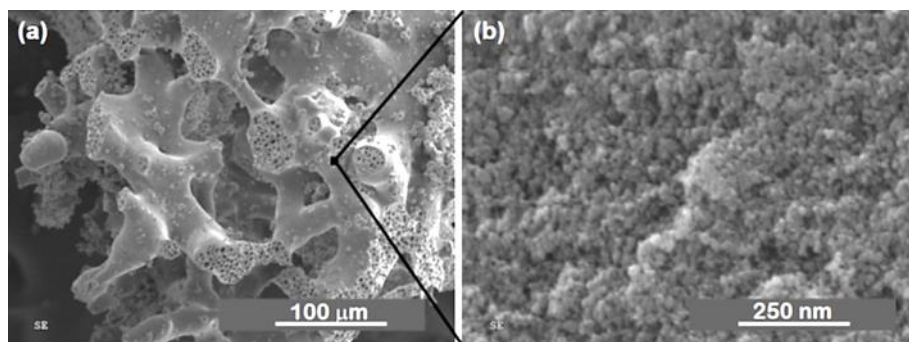


Figure 2.12. SEM images of a heat-treated monolith of composition 70%SiO₂-30%CaO (mol%), prepared by the sol-gel/phase separation technique with addition of PEO: (a) magnification of 300x; (b) magnification of 120,000x. Reprinted by permission from Springer:Springer Nature, Journal of

Materials Research, Sol-gel-derived glass scaffold with high pore interconnectivity and enhanced bioactivity, A.C. Marques, R.M. Almeida, A. Thiema, S. Wang, M.M. Falk and H. Jain [3]. Copyright Springer Nature 2009.

Figure 2.13a shows the pore size distribution curves obtained from MIP. The peak macropore size for the monoliths prepared with PEO was around 60 μm and it ranged from ~ 5 to 300 μm , whereas the sample prepared without PEO did not present any measurable amount of macropores. Mesopores were found to be larger, ~ 10 nm in size, for samples prepared with solvent exchange, than without solvent exchange. SEM image (Figure 2.12b) shows the presence of mesopores and transmission electron microscopy (TEM) image (Figure 2.13b) shows that their size varies between ca. 10 and 20 nm.

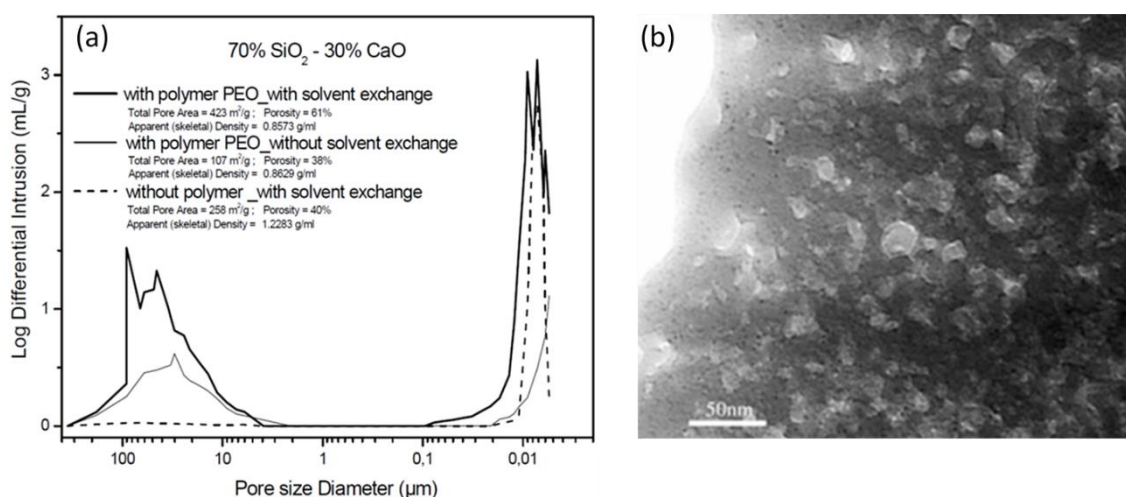


Figure 2.13. (a) Interconnected pore size distributions for SiO₂-CaO heat treated monoliths, determined by MIP. The samples analyzed were prepared both with and without PEO, as well as with and without solvent exchange. Reprinted by permission from Springer:Springer Nature, Journal of Materials Research, Sol-gel-derived glass scaffold with high pore interconnectivity and enhanced bioactivity, A.C. Marques, R.M. Almeida, A. Thiema, S. Wang, M.M. Falk and H. Jain [3]. Copyright Springer Nature 2009; (b) Bright field TEM image of the monolith prepared with PEO and solvent exchange procedure. Reprinted by permission from Springer Nature:Springer Nature, Journal of Sol-Gel Science and Technology, Nano/macroporous monolithic scaffolds prepared by the sol-gel method, A.C. Marques, H. Jain, C. Kiely, K. Song, C.J. Kiely and R.M. Almeida [4]. Copyright Springer Nature 2009.

Regarding ternary systems, cordierite (MgO–Al₂O₃–SiO₂) and Al₂O₃–SiO₂–TiO₂ porous monoliths were developed by Guo *et al.* [97] and Sun *et al.* [98]. Porous cordierite monoliths were prepared via the sol-gel process in the presence of PAAm phase separation inducer [97]. This ternary system has numerous applications because of its excellent mechanical properties, such as thermal shock resistance, and good

chemical durability. Again, PO was used to act as an acid scavenger, mediating the gelation through the ring-opening reaction. Magnesium chloride, aluminum chloride, and TMOS were used as precursors. In what regards $\text{Al}_2\text{O}_3\text{-SiO}_2\text{-TiO}_2$ ternary system, PEO and formamide were used as phase separation inducer and gelation agent, respectively, and acetic acid as chelating agent [98]. Stirring was done under ice-cooling conditions. The obtained amorphous gel was transformed into $\text{Al}_4\text{Ti}_2\text{SiO}_{12}$ after a heat treatment at $1050\text{ }^\circ\text{C}$, losing its meso/micropores, but keeping the macroporosity, as already evidenced from other compositions.

2.3. Macroporous non-siliceous single and multi-oxide, and non-oxide monoliths

Single and multi-oxide monoliths with 3-D interconnected macropores, sometimes with hierarchical mesoporosity, can be prepared by the transient state's spatial arrestment during the spinodal decomposition caused by the gelation and/or self-assembly of the precursors. By controlling the reactional parameters, e. g., type of precursors, precursor/water molar ratio, pH, temperature, presence of cosolvents, gelling agents and phase separation inducer additives, the morphology of the 3-D macropore network can be controlled. Varied synthesis strategies are listed in

Table 2.3 and Table 2.4, for different types of non-siliceous materials (oxides and non-oxides), including recent developments on carbon (C), C/oxides and metal organic frameworks (MOFs).

The study of silica based multi-oxide monoliths established the baseline for the study of non-siliceous single and multi-oxide systems. According to the literature, the first non-siliceous porous monoliths prepared by sol-gel/phase separation were made of TiO_2 in 2004 [100]. However, structural development control during hydrolysis and polycondensation was harder to manage than for silica-based materials, due to the high reactivity of titanium alkoxides. The electronegativity of the central metallic atom played an important role in hydrolysis and condensation rates. The lower electronegativity caused them to be more electrophilic, and therefore less stable to nucleophilic reactions like hydrolysis and condensations. Because of the greater reactivities and rapid kinetics, it is essential to have greater control of hydrolysis' conditions, including moisture, to avoid obtaining precipitates.

2.3.1. Titania (TiO₂) macroporous monoliths

It is common knowledge that titanium dioxide monoliths are very important, for instance, in the field of catalysis, among other applications. TiO₂ monoliths achieved by polymerization induced phase separation were produced through two approaches: 1 – formamide system [100–102] and 2 – chelation system [103,104].

2.3.1.1. Formamide systems

The first approach to achieve macroporous TiO₂ monoliths involved the use of aqueous titania colloid instead of highly reactive titanium alkoxide, in 2004, by Fujita *et al.* [100]. The gelation/assembly (physical aggregation) of titania (anatase) colloidal particles was controlled in this case by the intrinsic and gradual increase of pH, due to the hydrolysis of formamide in acidic conditions that produces ammonia. Phase separation was induced by the presence of PEO in the reaction mixture. An increase in pH leads to a reduction in zeta potential (low charged surfaces), weak repulsive forces and, therefore, higher tendency to the colloidal particles' agglomeration. The thermodynamic instability was generated by the repulsive interaction between the solvent and the PEO chains adsorbed on the aggregating TiO₂ particles. Since these wet gels are fragile, a freeze-drying process was needed to maintain the monolithic gel. It was also observed that during the gelation process, the small primary particles aggregated into larger secondary particles, resulting in a wide range of mesopores, and specific surface areas of 350 m²/g.

In 2006, Konishi *et al.* [102] reported a method for synthesizing porous TiO₂ monoliths using an alkoxy-derived sol-gel process accompanied by phase separation. This method involved a relatively high concentration of acid solution (HCl) in order to suppress the condensation of hydrolyzed Ti alkoxide by electrostatic repulsion, a gelation agent (formamide) and no polymeric additive as phase separation inducer (template-free). Essentially, this process was a one-pot synthesis with an initial hydrolysis step under a strong acidic condition, and a subsequent condensation step under alkaline condition, from the formamide decomposition into ammonia. In this sense, polycondensation was favored, inhibiting heterogeneous TiO₂ precipitation. Another advantage of formamide was its high polarity and hydrogen bonding character, contributing to phase separation. There is no need for strongly hydrogen bonding additives, such as PEO. A

comparison with colloid derived TiO₂ gels was carried out in this paper. However, the search for milder sol–gel reactions (especially in industrial environment), led to the development of new methods involving the use of chelating agents and mineral salts.

In 2009, the same authors described a practical synthetic pathway to such porous TiO₂ monoliths envisaging chromatographic use [105]. The process involved, as well, strongly acidic condition, but also the use of PEO as phase separation inducer, and N-methylformamide (NMF) as a proton scavenger (Figure 2.16c). NMF is known by increasing more gently the solution pH, and PEO was added to counterbalance the effect of propanol release during hydrolysis that weakens the tendency for phase separation. They addressed typical issues in monolithic TiO₂ gels, namely poor control of the mesoporous structure and shrinkage (deformations and/or crack formation), utilizing high-temperature aging treatments of the wet gel in the mother liquor between 100 and 200 °C, as a post-gelation process to remove the solvent phase. By this approach, mesopore size was increased. Subsequent treatments to 400 °C were employed as a final step. Phosphorous-containing compounds were effectively separated using the monolithic TiO₂ monoliths as high-performance liquid chromatography (HPLC) columns. Other Ti precursors (titanyl sulfate, TiOSO₄) and phase separation inducer agents (PVP) were employed by Li *et al.* in 2013 [106]. The effect of parameters, such as amount of PVP, formamide, water and ethylene glycol (EG) were studied. This latter compound was suggested to be acting as chelating agent. Figure 2.14 shows the evolution of the monoliths' morphology for increasing PVP contents. In this case, PVP was found to be mostly present in the solvent-rich phase, which is similar to sol-gel systems of SiO₂ incorporated with HPAA (entropy-loss driven). This finding explains the morphologies obtained for lower amounts of PVP (Figure 2.14a and b), of the type isolated macropores, because they refer to lower volume fraction of the solvent-rich phase, besides a possible retarded phase separation phenomenon.

Anatase and rutile phases were obtained at 500 and 900 °C without disturbing the macroporosity, which enabled this compound to be potentially used in photocatalytic applications. However, a decrease of the specific surface area from 228 to 73 m²/g was achieved with heat treatments above 600 °C [106].

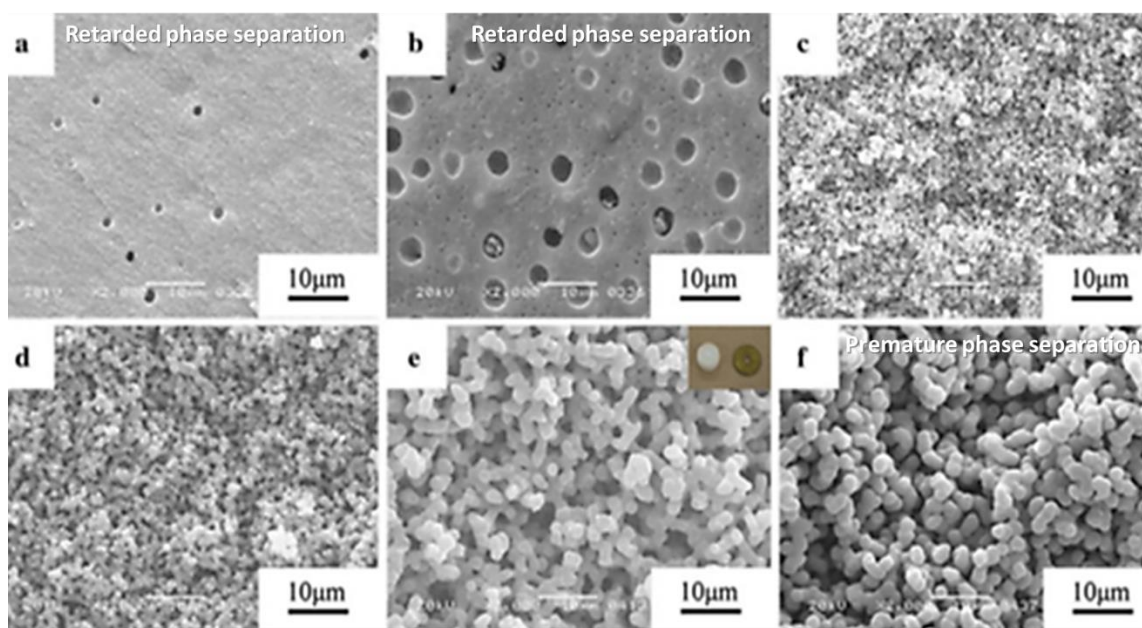


Figure 2.14. SEM images of the dried TiO₂ gels prepared with different PVP contents (x): (a) 50 mg; (b) 70 mg, (c) 90 mg; (d) 100 mg; (e) 110 mg; (f) 115 mg (quantities used in the formulation: 0.5g TiOSO₄.xH₂O: 1ml H₂O: 0.3ml EG: 0.248 ml formamide: x mg PVP). Reprinted by permission from Springer Nature Customer Service Centre GmbH: Springer, J. Sol-Gel Sci. Technology, Sol-gel synthesis of macroporous TiO₂ from ionic precursors via phase separation route, Li W, Guo X, Zhu Y, Hui Y, Kanamori K, Nakanishi K, © Kluwer Academic Publishers. Manufactured in The Netherlands (2013) [106].

2.3.1.2. Chelated systems

In 2007, Backlund *et al.* [107] developed a new template-free method (no polymer phase separation inducer additive) where a macro and mesoporous TiO₂ monolith were produced by using reaction rate controlling additives, namely a chelating agent (acetic acid) to control the high reactivity of the Ti precursor and a strong acid (HCl) (Figure 2.16a). A significant amount of water is also added to the system and the type of macroporous structure that develops is interconnected particle aggregates, maybe because gelation occurs at a later stage of phase separation. The majority of the chelating agents are removed by hydrolysis and posterior decarbonation through gradual solvent exchange procedures.

As already mentioned, the reduction of the Ti alkoxides reactivity can be tackled either by using a strong acid, e.g. HCl or HNO₃, or/and by adding a chelating agent, e.g. acetic acid. Additionally, other synthesis strategies were pursued to induce the homogeneous gelation of the monolithic materials.

Hasegawa *et al.* in 2010 developed titania homogeneous (transparent, non-macroporous) monoliths using milder conditions instead of strongly acidic conditions, by employing a chelating agent (ethyl acetoacetate, EtAcAc) and a mineral salt [108]. The novelty of this method consisted of using a conjugate base of a strong acid, such as nitrate ions and halide ions, in conjunction with the chelating agent, which further stabilized the chelated species and decreased the reactivity during hydrolysis, in particular. A variety of strong acid anions were tested in this work, and it was found that the ability of salts to suppress the too rapid sol-gel reaction strongly depended on the electronegativity of the anions and valence of the cations. Ammonium nitrate (NH_4NO_3) was found to be the best salt to prevent Ti atoms from being exposed to nucleophilic reactions. The template-free reaction was reported to occur in a nearly neutral condition in one-pot and the gelation could be controlled, yielding homogeneous monolithic gels without macroporosity. In order to fabricate hierarchically porous TiO_2 monoliths, this was followed, by the same authors, by incorporating in the batch containing titanium(IV) isopropoxide (TiPOT), 1-propanol and ethyl acetoacetate (EtAcAc), a phase separation inducer additive, PEO [103,104], as represented in Figure 2.16b.

2.3.2. Zirconia and alumina macroporous monoliths

Zirconium has a larger positive partial charge than silicon and titanium, being more predisposed to a nucleophilic attack and exhibiting greater reactivity. Besides, the higher reactivity exhibited by Zr alkoxides, ZrO_2 monoliths also exhibit lower thermal stability, than SiO_2 or TiO_2 ones, exhibiting pore collapse when submitted to temperatures above 400 °C. In 2008, Konishi *et al.* were able to tackle these barriers and reported the production of thermally stable macro and mesoporous crystalline ZrO_2 monoliths [109]. First, they slowly induced the condensation of hydrolyzed zirconium propoxide (9.36 g) using NMF (2.88 g) in a strongly acidic media (2.3 g of 65wt% aq. HNO_3), which, as already explained before, leads to a more gradual pH increase than formamide. PEO was added at contents ranging from 0.04 to 0.15 g. Secondly, to increase the monolith's thermal stability, an alcoholic solvent exchange followed by heat treatment was applied to the wet ZrO_2 gels. The authors proved that, for this composition, crystallinity and mesoporosity could be modified without

affecting the macroporous morphology. These findings were applied to the synthesis of porous TiO₂ monoliths by the same team [105].

Tokudome *et al.* [110], in 2007, Wu *et al.* [111], in 2014 and Guo *et al.* [112], in 2015, were able to demonstrate the preparation of hierarchical macro/mesoporous alumina (Al₂O₃), zirconia (ZrO₂) and magnesia and yttria stabilized ZrO₂ monoliths. They used a milder reactional medium (without addition of strong acids or bases), an epoxide (PO) driven approach together with a phase separation approach (PEO), and cheaper metal sources (ionic precursors): aluminum chloride hexahydrate (AlCl₃·6H₂O) and zirconium chlorides, which are not as reactive as the corresponding metal alkoxides [111] (Figure 2.17a). Macropore morphologies are shown in Figure 2.15 for alumina monoliths prepared with increasing amounts of PEO. As explained in section 4, this synthetic approach is based on the direct condensation of the ionic precursor promoted by pH increase, after the ring-opening reaction of PO.

However, in the synthesis of 100% ZrO₂ materials, even when using anhydrous Zr chloride, the high gelation rate of Zr⁴⁺ upon ring-opening reaction still caused ZrO₂ oligomers to quickly polymerize, with formation of 3D Zr–O–Zr gel network, inhibiting the rearrangement with PEO for phase separation. To prevent such quick solid gel network formation, the polymerization rate of zirconia oligomers was slowed down by adding, to the primary precursor, magnesium or yttrium precursors, which have low tendency to form a network by the epoxide-driven sol-gel method [111]. NMF has also been employed to promote the phase separation phenomenon [109], i.e., since it slows down the gelation process, it allows the diffusion of PEO moieties toward the oligomers, as well as the formation of gel-rich and solvent-rich phases.

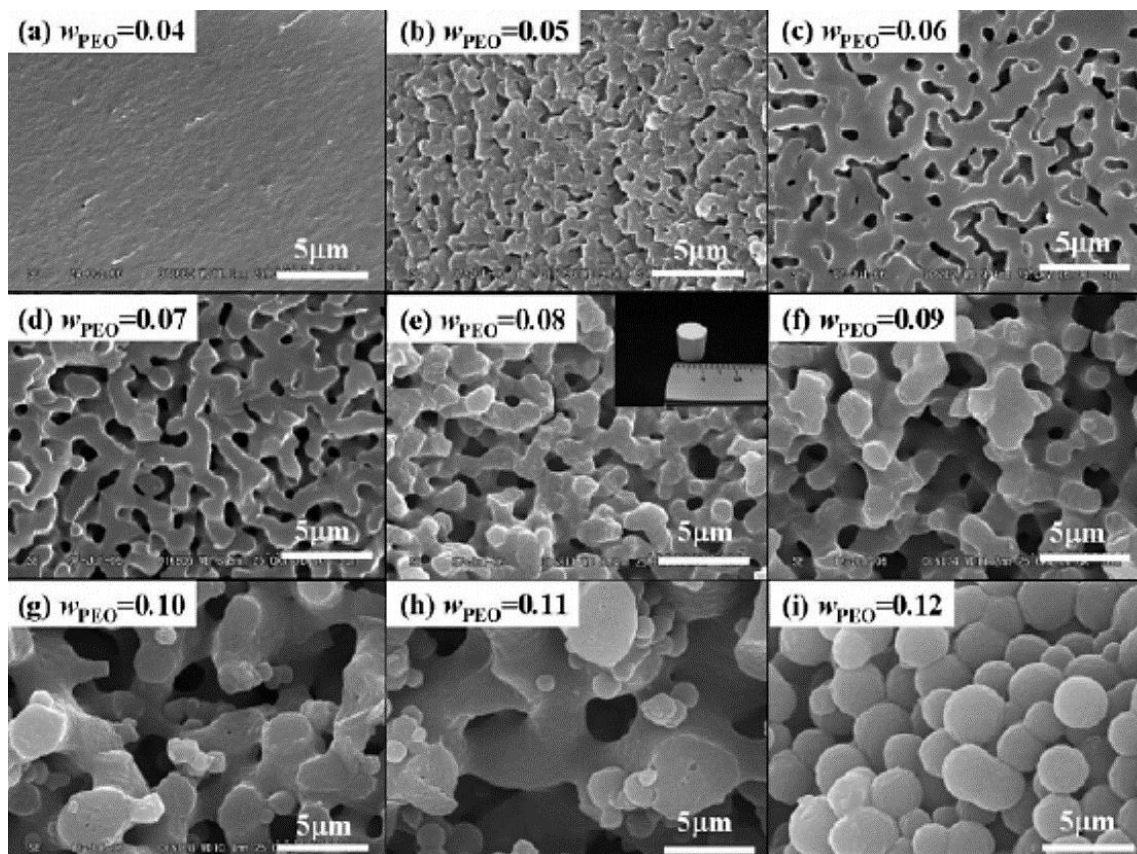


Figure 2.15. SEM images of Al_2O_3 dried monoliths prepared with different amounts of phase separation inducer additive, PEO (1000000Mw). Reprinted (and adapted) with permission from Tokudome Y, Fujita K, Nakanishi K, Miura K, Hirao K (2007) Synthesis of monolithic Al_2O_3 with well-defined macropores and mesostructured skeletons via the sol-gel process accompanied by phase separation. *Chem Mater* 19:3393–3398. <https://doi.org/10.1021/cm063051p> [110]. Copyright 2007 American Chemical Society.

The just described mechanisms, followed in [110,112], are similar to that used for achieving macroporous cordierite monoliths [97], where the best compromise between PO and PEO contents, i.e. gelation and phase separation time, was achieved to generate interconnected macropores and co-continuous skeletons of Al_2O_3 or ZrO_2 . By DTA/TG and FTIR spectroscopy the authors observed that PEO was present on the dried gels. In this case, PEO was expected to be absorbed on the surface of ZrO_2 oligomers through hydrogen bonds [112], and therefore increased the hydrophobic-hydrophilic repulsion with the solvent phase, causing phase separation. A solvothermal process using an ethanol solution of ammonia was found to tailor the mesopores and increase the specific surface area from 171.9 to 583.8 m^2/g [112], and tetragonal and monoclinic ZrO_2 crystals were precipitated at 400 and 600 °C, respectively.

In 2016 and 2017, the same authors extended this method to produce yttria-stabilized zirconia (YZA) and barium zirconate, obtaining xerogels with high porosity and surface area [113,114]. In this case, formamide was also added as a gelation agent (Figure 2.17b). The amount of PEO, PO, water, or ethanol was made to vary, while the remaining quantities were kept constant: $ZrOCl_2 \cdot 8H_2O$ (1.610 g), formamide (0.2 ml) and EG (0.4 ml). This latter compound was found to form complexes with Ba^{2+} or Y^{3+} ions, which, together with the weak hydrogen bonds established between PEO and the inorganic oligomers, results in a distribution of PEO among the solvent-rich phase, during phase separation (entropy-driven process). This is contrary to what was observed in reference [112] where no EG is used. The sol-gel/phase separation process is schematically represented at [114]. Optimized amounts of PEO and PO were found at 0.1 g and 0.36 ml, respectively, and it should be noted that TMOS or TEOS were employed for solvent exchange. X-ray diffraction (XRD) data signaled that $BaZrO_3$ phase was formed at $1100^\circ C$ with a few monoclinic ZrO_2 phase, and cubic YZA was formed at $1200^\circ C$ for high yttria doping amount.

2.3.3. Other non-siliceous macroporous monolithic systems

Titania, zirconia, and alumina systems were one of the first non-siliceous single oxides synthesized by the sol-gel/phase separation method, and the most studied in the literature, so that they can be considered as the baseline studies regarding single oxide monoliths. A scheme of some of the most representative synthesis strategies is shown in Figure 2.16, when metal alkoxides are employed.

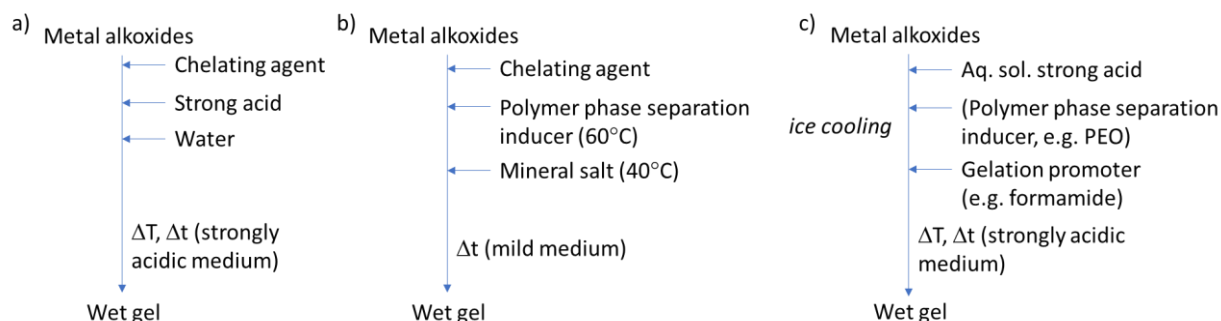


Figure 2.16. Representative synthesis schemes, employing metal alkoxides, for macroporous monoliths of non-siliceous oxide composition, based on the sol-gel/phase separation method.

When less reactive ionic precursors (metal salts) were used, synthesis strategies involved, most of the times, an epoxide mediated method, combined with polymerization induced spinodal decomposition, as shown in Figure 2.17, where two of the most representative synthesis schemes are shown. Macroporous oxide monoliths of compositions Al_2O_3 , TiO_2 , ZrO_2 , Cr_2O_3 , MgO and Fe_2O_3 , among others, have been successfully prepared by these approaches [106,110,112,115–117], as well as zirconates [114,118], spinels [119–121] and titanates [122].

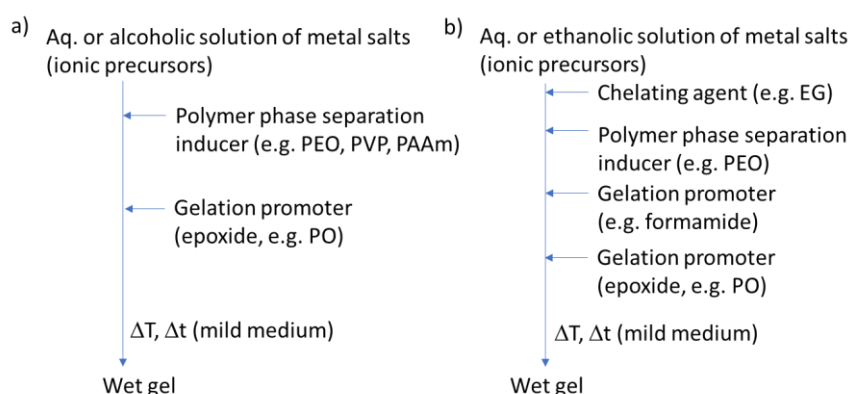


Figure 2.17. Representative synthesis schemes, employing metal salts (ionic precursors) for macroporous monoliths of non-siliceous single and multi-oxide compositions, based on the epoxide mediated sol-gel/phase separation method.

As stated before, precursors of high-valence elements (Si, Ti, Zr, Al) were found in the form of alkoxides, or inorganic salts. These latter ones, when in aqueous solutions, exist as hydrated ions, have a strong acidity and were able to experience sol-gel reactions. However, when dealing with low-valence elements (Fe^{2+} , Co^{2+} , Ni^{2+} , Zn^{2+} , Mn^{2+}), the control of hydrolysis and polycondensation is more complex, hydrolysis activity is weaker and the formation of particles to generate 3D frameworks is more difficult.

Epoxides have shown to play two roles, either as (i) acid scavengers to raise the solution pH homogeneously and promote polycondensation or induce the coordination with metal cations [123], and (ii) phase separation inducers, via coordination to metal cations, resulting in low solubility and low compatibility oligomers in the mixed solvent [123].

An adaptation of the epoxide mediated sol-gel process could enable the synthesis of more homogeneous porous monoliths derived from low-valence metal salts, i.e. divalent oxidation state metals. According to the literature, Gash *et al.* [124], in 2004, were the first ones to report the synthesis with these elements, for the preparation of NiO₂ aerogels. The difficulty of this synthesis was the low electronegativity of the central metal atoms, high positive partial charge of the cations, which results in heterogeneity of the resulting monoliths. The role of the metal salt counter ion was found to be very important. Lu *et al.* [125] addressed this issue and were able to obtain homogeneous gelation for three kinds of low-valence metal salts. They studied factors, such as the concentration of the polymer (Cu-system), the Mw (Co-system) and amount of HCl (Mn-system), in what regards the 3D interconnected macroporosity of the resulting monoliths. Their strategy was based on the preparation of brominated metal alkoxides, achieved by reaction of metal bromides (MBr₂ with M=Cu, Co, Mn) with epichlorohydrin in N,N-dimethylformamide (DMF), by ring-opening reaction, whose kinetics could be controlled by ice cooling. Such brominated alkoxides (Br-M-OR), with a highly electronegative Br ligand and reduced negative charge on oxygen atoms, reduced the rates of hydrolysis and polycondensation and allowed preparation of a homogeneous composite oxide gel. PEO and PVP were employed as phase separation inducers (Cu-system) and tended to locate at the solvent-rich and gel-rich phases, respectively. For Co-system, higher Mw PEO (up to 600000 Da) had to be employed for phase separation to occur at an optimum level, while for Mn-system, the amount of aqueous solution of HCl was varied, keeping constant the amount of PEO (100000 Da) and PVP (40000 Da). HCl promoted hydrolysis and polycondensation resulting in the freezing of the structure at earlier stages of phase separation phenomenon.

Mixed metal oxides with a spinel structure (AB₂O₄), such as NiAl₂O₄, exhibiting hierarchical pore structures [119], have been implemented also in the field of heterogeneous catalysis. The small mesopores can significantly increase the specific surface area and thus increase the contact between the catalyst and reagents. On the other hand, due to the presence of macropores a very efficient mass transfer to and from the reaction pores can be achieved, avoiding the diffusion issues often present during catalytic reactions.

Kido *et al.* [126] prepared different spinel compositions in the form of macroporous monoliths, using the epoxide method, and they found that when Fe³⁺ and Zn²⁺ inorganic salt precursors were used to prepare those monoliths, the obtained structure gradually transitioned from a cocontinuous macroporous structure to the accumulation of particles with the increase of the binary precursor content. This was due to the large difference in hydrolysis rate between Fe³⁺ and Zn²⁺ (hydrolysis rate constants pK_a(Fe³⁺)(2.2) and pK_a(Zn²⁺)(9.2)). When such a difference is in place, the element with a faster hydrolysis rate tends to form in advance the corresponding products, which leads to a large difference in local structure and composition.

Table 2.3. Specific examples of synthetic strategies for the achievement of non-siliceous single and multi-oxide porous monoliths, prepared via sol-gel/phase separation processing.

Composition	Synthesis strategy	Authors, year reference
TiO ₂	Formamide mediated sol-gel reaction (acidic medium) + phase separation inducer (PEO, 300000 and 100000Mw). Precursor: colloidal anatase-type TiO ₂ (7 nm size particles, aqueous dispersion, pH 1.7)	Fujita <i>et al.</i> , 2004 and 2006 [100,101]
	Formamide mediated sol-gel reaction (strongly acidic medium, HCl) + low temperatures. Precursor: TiPOT	Konishi <i>et al.</i> , 2006 [102]
	Reaction rate controlling additives: strongly acidic sol-gel synthesis (HCl) + chelating agent (acetic acid). Precursor: TiPOT	Backlund <i>et al.</i> , 2007 [107]
	NMF mediated sol-gel reaction (strongly acidic medium, HCl) + low temperatures + phase separation inducer (PEO, 10000Mw). Precursor: TiPOT	Konishi <i>et al.</i> , 2009 [105]
	Nearly neutral sol-gel synthesis using chelating agent (EtAcAc) + mineral salt (NH ₄ NO ₃) + phase separation inducer (PEO, 10000Mw). Precursor: TiPOT	Hasegawa <i>et al.</i> , 2010 [103]
	Formamide mediated sol-gel reaction (acidic medium) + phase separation inducer (PVP, 10000Mw) + EG as chelating agent. Precursor: TiOSO ₄	Li <i>et al.</i> , 2013 [106]
ZrO ₂	NMF mediated sol-gel reaction (strongly acidic medium, HNO ₃) + low temperatures + phase separation inducer (PEO, 35000Mw). Precursor: Zirconium isopropoxide	Konishi <i>et al.</i> , 2008 [109]
	Epoxide (PO) mediated sol-gel reaction + phase separation inducer (PEO, 1000000Mw) Precursors: Zirconium oxychloride octahydrate (ZrOCl ₂ ·8H ₂ O)	Guo <i>et al.</i> , 2015 [112]
Magnesia and yttria stabilized ZrO ₂	Epoxide (PO) and NMF mediated sol-gel reaction + phase separation inducer (PEO, 1000000Mw) Precursors: anhydrous zirconium chloride (ZrCl ₄) and MgCl ₂ ·6H ₂ O or YCl ₃ ·6H ₂ O	Wu <i>et al.</i> , 2014 [111]

Yttria stabilized ZrO ₂ (YZA)	Epoxide (PO) and formamide mediated sol-gel reaction + phase separation inducer (PEO, 300000Mw) + EG as chelating agent Precursors: Zirconium oxychloride (ZrOCl ₂ ·8H ₂ O) and yttrium chloride (YCl ₃ ·6H ₂ O)	Guo <i>et al.</i> , 2016 [113]
Al ₂ O ₃	Epoxide (PO) mediated sol-gel reaction + phase separation inducer (PEO, 1000000Mw) Precursors: AlCl ₃ ·6H ₂ O	Tokodume <i>et al.</i> , 2007 [110]
Cr ₂ O ₃	Epoxide (PO) mediated sol-gel reaction + phase separation inducer (HPAA) + urea. H.T under air atmosphere. CrN-C and Cr ₃ C ₂ -C composites will form if H.T. is under N ₂ atmosphere. Precursors: chromium chloride hexahydrate CrCl ₃ ·6H ₂ O	Kido <i>et al.</i> , 2014 [115]
MgO	Epoxide (PO) mediated sol-gel reaction + phase separation inducer (PVP, 100000Mw). Precursors: Magnesium chloride hexahydrate (MgCl ₂ ·6H ₂ O)	Li <i>et al.</i> , 2016 [127]
	Epoxide (PO) mediated sol-gel reaction + phase separation inducer (PVP, 10000Mw) + 1,3,5-benzenetricarboxylic acid to preserve the fine crystallite size. Precursors: Magnesium chloride hexahydrate (MgCl ₂ ·6H ₂ O)	Lu <i>et al.</i> , 2019 [117]
ZnO	Epoxide (PO) mediated sol-gel reaction + citric acid to coordinate to Zn cations and promote phase separation. 1,2-epoxybutane was also tested and found to have lower solubility and compatibility than PO, enhancing phase separation. Precursors: Zn(NO ₃) ₂ ·6H ₂ O	Lu <i>et al.</i> , 2019 [123]
CoO ₂ , CuO ₂ , MnO ₂	Epoxide (epichlorohydrin) mediated sol-gel reaction (acidic medium) + phase separation inducer (PEO 100000-600000 Mw and/or PVP 40000Mw). Precursors: metal bromides (MBr ₂ , with M=Cu,Co,Mn), which transform into brominated metal alkoxides, by reaction with epichlorohydrin.	Lu <i>et al.</i> , 2020 [125]
Fe ₂ O ₃	Epoxide (PO and trimethylene oxide) mediated sol-gel reaction + phase separation inducer (PAAM, 10000Mw). Precursors: Iron(III) chloride hexahydrate (FeCl ₃ ·6H ₂ O)	Kido <i>et al.</i> , 2012 [116]
Fe ₃ O ₄	Epoxide (PO) mediated sol-gel reaction + phase separation inducer (PAAM, 10000Mw). Precursors: Iron(II) chloride tetrahydrate (FeCl ₂ ·4H ₂ O)	Wang <i>et al.</i> , 2020 [128]

Transition metal hydroxide porous monoliths have also been developed recently (Table 2.4), in the presence of PO and HPAA [129], involving low-valence elements Mn²⁺, Fe²⁺, Co²⁺, Ni²⁺ and Zn²⁺). Inorganic metal salts were employed in this case, which undergo hydrolysis to form hydrated metal ions complexes with water molecules. These will further condensate to form particles, which will combine with the HPAA macromolecules forming porous gel frameworks by phase separation (entropy-driven system). Figure 2.18 displays the pore morphology obtained for varied transition metal hydroxide monoliths synthesized by the epoxide method. The effect of varied synthesis parameters was also studied in the same work. Larger

amounts of water promoted the hydrolysis reaction of Zn precursor and, therefore, an increased number of OH groups at the surface of the oligomers, which establish strong H bonds with HPAA, delaying phase separation, and resulting in finer phase separated domains. On the other hand, larger amounts of glycerol inhibit hydrolysis reactions, leading to an earlier phase separation, and coarser skeletons. Also, larger amounts of precursor lead to coarser skeletons and broader macropore size distribution. Binary compositions involving these elements were studied and, interestingly, it was found that the combination of elements with significant difference in hydrolysis rate constants failed to give a cocontinuous macroporous structure. An example for such case is the Zn^{2+} and Mn^{2+} system, where the difference in hydrolysis rate between Zn^{2+} and Mn^{2+} was 1.6. While for Ni^{2+} and Co^{2+} , Zn^{2+} and Fe^{2+} systems, of low difference in hydrolysis rate (0.9 and 0.7), binary macroporous transition metal composites were possible to be obtained via the sol-gel process accompanied by phase separation.

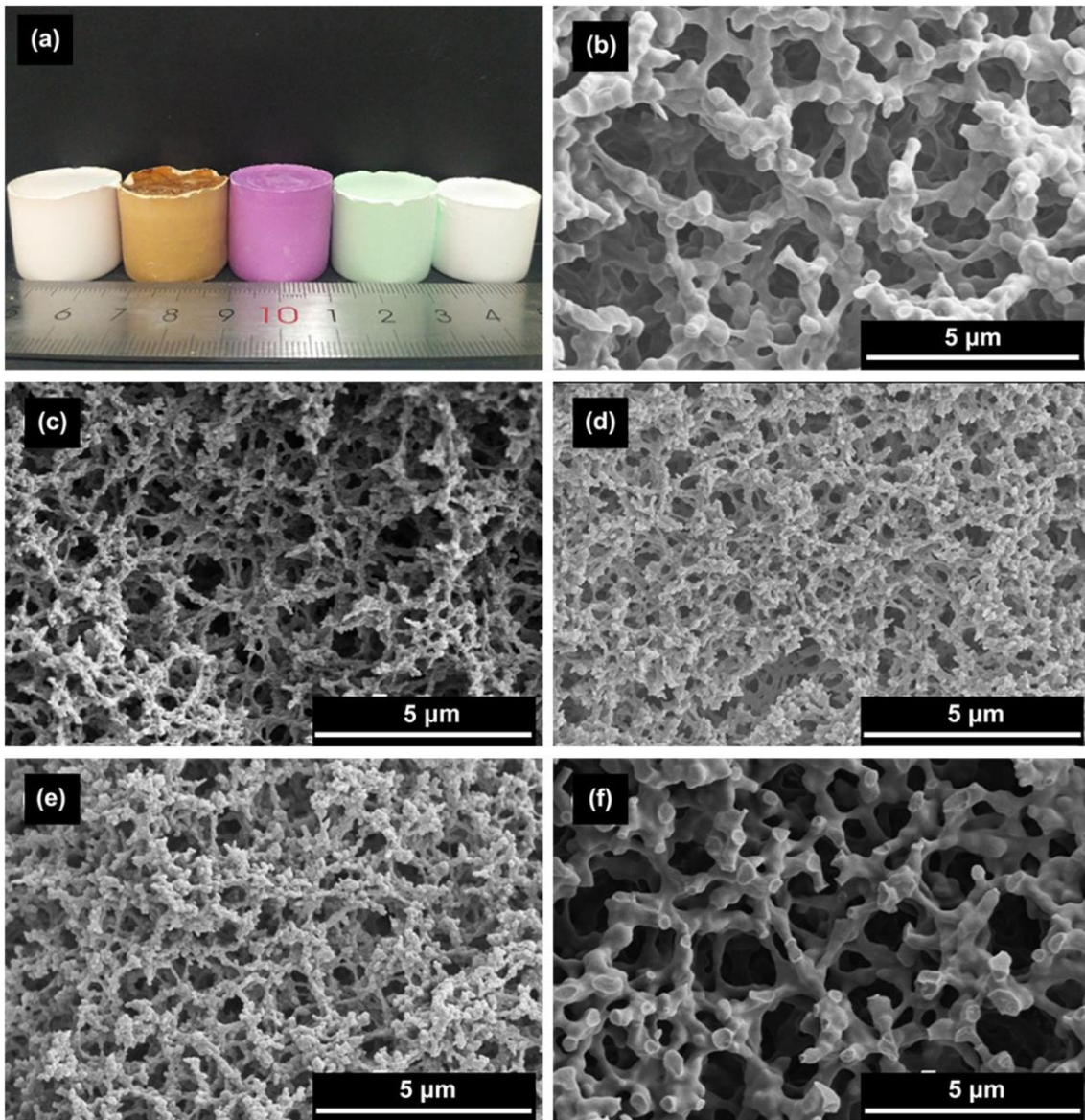


Figure 2.18. (a) Appearance of typical xerogel transition metal hydroxide monoliths; (b) Corresponding SEM images exhibiting the monoliths' microstructure, derived from precursors of following low-valence elements: (b) Mn^{2+} , (c) Fe^{2+} , (d) Co^{2+} , (e) Ni^{2+} and (f) Zn^{2+} , respectively. Reprinted from the open access paper by F. Liu, D. Feng, H. Yang, X. Guo, "Preparation of macroporous transition metal hydroxide monoliths via a sol-gel process accompanied by phase separation.", *Sci. Rep.* 10 (2020) [129]. <http://creativecommons.org/licenses/by/4.0/>.

Table 2.4. Specific examples of synthetic strategies for the achievement of non-siliceous multi-oxide and non-oxide porous monoliths, prepared via sol-gel/phase separation processing.

Composition	Synthesis strategy	Authors, year reference
Aluminum phosphate AlPO_4	Epoxide (PO) mediated sol-gel reaction + phase separation inducer (PEO, 10000Mw). Precursors: $\text{AlCl}_3 \cdot 6\text{H}_2\text{O}$ and H_3PO_4	Li <i>et al.</i> , 2013 [130]
Metal zirconium phosphates ($\text{MZr}_2(\text{PO}_4)_3$)	Acidic sol-gel synthesis adding a phase separation inducer (PEO, 35000Mw and PAAm, 10000Mw). Precursors: $\text{ZrOCl}_2 \cdot 8\text{H}_2\text{O}$, H_3PO_4 and several metal chlorides	Zu <i>et al.</i> , 2016 [131]
Lithium zirconate Li_2ZrO_3	Epoxide (PO) mediated sol-gel reaction + phase separation inducer (PEO, 1000000Mw). Precursors: $\text{ZrOCl}_2 \cdot 8\text{H}_2\text{O}$, lithium acetate dehydrate ($\text{LiOAc} \cdot 2\text{H}_2\text{O}$)	Guo <i>et al.</i> , 2017 [118]
Barium zirconate BaZrO_3	Epoxide (PO) and formamide mediated sol-gel reaction + phase separation inducer (PEO, 300000Mw) + EG as chelating agent. Precursors: Zirconium oxychloride ($\text{ZrOCl}_2 \cdot 8\text{H}_2\text{O}$) and barium chloride dihydrate ($\text{BaCl}_2 \cdot 2\text{H}_2\text{O}$)	Guo <i>et al.</i> , 2017 [114]
Zirconium titanate ZrTiO_4	<i>N</i> -methyl formamide mediated sol-gel reaction (strongly acidic medium, HNO_3 , ice cooling) + low temperatures + phase separation inducer (PEO, 100000Mw). Precursor: $\text{ZrOCl}_2 \cdot 8\text{H}_2\text{O}$ and TiPOT	Sun <i>et al.</i> , 2019 [122]
CaTiO_3 , SrTiO_3 and BaTiO_3 perovskite	Impregnating corresponding alkaline-earth metal ions into preformed macroporous TiO_2 monoliths in a solution containing urea impregnating corresponding alkaline-earth metal ions into preformed macroporous TiO_2 monoliths in a solution containing urea. Impregnation of preformed macroporous TiO_2 monoliths, with alkaline-earth metal ions, in urea solution. Nearly neutral sol-gel synthesis using chelating agent (EtAcAc) + mineral salt (NH_4Cl) + phase separation inducer (PEO, 10000Mw). Precursors: TiPOT, $\text{CaCl}_2 \cdot 2\text{H}_2\text{O}$, $\text{SrCl}_2 \cdot 6\text{H}_2\text{O}$, $\text{BaCl}_2 \cdot 2\text{H}_2\text{O}$	Ruzimuradov <i>et al.</i> , 2011 [132]
$\text{La}_2\text{Zr}_2\text{O}_7$	Epoxide (PO) and formamide mediated sol-gel reaction + phase separation inducer (PEO, 300000Mw). Precursors: $\text{Zr}(\text{NO}_3)_4 \cdot 5\text{H}_2\text{O}$, $\text{ZrOCl}_2 \cdot 8\text{H}_2\text{O}$, $\text{La}(\text{NO}_3)_3 \cdot 6\text{H}_2\text{O}$ and $\text{LaCl}_3 \cdot 6\text{H}_2\text{O}$	Wang <i>et al.</i> , 2016 [120]
Aluminum titanate Al_2TiO_5	Formamide mediated sol-gel reaction + phase separation inducer (PEO, 100000Mw) + chelating agent (citric acid) and ice cooling. Precursors: $\text{AlCl}_3 \cdot 6\text{H}_2\text{O}$, titanium tetrabutoxide ($\text{Ti}(\text{OBU})_4$)	Guo <i>et al.</i> , 2015 [133]
ZnFe_2O_4 spinel	Epoxide (PO) mediated sol-gel reaction + phase separation inducer (PAAm, 10000Mw). Precursors: $\text{FeCl}_3 \cdot 6\text{H}_2\text{O}$, ZnCl_2 (Zn/Fe, R = 0.50 in molar ratio) (low-valence elements)	Kido <i>et al.</i> , 2013 [126]
NiAl_2O_4 and CoAl_2O_4 spinel	Epoxide (PO) mediated sol-gel reaction + phase separation inducer (PEO, 900000Mw). Precursors: $\text{AlCl}_3 \cdot 6\text{H}_2\text{O}$, $\text{NiCl}_2 \cdot 6\text{H}_2\text{O}$ or $\text{CoCl}_2 \cdot 6\text{H}_2\text{O}$ (low-valence elements).	Herwig <i>et al.</i> , 2018 [119]
ZnAl_2O_4 spinel	Epoxide (PO) mediated sol-gel reaction + phase separation inducer (PEO, 1000000Mw). Precursors: ZnCl_2 , $\text{AlCl}_3 \cdot 6\text{H}_2\text{O}$ (low-valence elements)	Guo <i>et al.</i> , 2017 [121]
CoMn_2O_4 spinel	Epoxide (epichlorohydrin) mediated sol-gel reaction (acidic medium) + phase separation inducer (PEO 400000Mw and/or PVP 10000, 40000, 360000Mw). Precursors: metal bromides (MBr_2 , with M=Co,Mn),	Lu <i>et al.</i> , 2020 [134]

	which transform into brominated metal alkoxides, by reaction with epichlorohydrin. (low-valence elements)	
Transition metal hydroxides, ZnOH, CuOH, MnOH and binary compositions	Epoxide (PO) mediated sol-gel reaction + phase separation inducer (HPAA, 10000Mw). Precursors: ZnCl ₂ , CoCl ₂ ·6H ₂ O, NiCl ₂ ·6H ₂ O, MnCl ₂ ·4H ₂ O, FeCl ₂ ·4H ₂ O.	Liu <i>et al.</i> , 2020 [129]
C/TiO ₂	Formamide mediated sol-gel reaction + phase separation inducer and C source (PVP, 10000Mw) + ethylene glycol and solvent and chelating agent. Precursors: TiOSO ₄ ·xH ₂ O	Zhu <i>et al.</i> , 2015 [135]
Resorcinol formaldehyde (RF) and C	Acidic sol-gel synthesis, using surfactant F127 as phase separation inducer and pore directing agent, TMB and benzyl alcohol BzOH (cosurfactant) as micelles' swelling agents and TEG as compatible solvent with RF/F127 oligomers to suppress too much phase separation. Precursors: resorcinol (and formaldehyde)	Hasegawa <i>et al.</i> , 2016 [136]
RF and C	Acidic sol-gel synthesis, using surfactant F127, TMB, BzOH, TEG and inorganic salt KCl. Precursors: resorcinol (and formaldehyde)	Hasegawa <i>et al.</i> , 2020 [64]
RF/TiO ₂ and C/TiO ₂	Acidic sol-gel synthesis, using surfactant F127, TMB, BzOH, TEG. Precursors: resorcinol, (formaldehyde) and ethylene glycol modified titanate (EGMT)	Schoiber <i>et al.</i> , 2021 [137]
Metal organic frameworks (MOFs)	Sol-gel synthesis and self-assembly induced phase separation, using PPG (1000Mn), solvent DMF and acetic acid as mediator for reorganization of the microstructure. Precursors: ZrOCl ₂ ·8H ₂ O and 2-aminoterephthalic acid (BDC-NH ₂) as organic linker	Hara <i>et al.</i> , 2019 [138]

C and C/oxide based monoliths, in particular C/TiO₂ nanocomposites, are presently under investigation for applications, such as catalysis and photocatalysis, energy storage, dye-sensitized solar cells, anode materials for lithium ion batteries, etc. Porous TiO₂ monoliths can be synthesized and/or combined with a C source followed by carbonization, or TiO₂ can be *in-situ* generated, from TiCl₄ or Ti(OⁿBu)₄ sources, within a phenolic resin. For instance, hierarchically porous TiO₂/C composites, with *in situ* distributed C, were synthesized by using PVP as phase separation inducer and C source [135], after calcination of the dried gels in an argon atmosphere at 500-800°C. Formamide was used to promote gelation. This material was shown to have good electrochemical performance with fast Li ion diffusion and high electronic transport efficiency, but specific surface area was found to decrease from 170 to 7 m²/g, when calcination temperature was increased from 500 to 800°C. Resorcinol and formaldehyde have also been used as organic C sources, however, the achievement of ordered mesopores or specific hierarchical structures was not straightforward.

Porous monoliths of C based compositions and metal organic frameworks (MOFs) have not been prepared following exactly the approaches represented at Figure 2.16 or Figure 2.17, instead, they have derived from self-assembly induced phase separation processes, as described below.

Hasegawa *et al.* (2016 and 2020) [64,136] prepared resorcinol formaldehyde (RF) monoliths and C monoliths (by subsequent carbonization), by controlling three phenomena which are made to occur in parallel: polymerization, self-assembly and phase separation by spinodal decomposition. In this process, there is polycondensation of resorcinol and formaldehyde and cooperative self-assembly of RF oligomers and F127 takes place concomitantly with the occurrence of spinodal decomposition, resulting in a macroporous skeleton with embedded mesopores. This is a kind of self-assembly induced phase separation process. Basically, the hydroxyl groups on RF oligomers interact with the hydrophilic moieties of F127 via hydrogen bonding, leaving their hydrophobic region facing outward. TMB and benzyl alcohol (BzOH) were also employed to enlarge the RF/F127 micelles and as a cosurfactant, respectively, and triethylene glycol (TEG) was used as a solvent with high compatibility with the micelles to not limit the extent of phase separation. The relatively high hydrophobicity of the RF/F127 units promotes macroscopic phase separation in aqueous media. The growth of the phase-separated RF/F127 domains stops at the moment of the sol-gel transition. The porous RF monoliths were then obtained and readily converted to the C monoliths through thermal treatment without observing any modification in the bimodal pore system. KCl was also used in some cases [64] to improve the mesopore arrangement, however it was still not enough for achieving an ordered mesostructure with a periodicity at long range.

Schoiber *et al.* [137] from Hüsing group, developed in 2021 a methodology also based on self-assembly induced phase separation, involving ethylene glycol modified titanate (EGMT) as Ti precursor to achieve hierarchical porous RF/TiO₂ materials, which are converted into C/TiO₂ composites via carbonization. The morphology of the monoliths synthesized with increasing amounts of the Ti precursor is shown in Figure 2.19. A comparison with the method proposed by Hasegawa *et al.* [64] was discussed in this work. The advantage reported for EGMT was its stability, i.e. not too high reactivity towards water and good solubility in the RF system, and also the

release of EG, compatible with F127, instead of monohydric alcohols during hydrolysis. The mechanism proposed was: (a) formation of hexagonal ordered F127 micelles at room temperature (RT), (b) polycondensation of resorcinol and formaldehyde around F127 micelles at 60°C, (c) further polycondensation of resorcinol and formaldehyde and sol-gel reaction of Ti precursor at 60°C, (d) carbonization of RF/TiO₂ composite to obtain C/TiO₂ at 850°C. It was shown in this work that the lower the polarity of the solvent employed, the better the quality of the hierarchical structure obtained. TEG exhibited better results than diethylene glycol (DEG) or EG. Since protons (pH value) played a role in the catalysis of the condensation reactions, but also in the interaction between the solvent molecules, their concentration had to be carefully adjusted to the solvent used. The hierarchically organized porous C/TiO₂ monolithic materials were obtained using a good combination of diol-based solvent and pH value, and the control between phase separation induced by an oligomeric block copolymer (F127) and gelation of RF.

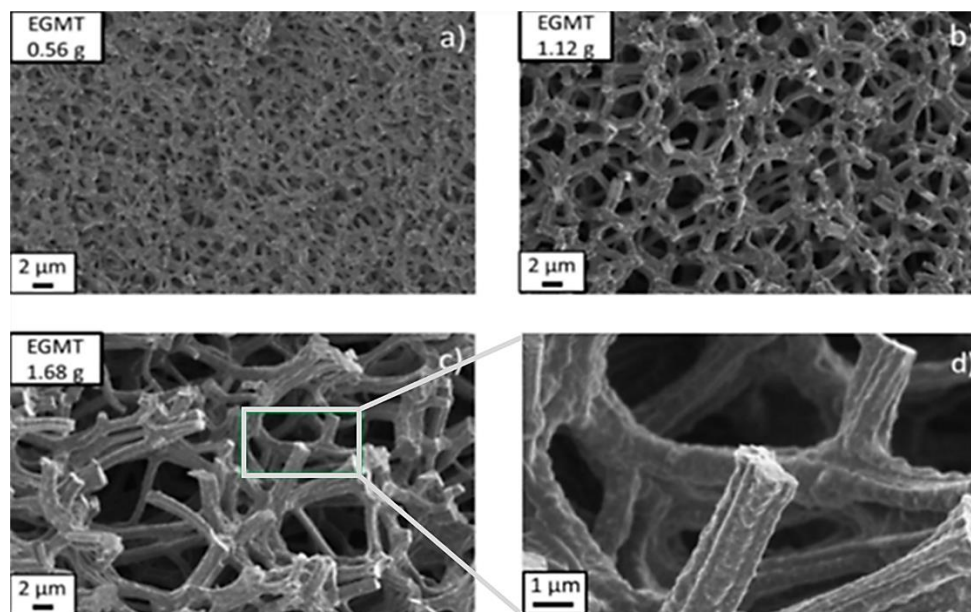


Figure 2.19. SEM images of C/TiO₂ with increasing amounts of TiO₂ (Ti precursor EGMT). Reprinted with permission from J. Schoiber, C. Koczwar, S. Rumswinkel, L. Whitmore, C. Prehal, F. Putz, M. S. Elsaesser, O. Paris, N. Hüsing, Chempluschem, Copyright © 2021 WILEY-VCH Verlag GmbH & Co. KGaA, Weinheim [137].

The sol-gel/self-assembly induced phase separation process was also applied to develop porous monolithic MOFs gels, with trimodal porosity (at the micro, meso and macroscale). The focus was on a Zr-based UiO-66 type metal organic framework

(MOF) with the formula $[\text{Zr}_6\text{O}_4(\text{OH})_4(1,4\text{-benzenedicarboxylate})_6]$, reported by Hara *et al.* [138]. It started by the self-assembly of the Zr moieties (from an inorganic precursor, namely $\text{ZrOCl}_2 \cdot 8\text{H}_2\text{O}$) and terephthalic acid, namely 2-aminoterephthalic acid (BDC-NH₂). This latter one is used as organic linker to obtain the Zr-terephthalate-based MOF (Zr-BDC-NH₂ clusters, hydrophilic) with good solubility in DMF, to which self-assembly induced phase separation was applied. A phase separation inducer (polypropylene glycol, PPG), hydrophobic, was added, and a reorganization process of such clusters at the microscale, induced by acetic acid, was able to convert the macroporous structure from low crystalline framework to crystalline UiO-66 (macroporous UiO-66-NH₂). PPG was found to not strongly interact with Zr-BDC-NH₂ and it was assumed to be distributed both at the solvent, and gel-rich phases, acting as co-solvent [138].

2.4. Macroporous microspheres

The previous sections of this chapter gave an extensive view on different synthesis strategies, based on sol-gel/phase separation methodology, targeting macroporous or hierarchical macro and mesoporous monolithic products. Thin films produced by the same approach and exhibiting similar kinds of porosity are not so frequent in the literature, but can also be found, as for example TiO₂ (Figure 2.20) and SrTiO₃ thin films [139–141], where PEO was used as phase separation inducer additive.

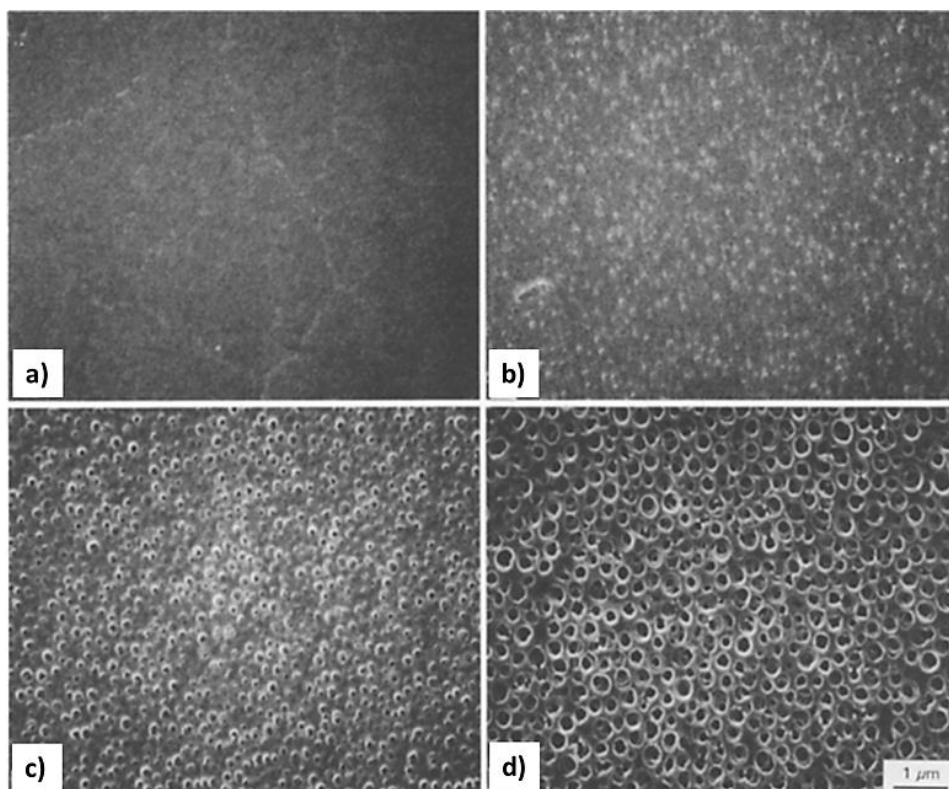


Figure 2.20. Morphology of TiO_2 thin films prepared with increasing amounts of phase separation inducer, PEO (1800-2200 Mw), and obtained by dip-coating at 100 mm/min withdrawal speed: (a) 0 g; (b) 0.5 g; (c) 1 g; (d) 2 g PEO. Reprinted by permission from Springer Nature Customer Service Centre GmbH: Springer, J. Mat. Sci., Morphology of thin anatase coatings prepared from alkoxide solutions containing organic polymer, affecting the photocatalytic decomposition of aqueous acetic acid, Kato K, Tsuzuki A, Torii Y, Taoda H, Kato T, Butsugan Y, ©1995 Chapman & Hall [139].

However, monoliths and thin films may pose some limitations in specific applications, due to their fixed shape. Controlling porosity through phase separation and transferring this know-how into the realm of microscopic spheres is of great importance, but brings specific challenges, since a further phenomenon, i.e. spheroidization by soft templating methods (emulsion) needs to be controlled in the synthesis process. Emulsion destabilization phenomena, like emulsion flocculation, sedimentation, and droplet coalescence, can have a strong impact on the macropores formation. Moreover, all the complex processes before described, such as phase separation thermodynamics and sol-gel kinetics, must occur within the tiny droplets of an emulsion, which may pose geometrical or space limitations for generating the desired interconnected macroporosity. Yanagisawa *et al.* studied the spontaneous patterning of polymer microgels by confining a polymer blend (PEG and gelatin) within microspheres, showing the interplay among phase separation, wetting and gelation in the presence of droplet confinement [142].

As for silica and non-siliceous based porous microspheres, these are promising materials, since they can act as support materials and are of great interest in many fields, ranging from chromatography to catalysis, including storage and delivery, phosphor materials (white-light emitting diodes), antibacterial activity and enzyme fixation [25]. One further example is the potential use of silica-based porous microspheres as support materials for chemical immobilization and catalysis.

The published works on interconnected macroporous microspheres, obtained by sol-gel polymerization induced phase separation, are very scarce. The development of microspheres with varied pore morphology has been achieved mainly by the sol-gel route combined with self-assembly technology [143], emulsion process [24,39], dispersion process [144], nanocasting [145,146] or using hard templates, such as polystyrene (PS) beads, to reach the desired macroporosity [147,148].

In what regards template-free synthesis protocols, mesoporous microspheres, of composition InVO_4 , were developed through Oswald ripening and self-assembly aggregation of preformed InVO_4 NPs, in the presence of CTAB, which binds the NPs together through electrostatic interaction after their aggregation has taken place. These porous microspheres were reported to exhibit enhanced visible-light absorption ability [149], however poor cohesiveness (not directly assessed in this work) might be an issue for these materials. *In-situ* growth of TiO_2 NPs on these microspheres was performed to achieve $\text{TiO}_2/\text{InVO}_4$ nanocomposite microspheres [149], with high photocatalytic activity and recycling ability. Also targeting photocatalysis, the same authors have studied composites made from the mixture of the porous InVO_4 microspheres with C quantum dots under reflux [150].

Hollow (core-shell) microspheres of different compositions, loaded with NPs within their mesoporous-structured shell have been fabricated for applications, such as light diffusers and magnetic-assisted separation agents. One example was the synthesis of AgNPs@silica hollow microspheres (microcapsules), which started from PS beads, as a template, and made use of polyvinylpyrrolidone (PVP) as a Ag^+ reduction agent and mesoporosity inducer at the shell. Both, PVP and PS, were removed by calcination at the end of the synthesis [143]. The resulting AgNPs@silica core-shell microspheres were able to protect the immobilized AgNPs located within

the microspheres' shell and, simultaneously, maintain antibacterial activity for long periods, through the release of the remaining Ag^+ ions in aqueous solution.

Nanocrystalline Fe_2O_3 , SnO_2 , ZrO_2 and Mn_2O_3 microspheres with additional internal mesopores and/or macropores have been prepared by nanocasting using commercially available mesoporous silica spheres of different diameters, as the template. These were loaded by the metal salt solutions and silica was leached out in HF or NaOH solution [145]. Other works also involved hard-templating methods for the preparation of metal or metal oxide porous microspheres, such as pre-formed microspheres made of poly(GMAco-EGDMA), a polymer of glycidyl methacrylate (GMA) cross-linked with ethylene glycol dimethacrylate (EGDMA), which were functionalized with ethylenediamine (EDA) and infiltrated with Si, Ni or Zr precursors to give porous metal oxide, or metal microspheres, after calcination [151–153], to be applied as catalysts, or in chromatography columns. These techniques, despite resulting in spheres of good quality and uniform size distribution, involved several synthesis steps and expensive reagents and were time consuming (more than 2 days of synthesis).

A different strategy was introduced by Mori *et al.*, in 1993 [154], where a water-in-oil (W/O) emulsion was prepared to obtain microspheres of SiO_2 - B_2O_3 - Na_2O composition, with some degree of macroporosity, by extracting, after a heat treatment at 600-750°C for 16h, soluble parts of the glass using sulfuric acid. In this process the W phase contained TMOS and B and Na precursors, together with DMF and a high amount of water ($\text{H}_2\text{O}/\text{TMOS}=20$), while the O phase was made of kerosine and Span[®]80. The heat treatment of the resulting spheres promoted phase separation, which together with a subsequent extraction of the soluble phase (mainly based on boron and sodium) by sulfuric acid, led to the generation of interconnected macroporosity, especially at the surface of the spheres [154]. In fact, phase separation was found to proceed more effectively, when temperature was raised up. This technique does not involve the type of phase separation by spinodal decomposition (chemical cooling) reported in sections 2-4 of this chapter.

2.5. Macroporous microspheres by sol-gel/phase separation

Different types of emulsions and of sol-gel/phase separation phenomena are among the strategies yield macroporous microspheres, either with incontinuous inner macroporosity (multicavities), or with interconnected continuous macroporosity, or even with hierarchical interconnected porosity at different length scales.

2.5.1. Multicavities / incontinuous inner macroporosity

Oil-in-water (O/W) emulsions combined with sol-gel processing in the presence of PVP additive have been employed to create metallic oxide microspheres, with a smooth surface, exhibiting multicavities in their core. The oil phase is composed by 1-octanol, metal alkoxide and PVP. The latter one was found in this case to induce a nucleation growth phase separation phenomenon, followed by sol-gel transition and drying, which resulted in the incontinuous inner macroporosity [22,23,155,156]. Potential applications for these microspheres are on heat insulation and separation (liquid chromatography) [155]. Cai *et al.* (2014) [22] reported on this synthesis for the preparation TiO₂, ZrO₂ and Al₂O₃ microspheres [22,155,156] with incontinuous multicavities of sizes (diameter) in the range of 150 nm to 1.3 μm. The larger the PVP amount, the larger the cavities' size. Their morphology (inner macroporosity) is shown in Figure 2.21 for increasing amounts of PVP.

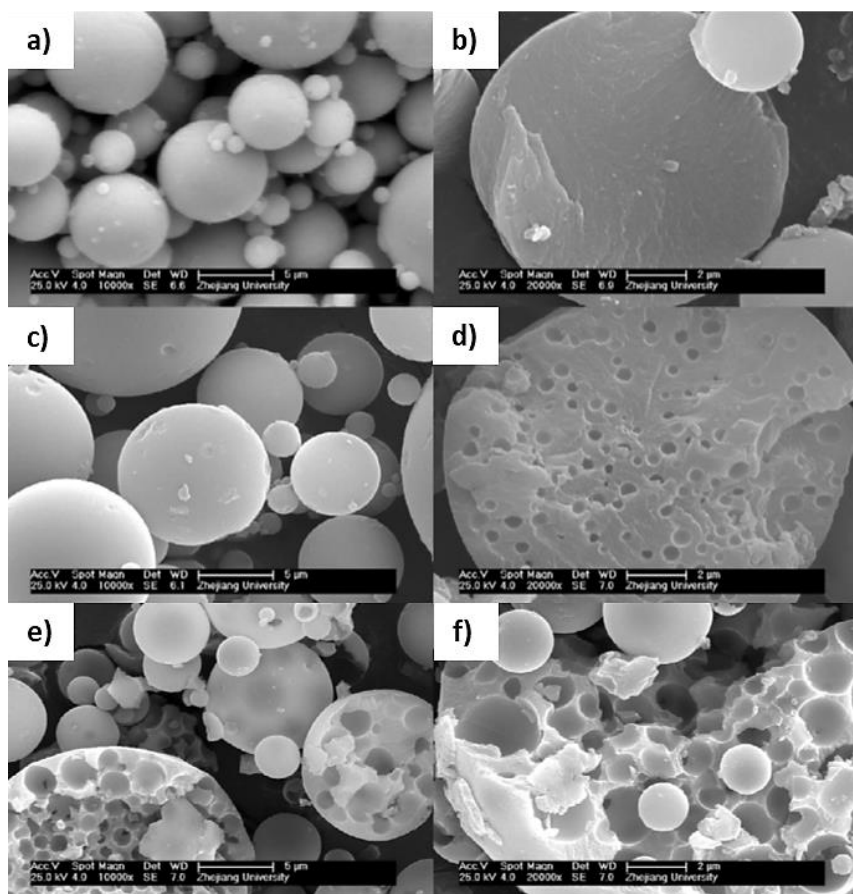


Figure 2.21. SEM images of TiO₂ microspheres exhibiting inner incontinuous macroporosity, prepared by O/W emulsion method combined with sol-gel transition and phase separation. The larger the amount of phase separation inducer (PVP), the larger the pore volume and size. (a and b) 0 g PVP; (c and d) 0.190 g PVP; (e and f) 0.571 g PVP; (h and i) 1.142 g PVP; (j and k) 1.903 g PVP. Reprinted from Chinese Chem. Lett., Vol. 25, W. W. Cai, H. Yang, X. Z. Guo, A facile one-step route to synthesize titania hollow microspheres with incontinuous multicavities, Pages 441-446, , Copyright (2014), with permission from Elsevier [22].

The oil (O) phase is composed by 1-octanol, metal alkoxide and PVP, as well as a chelating agent, to suppress the fast hydrolysis of the metal alkoxides, and a surfactant (Span®80), used to stabilize the oil droplets of the emulsion and to preserve their spherical shape [22]. The general process is summarized in Figure 2.22. A polar solvent was selected (1-octanol) to facilitate the diffusion of water in the O phase and accelerate the sol-gel reactions. Surfactants alkylphenol ethoxylates (OP-10) and sodium dodecyl sulfate (SDS) were added to the water (W) phase of the emulsion to lead to a more homogeneous particle size distribution. Similar to the works reporting on porous monoliths, the phase separation was induced by the strong interaction between PVP and the metal oxide oligomers, which lead to a hydrophilic-hydrophobic repulsion between the oligomers and the solvent. The

influence of the heat-treatment on the crystalline phase and the porous structure was also investigated in these works.

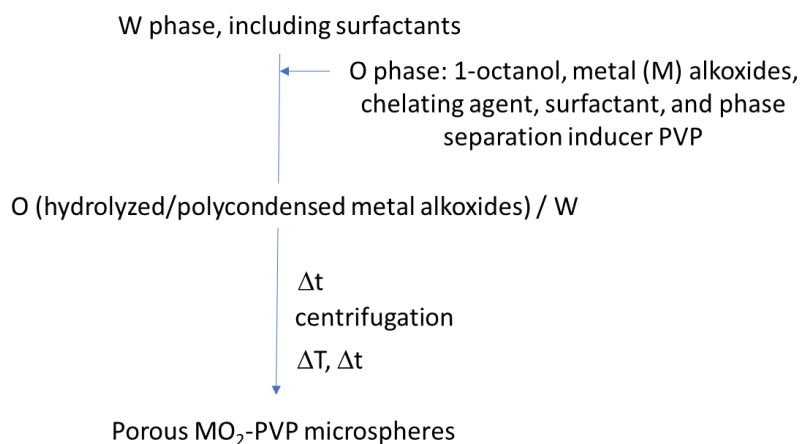


Figure 2.22 – Representative synthesis flowchart, employing O/W emulsification as soft template, and sol-gel/phase separation, for the achievement of metal oxide microspheres with incontinuous inner macroporosity.

2.5.2. Interconnected macroporosity

Yang *et al.* (2006) [23] made some of the first attempts to achieve silica microspheres with mesoporosity, which also exhibited some macroporosity, but still with some space for improvement, especially in terms of spherical morphology and pore size and shape control. They employed PEO and F127 to induce porosity formation in a pre-hydrolyzed silica sol, and a mechanism based on a pH-induced rapid colloid aggregation, by addition of triethylamine (TEA) or trioctylamine (TOA), for the formation of the silica spheres all inside the water phase droplets of a water-in-oil (W/O) emulsion. The addition of PEO accelerated gelation of the sol and the formation of silica spheres, mainly through reducing the primary particle size. F127 acted as surfactant to produce mesopores, while PEO acted as auxiliary template to produce macropores.

Silica microspheres with hierarchical interconnected macro/mesoporosity were obtained by Shi *et al.* [24], in 2008, using the synergetic interaction of phase separation and sol-gel transition in a confined W/O emulsion droplet. These synthesis strategies are schematically represented in Figure 2.23.

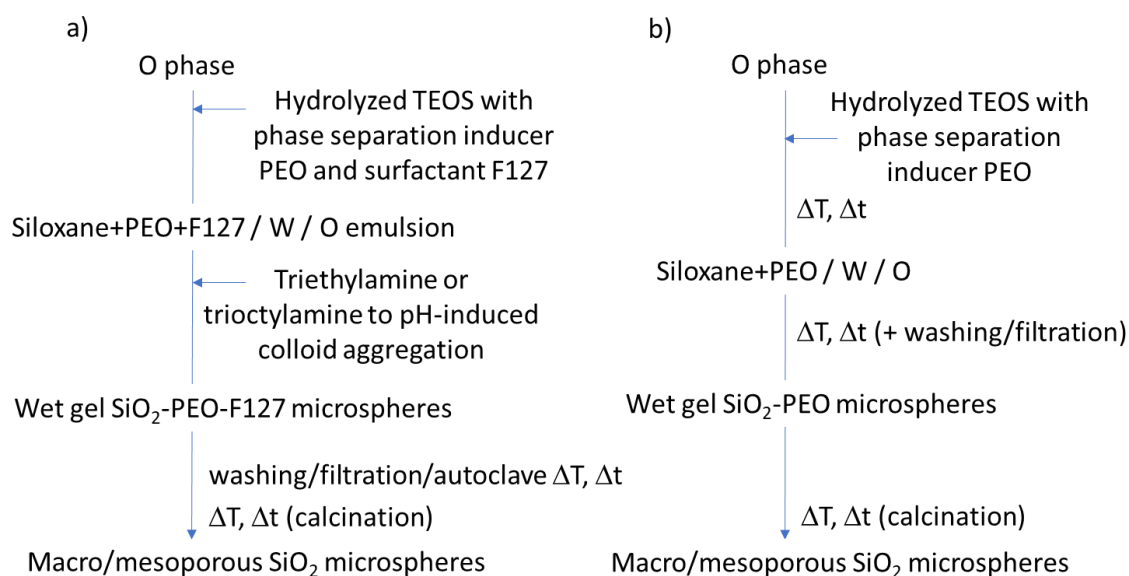


Figure 2.23. Representative synthesis flowcharts, employing W/O emulsification as soft template, for the achievement of sol-gel derived macro/mesoporous SiO₂ microspheres: a) method developed by Yang et al. [23]; b) method developed by Shi et al. [26]. The O phase is composed by paraffin oil and Span®80.

TEOS was hydrolyzed in HCl to form silica sol (W phase) and ethanol as byproduct, to which PEO was added. Since ethanol was miscible with the O phase (paraffin oil), it was first eliminated using vacuum distillation. Emulsification was carried out by magnetic stirring, while heating at 60 °C during 20 h was employed to promote gelation and phase separation within the droplets of the emulsion. The presence of PEO was responsible for phase separation by spinodal decomposition to occur. The two transient continuous phase domains of silica-rich and solvent-rich phase coarsened as the sol-gel transition proceeded. After liquid elutriation, spheres with diameters ranging from 6 to 10 μm were gathered and proceeded for characterization. By calcination, the solvent-rich phase and PEO were burned off forming the macropores, which can be observed in Figure 2.24.

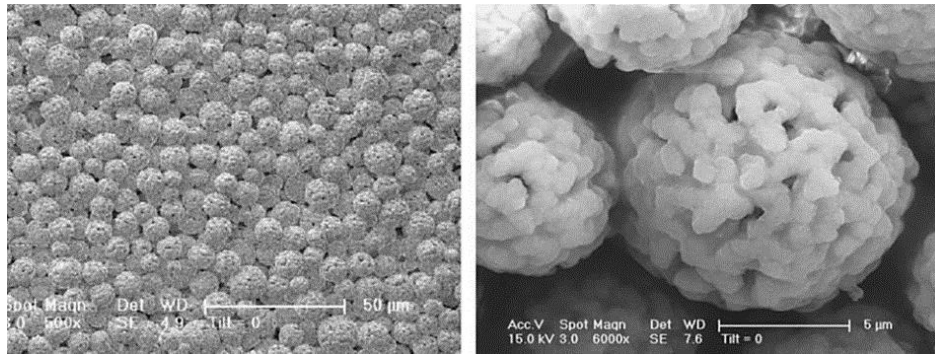


Figure 2.24. SEM images for the SiO₂ microspheres prepared by the W/O emulsion method combined with sol-gel transition and phase separation, using TEOS as Si precursor and PEO as phase separation inducer additive. Their narrow size distribution is due to liquid elutriation techniques, which allowed to select microspheres of diameter ranging from 6 to 10 µm. Reprinted from *Microporous Mesoporous Mater.*, Vol. 116, Z. G. Shi, Y.Q. Feng, Synthesis, and characterization of hierarchically porous silica microspheres with penetrable macropores and tunable mesopores, Pages 701-704, Copyright (2008), with permission from Elsevier [24].

PEO was found to have two functions in the microspheres formation process: phase separation induction and porogenic function [24]. However, the small mesopores developed within the spheres' skeleton had to be enlarged and this was achieved by a treatment with aqueous solution of NH₄OH 0.01 M at 120°C (dissolution-reprecipitation process). Consequently, the surface area decreased by 33%, but the pore volume increased by 50%. The mechanical strength of these microspheres is expected to be larger than that of the microspheres obtained by self-assembly, or those with discontinuous pores, in particular multicavities of large diameter and thin walls.

Over the years, similar microspheres were obtained through the described emulsion method (Figure 2.23b), with slight variations, such as addition of Span®80 and/or NH₄OH to the O phase of the emulsion, and the resulting porous microspheres were applied mainly to chromatography [24–31], but also in drug delivery [32,33], adsorption [34] and composites production [35]. In this latter one, the porous SiO₂ microspheres were incorporated in phenolphthalein-based poly(arylene ether sulfone) resin. Another adaptation of the technique of Figure 2.23, targeting hybrid SiO₂ microspheres, consisted of the employment of silanes TEOS and Bis(trimethoxysilyl)ethane (BTME), and a slightly different O phase made of petroleum ether, Triton X-100 and Span®80 [25,36].

Another attempt for porous microspheres involved the previous preparation of polyethoxysiloxane, from TEOS, containing oligomeric PEG additive of 400 Mw and using cyclohexane as stabilizer, which was mixed within an acidic solution of water and ethanol [36]. The resulting microspheres were small, ca. 4-5 μm , and without macroporosity, only mesoporosity. PEG was responsible for the presence of mesopores (\sim 5-7 nm) and a specific surface area of ca. 230 m^2/g . Too much PEG was found to degrade the spherical shape of the particles. These microspheres were used in liquid chromatography for chiral separation of flurbiprofen axetil stereoisomers. Mesoporous microspheres of rare earth doped yttrium aluminum garnet $\text{Y}_3\text{Al}_5\text{O}_{12}$ (YAG:RE³⁺), namely YAG:Ce³⁺, were obtained through a fast epoxide-driven sol-gel route using inorganic metal salts as precursor, in particular $\text{YCl}_3 \cdot 6\text{H}_2\text{O}$, $\text{AlCl}_3 \cdot 6\text{H}_2\text{O}$ and cerium chloride heptahydrate [37]. Formamide and PO were used, as well as F127. The particles were heat treated under a flowing gas mixture (5% H_2 + 95% N_2) for 6 h at 1000–1600°C. The authors reported that gelation in this case was faster than in traditional epoxide sol-gel process, because of the larger amount of metal ion and PO/metal ion molar ratio. The lack of macroporosity of the resulting microspheres and their small size (ca. 2 μm) might have been caused by the fast gelation process which occurred sooner than the onset of phase separation inhibiting it from occurring.

Although a few authors successfully made hierarchical macro/mesoporous spheres by using PEO, or PVP as phase separation inducer additives, and surfactants in the water phase droplets of the emulsion (Table 2.5), an original and simple approach was developed by Marques *et al.*, based, as well, on sol-gel transition and phase separation between siloxane-rich domains and water-rich domains, within the droplets of a W/O emulsion, but where no specific gelation, nor phase separation promoting additives are needed. Instead, a special kind of silane, called GPTMS was selected as one of the precursors. GPTMS is an trimethoxysilane with a relatively long carbon chain and a PO group in the end which confers inherent phase separation and functionalization capabilities. This method has a few similarities both with phase separation in alkylene-bridged silsesquioxanes sol-gel systems [73], and with the epoxy mediated synthesis approaches, before reported for monolithic macroporous gels [93], but no specific gelation additives, such as PO or formamide,

are needed, nor hydrophilic polymers as templates for phase separation, which eliminates the need for calcination to get rid of the polymeric additives, and achieve the macroporous material. A simple drying of the spheres is enough to eliminate the solvent remaining within the 3D interconnected co-continuous porous structure. A simplified flowchart and scheme regarding the porous microspheres preparation is shown in Figure 2.25 (a and b), together with optical microscopy images (Figure 2.26) showing the evolution of the reaction medium during the synthesis, until a free-flowing powder is obtained after drying at 40°C. A heat treatment at temperatures above 500°C can be done just in case purely inorganic porous microspheres are desired. In the present methodology, phase separation tends to occur via siloxane formation by polycondensation of the silanol groups, but also from the epoxy ring opening reaction, being both an entropy and enthalpy driven process. This synthesis is the core of this dissertation, and it will be studied, modified and improved in the subsequent chapters.

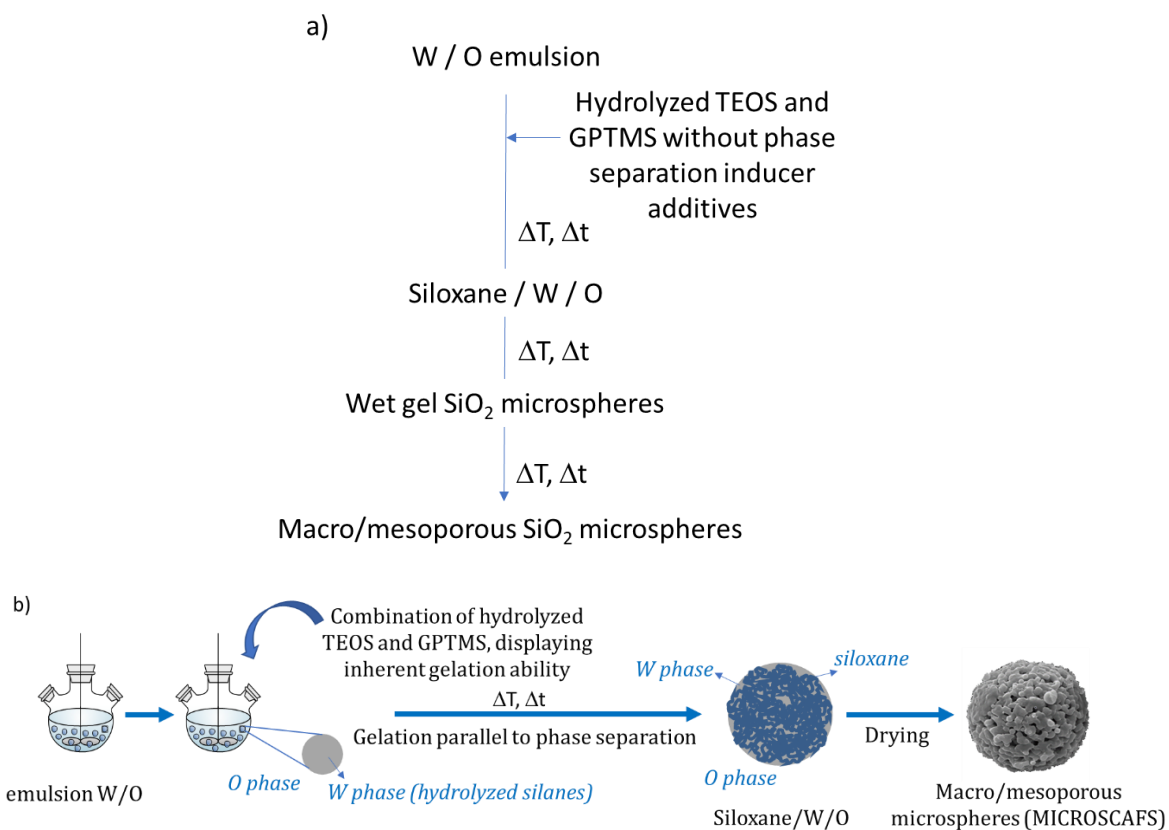


Figure 2.25. a) Preparation schemes for the sol-gel derived macro/mesoporous SiO₂ microspheres (MICROSCAFS[®]), synthesized from TEOS and GPTMS, obtained by W/O emulsion combined with sol-gel transition and phase separation, in the absence of any gelation or phase separation inducer additive: a) Representative synthesis flowchart; b) drawing scheme. The O phase is composed by decahydronaphthalene (decalin) and Span[®]80.

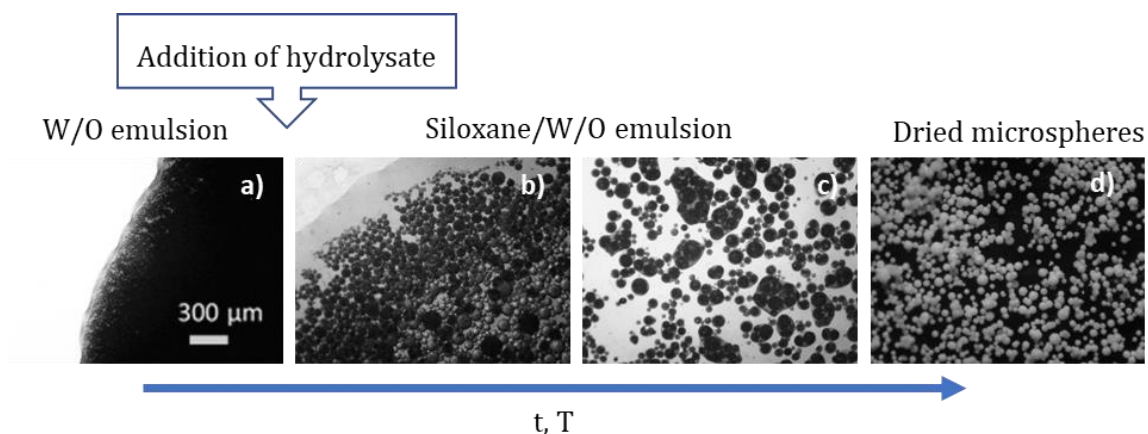


Figure 2.26. Optical microscopy photographs of reaction medium aliquots taken at different stages of the MICROSCAFS[®] synthesis. (a) emulsion, (b) emulsion after addition of the hydrolysate, 1h at 65 °C, (c) after 1h at 80 °C, (d) epoxy functionalized silica based porous microspheres dried at 40 °C. Bar scale = 300 μ m (a-d). Photos acquired in transmission mode (a-c). Photos acquired in reflection mode (d).

The first report on such synthesis occurred in 2018 [41], where the as-prepared porous epoxy-functionalized silica microspheres, shown in Figure 2.27 were grafted with a biocide (Econea®), by covalent bonding between the NH groups of the biocide and the epoxy group of the microspheres, targeting anti-fouling capability by contact.

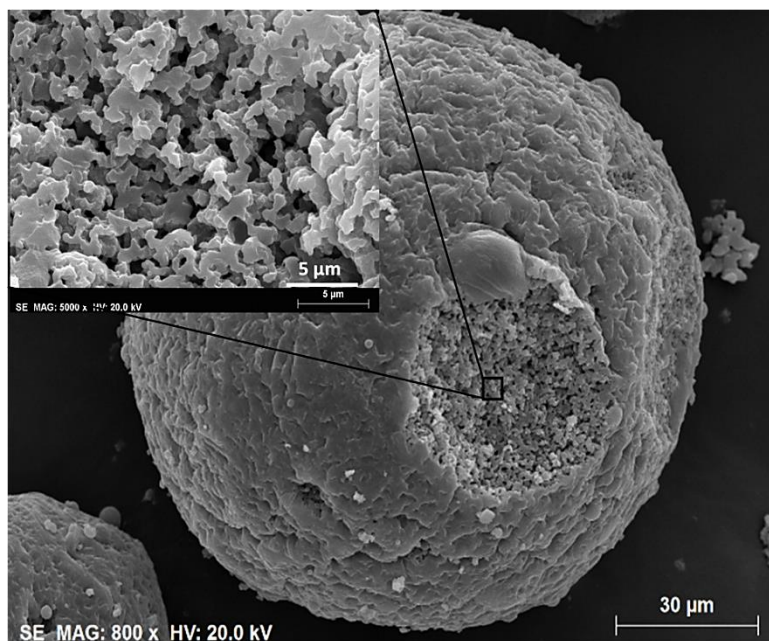


Figure 2.27. Macro/mesoporous epoxy-functionalized silica microspheres (MICROSCAFS®), synthesized from TEOS and GPTMS, obtained by emulsion combined with sol-gel transition and phase separation, in the absence of any gelation or phase separation inducer additive. Reprinted from *Microporous Mesoporous Mater.*, Vol. 261, M.V. Loureiro, M. Vale, A. De Schrijver, J.C. Bordado, E. Silva, A.C. Marques, Hybrid custom-tailored sol-gel derived microscaffold for biocides immobilization, Pages 252-258, Copyright (2018), with permission from Elsevier [41].

Table 2.5 provides a list of the works (synthesis strategies) found in the literature for the achievement of sol-gel derived microspheres displaying macroporosity, due to phase separation. The most relevant applications for each case are also described.

Table 2.5. Compilation of specific examples of macroporous microspheres and their synthesis strategies based on the emulsion method combined with sol-gel transition and phase separation.

Characteristics of the microspheres		Synthesis strategy / Applications	Author, year reference
Incontinuous multicavities	TiO ₂ , ZrO ₂ and Al ₂ O ₃ hollow microspheres with incontinuous multicavities	<p>1) O/W emulsion (O phase: metal alkoxide, EtAcAc, 1-octanol, Span[®]80, PVP; W phase: DI water and surfactants SDS and OP-10)</p> <p>2) nucleation growth phase separation</p> <p>3) nearly neutral sol-gel synthesis using chelating agent (EtAcAc) + phase separation inducer (PVP 30000Mw) and Span[®]80 as phase separation and spherical morphology stabilizer.</p> <p>Precursor: TBOT, or zirconium propoxide, or aluminum tri-sec-butoxide</p> <p>Applications: liquid chromatography and heat insulation</p>	Cai <i>et al.</i> , 2014 [22]
	Inorganic SiO ₂ microspheres	<p>1) W/O emulsion (W phase: hydrolyzed silane solution, F127 as surfactant, PEO 20000Mw as macropore former); O phase: paraffin oil and Span[®]80</p> <p>2) pH induced rapid colloid aggregation method, by addition of triethylamine (TEA): sol-gel transition in parallel with phase separation.</p> <p>3) calcination</p> <p>Precursors: TEOS</p> <p>No specific application tested</p>	Yang <i>et al.</i> , 2006 [23]
Macro/mesoporosity	Inorganic SiO ₂ microspheres	<p>1) W/O emulsion (W phase: hydrolyzed silane solution, PEO 100000Mw); O phase: paraffin oil and Span[®]80</p> <p>2) growth of siloxane oligomers: sol-gel transition in parallel with phase separation; burning of PEO leads to mesopores and fluid phase evaporation leads to macropores.</p> <p>3) calcination</p> <p>Precursors: TEOS</p> <p>Applications: SiO₂ porous microspheres covalently bonded with octadecyl tested for liquid chromatography (fast separation)</p>	Shi <i>et al.</i> , 2008 [24]
	Hybrid, epoxy functionalized SiO ₂ microspheres	<p>1) W/O emulsion (W phase: hydrolyzed silanes solution); O phase: Decahydronaphthalene and Span[®]80</p> <p>2) growth of silica-epoxy oligomers: sol-gel transition in parallel with phase separation inside the emulsion droplets; no need for templates or phase separation inducer additives, no need for calcination to obtain meso and macroporosity</p> <p>Precursors: TEOS and GPTMS</p> <p>Applications: Biocide Econe[®] immobilization within the porous microspheres (grafting) for antifouling applications</p>	Loureiro <i>et al.</i> , 2018 [41]
	Waxberry-like and ethyl-bridged hybrid	<p>1) W/O emulsion (W phase: hydrolyzed silanes solution, PEO 100000Mw); O phase: petroleum ether, Triton X-100, Span[®]80</p>	Li <i>et al.</i> , 2019 [25]

SiO₂ microspheres 2) growth of siloxane oligomers: sol-gel transition in parallel with phase separation; burning of PEO leads to mesopores and fluid phase evaporation leads to macropores
Precursors: TEOS and BTME
Applications: Alkali resistant carrier with fast mass transfer property; tested for catalysis and liquid chromatography

2.6. Final Remarks

The pioneering works by Nakanishi and Soga, in the early nineties, on the enlightenment of phase separation induced by polymerization as a viable mechanism for porosity control in sol-gel systems, were at the origin of a variety of enabling materials for emerging technologies and advanced synthetic approaches towards tailored porous materials. This topic, extremely important for the development of advanced porous support materials, is still rapidly evolving, either in the field of monolithic materials or microspheres. The characteristic advantage of these materials is their interconnected porosity on the micrometer length scale, which takes place when the phase separation process, by spinodal decomposition, is occurring concomitantly to the gelation process. Structures with different coarsening extension (characteristic size) can be achieved depending on the timing between phase separation and sol-gel transition, the stability of the heterogeneous phases and the volume fraction of the gel-rich and solvent-rich phases. Therefore, the control of all parameters resulting in faster sol-gel reactions (kinetics), or that induce phase separation is critical. Over the last thirty years, various synthesis strategies have been developed resorting to different kinds of alkoxides and salt precursors, to reach hierarchical macroporous monolithic products made of a variety of materials: silica (inorganic or hybrid), either single oxide or multi-oxide composition, non-siliceous oxides, including C/oxides, and non-oxides, such as C, or MOFs. These findings, herein compiled and critically discussed, serve as an inspiration for the development of multicomponent oxide porous microspheres, the main topic of this thesis.

This page was purposely left in blank.

Chapter

Silica-based MICROSCAFS®

3

The following chapter is based on the peer-reviewed article:

M. Vale, M. V. Loureiro, M.J. Ferreira, A.C. Marques, Silica-based microspheres with interconnected macroporosity by phase separation, J Solgel Sci Technol 95 (2020) 746–759. <https://doi.org/10.1007/s10971-020-05257-4>

3.1. Introduction

In this chapter S MICROSCAFS® are prepared and characterized and the effect of multiple synthesis parameters on their final porosity and size is systematically investigated. The goal is to better understand and optimize S MICROSCAFS® previously reported by the TPMI group [157–160]. For achieving the microspheres with the desired interconnected macroporosity, a water-in-oil (W/O) emulsion is prepared, and phase separation between siloxane-rich domains and water-rich phase is promoted to occur within the aqueous droplets of the emulsion. The effect of the synthesis parameters linked to the degree of polymerization (hydrolysate viscosity), namely HCl/silanes molar ratio and pre-hydrolysis time, and parameters linked to the microemulsion, namely the quantity of surfactant are studied.

3.1.1. Synthesis of the silica (S) MICROSCAFS®

In this study, the porous silica microspheres, called S MICROSCAFS® were prepared by adding a pre-hydrolyzed silane solution, whose viscosity was assessed (ii, Figure 3.1), to a water-in-oil (W/O) emulsion (i, Figure 3.1). This was followed by a pre-established temperature raise protocol (iii-vii, Figure 3.1), up to 95 °C, with a recurrent observation of the reaction medium with an optical microscope. At the end of the synthesis, the resulting microspheres were washed and obtained by filtration (viii, Figure 3.1).

In the hydrolysis phase, 21.4 ml of TEOS (98%, Sigma-Aldrich) and 18.7 ml of (3-GPTMS (Xiameter OFS-6040, >98.5%, Dow) were mixed in a closed container under magnetic stirring with 15 ml of an aqueous HCl solution for a predetermined time, namely 1 h or 24 h.

In parallel, the W/O emulsion was prepared by mixing 100 g of decahydronaphthalene (mixture of cis and trans isomers, 98%, Merck), 45 g of distilled water and a predetermined quantity (2 or 4 g) of sorbitan monooleate surfactant (Span® 80, HLB: 4.3, Merck), at a selected emulsification speed of 9800 rpm using a dispersing instrument (IKA T18 digital ULTRA-TURRAX®) for 10 minutes.

The emulsion was then added to the reactor to which the pre-hydrolyzed silanes solution was sequentially added, being kept at a stirring speed of 600 rpm for the time/temperature protocol specified in Table 3.1.

Table 3.1. S MICROSCAFS® steps' temperature and times.

Time	Temperature (°C)
1h	RT
1h30min	65
10min	70
1h	80
1h	85
1h	90
30min	95

In the end, the microspheres were washed with n-hexane through vacuum filtration and dried overnight at 45 °C.

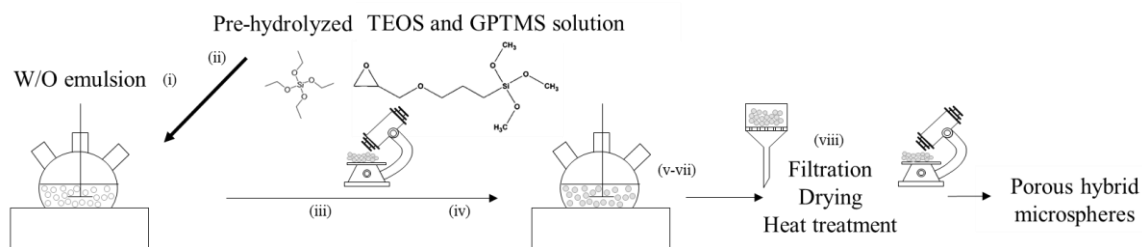


Figure 3.1. Schematic of the S MICROSCAFS® synthesis.

The modified reaction parameters involved in each synthesis of this work are listed in Table 3.2. Viscosity was measured at the end of the hydrolysis step using a Brookfield Viscometer DV-II+ Pro equipped with a CP40 spindle at 12 rpm.

3.1.2. Characterization

A field emission gun (FEG)–SEM JSM 7001F (JEOL, USA) scanning electron microscope was used to obtain the SEM images of the microspheres aimed at assessing their morphology, size, and porosity. A 15 nm layer of gold–palladium was sputtered on the samples before observation using a turbomolecular pumped coater Q150T ES (Quorum Technologies, UK).

The specific surface areas, pore size distributions, and pore volumes of the microspheres were obtained by nitrogen (N₂) adsorption/desorption BET method at -196 °C using a ASAP 2020 (Micromeritics, USA) adsorption analyzer. For these experiments, ~300 mg of sample was sequentially outgassed at 90 and 350 °C for 1 and 4 h, respectively, with a high vacuum pump, to remove moisture and other surface contaminants before the analyses. The cumulative volume of pores and average pore diameter were calculated by the BJH method, applied to the adsorption and desorption branches of the isotherms. MIP was performed to quantify the pore size distribution, pore volume and porosity, using a porosimeter Autopore IV 9500 (Micromeritics, USA). A constant contact angle of 140° was selected in the analysis. The samples were subjected to 120 °C for 2 h before measurements.

The microspheres' size distributions were obtained by measuring the diameter of 100 microspheres using the Fiji software [161]. The characteristic size of the internal porosity of the final particles was defined as the average of 20 measurements of half of the sum between the thickness of the structure and the width (diameter) of an adjacent pore [88]. The measurements were carried out directly from the SEM images. The term “characteristic size” will be used throughout this chapter.

FTIR-ATR spectra of the microspheres were obtained using Spectrum Two (PerkinElmer, USA), FTIR spectrometer equipped with a UATR Two accessory, at 4 cm⁻¹ resolution and 8 scans of data accumulation. The samples were heat-treated at 150 °C for 1 h and 700 °C for 1 h before the acquisition of the infra-red (IR) data.

Sample 2S-REF was analyzed by solid-state NMR. ~200 mg of sample was packed into a 7 mm o.d. zirconia rotor, equipped with a Kel-F cap. The ¹³C cross polarization/magic angle spinning (CP/MAS) spectrum was obtained at 75.49 MHz,

on a Tecmag Redstone/Bruker 300WB (Bruker Corporation, USA), with a spinning rate of 3.5 kHz. The contact time used was 3 ms and the 90° RF pulse was 4.5 μs. A relaxation delay of 3 s was used. ¹³C spinning sidebands were suppressed using the TOSS sequence (T^OTal S^Uppression of S^Pinning S^Idebands). ¹³C chemical shifts were referenced with respect to external glycine (¹³CO observed at 176.03 ppm) .

²⁹Si CP/MAS and ²⁹Si MAS spectra were recorded at 59.63 MHz, with 4 ms contact time and a 3 s recycle delay. The spectra were externally referenced with tetrakis(trimethylsilyl) silane (²⁹Si(CH₃)₃ at -9.8 ppm).

3.2. Results and discussion

3.2.1. Evolution of the reaction medium during the synthesis

The recurrent observation through optical microscopy of an aliquot from the reaction medium at different stages of the synthesis allowed to understand the occurring phenomena, namely: a certain emulsion instability after the addition of the silanes solution (ii, Figure 3.2) denoted by the coalescence of some of the water phase droplets, the formation of emulsion templated gel-rich regions (iii, Figure 3.2) inside the water phase droplets, the densification of the gel material by polycondensation reactions along the increasing temperature steps (iv, Figure 3.2) observed by transmission mode at the optical microscope, the evolution of the polycondensation reactions which leads to a significant increase in viscosity of the droplets, observed by reflection mode at the optical microscope (v, Figure 3.2), the individualization and solidification of the microspheres (vi and vii, Figure 3.2) and their isolation by a washing and filtration procedure (viii, Figure 3.2) giving rise a whitish free-flowing powder.

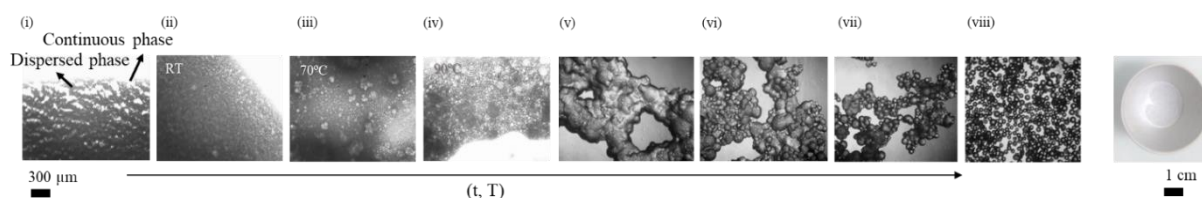


Figure 3.2. Optical microscopy photographs of reaction medium aliquots taken at different stages of the S MICROSCAFS® synthesis (2S-REF). Bar scale = 300 μm (i-viii). Photos acquired in transmission mode (i-iv). Photos acquired in reflection mode (v-viii). The photo on the right side was taken by a camera machine. Bar scale = 1 cm.

3.2.2. Microspheres size and characteristic size

In this sub-chapter, the effect of multiple variables tied to the emulsion and hydrolysis stages of the synthesis, namely surfactant amount, hydrolysis time, and HCl concentration, were studied.

All the different synthesis reported in this work and its respective parameters are listed in Table 3.2, as well as relevant characterization results such as hydrolysate viscosity, microspheres' diameter, and average characteristic size.

Table 3.2. Synthesis reaction parameters and relevant characterization results, such as hydrolysate viscosity, microspheres' diameter, and average characteristic size.

Sample acronym	Surfactant quantity (g)	Hydrolysis time (h)	HCl concentration (mol/L)	Hydrolysate viscosity (cP)	Microsphere diameter (peak maximum mode) (μm)	Average characteristic size (nm)
2S-REF	2	1	0.004	8.74	70 and 130 ^a	149 \pm 11
2S-H	2	1	0.035	9.72	64 and 106 ^a	222 \pm 28
2S-t	2	24	0.004	11.3	39 and 64 ^a	478 \pm 26
4S	4	1	0.018	9.02	49 ^b	391 \pm 30
4S-H	4	1	0.029	9.39	26 ^b	485 \pm 38

^aBimodal normal distribution

^bMonomodal lognormal distribution

Samples with 2S in their acronym were produced using 2 g of Span[®] 80 surfactant, whereas samples with 4S with 4 g. In the 2S samples, the effect of the pre-hydrolysis HCl concentration and the pre-hydrolysis time were studied, and both samples were named with "-H" and "-t" acronym, respectively. In the 4S samples only the effect of pre-hydrolysis HCl concentration was studied.

The SEM images of the outer surface of the microspheres and their interior are presented in Figure 3.3 and Figure 3.4, respectively.

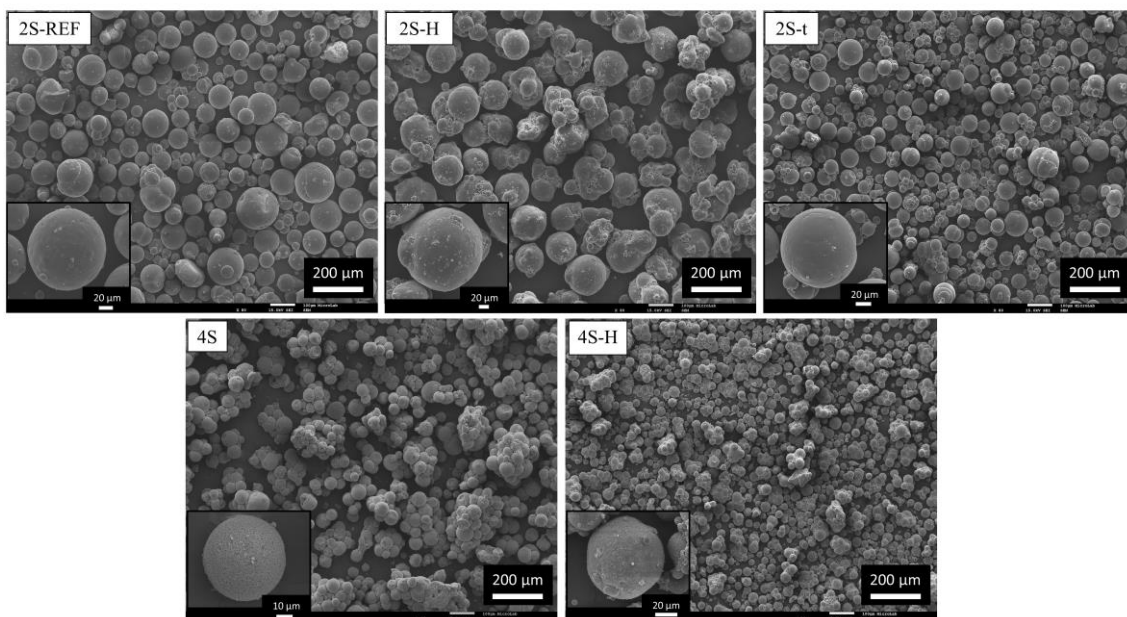


Figure 3.3. SEM images of the produced particles. The inset shows a magnified image of one microspheres for each case.

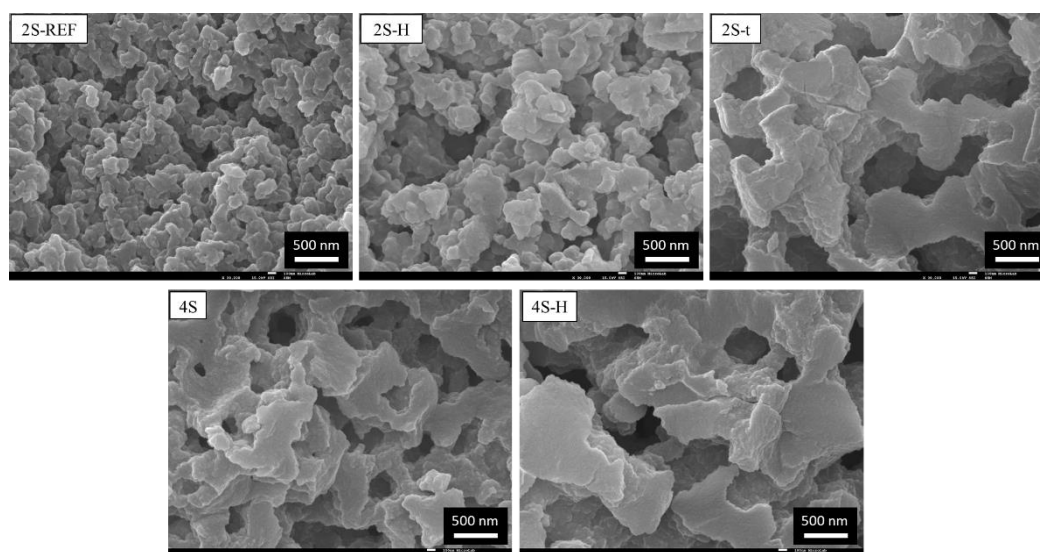


Figure 3.4. SEM images of the internal structure of the produced particles.

The S MICROSCAFS® size (diameter) distributions and the evolution of the hydrolysate viscosity with the HCl concentration are presented in Figure 3.5 and Figure 3.6, respectively. This latter one shows, as expected, an increase in the viscosity of the hydrolysate, when the HCl concentration increases, as well.

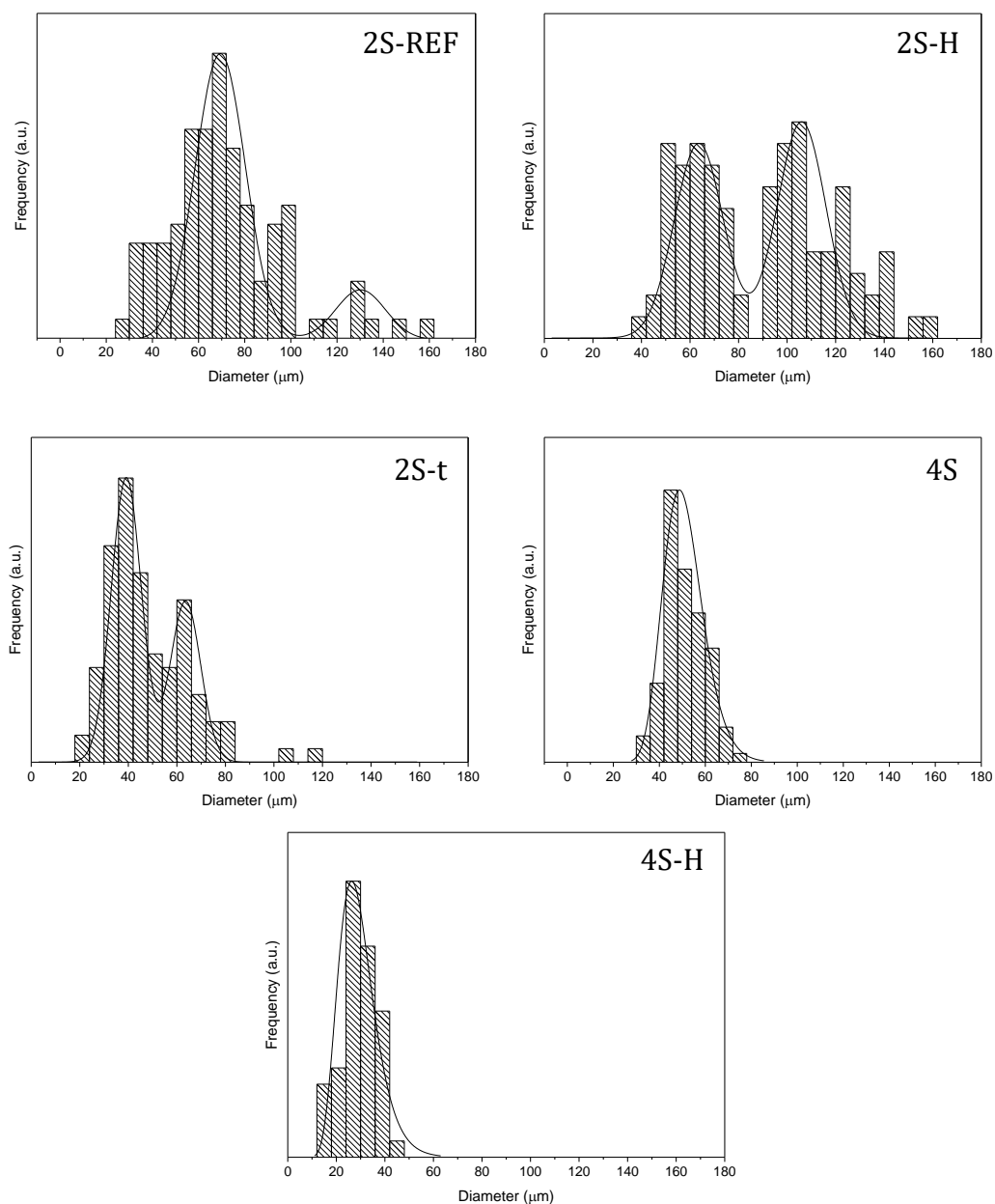


Figure 3.5. Size distributions of the S MICROSCAFS®.

Figure 3.5 shows that the amount of surfactant employed in the syntheses plays a significant role in the size (diameter) of the microspheres, i.e., the larger the surfactant content, the smaller the microspheres.

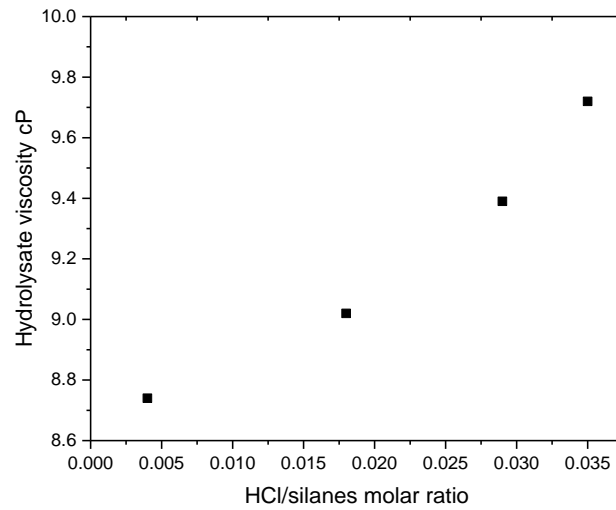


Figure 3.6. Evolution of the silica hydrolysate viscosity with the HCl/silanes molar ratio.

Also, both the increase in the HCl concentration or in the pre-hydrolysis time led to significantly larger characteristic sizes, suggesting that the more viscous silane solute (hydrolysate), the more evolved the phase separation is, i.e., the more coarsening of the siloxane domains. (Figure 3.7).

The increased viscosity of the silane hydrolysate, achieved by either increasing the hydrolysis catalyst amount or the reaction time, revealed an increased polymerization degree of the siloxane solution right before being added to the W/O emulsion, which might induce phase separation of the siloxane domains and the water-rich phase, inside the dispersed water phase (droplets) of the emulsion.

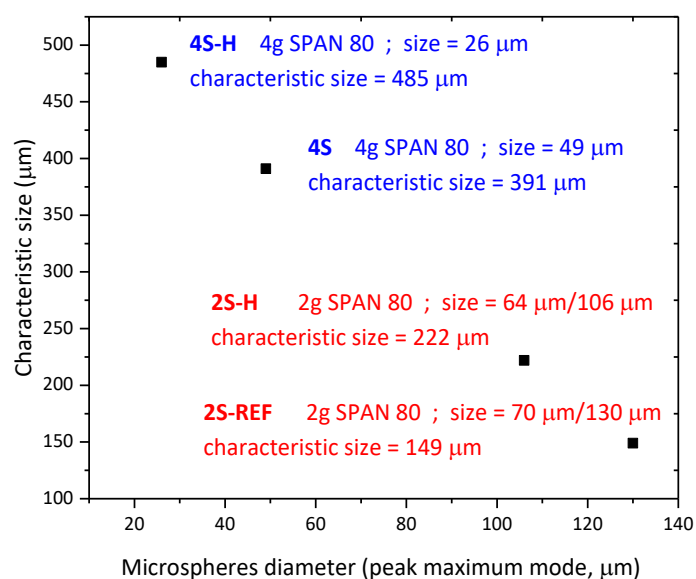


Figure 3.7. Evolution of the S MICROSCAFS® characteristic size with their diameter (size), for the syntheses where the pre-hydrolysis time is 1 h. The inset shows the values for the surfactant amount employed in the corresponding synthesis, and the value for the MICROSCAFS® size and characteristic size.

A direct relationship between the hydrolysate viscosity, which can be tailored by increasing the HCl concentration and the hydrolysis duration, and the characteristic size of the microspheres was found to exist (Figure 3.6 and Figure 3.7). The higher the viscosity, i.e., the degree of polymerization, the larger the characteristic size of the microspheres.

Phase separation induced by the condensation of alkoxy silanes is a complex process when compared with phase separation in other polymeric systems. Thermodynamically, it occurs when the free energy of the system ΔG increases as the silane condensation progresses. When the gel network forms, phase separation occurs due to a loss of entropy ΔS , because it is inversely proportional to the increasing degree of polymerization, but also due to an enthalpy ΔH rise originated from the loss of polarity resulting from the polycondensation of the silanol groups formed during the hydrolysis step. Therefore, phase separation induced by polymerization, which in the particular case of the present work occurs via siloxane formation by polycondensation of the silanol groups, but also from the epoxy ring opening reaction, is both an entropy and enthalpy driven process [162].

It should be noted that the acidic reaction medium is expected to result in the protonation of the epoxide oxygen and subsequent irreversible ring-opening reaction. These successive reactions increase the pH of the reaction medium and therefore promote the condensation (gelation) step.

Chemical quenching happens during a polymerization-induced phase separation. It occurs when the binodal and spinodal curves move and plunge the reactional system into the unstable region of the phase diagram [19]. The Flory–Huggins theory states that the critical point, ϕ_c , i.e., the composition at which the instantaneous conversion from the solubility state of a polymer blend to the phase separation by spinodal decomposition state occurs, is dependent on the number of statistical segments (N), i.e., polymerization degree, as stated in Equation 2.1. Considering that the solvent employed in this work (water) displays $N_1 = 1$, Equation 2.3 will assume the form in Equation 3.1, being the resultant phase diagram strongly asymmetric with its critical point shifted to low compositions:

$$\phi_c = \frac{1}{\sqrt{N_2} + 1} \quad (3.1)$$

Also, the temperature of the critical point (T_c) will rise since it is inversely proportional to the critical interaction parameter χ_c and, therefore, directly proportional to the number of statistical segments of the polymer (N_2) in a polymeric solution, according to Equations 3.2 and 3.3:

$$\chi_c = A + \frac{B}{T_c} \Leftrightarrow T_c = \frac{B}{\chi_c - A} \quad (3.2)$$

$$\chi_c = \frac{1}{2} \left(\frac{1}{\sqrt{N_2}} + 1 \right)^2 \quad (3.3)$$

As stated in chapter 2.1, the temperature-independent term A is called “entropic part” and the term B/T_c “enthalpic part” [56].

As the sol–gel reaction progresses, possibly together with some epoxy ring-opening reaction, the number of statistical segments of the forming siloxane-based network (N_2) will increase, resulting in an upward movement of the binodal and spinodal lines called “chemical quenching”, plunging the system into the unstable two-phase region [19].

The type of phase separation of the obtained structure, being either fast spinodal decomposition, slow nucleation and grow, or eventually nucleation and grow followed by spinodal decomposition, will directly be dependent on the speed of the quench but also on the region where the system crosses the phase separation lines. The gelation/solidification of the silica-based domains should be coincident, as maximum as possible, with the critical point, ϕ_c , i.e., with the point where phase separation by spinodal decomposition occurs. This work is the result of optimization studies to address this challenge, to ensure the generation of the interconnected macroporosity present in the S MICROSCAFS®. The starting point was the synthesis of silica-based microspheres by a similar procedure, reported by the team [41,163], where the freezing of the structure was not optimized for occurring at the spinodal decomposition.

Since spinodal phase separation occurs when a fast movement of the curve happens, the challenge is to freeze the structure precisely at the point of phase separation. Figure 3.4 shows that the freezing of the structures occurred around the critical point, as desired, however there are some differences in terms of characteristic size of the worm-like macroporous networks shown in Figure 3.4, which reveals that the freezing of the structure occurred at a specific $\phi_c \pm \Delta\phi$ or/and with a certain delay after the spinodal decomposition takes place, leading to the coarsening of the siloxane-based domains and a larger characteristic size.

The chemical nature of the alkoxy silanes might also play a significant role in inducing faster hydrolysis/gelation rates, i.e., higher hydrolysate viscosity. In acidic media, the epoxy ring present in the GPTMS will open and be converted into the corresponding secondary alcohols [164], contributing to an increasing of the final

degree of polymerization of the siloxane domains. Therefore, the epoxy group belonging to the epoxy silane GPTMS may act as an inherent gelation promoting agent, excluding the need for using the typical gelation promoting additives, such as NaPSS [165] or HPAA [166]. It should be noted that, according to Table 3.2, that the pH of the hydrolysate is lower for larger amount of catalyst employed or longer hydrolysis step, which might further promote the epoxy ring opening.

MIP data of the microspheres obtained in this chapter is present in Table 3.3. To account for the interparticle spaces, the porosity data achieved above 10 μm was not considered in this analysis, which does not mean that there are no interconnected macropores with a length above 10 μm . These larger pores might not be considered in this work, leading to an underestimation of the macroporosity value. In this regard, the initially achieved porosities of ca. 60-70%, calculated for the full pore size range, were reduced to 20-30%, as can be observed in Table 3.3.

Table 3.3. MIP results, upon elimination of the porosity data above 10 μm .

Sample acronym	Cumulative pore volume (cm^3/g)	Total porosity (%)
2S-REF	0.55	28
2S-H	0.52	24
2S-t	0.57	31
4S	0.59	23
4S-H	0.37	19

Regarding the pore size distribution curves of the porous microspheres, shown in Figure 3.8, one can conclude that they follow the same trend when comparing average characteristic size obtained from the SEM images (Table 3.2) with the pore size diameter at the peak maximum. The pore size diameter at the peak maximum increases with the catalyst amount or reaction time at the pre-hydrolysis step, while the full width at half maximum (FWHM) is found to decrease, i.e., a narrower pore size distribution is achieved. Samples 2S-t and 4S-H were the ones that revealed larger porosity and narrower pore size distribution.

MIP is not as adequate as N_2 adsorption-desorption technique for the determination of mesoporosity. However, Figure 3.8 reveals that the amount of micro and

mesopores was very small, almost negligible in some cases, being macroporosity the dominant type of porosity exhibited by these materials.

It should be noticed the reduction or even disappearance of mesopores when the pore size diameter at the peak maximum increases, which suggests that the macroporosity is generated at the expense of mesoporosity.

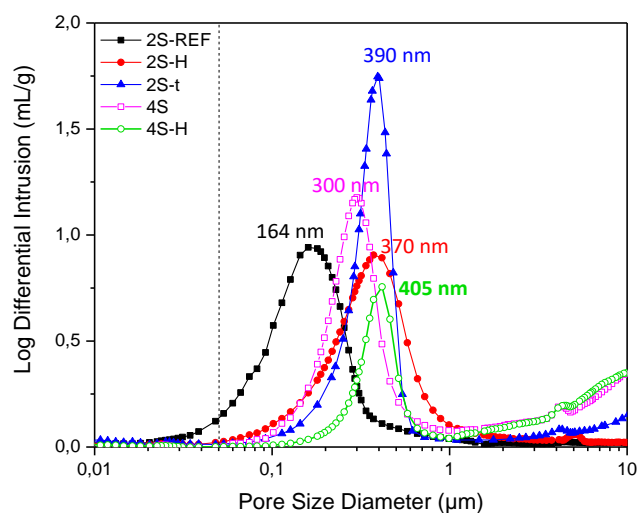


Figure 3.8. Pore size distribution curves of the S MICROSCAFS®.

The N₂ adsorption-desorption isotherms (Figure 3.9) are all of Type III (International Union of Pure and Applied Chemistry (IUPAC) classification) characteristic of non-porous or macroporous materials (pore diameter > 50 nm). The continuous curvature without the formation of a significant hysteresis characterized the unrestricted monolayer-multilayer adsorption. The small quantity of N₂ adsorbed at lower relative pressures indicated the point at which the monolayer coverage was complete [167].

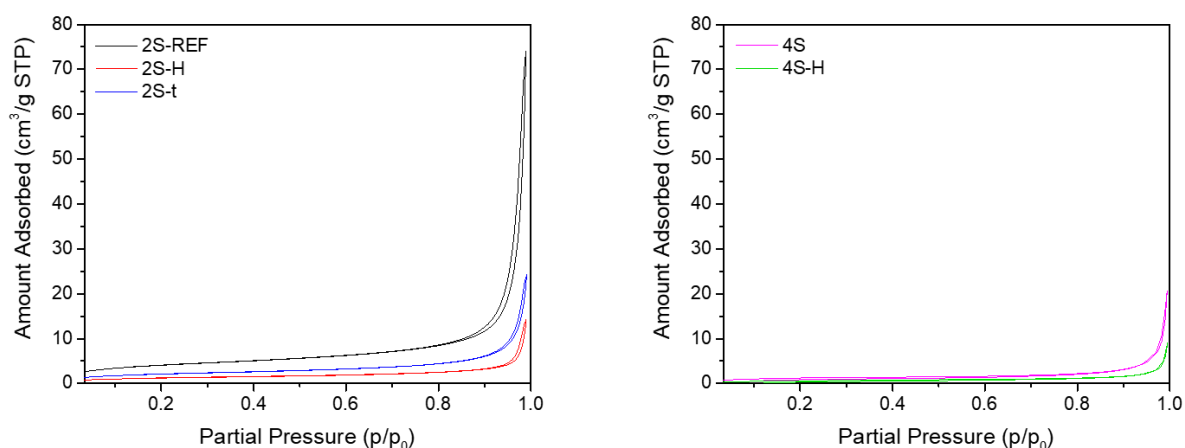


Figure 3.9. N₂ adsorption-desorption isotherms of the S MICROSCAFS®.

When the HCl concentration or the pre-hydrolysis time was increased, the surface area decreased, which is in line with a decrease of the mesopores volume fraction, as seen in Table 3.4.

Table 3.4. N₂ adsorption/desorption data of the S MICROSCAFS®.

Sample acronym	BET Surface Area (m ² /g)	BJH cumulative volume of pores (cm ³ /g) adsorption	BJH cumulative volume of pores (cm ³ /g) desorption	BJH adsorption average pore diameter (4V/A) (nm)	BJH desorption average pore diameter (4V/A) (nm)
2S-REF	14.51	0.082	0.102	36	37
2S-H	4.44	0.022	0.022	24	25
2S-t	7.79	0.037	0.037	23	25
4S	4.64	0.031	0.032	52	40
4S-H	2.46	0.014	0.015	31	18

When compared to macropores, mesopores are the main drivers to a high specific surface area. The dominance of macroporosity and the small surface area values are further proof of the macroporosity of the produced microspheres, which can enable the incorporation and immobilization of many chemical species, either in the liquid or in the solid (powdered) form, such as NPs. Also, this macroporosity allows these materials to be used as a mass transport system for liquids and gases, increasing the accessibility to the smaller pores. Some mesoporosity of average pore size ranging from 18 to 50 nm is present in sample 2S-REF, which explains the relatively higher

surface area of these microspheres, compared to the remaining samples. The samples with smaller macroporosity are the ones that exhibit larger mesopores diameter and volumes, as well as larger specific surface areas. Many techniques might be employed in order to increase silica-based materials' mesoporosity, in case it would also be required for some specific applications, such as hydrothermal methods, solvent exchange, and pore directing agents [1,168–172].

3.2.3. Chemical structure of the dried and heat-treated microspheres

Sample 2S-REF was studied by ^{29}Si MAS, ^{29}Si CP/MAS and ^{13}C CP/MAS TOSS solid-state NMR, with the main goal of assessing the type of Si species present in these microspheres, as well as drawing conclusions regarding the role played by the epoxy ring from GPTMS in the phase separation and gelation phenomena, i.e., if its epoxy ring has opened. From ^{29}Si MAS and ^{29}Si CP/MAS spectra (Figure 3.10 and Figure 3.11), it was found that both T (trifunctional) and Q (tetrafunctional) siloxane branching groups are present in the microspheres.

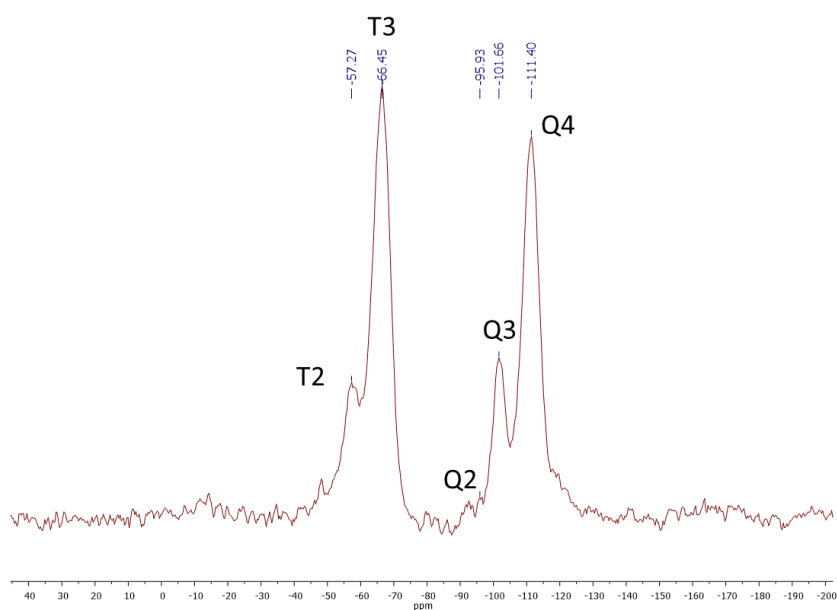


Figure 3.10. ^{29}Si MAS spectrum of microspheres 2S-REF.

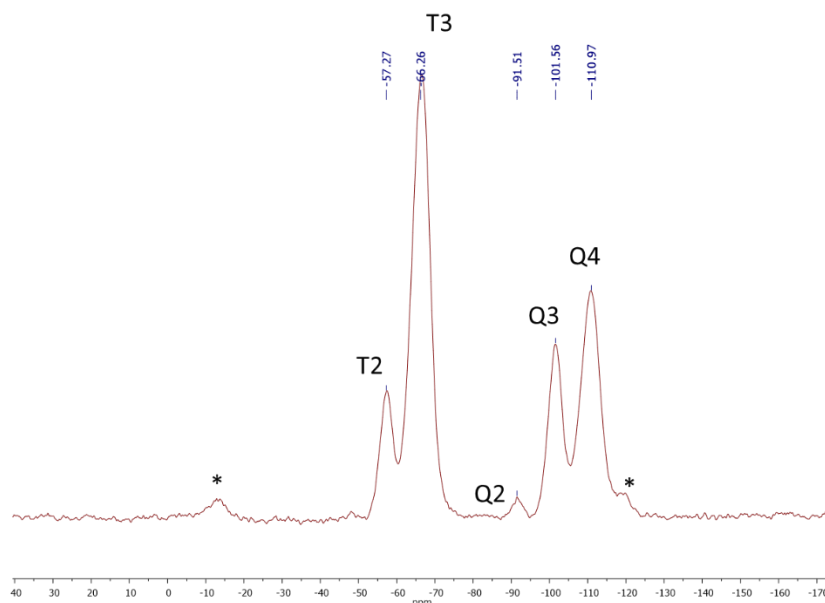


Figure 3.11. ^{29}Si CP/MAS spectrum of microspheres 2S-REF. *spinning side bands

In the T region, T2 and T3 centers are visible in both spectra, and T3 prevails over T2 as attested by the more intense signal in the ^{29}Si MAS spectrum (Figure 3.10). In the Q region, Q2, Q3, and Q4 centers were identified, with Q4 being the most significant signal of this region. The Q2 signal is very small, being only unequivocally observed in ^{29}Si CP/MAS, where it is inflated by CP. The number after the T and Q indicate the number of neighboring silicon atoms of the respective T and tetra Q siloxane center.

The analysis of both spectra above suggests that the Si-OH groups present on the surface have reacted, by polycondensation, as no Q1 and only a residual amount of Q2 were detected, together with the large signals present in the T region.

The ^{13}C CP/MAS TOSS depicted in Figure 3.12 is consistent with the presence of structure III (Figure 3.13), where the secondary alcohol group arises from the epoxy ring-opening reaction in the precursor GPTMS. The signals between 63 and 75 ppm are assigned to carbons attached to oxygen atoms, and the signals from 5-25 ppm belong to CH_2 groups attached to silicon or to just other carbons.

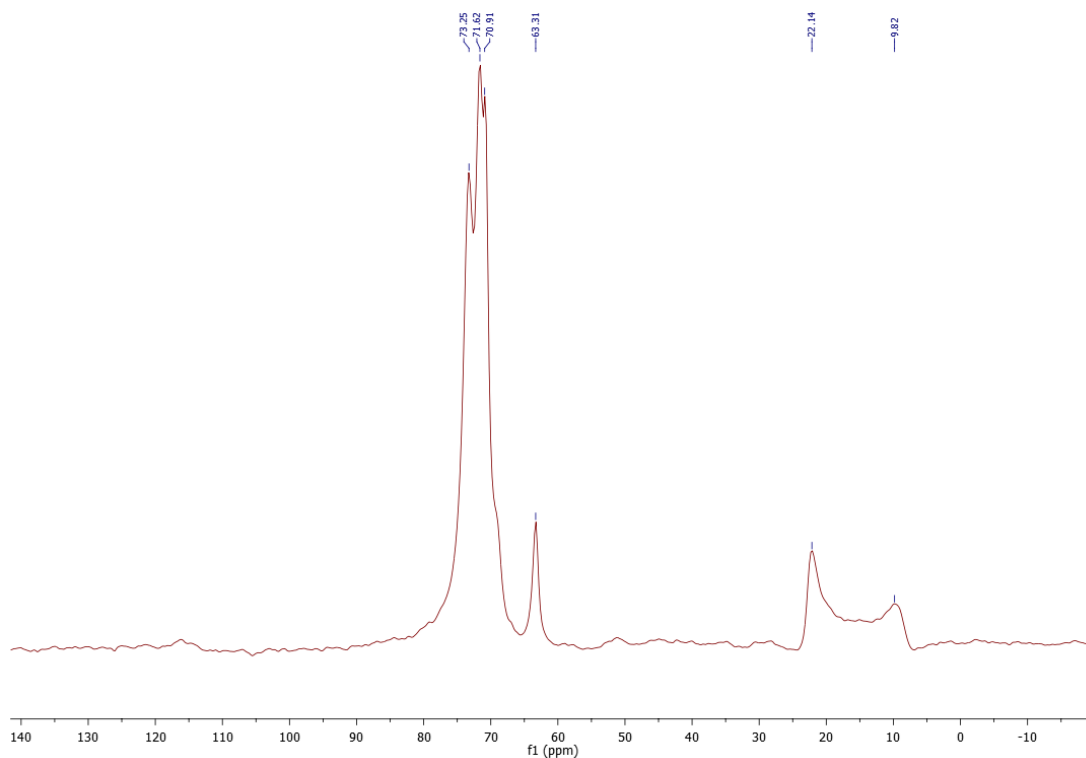


Figure 3.12. ^{13}C CP/MAS TOSS of microspheres 2S-REF.

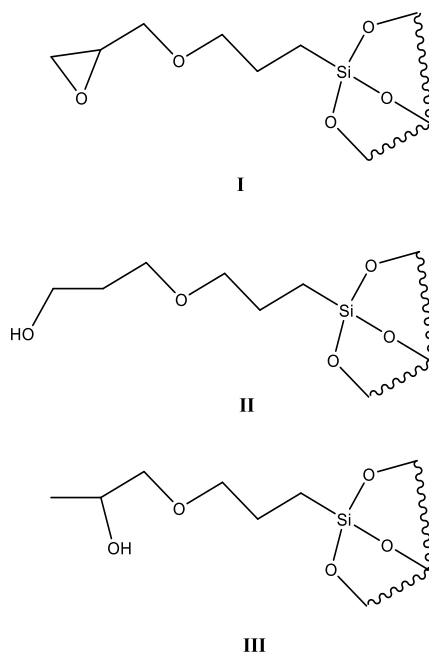


Figure 3.13. Possible structures of unreacted and reacted epoxy group in GPTMS.

The presence of structures I and II, although probable, is not significant in the spectrum. The structure I should present signals around 30-40 ppm for the epoxy

ring and the structure II a signal at ca. 30 ppm for the HOCH₂CH₂CH₂O-carbon. There are some low-intensity signals present between 25 and 55 ppm, which may account for the presence of small amounts of structures I and II. However the signals are too small for unequivocal identification. Therefore, it can be stated that a majority of the epoxy rings of GPTMS have opened during the microspheres synthesis, generating secondary alcohols that contributed to the polymerization induced phase separation.

Figure 3.14a shows the FTIR-ATR spectra of the obtained porous microspheres after being dried for 1 h at 150 °C. Comparing the spectra with those of Span[®] 80, decalin and also those of TEOS and GPTMS (Figure 3.15), one can note the absence of a band at ca. 1720 cm⁻¹, which reveals that there is no significant amount of surfactant Span[®] 80 left on the samples. On the other hand, the presence of decalin, the organic phase of the W/O emulsion, is still found in the spectra, in a minimal amount, which was expected, as 150 °C is lower than the boiling point of decalin (190 °C). Moreover, the bands associated with the presence of TEOS, at 1075, 1102, 1168, 1299, and 1400 cm⁻¹, are no longer detectable.

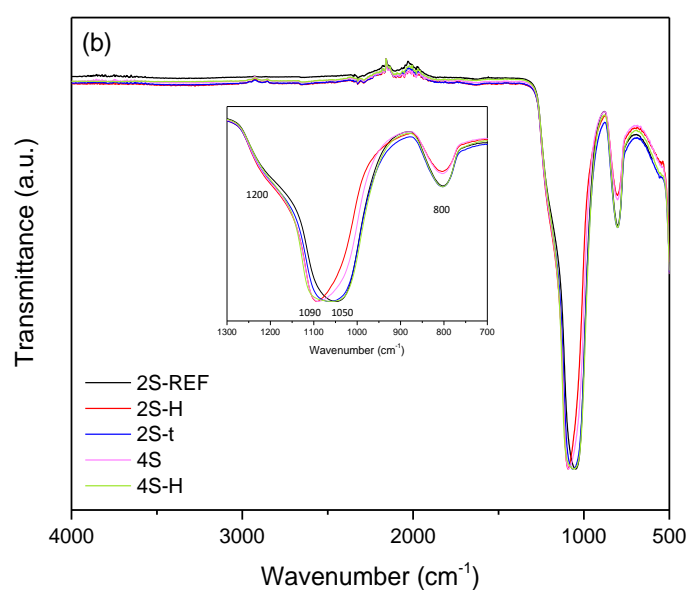
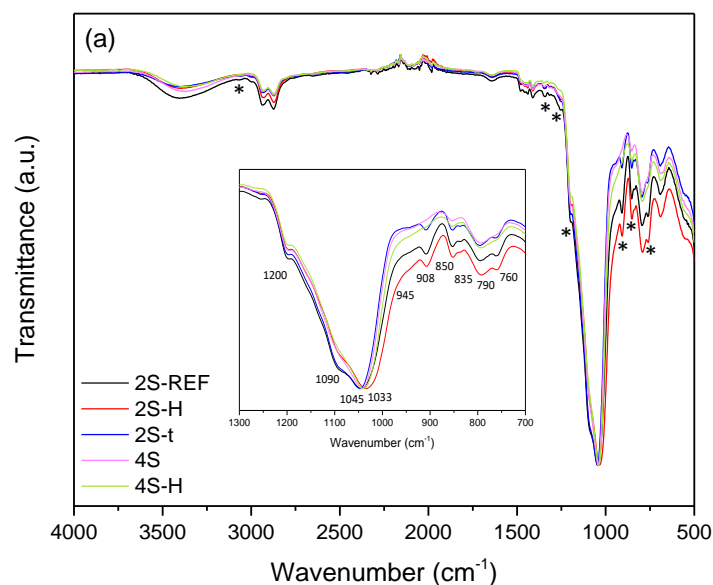


Figure 3.14. FTIR-ATR spectra of the porous microspheres, heat-treated for 1 h at 150 °C (a) and 700 °C (b). The inset shows the magnified region of the spectra, from 1300 to 700 cm^{-1} .

It should be noted that the band at 1075 cm^{-1} , present in the spectrum of the silane precursors, is ascribed to the asymmetric stretching of Si-O-alkyl groups, which after the hydrolysis and polycondensation reactions, with the formation of Si-OH and Si-O-Si groups, tends to disappear. Instead, a broad band at ca. 1040 cm^{-1} with a shoulder at ca. 1090 cm^{-1} is present in the spectra of Figure 3.14a. As the siloxane

chains become longer or branched, the Si-O-Si absorption is also known to become broader and more complex, showing several overlapping bands. Polysiloxanes made up of T units $[\text{RSiO}_{1.5}]_x$ typically shows a broad, structureless absorption band covering the entire region between 1160-1000 cm^{-1} . This observation is corroborated by the NMR spectra shown above, which revealed the presence of Q units, but mainly T units in the microspheres structure. The presence of these broader bands associated with Si-O-Si absorption has also been described in the literature for hybrid silica materials heat-treated at temperatures below 600 $^{\circ}\text{C}$ [173].

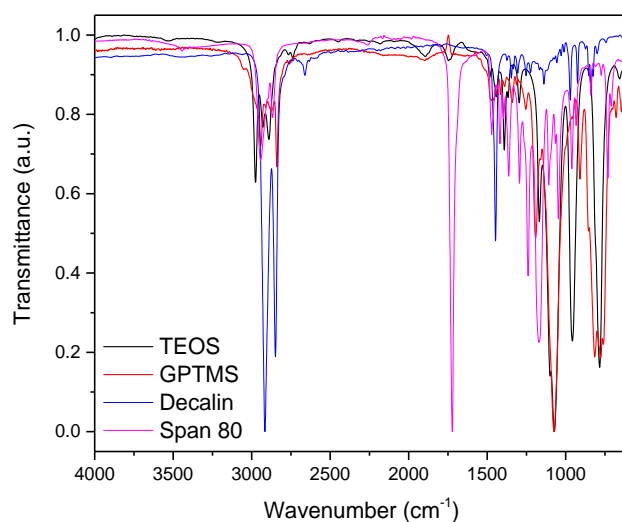


Figure 3.15. FTIR-ATR spectra of the pure compounds.

Also, the relatively sharp band at $\sim 960 \text{ cm}^{-1}$, related to the CH_3 rocking in TEOS, is replaced by a somewhat broader band near the same position, characteristic of a wet gel, which indicates the presence of Si-OH or Si-O $^-$ species [174]. The broad band around 3400 cm^{-1} is representative of the stretching vibration of OH groups, namely from Si-OH species or adsorbed moisture, while the band at ca. 1640 cm^{-1} is ascribed to the bending mode of OH in H_2O molecules.

On the other hand, it is possible to identify the influence of GPTMS in all the spectra of the samples dried at $150 \text{ }^{\circ}\text{C}$, mainly on samples 2S (denoted by *, in Figure 3.14a). In particular, the bands at 906 cm^{-1} and 850 cm^{-1} , ascribed to C-O and C-O-C stretching of the GPTMS' epoxy groups confirm its presence in the obtained

microspheres. The characteristic bands of the glycidyloxy group can be detected at 1250 cm^{-1} and 3045 cm^{-1} (weak bands) [157,158], which confirms the hybrid character of the microspheres dried for 1h at $150\text{ }^{\circ}\text{C}$, derived from the organically modified Si precursor, GPTMS.

It should be pointed that although the NMR analyses revealed that the majority of the epoxy groups had reacted, by ring-opening polymerization, the FTIR is herein showed to be sensitive to the presence of the remaining epoxy groups that did not have reacted during the synthesis. The epoxy organic functionality still present on the dried microspheres, despite being in a minor fraction, could enable the grafting (covalent chemical bonding) of selected chemical species, such as amine-based species, onto the microspheres in specific future applications.

After the heat treatment at $700\text{ }^{\circ}\text{C}$, broad and strong absorption bands are observed between $900\text{-}1300\text{ cm}^{-1}$ and near 800 cm^{-1} , revealing the presence of an inorganic material (Figure 3.14b). In particular, there is the appearance of an intense and broad band at $\sim 1090\text{-}1050\text{ cm}^{-1}$, typically assigned to asymmetric stretching of Si–O–Si bonding sequences (transverse optical, or TO component), which presents a clearly visible high-frequency shoulder at $\sim 1200\text{ cm}^{-1}$ (longitudinal optical (LO) component of the same vibration) [175]. Regarding the band at $\sim 800\text{ cm}^{-1}$, it may be assigned to symmetric stretching of the oxygen atoms along the bisector of the Si–O–Si bridging angle, again with some simultaneous Si cation motion [176,177].

In fact, for silicates, two of the main features associated with higher densification levels, obtained by heat treatment of the samples, are the increase in frequency and intensity of the Si–O–Si stretching band at $\sim 1070\text{ cm}^{-1}$ and the simultaneous reduction in the intensity of the OH-related bands, such as that at 950 cm^{-1} [174].

A broad band at $\sim 1090\text{-}1050\text{ cm}^{-1}$ is found in Figure 3.14b, for the microspheres heat-treated at $700\text{ }^{\circ}\text{C}$, possibly due to an overlapping of bands ascribed to a variety of Si species, such as T units and Q units, detected by NMR in this work. The large FWHM of this band (at ca. 1070 cm^{-1}) was also reported to correspond to a broadening of the bond angle distribution [174]. The large porosity observed in these microspheres might have induced a strain in the Si–O–Si bonds at the surface of the pores, which leads to larger bridging angles and longer Si–O bonds, compared

to bulk silica glass, causing the broadening and shift of the Si-O-Si band to lower frequencies. Finally, the significant intensity found for the band (shoulder) at ca. 1200 cm⁻¹ (LO mode) in Figure 3.14b, might be associated with the presence of residual material porosity, which scatters a normal incidence IR beam in all directions [177] leading to the activation of the LO mode, which makes sense in this work due to the broad distribution of macroporosity exhibited by the porous microspheres.

3.3. Conclusion

The present chapter reports on the effect of the synthesis parameters linked to the degree of polymerization (hydrolysate viscosity) and to the microemulsion, on the development of the porosity characteristic of the S MICROSCAFS®. Microspheres with diameter and characteristic sizes ranging from 26 to 130 μm and 149 ± 11 to 485 ± 38 nm, respectively, were prepared by an adapted sol-gel process, involving a successful combination of induced phase separation and a W/O emulsion templating. The porous spheres are generated inside the water droplets of the emulsion. This phase separation, proposed to be mostly enthalpy driven, due to the change in polarity of the formed siloxane oligomers, but also entropy driven due to polymerization reactions, is a dynamic phenomenon which needs to be controlled to occur simultaneously to the chemical quenching, i.e. gelation. Synthesis procedure and parameters were tuned to assure that the *freezing* of the structure occurs coincidentally with the critical point for phase separation by spinodal decomposition. By increasing the HCl concentration or the hydrolysis time, a general increase of the characteristic size was observed due to the higher viscosity of the Si precursor solution, i.e. higher chain-length oligomers. This work represents a step forward in the current state of the art because it allows the customization of MICROSCAFS®' size and porosity. MIP and N₂ adsorption/desorption analysis demonstrated that all the obtained microspheres were mainly macroporous with low specific surface areas ranging from 2.46 to 14.51 m²/g. Through NMR data, it was proven that most of the epoxy rings of GPTMS have opened during the microsphere's synthesis, acting as an inherent gelation and phase separation promoting agents, therefore dispensing the use of additional chemicals as gelation promoters. FTIR-ATR spectra

analysis of the microspheres dried at 150 °C revealed their hybrid character and that not all the epoxy rings were opened during the synthesis, enabling the possibility of grafting selected chemical species for any desired application. On the other hand, the heat-treated microspheres at 700 °C were found to be made of a fully inorganic material and the presence of macropores and the mixed Q and T Si units seemed to have an effect on the Si-O-Si FTIR bands.

This work opened the possibility to prepare, without pore forming agents, hybrid S MICROSCAFS® displaying some content of epoxy organic functionality and inorganic S MICROSCAFS®, which exhibit a large amount of interconnected macropores, peaked from 164 to 405 nm, and a small amount of mesopores. They were subsequently used as catalytic supports for water purification. This acquired knowledge formed the base for the production of multicomponent ST and STH MICROSCAFS® explained in the next chapter.

Chapter

Multicomponent Oxide MICROSCAFS®

4

The following chapter is based on the two peer-reviewed articles:

M. Vale, A.C. Marques, Mechanistic Study of the Formation of Multicomponent Oxide Porous Microspheres (MICROSCAFS®) by Cryo-Scanning Electron Microscopy, Gels 9 (2023) 704. <https://doi.org/10.3390/gels9090704>

M. Vale, S. Orišková, A. Mariquito, L. Reis, M. Pinto, A.C. Marques, Multicomponent oxide microspheres with designed macroporosity (MICROSCAFS®): a customized platform for chemicals immobilization, RSC Adv 13 (2023) 12951–12965. <https://doi.org/10.1039/D3RA00895A>

Chapter 4 describes the development of multicomponent oxide MICROSCAFS[®], their comprehensive characterization, a systematic study involving variation of the synthesis parameters and their effect on porosity, as well as an insight into the MICROSCAFS[®] generation mechanism.

4.1. Study on the effect of the ST and STH MICROSCAFS[®] synthesis' parameters

4.1.1. Introduction

Inspired by the work presented in chapter 3, the sol-gel based process, developed for S MICROSCAFS[®] synthesis, was modified to yield multicomponent ST and STH MICROSCAFS[®]. This subchapter reports on the role played by varied synthesis parameters in the ST and STH MICROSCAFS[®] morphology, in particular, their size and pore size distribution. Besides using most of the characterization techniques previously presented in this thesis, it includes, for the first time, a rheological study, x-ray computed tomography analysis, and a mechanical characterization of the particles, providing new insights on the synthesis/chemical structure and morphology/properties relationship of the ST and STH MICROSCAFS[®].

4.1.2. Experimental

4.1.2.1. Synthesis of the ST and STH MICROSCAFS[®]

The samples reported in this chapter were named using the following acronyms: composition of the MICROSCAFS[®] (ST or STH) / synthesis temperature / parameter change (AA+ = greater quantity of acetic acid, W+ = greater quantity of water in the W/O emulsion, GPTMS+ or - = higher or lower GPTMS/TEOS ratio).

Table 4.1 lists the main samples prepared for this study, and corresponding synthesis parameters.

A typical ST and STH MICROSCAFS[®] synthesis involved the preparation of three solutions: 1- hydrolysate solution: silane or silane/hafnium precursor aqueous solution (sol); 2 – chelated solution: titanium(IV) isopropoxide (TiPOT) and acetic acid solution, and 3 - W/O emulsion.

Table 4.1. ST and STH MICROSCAFS®' synthesis parameters.

Sample acronym	Reaction Temperature (°C)	GPTMS/TEOS molar ratio	TiPOT/CH ₃ COOH molar ratio	W/O mass ratio	Volume of NH ₄ OH 25% solution (ml)	Mass of HfOCl ₂ .8H ₂ O (g)
ST/85C	85	0.87:1	1:4	0.45:1	16.5	0
ST/50C	50	0.87:1	1:4	0.45:1	16.5	0
ST/RT	RT (25)	0.87:1	1:4	0.45:1	22.0	0
ST/50C/AA+	50	0.87:1	1:6	0.45:1	16.5	0
ST/50C/W+	50	0.87:1	1:4	0.68:1	16.5	0
ST/50C/GPTMS+	50	1.09:1	1:4	0.45:1	16.5	0
ST/50C/GPTMS-	50	0.65:1	1:4	0.45:1	16.5	0
STH/50C/GPTMS+	50	1.09:1	1:4	0.45:1	16.5	7.5

For the reference synthesis ST/50C, the hydrolysate solution (solution 1) was prepared as follows: 16.3 ml of TEOS (98%, Sigma-Aldrich), 13.8 ml of GPTMS, (Xiameter OFS-6040), >98.5%, kindly supplied by Dow), and 11.6 ml of 0.28 M HCl solution were mixed at RT in a closed container, under magnetic stirring for 65 minutes. In the case of the STH/50C/GPTMS+ synthesis, an additional 7.49 g of hafnium dichloride oxide octahydrate (HfOCl₂.8H₂O, >98%, Alfa Aesar) and a total of 17.3 ml of GPTMS was added in this step. At the end of the hydrolysis, the pH of the hydrolysate was measured using a Metria bench top meter model M21 with a Metria glass body dual pH electrode with an ATC probe.

In parallel, a complexation reaction of the TiPOT (solution 2) was carried out to decrease its reactivity and avoid the formation of titanium dioxide precipitates when in contact with water. 10 ml of TiPOT (98%, Acros Organics) and 8 ml of glacial acetic acid (>= 99%, Fisher Chemical) were mixed separately and left under stirring at RT for 45 minutes.

Finally, for the W/O emulsion (solution 3), 100 g of decahydronaphthalene (decalin, mixture of cis and trans isomers, 98%, Merck), 45 g of distilled water, and 6 g of sorbitan monooleate surfactant (Span® 80, HLB: 4.3, Merck) were mixed at 13 000 rpm for 10 minutes using a dispersing instrument (IKA T18 digital ULTRA-TURRAX®). Different concentrations of Span® 80, as well as a combination of Span® 80 with other surfactants, namely Tween® 80 and Pluronic® P-123, were also tested. Then the emulsion was transferred into the reactor and set the mechanical stirring speed to 600 rpm and the temperature to 50 °C. The reactor setup consisted of a

three-neck round bottom flask reactor, a heating mantle with a thermocouple, and a mechanical stirrer.

Subsequently, the chelated TiPOT solution (solution 2) was added to the hydrolysate solution (solution 1) drop-by-drop and stirred for 5 minutes. Then it was immediately transferred into the reactor, followed by the addition of 16.5 ml of aqueous ammonia solution (25%, Chem-Lab).

After 1 h and 30 min., the MICROSCAFS[®] were collected by vacuum-assisted filtration, washed with acetone, and dried overnight at 45 °C.

4.1.2.2. Characterization

Optical microscopy photos of the MICROSCAFS[®] were obtained using a digital video-eyepiece DE 3M accessory (A. Krüss Optronic GmbH, Hamburg, Germany) mounted on an MSZ 5600 optical microscope (A. Krüss Optronic GmbH, Hamburg, Germany).

The particle size volume-weighted distribution data were obtained using a Mastersizer Hydro 2000S (Malvern Panalytical, Malvern, UK) particle size analyzer from the average of three measurements. Three different percentiles at 10%, 50%, and 90%, named D (0.1), D (0.5), and D (0.9), respectively, were analyzed to study the MICROSCAFS[®]' size distribution. Also, the relative span of the distribution was used to express the size dispersion, and it represents the curve's full width at FWHM calculated using Equation 4.1:

$$\text{span} = \frac{[D (0.9) - D (0.1)]}{D (0.5)} \quad (4.1)$$

SEM images and EDS data were obtained using a Phenom ProX G6 benchtop SEM (ThermoScientific, Waltham, MA, USA) to assess the dried MICROSCAFS[®] morphology and porosity. Internal porosity was observed on purposely broken particles. Before observation, a 15 nm layer of gold-palladium was sputtered on the samples using a turbomolecular pumped coater Q150T ES (Quorum Technologies, Lewes, UK).

MIP was performed to quantify the pore size distribution, and cumulative pore volume, for a pore diameter interval from 0.01 to 10 μm using an Autopore IV 9500

(Micromeritics, Norcross, GA, USA). This procedure was employed to account for the interparticle spaces. Indeed, the porosity data achieved above 10 μm was not considered in this analysis, which does not mean that there are no interconnected macropores with a width or length above 10 μm . It should be noted that these larger pores might not be considered in this work, leading to an underestimation of the macroporosity value. A constant contact angle of 140° was selected in the analysis. The samples were subjected to 120°C for 2 h before measurements.

The specific surface areas and pore volumes of the microspheres were obtained by nitrogen (N_2) adsorption/desorption BET method at -196°C using an ASAP 2010 adsorption analyzer (Micromeritics, Norcross, GA, USA). The pore size distributions were obtained through density functional theory (DFT), assuming slit-shaped pores. For these experiments, ~ 300 mg of sample was sequentially outgassed at 200°C for at least 4 h, with a high vacuum pump, to remove moisture and other surface contaminants before the analyses.

FTIR spectroscopy was used to assess the chemical structure of the MICROSCAFS[®] dried at 45°C and heat treated for 1 h at 150 and 700°C . The used FTIR equipment was a Spectrum Two from (PerkinElmer, USA) equipped with a UATR Two accessory. The spectra were obtained at 4 cm^{-1} resolution, and eight scans of data accumulation.

Thermograms from the reference sample ST/50C dried at 45°C and heat-treated for 1 h at 700°C were obtained to assess the water and organic content of the MICROSCAFS[®]. The equipment used was a HITACHI STA (Simultaneous Thermal Analyzer) 7200 Thermal Analysis System (Ibaraki, Japan) under a controlled nitrogen atmosphere with a flow of 200 mL/min , at a temperature increase rate of 10°C/min , in the range of 45 - 900°C .

4.1.2.3. Rheological characterization

The hydrolysate apparent viscosity was determined using a rotary viscometer LV DV-II+Pro (Brookfield Engineering, Middleboro, MA, USA) using a CPE-52 spindle at 60 rpm and RT . The oscillatory time sweeps of the complex viscosity were measured using an MCR 92 modular compact rheometer (Anton Paar GmbH, Graz, Austria) with a CP50-1 cone-and-plate spindle with 50 mm diameter and 1° cone angle at a constant 0.101 mm gap. Approximately 1 ml of ST precursor sol was collected 5 min

after the addition of chelated TiPOT solution (solution 2) to the hydrolysate solution (Si precursors, solution 1). The setup was previously heated to the desired temperature (50 or 85 °C) before the start of the test. The complex viscosity was monitored under constant 1% shear strain and 2 Hz frequency over 30 minutes. These parameters were chosen to maintain the sol-gel samples in the viscoelastic regime [178]. Rotational tests were also performed to obtain the viscosity curves and compare different emulsions in terms of viscosity evolution along a shear rate ranging from 1 to 100 s⁻¹. Flow tests were also performed using the same system along a shear rate ranging from 1 to 100 s⁻¹. The flow curves analysis allowed a better understanding of different emulsions used as templates for the spherical particles.

4.1.2.4. X-ray computed tomography

X-ray computed tomography (CT) on the MICROSCAFS® ST/50C/GPTMS+ and ST/50C/GPTMS- was performed using a Skyscan 2214 (Bruker Corporation, USA) equipped with a flat panel and a CCD detector. Samples were placed inside a cylindrical plastic container without pressing, for analysis. For the acquisition of transmission images with the flat panel, the X-ray source was operated with a medium spot size at 50 kV and 120 µA of voltage and current, respectively, and the detector resolution was 1536 by 972 (2x2 pixel binning) at 7.15 µm pixel size, and a 180° sample rotation with a step of 0.2°. For the acquisition of transmission images with the CCD, the X-ray source was operated with a medium spot size at 90 kV and 89 µA of voltage and current, respectively. The detector resolution was 4032 by 2688 at 0.7 µm pixel size and a 360° sample rotation with a step of 0.15°. Reconstruction of the tomography images was carried out with the NRecon software (Bruker Corporation, USA), and the morphological analysis of the reconstructed images was done with the CTAn software (Bruker Corporation, USA).

4.1.2.5. MICROSCAFS® mechanical properties analysis

MICROSCAFS®' powder compressibility, relaxation, stiffness, and elastic recovery were calculated using an Instron 5566 universal testing machine with a 500 N load cell (Instron, Norwood, MA, USA) and a designed compaction probe accessory, following a test method developed by Stable Micro Systems (application study ref. POW4/IPC0.5), in a compression force measurement mode, and powder relaxation sequence, originally developed to compare the compaction and stress relaxation

properties of different powders. The test method consists of three phases: 1- loading phase (compression), 2- hold period (the stress relaxation phase), and 3- unloading phase (decompression). 1 mL of powder was placed inside a cylindrical aluminum sample holder of 15.7 mm in height and 15.0 mm in diameter. In the loading phase, a crosshead was displaced at a constant rate of 0.5 mm/s and compressed the sample until it reached 50 N. Then, the crosshead stopped, and the strain (or probe displacement) was kept constant for over 120 seconds. Finally, the crosshead was unloaded at a constant rate of 0.25 mm/s until it reached the point where the displacement was zero. Every compression test was made in triplicate, and the parameters were calculated by computing graphical data using Equations 4.2, 4.3, 4.4, and 4.5:

$$\text{Compressibility (\%)} = \frac{\text{initial column height} - \text{final column height}}{\text{initial column height}} \times 100 \quad (4.2)$$

$$\text{Relaxation (\%)} = \frac{\text{initial force of the relaxation phase} - \text{final force of the relaxation phase}}{\text{initial force of the relaxation phase}} \times 100 \quad (4.3)$$

$$\text{Stiffness (MPa)} = \frac{\text{initial unload linear slope of the unloading phase} \times \text{compressed column height}}{\text{probe area (176.72 mm}^2\text{)}} \quad (4.4)$$

$$\text{Elastic recovery (\%)} = \frac{\text{relaxed column height} - \text{compressed column height}}{\text{compressed column height}} \times 100 \quad (4.5)$$

4.1.3. Results and discussion

4.1.3.1. MICROSCAFS[®] formation mechanism and other features

The scheme below (Figure 4.1) shows the different main stages of the MICROSCAFS[®] formation process, with respective optical microscopy images of the reaction medium. In this methodology, a chelating agent (CH₃COOH) was used to control the reactivity of TiPOT, while Si alkoxides, TEOS and GPTMS, are hydrolyzed before being mixed with chelated TiPOT (for ST MICROSCAFS[®]). Hf precursor in the form of salt may be added to the Si alkoxides solution at the beginning of the hydrolysis step (for STH MICROSCAFS[®]). Such mixture is added to a W/O emulsion, a soft template for the characteristic spherical shape of the MICROSCAFS[®]. The presence of Ti and Hf

precursors increases the sol viscosity compared to 100% Si alkoxides. A proper combination of TEOS and GPTMS was selected to allow phase separation to occur via siloxane and Si-O-Ti formation by polycondensation of the silanol groups, and Ti-OH groups, but also from the epoxy ring opening reaction, being both an entropy and enthalpy-driven process. This phenomenon occurred inside the water droplets of the emulsion, resulting in droplets, containing an aqueous dispersion of polymerized species, dispersed in the oil phase. The relatively long alkyl chain and the epoxy group of GPTMS play an important role in the control of gelation and, consequently, the size and macroporosity of the MICROSCAFS[®]. However, ammonia can be added at this stage to increase the pH of the reaction medium and further catalyze the condensation reactions, favoring the chemical quenching, i.e. the freezing of the structure, at the moment spinodal decomposition occurs. This approach eliminates the need for calcination to get rid of the polymeric additives typically employed to achieve macroporous materials. A simple drying of the spheres was enough to eliminate the solvent remaining within the wet gel MICROSCAFS[®], resulting in a 3D interconnected co-continuous porous structure. In case purely inorganic MICROSCAFS[®] are desired, a heat treatment at temperatures above 500 °C shall be done.

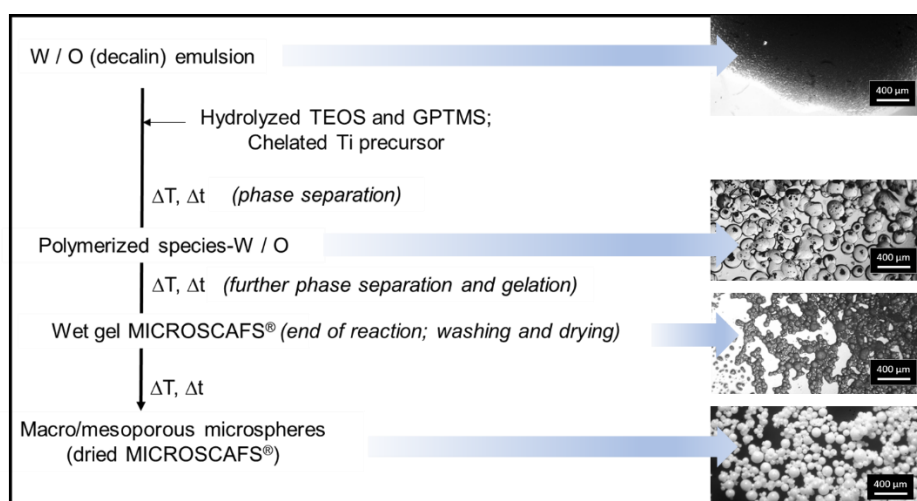


Figure 4.1. General scheme of ST MICROSCAFS[®] preparation, exhibiting the different main stages and associated optical microscopy images (scale bar = 400 μm).

Synthesis temperatures as low as RT (25 °C), 50°C, or 85 °C were used with success to obtain the wet gel MICROSCAFS[®], followed by drying at 45 °C to get hybrid epoxy-ST MICROSCAFS[®], and by further heat treatment at ca. 700 °C to achieve inorganic ST MICROSCAFS[®]. The chemical differences between these samples can be observed using the ATR-FTIR spectra exhibited in Figure 4.2.

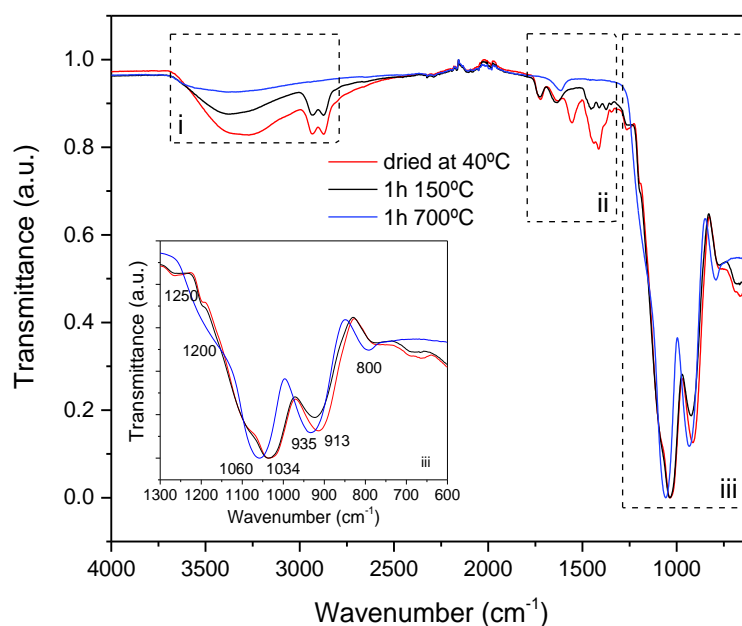


Figure 4.2. ATR-FTIR spectra of MICROSCAFS[®] ST/50C, dried at 40 °C, and heat treated for 1h at 150 °C and 700 °C.

The ATR-FTIR spectra of the sample heat treated for 1 h at 700 °C was typical of inorganic SiO₂-TiO₂ material, which revealed significant changes when compared to those from samples only dried or heat treated at 150 °C, namely: the OH stretching band (ca. 3400 cm⁻¹, zone i) is drastically reduced, almost eliminated, as well those typical of phenol, from Span[®] 80, namely OH bending, 1410 cm⁻¹, and C-O stretching at 1200 cm⁻¹ [179]; the bands at 2932 and 2872 cm⁻¹ (zone i) due to C-H stretching (in CH₂ units) and at 1440 cm⁻¹ (zone ii) due to C-H bending disappear, suggesting the complete elimination of decalin and Span[®] 80 residues from the MICROSCAFS[®], as well as of other organic residues, eventually from non-reacted alkoxides; also, the band at 1735 cm⁻¹, due to C=O stretching from Span[®] 80, disappears; and, finally,

contributions from the GPTMS epoxy ring, i.e. bands assigned to C-O- stretching at ca. 1250, 915 and 890-800 cm^{-1} are not evident anymore (zone iii).

The IR spectra of the MICROSCAFS[®] present a dominant band at about 1060 cm^{-1} (zone iii) due to the asymmetric stretching of the Si-O-Si bonding sequences (transverse optical, TO, component) and a weaker band on its low-frequency side, at $\sim 940 \text{ cm}^{-1}$, due to the overlap of Si-O- stretching vibrations in Si-O-Ti and a few Si-OH bonding environments [180]. The Si-O-Ti stretching band is characteristic of homogeneous gel/glassy network regions (achieved through heterocondensation), whereas the 1060 cm^{-1} band is indicative of silica-rich regions in the network [181], achieved due to homocondensation. The inorganic MICROSCAFS[®] (heat-treated at 700°C) exhibit robust scaffolding properties, including thermal and chemical stability. No significant weight loss is observed by TGA up to 900°C, while the same MICROSCAFS[®] only dried at 45°C displayed some weight loss at ca. 100°C and 400°C, due to water evaporation and organics elimination, respectively (Figure 4.3).

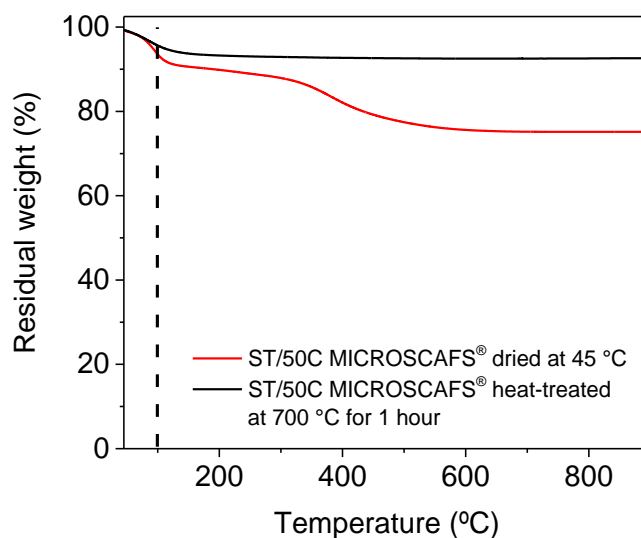


Figure 4.3. Thermogram of ST/50C MICROSCAFS[®] dried at 45 °C (red) and heat treated for 1 h at 700 °C (black).

Mesoporosity arises mainly from the oligomeric clusters that are bound together, forming the skeleton domains, while macroporosity is due to the phase separation process by spinodal decomposition. The thin layer that typically wraps the

MICROSCAFS® is so thin (just some nanometers thickness) and porous that it will not prevent the liquid flow inwards the MICROSCAFS® or species immobilization or grafting onto the inner pore surface of the MICROSCAFS®, according to previous experiments [38]. However, by treating the wet particles right after the synthesis with a 0.06 M LiOH (0.01 g MICROSCAFS®/ml) at 50 °C, such thin outer layer dissolves, exposing the skeleton domains, wormlike structure typical of the MICROSCAFS®, as shown in Figure 4.4.

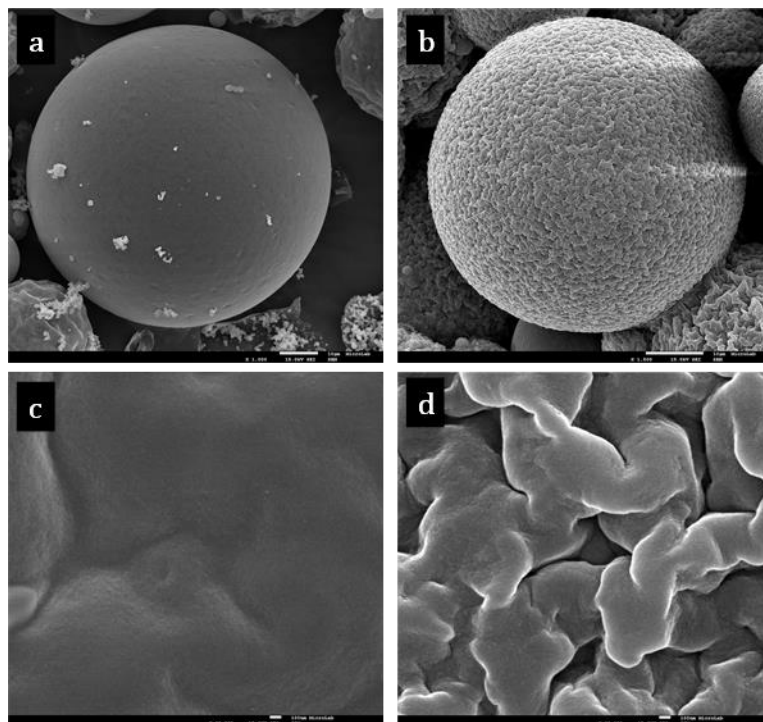


Figure 4.4. SEM images of MICROSCAFS® ST/85C: without LiOH treatment (a) scale bar: 10 μm , (c) scale bar: 100 nm; with LiOH treatment (b) scale bar: 10 μm , (d) scale bar: 100 nm.

ST MICROSCAFS® synthesis was revealed to be highly reproducible, despite the required control of the synthesis parameters to induce a simultaneous phase separation and gelation of the structure. Evidence for such reproducibility is shown in Figure 4.5 for the case of samples ST/85C and ST/50C/GPTMS+.

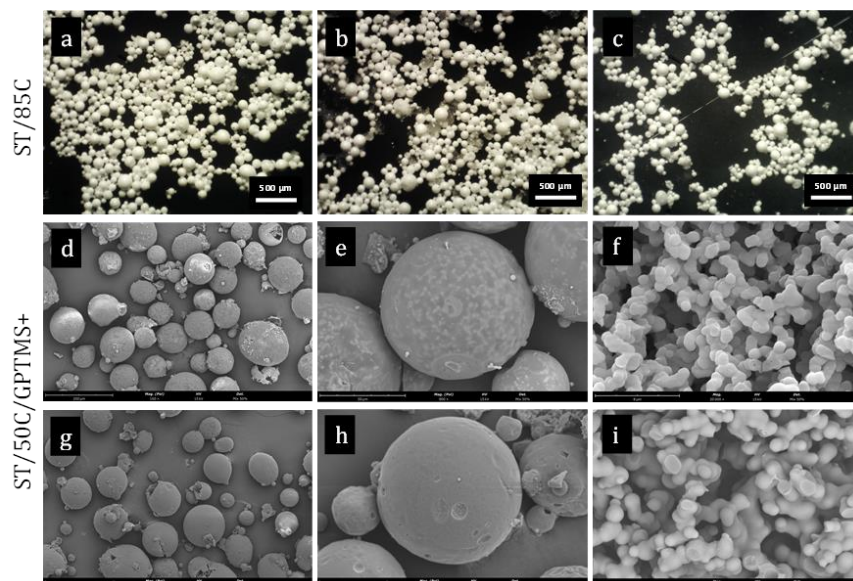


Figure 4.5. Evidence for synthesis reproducibility: (a, b, c) Optical microscopy images of three different batches of the same synthesis of MICROSCAFS® ST/85C; (d, g) SEM images (scale bar: 200 μm) of two different batches of the synthesis of MICROSCAFS® ST/50C/GPTMS+; (e,h) same as (d, g) with scale bar = 50 μm ; (f, i) same as (d, g) with scale bar = 5 μm . Note: d, e and f were acquired with a higher voltage (15 kV) than g, h and i (10 kV).

In general, greater quantities of surfactant Span® 80, in a range from 2 to 10 g, led to smaller particle diameters, narrower size distribution, and slightly smaller characteristic size (Figure 4.6). In general, the same type of wormlike macropore structure is present in all samples, suggesting that the temporal space between the "freezing" of the structure (gel time, t_g) and the onset of phase separation (t_{ps}) is very similar and, therefore, independent of the quantity of surfactant.

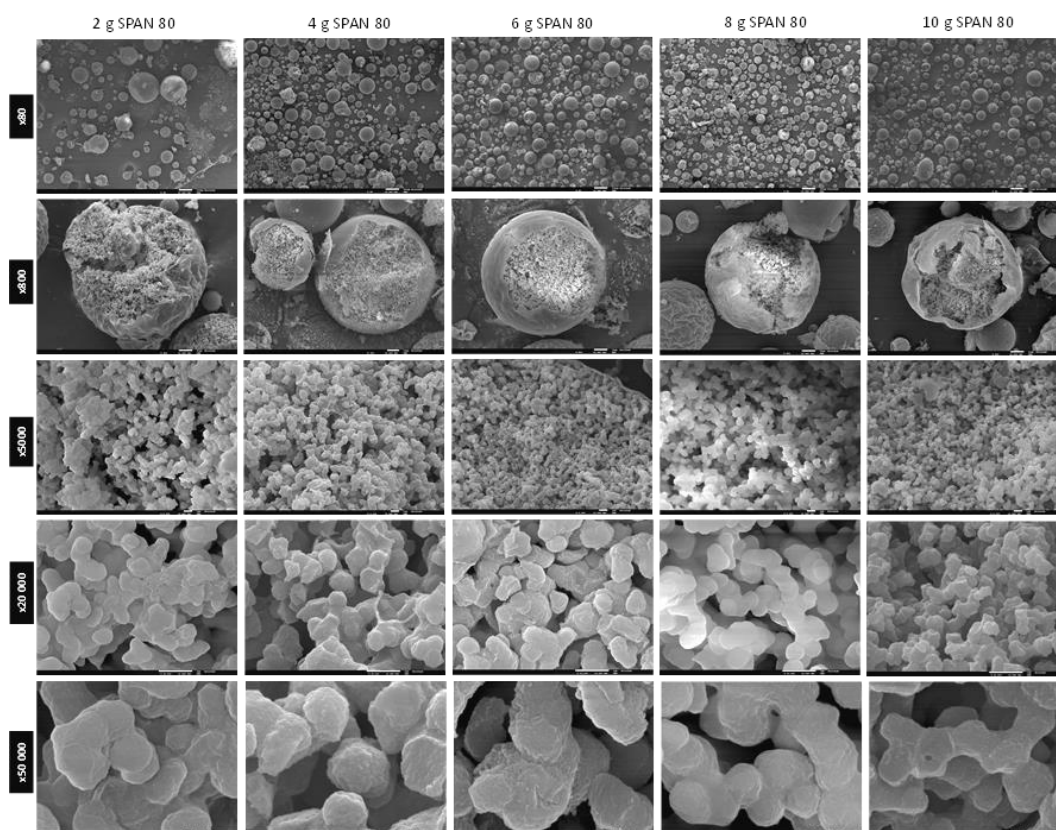


Figure 4.6. SEM images of the MICROSCAFS® ST/85C, at different magnifications, obtained using different quantities of surfactant SPAN®80: 2, 4, 6, 8 and 10 g. Scale bar (from top to bottom): 100 μ m, 10 μ m, 1 μ m, 1 μ m, 100 nm.

Different combinations of surfactants, Span® 80, Tween® 80, and Pluronic® P123, were also tested, keeping the mass of total surfactants fixed at 10 g, resulting in a drastic decrease of the MICROSCAFS® size, as shown in Figure 4.7, revealing the impact that different surfactants and different values of HLB (4.3 *versus* 5.2) have on the W/O emulsion droplets' size. An $HLB \leq 6$ is preferred for W/O emulsions. When testing a further increase of the Tween® 80 amount to attain an HLB of 12, the obtained particles were not regular spheres anymore but an agglomerated thin powder, lacking the special features typical of the MICROSCAFS®.

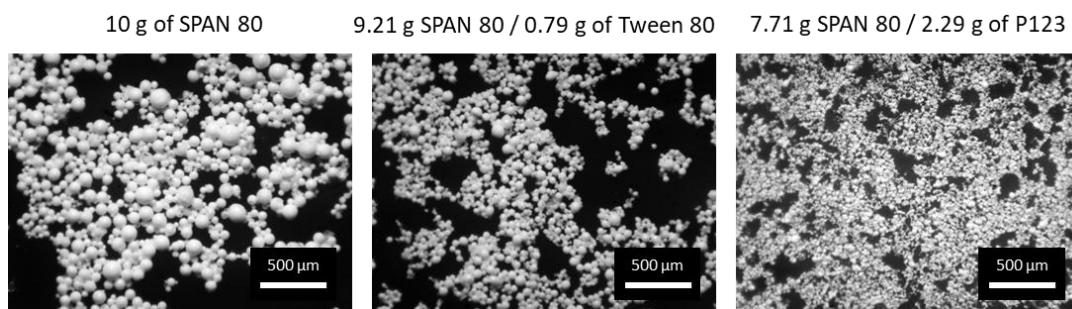


Figure 4.7. Optical microscopy images of the MICROSCAFS® ST/85C synthesized using different combinations of surfactants (from left to right): Span® 80 (HLB=4.3), Span® 80+Tween® 80 (HLB=5.2) and Span® 80 + Pluronic® P123 (HLB=5.2). Scale bar: 500 µm.

It should be noted that the quantity of surfactant Span® 80 was fixed at 6 g, and no combinations with other surfactants were carried out for the remaining studies in this work. This condition was chosen because preliminary tests with syntheses made at RT and 50°C revealed that 2 g Span® 80 were not enough to attain a stable emulsion and regular size MICROSCAFS®, while those obtained with 6 and 10 g Span® 80 displayed already very similar features, such as homogeneous, regular spherical shape and size (Figure 4.8).

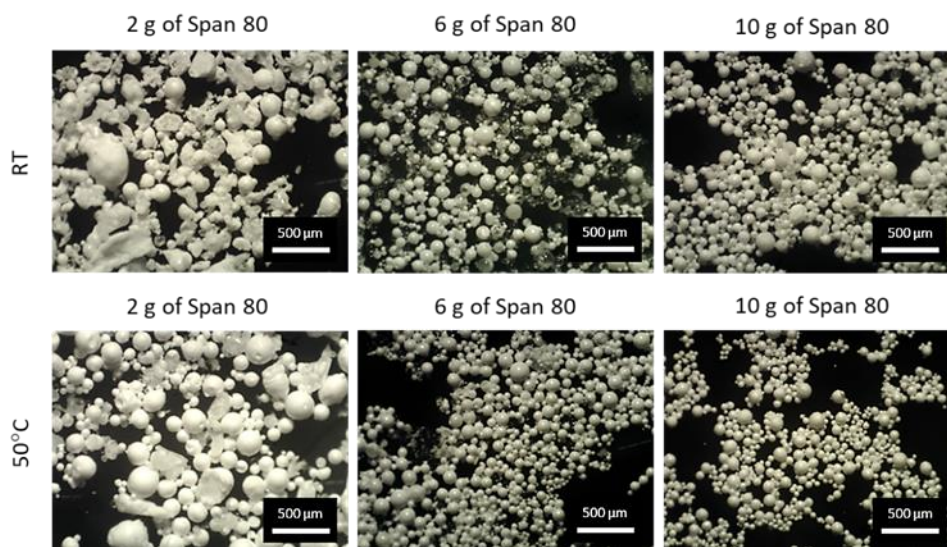


Figure 4.8. Optical microscopy images of the MICROSCAFS® ST/RT and ST/50C obtained using different quantities of surfactant Span® 80: 2, 6 and 10 g.

4.1.3.2. Effect of synthesis temperature on the ST MICROSCAFS® morphology

Temperature plays a crucial role in phase separation thermodynamics and sol-gel condensation kinetics. On the one hand, it favors the solubility of the different phases and promotes homogenization in an UCST type of sol-gel system [60]. On the other hand, it accelerates gelation (silane condensation reactions) [44,182].

The MICROSCAFS® size (diameter) distribution graphs (Figure 4.9) show a quite similar value for the mode of the three ST MICROSCAFS® samples prepared at RT (25°C), 50°C, and 85°C, which reveals that temperatures within this range do not significantly affect the emulsion stability. However, sample ST/50C exhibits a few particles of larger size, shown by the increase in span and D (0.9) values (Table 4.2).

Table 4.2. Particle size distribution data.

Sample acronym	D (0.1), μm	D (0.5), μm	D (0.9), μm	Span
ST/RT	40	89	169	1.45
ST/50C	44	102	220	1.72
ST/85C	47	96	172	1.31
ST/50C/GPTMS-	32	75	178	1.94
ST/50C/GPTMS+	66	102	190	1.11
ST/50C/AA+	64	134	242	1.33
ST/50C/W+	48	112	277	2.04
STH/50C/GPTMS+	44	103	253	2.03

Despite the similarity in MICROSCAFS® size, there was a significant change in pore morphology for different synthesis temperatures, as revealed by the SEM images (Figure 4.9). MIP graphs show a strong increase in the pore size for higher reaction temperatures, as well as a larger cumulative intrusion pore volume (Figure 4.9). For instance, the sample synthesized at 85 °C exhibits a broad and bimodal pore size distribution, peaked at ca. 135 and 1104 μm , mostly in the macropore range (> 50 nm) and a cumulative pore volume of 1.54 mL/g, more than three times larger than that of ST/RT. The fact that a higher synthesis temperature favors gelation (sol-to-gel transition) but not phase separation might lead to a delay in the onset of phase separation, explaining the presence of broader skeleton domains and larger macropores in the ST/85C MICROSCAFS®. On the other hand, the average synthesis

pH was lower than ST/50C (Table 4.3), which is probably due to the evaporation of ammonia at higher synthesis temperatures.

Table 4.3. Average hydrolysate viscosity and MICROSCAFS®' synthesis pH.

Sample acronym	Average hydrolysate viscosity (cP)	Average synthesis pH
ST/RT	16.2 ± 0.8*	9.23 ± 0.02
ST/50C	16.2 ± 0.8	8.51 ± 0.04
ST/85C	16.2 ± 0.8*	6.67 ± 0.08
ST/50C/GPTMS-	25.0 ± 1.2	9.22 ± 0.01
ST/50C/GPTMS+	14.8 ± 0.4	8.97 ± 0.01
ST/50C/AA+	14.8 ± 0.6	7.61 ± 0.01
ST/50C/W+	16.2 ± 0.8*	8.62 ± 0.02
STH/50C/GPTMS+	45.3 ± 0.3	9.05 ± 0.01

*same hydrolysate as for ST/50C

Regarding mesoporosity (pores below 50 nm, in the MIP graphs, Figure 4.9), it decreases with higher reaction temperatures, and ST/RT is the one that exhibits higher mesopore content.

The best compromise in terms of larger macropore size and volume and higher amount of mesopores was achieved for ST/50C. Therefore, this sample served as a reference in subsequent studies.

It should be also noted that compared to S MICROSCAFS®, reported in the previous chapter, ST/50C exhibited a larger average hydrolysate viscosity (16.2 versus 8.7 cP), a monomodal size distribution peaked at 98 µm *versus* a bimodal distribution peaked at 70 and 130 µm, broader pore size distribution extended to the larger macropores side (pore size mode value at 184 nm *versus* 164 nm), larger cumulative pore volume (1.39 mL/g *versus* 0.55 mL/g), larger total porosity (38% *versus* 28%, by MIP accounted for pores only below 10 µm) and a larger specific surface area (27.93 *versus* 14.50 m²/g).

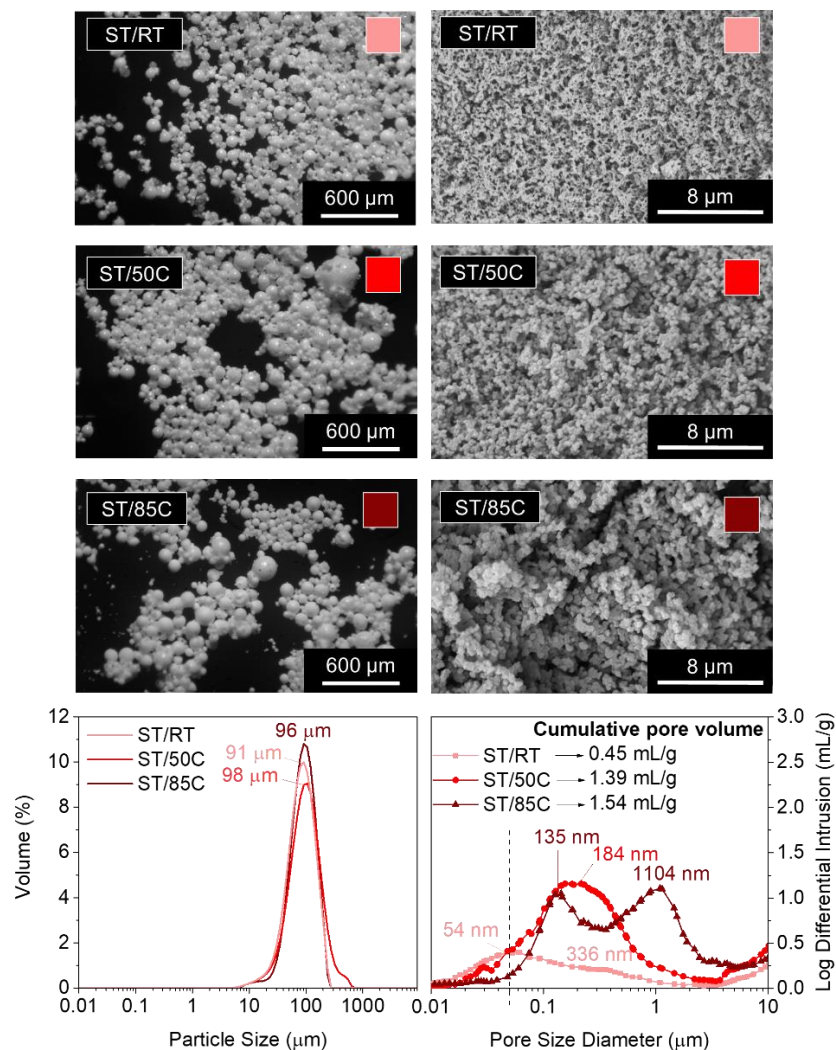


Figure 4.9. Morphology of ST MICROSCAFS[®] synthesized at room temperature (ST/RT), 50°C (ST/50C), and 85°C (ST/85C). Top left: Optical microscopy photographs (scale bar = 600 μm); Top right: SEM images (scale bar = 8 μm) of a particle cross-section; Bottom left: particle size distributions; Bottom right: MIP pore size distribution curves.

The N_2 adsorption-desorption isotherms (Figure 4.10) also followed the previous observations regarding mesoporosity. At first analysis, all the isotherms seem to be of type III (IUPAC classification), which is typical, in this case, of macroporous materials. This is corroborated by the SEM images and MIP results, as well as some hysteresis, characteristic of mesoporosity, for ST/RT and ST/50C and no hysteresis for ST/85C, which is in line with the MIP results presented above.

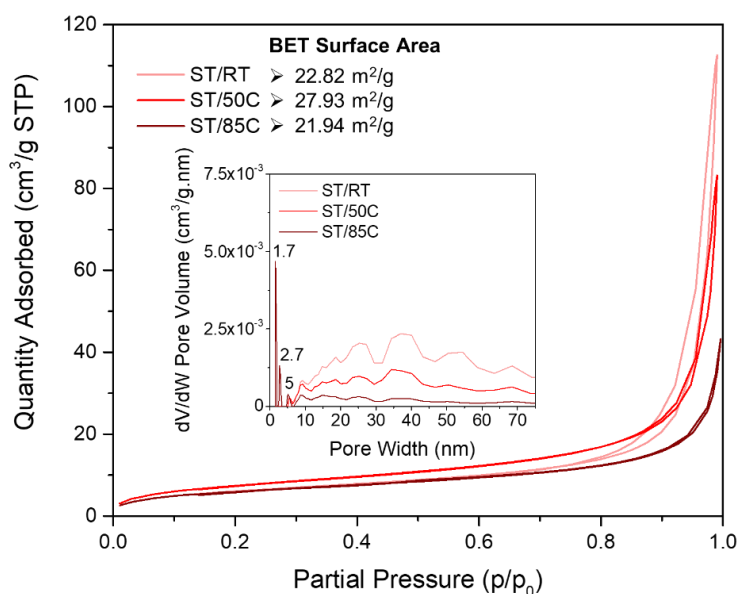


Figure 4.10. N₂ adsorption isotherm and DFT pore size distribution (inset) of MICROSCAFS[®] synthesized at room temperature (ST/RT), 50 °C (ST/50C), and 85 °C (ST/85C).

Oscillatory time sweeps of the complex viscosity (η^*) successfully monitor gelation and crosslinking phenomena over reaction time [183–185]. The gelation reaction process of a polymer gel is divided into three stages: an initial induction, a fast crosslinking, and a final stable period [185]. An abrupt increase in the complex viscosity is characteristic of the beginning of the gelation process [186]. Figure 4.11 shows an oscillatory time sweep analysis of hydrolysates prepared at RT, 50 and 85 °C. It shows the evolution of η^* along the reaction time for each of the three different reaction temperatures, without the addition of the catalyst ammonia.

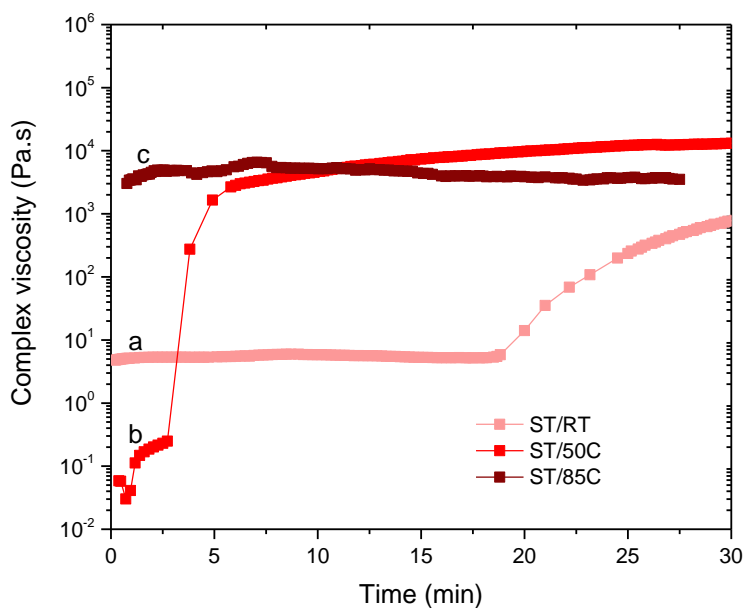


Figure 4.11. Complex viscosity evolution over time for the hydrolysates at (a) room temperature, (b) 50 °C, and (c) 85 °C.

As expected, the synthesis temperature strongly influenced the gelation of the precursors. At RT, the induction period was very long, and the viscosity began to increase only after ~20 min, suggesting relatively slow gelation. At 50 °C, the reaction was much faster, having a sharp increase of complex viscosity starting at ~2.5 min and reaching the stable period at ~5 min. At 85 °C, the gelation was already in the final stable period, so no abrupt increase in viscosity is observed within the time frame of the analysis, which suggests that gelation quickly happens during the mixture of the different compounds and the launching of the testing. This analysis helped to conclude the effect of the synthesis temperature on the kinetics of the gelation phenomenon, which is related to the chemical quenching and the “freezing” of the phase separated structure. However, the addition of ammonia to catalyze condensation might neutralize this effect.

4.1.3.3. Effect of the Si alkoxide type on the ST MICROSCAFS® morphology

Different sol-gel alkoxide precursors, and their combinations at different molar ratios, play a role in the final porosity of the material as they might influence the hydrolysis and condensation kinetics, as well as the phase separation between the siloxane-rich and the water-rich phases inside the water droplets of the emulsion.

Three different molar ratios of the employed Si alkoxides (TEOS and GPTMS) were studied: GPTMS/TEOS at 0.65, 0.87, and 1.09. The MICROSCAFS® size distribution (Figure 4.12) displays a slightly increased value of the mode for higher GPTMS/TEOS ratio but narrower size distribution, given by the span value (1.1) of the curve (Table 4.2). This effect might be linked to the slower condensation rate induced by higher GPTMS content since trialkoxysilanes are less prone to form 3D networks than tetraalkoxysilanes, and the presence of the glycidyloxy group might lead to some steric hindrance effect. Also, the alkyl chain and some remaining epoxy groups present in the hydrolyzed species of GPTMS, associated with the lower viscosity measured for ST/50C/GPTMS+ hydrolysate (14.8 *versus* 25.0 cP for ST/50C/GPTMS-), might lead to a higher tendency for an even, controlled W/O emulsion droplets coalescence, which explains the larger diameter but lower span value of the MICROSCAFS® ST/50C/GPTMS+.

MIP data and SEM images (Figure 4.12) show a drastic change in pores morphology. A higher GPTMS/TEOS ratio strongly increases the pore size, exhibiting a larger macropore volume and size at the expense of mesopores. It should be noted that sample ST/50C/GPTMS+ displays a cumulative pore volume as high as 2.48 mL/g and a broad macropore size distribution peaked at ca. 1929 μm . These characteristics might be due to the delay in the chemical quench of the phase-separated system. On the contrary, the intrusion was almost zero for sample ST/50C/GPTMS- because of the fast overall gelation, which "freezes" the system much before the onset of phase separation by spinodal decomposition and, therefore, yields a denser structure. The SEM image in Figure 4.12 shows that ST/50C/GPTMS- is denser close to the surface. The ammonia solution might have promoted this phenomenon, which further catalyzes the condensation reactions at the surface of the droplets. However, when more GPTMS is employed, such an effect is attenuated.

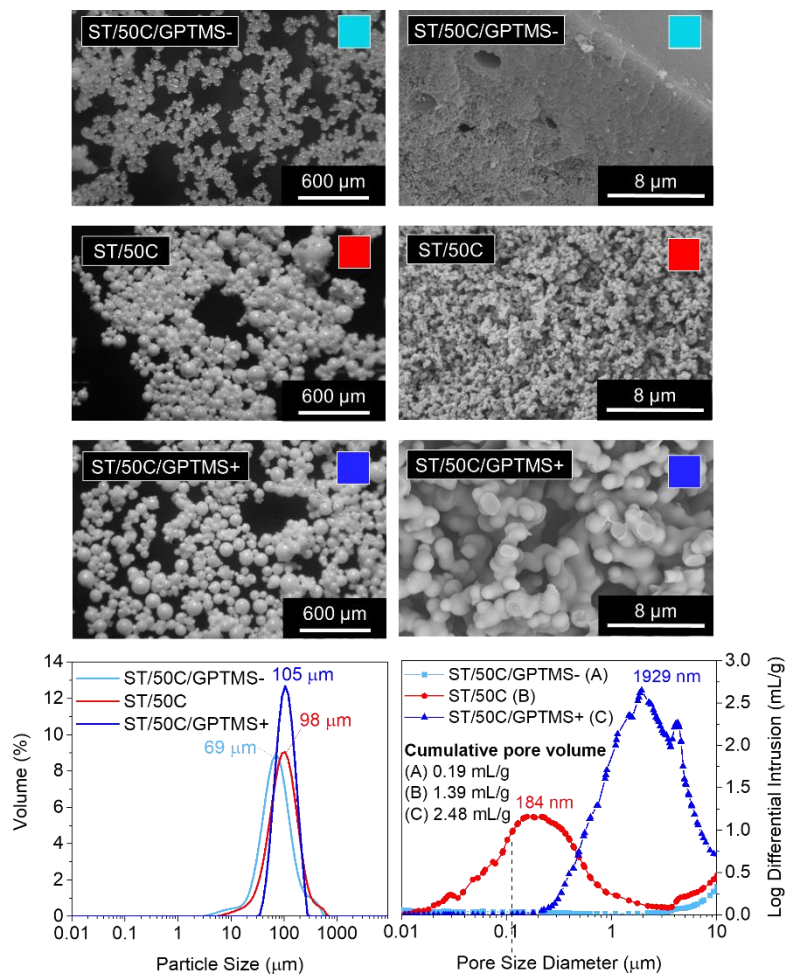


Figure 4.12. Morphology of ST MICROSCAFS[®] synthesized using 0.65 (ST/50C/GPTMS-), 0.86 (ST/50C), and 1.08 (ST/50C/GPTMS+) GPTMS/TEOS molar ratios. Top left: Optical microscopy photographs (scale bar = 600 μm); Top right: SEM images (scale bar = 8 μm) of a particle cross-section; Bottom left: particle size distributions; Bottom right: MIP pore size distribution curves.

Figure 4.13 shows a CT cross-section of MICROSCAFS[®] ST/50C/GPTMS- and ST/50C/GPTMS+ when placed, without pressing, inside a cylindrical container, together with pore and skeletons size distributions and calculated porosity obtained from the analysis of the image data set. ST/50C/GPTMS+ exhibited much more void space between the particles. CT corroborates the findings from SEM, MIP, and optical microscopy, in that ST/50C/GPTMS+ displays larger particle size and porosity. The images were segmented in order to consider only the areas/volumes corresponding to the particles as the region of interest for the morphological analysis, excluding the interparticle space. This strategy ensures that the obtained values represent the intraparticle region of interest. The obtained values of open and total porosity demonstrate that, for both samples, the pores detected by this technique are open

to the external volume of the particles, with ST/50C/GPTMS+ displaying a significantly higher pore volume (ca. 67%) than ST/50C/GPTMS-. On the contrary, the volume of the silica walls (skeleton) is similar in both samples.

The pore size distribution displays the presence of macropores of size above 10 μm , for ST/50C/GPTMS+, which reinforces the fact that macropore size and porosity estimation might be underestimated by MIP. This latter technique cannot distinguish internal from external (interparticle) volume and, therefore, only the range only below 10 μm for MIP was considered for data treatment. On the other hand, the resolution of both techniques, CT and MIP is not the same. The former technique appears to be preferable in the larger size range ($>10 \mu\text{m}$) for these microparticles, while the latter one appears to be better in the smaller size range. These factors may explain the different values achieved for total porosity: e.g. 41% through MIP, and ca. 67% through CT, for ST/50C/GPTMS+.

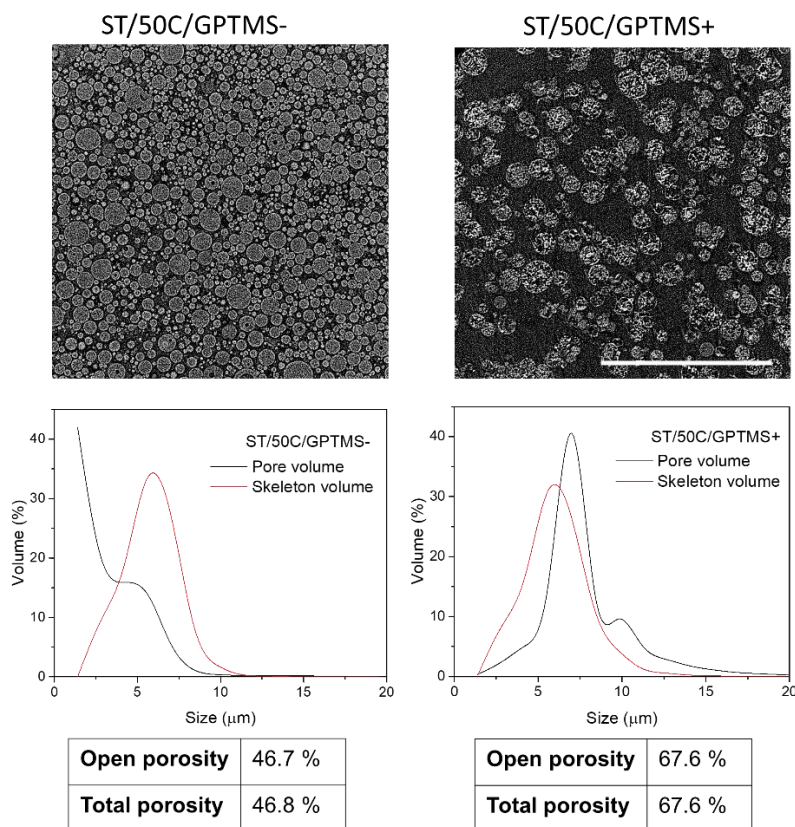


Figure 4.13. Top: Cross-section images obtained by CT from MICROSCAFS® ST/50C/GPTMS- and ST/50C/GPTMS+ obtained with the CCD detector when placed, without pressing, inside a cylindrical container. Scale bar = 700 μm ; Middle: Pore and skeleton size distributions, calculated from CT images; Bottom: open and total porosity calculated from CT images.

The graphs resulting from oscillatory time sweep analyses (Figure 4.14) show a longer induction period and a slower gelation process for a higher GPTMS/TEOS molar ratio (ST/50C/GPTMS+).

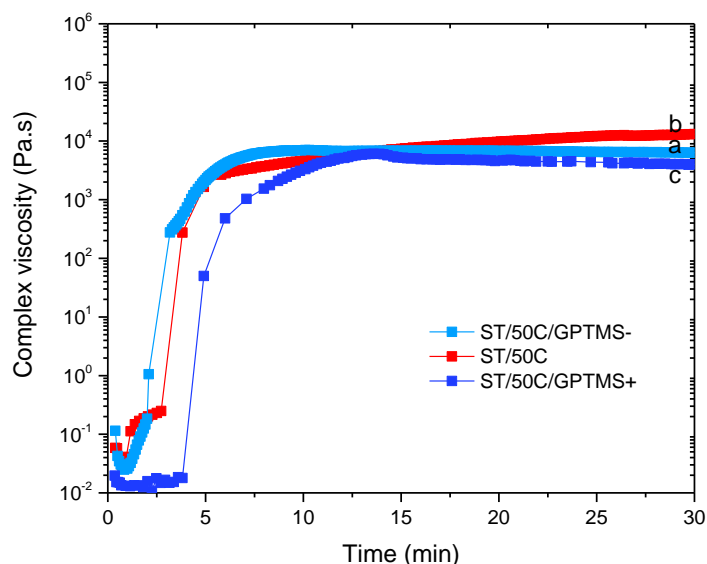


Figure 4.14. Complex viscosity evolution over time of the hydrolysates with (a) 0.65, (b) 0.86, and (c) 1.08 GPTMS/TEOS molar ratio.

Steric hindrance and the hydrophobic character from the relatively long glycidyoxypropyl chain of GPTMS may be the cause for slower condensation [44,187], but also for higher tendency for phase separation, which results in the coarsening of the skeleton domains and larger pore sizes and volumes, typical of ST/50C/GPTMS+. Corroborating this finding, the hydrolysate for ST/50C/GPTMS+ exhibits a slightly lower viscosity than the reference ST/50C. This means the oligomers had lower molecular weight, due to a longer time required for gelation, explaining the obtained coarse macroporosity.

On the other hand, the relatively higher hydrolysate viscosity measured for ST/50C/GPTMS- (Table 4.3) indicates a relevant condensation concomitant to the hydrolysis step. The presence of higher molecular weight oligomers places the system closer to the gel point so that the "freezing" of the structure occurs well before the onset of phase separation. Thus, the MICROSCAFS® exhibit a denser

structure and a very different pore morphology from samples ST/50C and ST/50C/GPTMS+.

The N₂ adsorption-desorption isotherms (Figure 4.15) are of type III (IUPAC classification), suggesting a relatively weak adsorbent-adsorbate interaction.

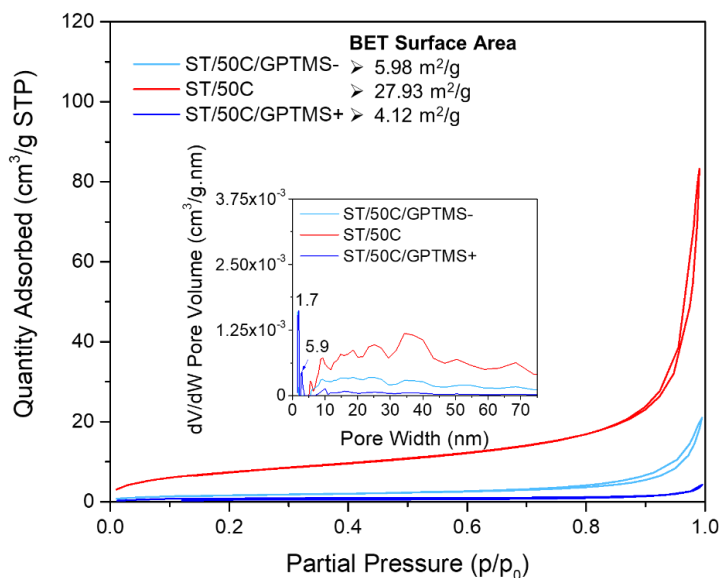


Figure 4.15. BET adsorption isotherm and DFT pore size distribution (inset) of MICROSCAFS® synthesized using 0.65 (ST/50C/GPTMS-), 0.86 (ST/50C), and 1.08 (ST/50C/GPTMS+), GPTMS/TEOS molar ratio.

Both samples, ST/50C/GPTMS- and ST/50C/GPTMS+, showed lower BET surface areas than the ST/50C reference, corroborating the MIP data, which shows no relevant intrusion below 50 nm of pore diameter. It should be emphasized that BET surface areas of ca. 5 m²/g are very close to the limit value detected by this technique. Hence, there might be some errors associated with these values. Also, the nanopore size distributions (insets of Figure 4.10 and Figure 4.15) reveal peaks at 1.7 nm, which might be an effect from the model when applied to a low adsorption isotherm, with irregularities at low pressures.

EDS analysis (Table 4.4) showed that the higher the GPTMS/TEOS molar ratio, the closer the Si and Ti atomic percentage is to the theoretical one, for ST composition (80% SiO₂-20% TiO₂ (molar)).

Table 4.4. EDS relative atomic concentrations of the dried MICROSCAFS®.

Sample acronym	Relative atomic concentration %		
	Si	Ti	Hf
ST/50C/GPTMS-	84.3	15.7	0
ST/50C	82.8	17.3	0
ST/50C/GPTMS+	79.7	20.3	0
STH/50C/GPTMS+	80.3	12.1	7.6

The slower condensation induced by a greater quantity of GPTMS is herein suggested to improve the Ti incorporation into the network. Previous NMR studies for S MICROSCAFS® have shown the presence of T and Q Si units, with T3 prevailing over T2 units [39]. Greater amounts of trialkoxysilane GPTMS promote larger silica network disruption, which is expected to facilitate the incorporation of Ti species in the MICROSCAFS® 3D network.

The FTIR spectra of these samples, when heat treated at 700 °C, reveal features that corroborate the above-mentioned findings. A slight shift of the TO band to lower frequencies (from 1060 to 1050 cm⁻¹), as seen in Figure 4.16, is observed for higher ratios GPTMS/TEOS.

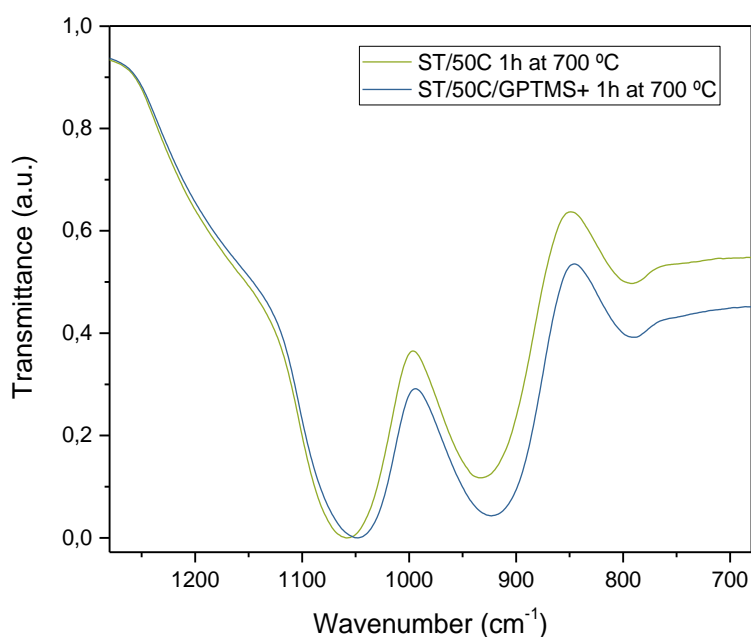


Figure 4.16. ATR-FTIR spectra of MICROSCAFS® ST/50C and ST/50C/GPTMS+, with heat treatment for 1h at 700°C.

This decrease in the frequency of the TO band may be associated with the larger macroporosity observed for ST/50C/GPTMS+. This porosity, in turn, induces the strain in the Si–O–Si bonds at the surface of the pores, which leads to larger bridging angles and longer Si–O bonds, compared to ST/50C/GPTMS- and ST/50C, causing a decrease of the TO band frequency [188]. Also, the Si-O-Ti (Si-O⁻) stretching band appears to be more intense for ST/50C/GPTMS+, corroborating the larger amount of Ti species in the network, detected by EDS, and therefore more Si-O-Ti bonds.

4.1.3.4. Effect of the Ti precursor's chelating agent and emulsion characteristics on the ST MICROSCAFS®' morphology

The modification of TiPOT with glacial acetic acid (chelation) reduces the availability of groups that easily hydrolyze through the formation of a stable complex, typically $\text{Ti}(\text{OCOCH}_3)(\text{O}i\text{Pr})_2$ [189]. The effect of increasing the amount of the Ti precursor's chelating agent, acetic acid (CH_3COOH), was studied up to the point of excess (TiPOT/ CH_3COOH molar ratio from 1/4 to 1/6), which resulted in a decrease of the average synthesis pH from 8.51 to 7.61. The MICROSCAFS® size distribution graph (Figure 4.17) shows an apparent increase in the particle size mode and all the

percentiles (Table 4.2) for a higher quantity of acetic acid (lower TiPOT/CH₃COOH molar ratio, sample ST/50C/AA+).

On the contrary, a larger water phase volume in the emulsion and, therefore, a higher concentration of water droplets, acting as a soft template for the MICROSCAFS[®], did not change the particle size mode significantly. Instead, there was an increase in the D (0.9) percentile and, consequently, the span value, indicating greater size dispersions (Table 4.2). This effect is also visible in the optical microscopy photograph of sample ST/50C/W+ (Figure 4.17).

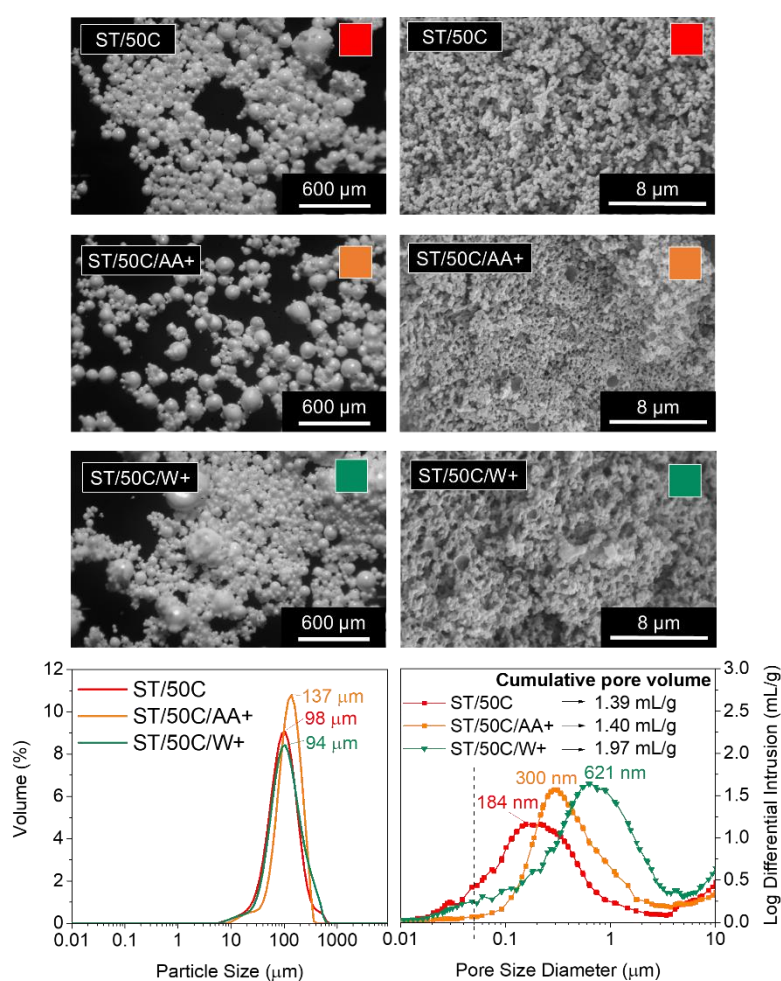


Figure 4.17. Morphology of ST MICROSCAFS[®] synthesized using 1:4 (ST/50C) and 1:6 (ST/50C/AA+) TiPOT/CH₃COOH molar ratios, and 0.45 (ST/50C) and 0.68 (ST/50C/W+) W/O mass ratios. Top left: Optical microscopy photographs (scale bar = 600 μm); Top right: SEM images (scale bar = 8 μm) of a particle cross-section; Bottom left: particle size distributions; Bottom right: MIP pore size distribution curves.

Based on the theoretical models proposed by Pal. et al., these emulsions are considered concentrated or highly concentrated [190]. In these domains, the increase of dispersed phase concentration leads to more closely packed water droplets that interact much more with one another. Destabilizing phenomena such as coalescence and flocculation are more pronounced in these domains, leading to an increase in polydispersity of the template emulsion as the water phase increases [191,192], and to the presence of a fraction of larger MICROSCAFS®, with sizes ranging from 200 to 500 μm . The closely packed water droplet's structure will also be responsible for a pronounced increase in emulsion viscosity, found in the present work (Figure 4.18), for increasing W/O mass ratios, in the range of 0.2 to 1.1.

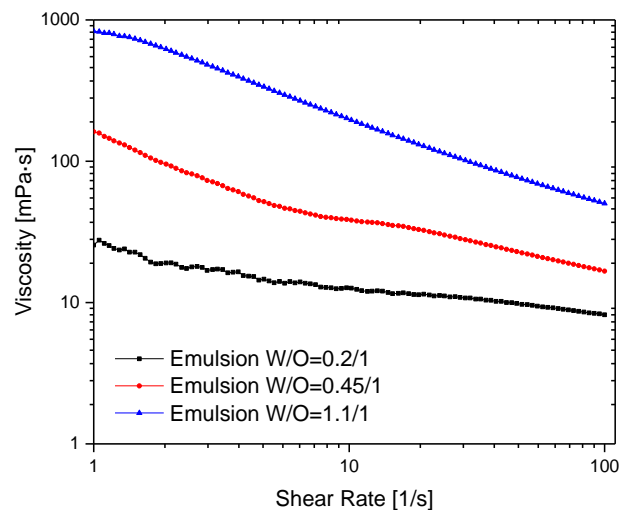


Figure 4.18. Flow test curves of three groups of emulsion each belonging to different W/O ratios.

This behavior can be justified by increased friction between droplets imputable to movement restrictions for the overall 3D emulsion network [193].

Regarding macroporosity, MIP data and SEM images (Figure 4.17) showed that higher quantities of both the emulsion's water phase and TiPOT's chelating agent (acetic acid) lead to bigger macropore size, however, not so intensely as for samples ST/85C and ST/50C/GPTMS+.

An excess of acetic acid tends to slow down the alkaline condensation reaction, leading to a delay in the "freeze" of the phase-separated structure, which results in the coarser skeleton domains of ST/50C/AA+, and an increase of its macropores size, at the expense of mesopores.

However, when performing oscillatory time sweep analysis on the hydrolysate without adding ammonia (Figure 4.19), the acidic condensation reaction is kinetically more favorable.

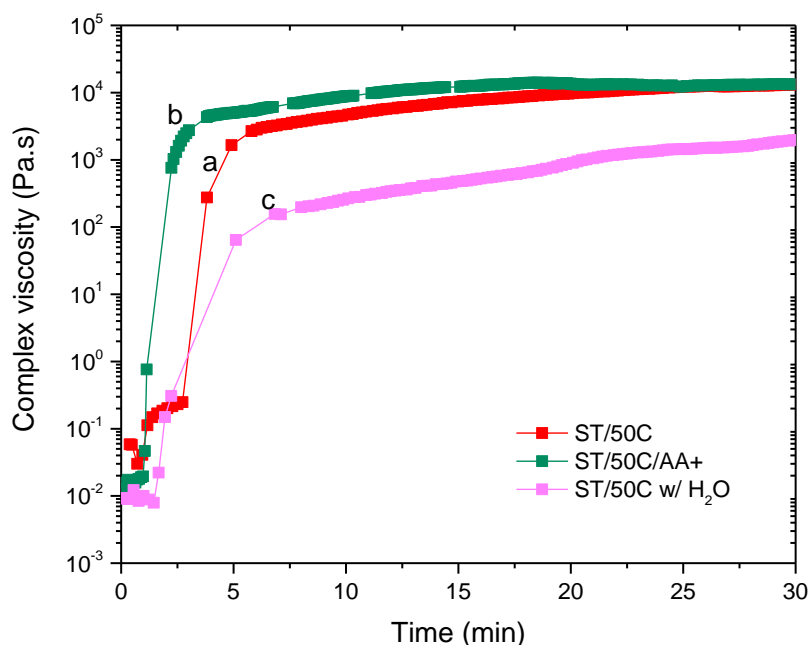


Figure 4.19. Complex viscosity evolution over time of the hydrolysates with (a) 1:4 TiPOT:CH₃COOH molar ratio (sample ST/50C), (b) 1:6 TiPOT:CH₃COOH molar ratio (sample ST/50C/AA+), and (c) 1:4 TiPOT:CH₃COOH molar ratio, diluted with an equivalent amount of the excess of emulsion water.

An increase of η^* along the reaction time occurred slightly faster when more acetic acid was used. It has been reported that TiPOT only forms bidentate ligands with acetic acid at a 1:2 ratio. Therefore, all the excess acid remains in the solution and hinders the alkaline condensation of the precursors, increasing the pore size [189].

By observing Figure 4.17, a higher W/O mass ratio yielded MICROSCAFS[®] with larger pores. This might be caused by a dilution effect of the clusters, which delays the gelation as there is more water in the polymerized species-W/O dispersion. Also,

protonic solvents (e.g., water) have been reported to decrease condensation reactions in alkaline media [194], which might also increase the time between the phase separation and gelation and yield greater pore sizes. When an equivalent amount of the excess water was added to the ST/50C hydrolysate solution and ran oscillatory time sweep measurements (Figure 4.19), the gelation achieved approximately maximum η^* one order of magnitude lower than the reference sample ST/50C. Regarding mesoporosity, a decrease in BET surface area was detected for this sample (8.73 m²/g *versus* 27.93 m²/g for ST/50C) (Figure 4.20), in line with the lower amount of mesopores (Figure 4.17). The isotherm of the ST/50C/W+ is also type III, characteristic of a relatively weak adsorbent-adsorbate interaction.

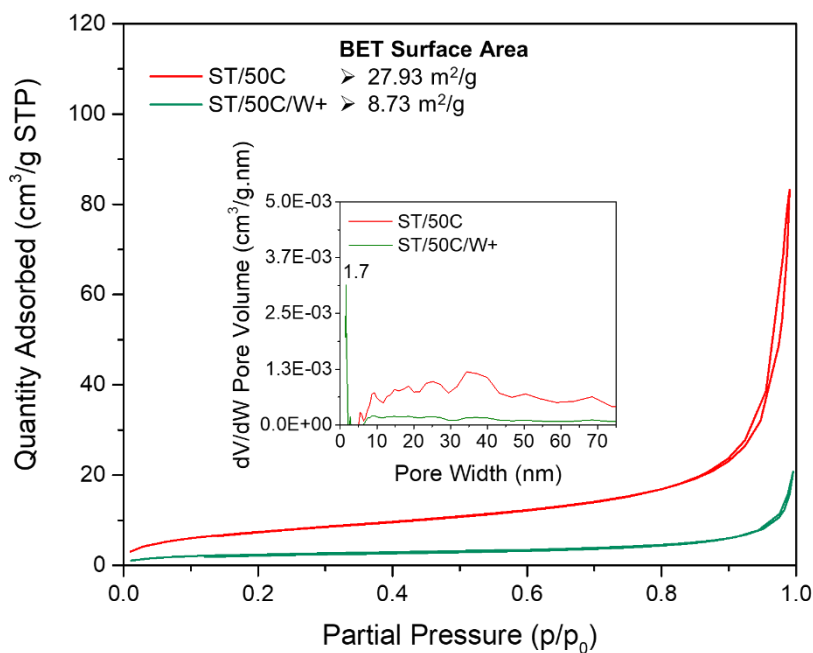


Figure 4.20. N₂ adsorption isotherm and DFT pore size distribution (inset) of MICROSCAFS[®] synthesized at 0.45:1 (ST/50C) and 0.68:1 (ST/50C/W+) W/O mass ratios.

4.1.3.5. Development of multicomponent oxide $\text{SiO}_2\text{-TiO}_2\text{-HfO}_2$ (STH) MICROSCAFS®

Hafnium dichloride oxide octahydrate salt was added during the silanes hydrolysis step of an ST/50C/GPTMS+ MICROSCAFS® synthesis to produce multicomponent oxide STH MICROSCAFS®, aiming at enlarging the scope of applications for these particles. As a base, the ST/50C/GPTMS+ synthesis was chosen, instead of the reference (ST/50C), due to its greater macroporosity. The changes occurring in the final porosity of these new MICROSCAFS® were evaluated.

Adding Hf salt led to a particle size distribution with larger dispersion (Figure 4.22), indicated by a broader curve with a higher span value (Table 4.2). This might be related with the higher viscosity of the corresponding hydrolysate (45.3 cP versus 16.2 cP for ST/50C, Table 4.3).

However, all particles have a regular spherical shape. The SEM images and MIP pore size distribution in Figure 4.22 show a steep decrease in pore size and cumulative pore volume for STH/50C/GPTMS+ when compared to the ST analogue. EDS data show that the initial relative molar concentration of 80% Si was kept in the final MICROSCAFS® network composition (Table 4.4). On the other hand, 7.6% of the Ti atoms was replaced by Hf atoms, suggesting their incorporation into the network. Doubling further the Hf precursor quantity generated irregular particles of non-spherical shapes and heterogeneity in terms of pore morphology and size (Figure 4.21).

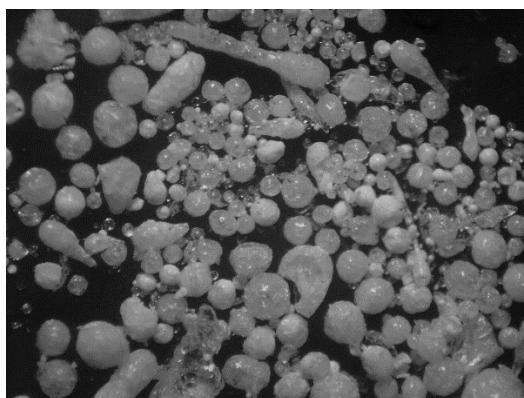


Figure 4.21. Optical microscopy photograph of STH MICROSCAFS® made using 13.7 g of hafnium dichloride oxide octahydrate salt.

The reported high viscosity of the hydrolysate in the presence of Hf precursor resulted in faster gelation. It is known that HfOCl_2 provides HCl, which catalyzes the hydrolysis of the silanes present in this system. Also, high atomic number elements, such as Hf, when bonded to Cl increase reactivity and accelerate the gelation process. The large ionic strength of Hf-Cl bonds (large electronegativity difference) existing in the Hf precursor might easily destroy the protection of the repulsive double layer around primary particles, resulting in their aggregation and formation of a gel. The triple oxide system thus condensates and "freezes" the phase-separated structure faster than the double oxide system. This effect prevents coarsening and macropore enlargement expansion, originating smaller porosities than the double oxide system (Figure 4.22). When the Hf precursor was present, the delayed condensation, typical of greater quantities of GPTMS precursor, had no significant impact on the developed structure.

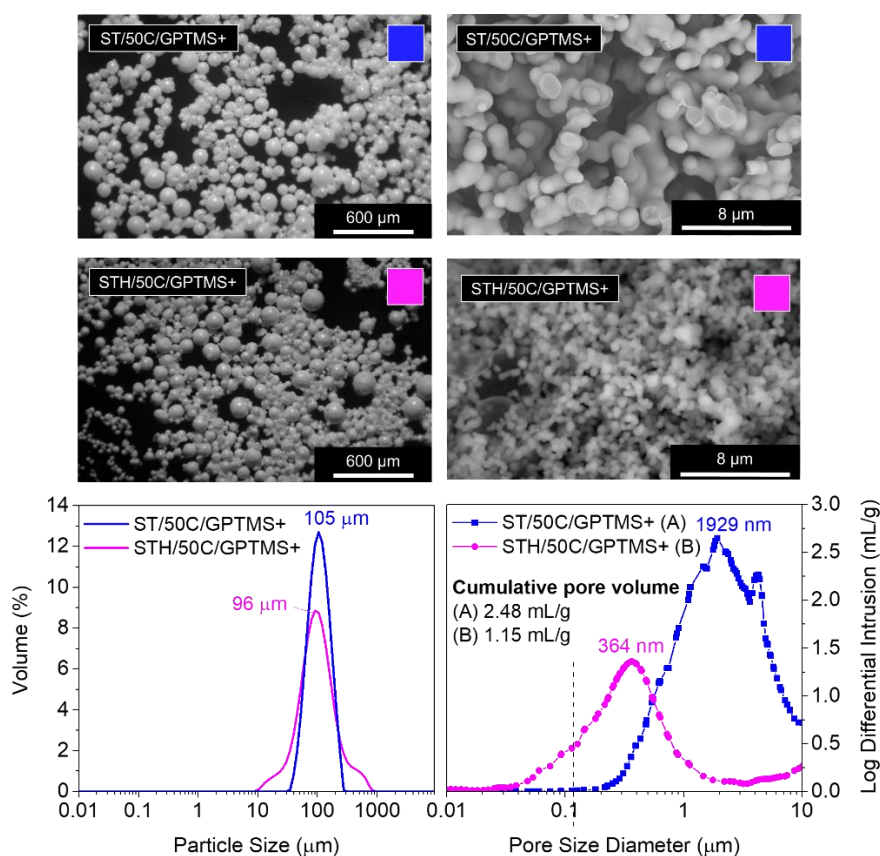


Figure 4.22. Morphology of double (ST/50C/GPTMS+) and triple (STH/50C/GPTMS+) oxide MICROSCAFS®. Top left: Optical microscopy photographs (scale bar = 600 μm); Top right: SEM images (scale bar = 8 μm) of a particle cross-section; Bottom left: particle size distributions; Bottom right: MIP pore size distribution curves.

After heat treatment at 700 °C, the major difference when comparing STH MICROSCAFS® with ST MICROSCAFS®, consists of a much weaker band at ~936 cm⁻¹, slightly shifted to lower frequencies (Figure 4.23), assigned to Si–O asymmetric stretching, which is characteristic of homogeneous gel/glass network regions, where Si–O–Ti and Si–O–Hf bonds are also included [195].

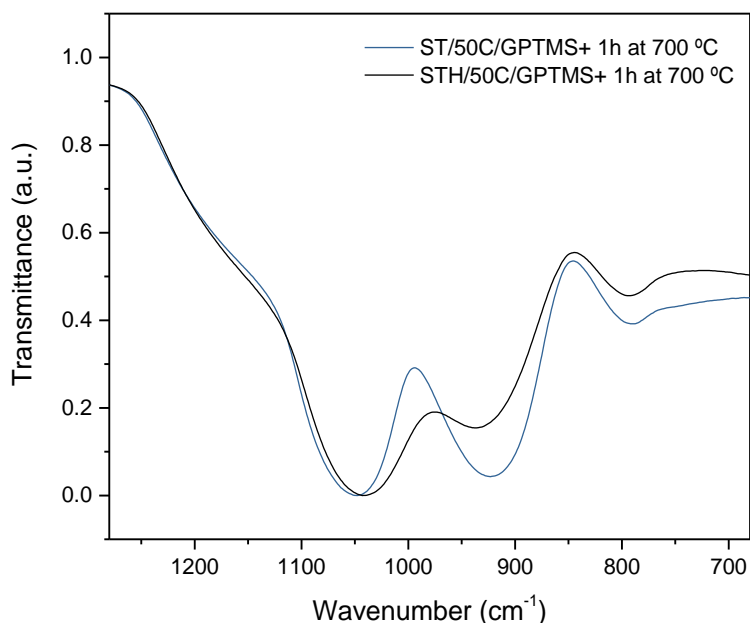


Figure 4.23. ATR-FTIR spectra of MICROSCAFS® ST/50C/GPTMS+ and STH/50C/GPTMS+, with heat treatment for 1h at 700 °C.

Si–O–Hf bands are typically much weaker than Si–O–Ti bands, which might be due to a higher degree of heterogeneity, in the former case, but it could also arise in part from a lower IR activity of the Si–O–Hf vibrational mode, due to structural differences, such as different distributions of the Si–O–Hf and Si–O–Ti angles.

4.1.3.6. MICROSCAFS®' mechanical properties

The mechanical properties of the MICROSCAFS® impact their performance, so their evaluation is relevant for future applications. Considering a continuous flow setup for photocatalysis tests [38] as a possible application in the framework of environmental remediation, it is beneficial to understand how the MICROSCAFS®

behave when subject to compression in a confined space (reservoir). A more cohesive powder, i.e., a less free-flowing powder, exhibits higher compressibility and allows more MICROSCAFS® to fit inside the confined space, resulting in an increase of the bulk density under compressive stress. This characteristic may impact the photocatalytic activity and the flow of the solution that is being purified. The stiffness and mechanical strength of the materials give us an insight into how easily these catalytic supports will break, playing a significant role in the photocatalyst's activity, reusability, and recyclability.

The different MICROSCAFS® were subject to a loading/hold/unloading process to evaluate various properties of the powders, namely compressibility, relaxation, elastic recovery, and stiffness. The loading period involves elastic and plastic deformation, while the hold period (stress relaxation) is generally purely plastic. It allows the study of the viscoelastic (time-dependent) behavior of the compacted MICROSCAFS® since the particles undergo plastic deformation and move into void spaces. The force usually drops off quickly, followed by a slighter decrease until reaching a plateau. The more viscoelastic the powder, the more the force drops during the hold period. The unloading period is generally purely elastic and (the initial slope) allows the measurement of the stiffness of the compact, while the elastic recovery upon unloading is a function of the loaded and relaxed column heights.

Figure 4.24 compiles the impact of all the different reactional parameters on the MICROSCAFS® powder compression parameter (compressibility), force hold ratio (relaxation), unload strain (elastic recovery), and unload gradient (stiffness). The increase in reaction temperature, GPTMS/TEOS molar ratio, emulsion W/O mass ratio, and decrease in TiPOT/CH₃COOH molar ratio yielded MICROSCAFS® with higher compressibility and elastic recovery but lower stiffness than the corresponding reference ST/50C (marked with a red dashed line rectangle). These parameters increase the temporal space between the “freezing” of the structure and the onset of phase separation, resulting in larger porosity and, therefore, less stiff MICROSCAFS® with larger elastic recovery upon unloading. The change in morphology (broader skeletons, larger pores) might also result in less free-flowing, more cohesive, and, therefore, more compressible powders under compressive

stress. There is clearly more free space between the particles, for MICROSCAFS® ST/50C/GPTMS+, before being pressed, as shown in Figure 4.25. The CT scan results determined that the object (solid matter) volume was 53.2 % for ST/50C/GPTMS- and 32.4 % for ST/50C/GPTMS+. This fact resulted in higher compressibility when the sample ST/50C/GPTMS+ was subject to a compression force, explaining the recurrent high compressibility value obtained for higher contents of GPTMS. Inversely, adding Hf salt yielded stiffer MICROSCAFS®, exhibiting as well lower compressibility and lower elastic recovery. Finally, the stress relaxation (viscoelasticity) of the compacted MICROSCAFS® was only slightly affected (increased) for higher GPTMS/TEOS molar ratios, which suggests a similar level of plastic deformation of the MICROSCAFS® reported in this chapter.

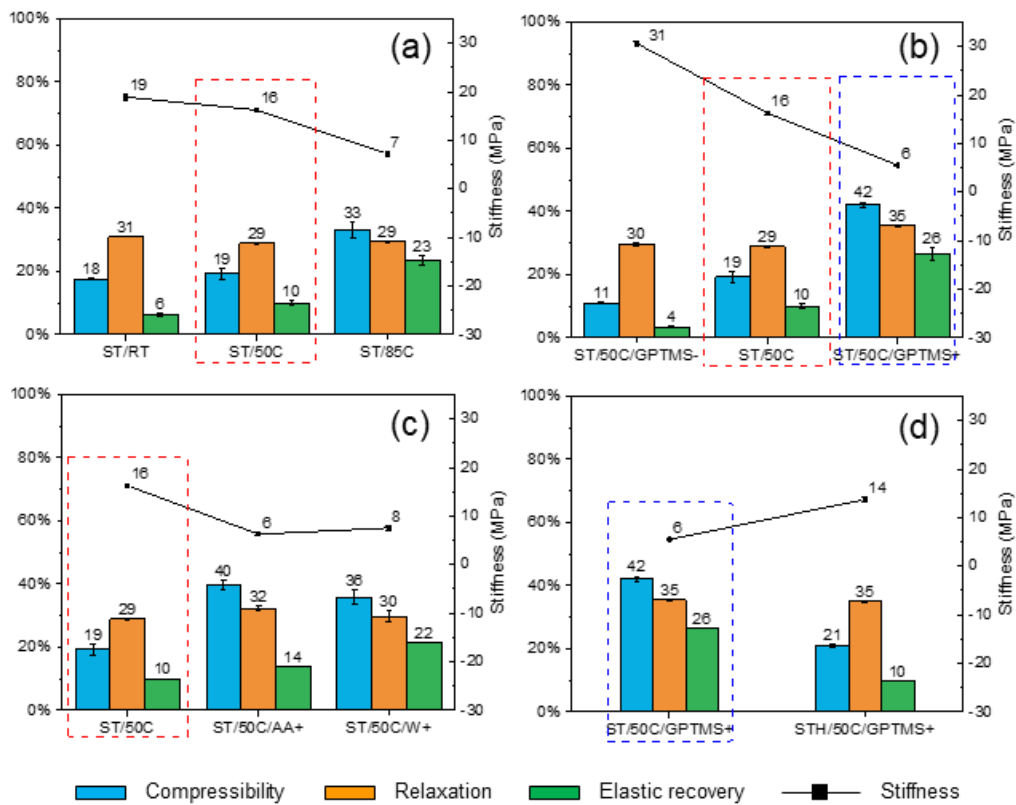


Figure 4.24. Effect of (a) reaction temperature, (b) GPTMS/TEOS molar ratio, (c) TiPOT/CH₃COOH molar ratio and W/O mass ratio, and (d) addition of Hafnium dichloride oxide salt (STH multicomponent oxides) in the MICROSCAFS®' mechanical properties.

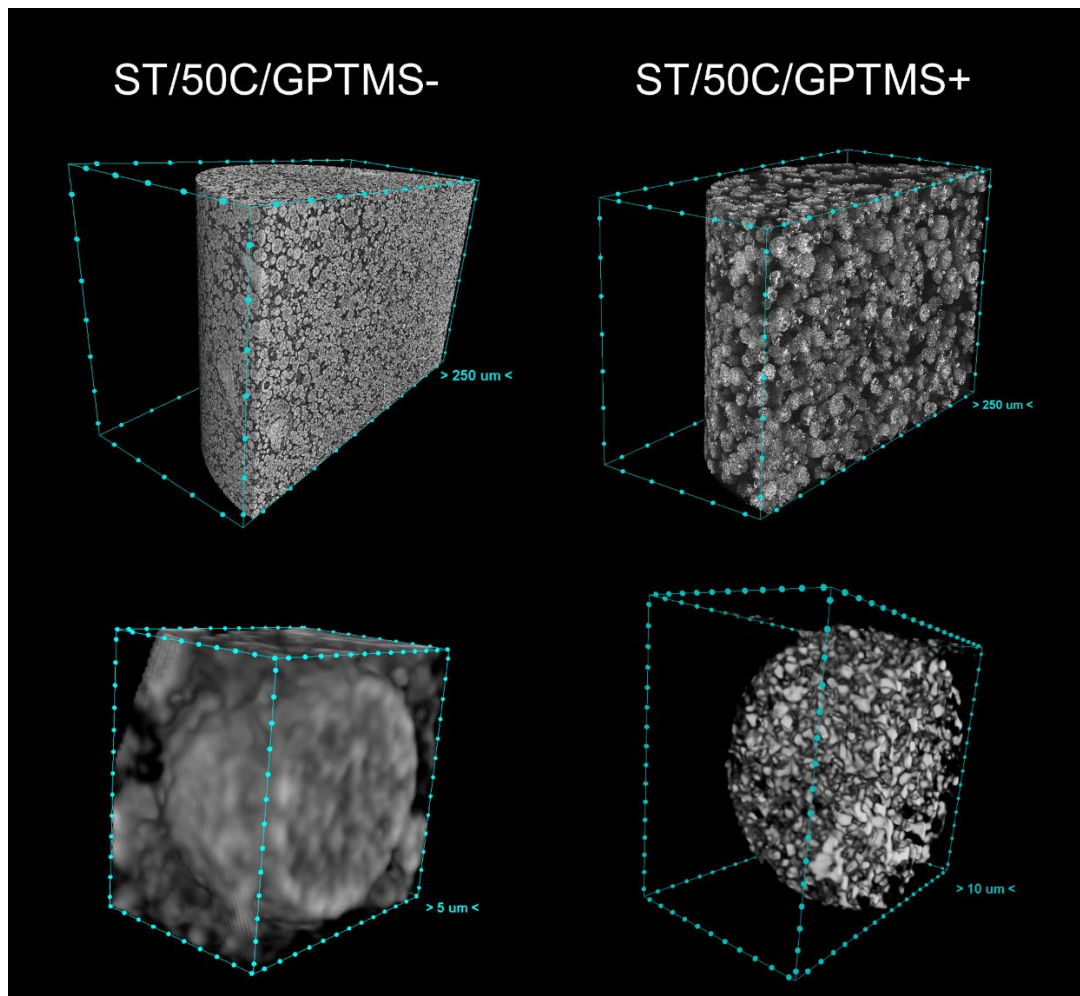


Figure 4.25. Cross-sectional 3D CT image of the powder (top line) and a single microsphere (bottom line) of the ST/50C/GPTMS- and ST/50C/GPTMS+ MICROSCAFS® (scale, distance between points: top left = 250 μm, top right = 250 μm, bottom left = 5 μm, bottom right = 10 μm).

The effect of MICROSCAFS®' cumulative pore volume on the four evaluated parameters was represented in Figure 4.26. Graphics containing the effect of pore size mode and particle size mode were also represented and can be found in Figure 4.27 and Figure 4.28.

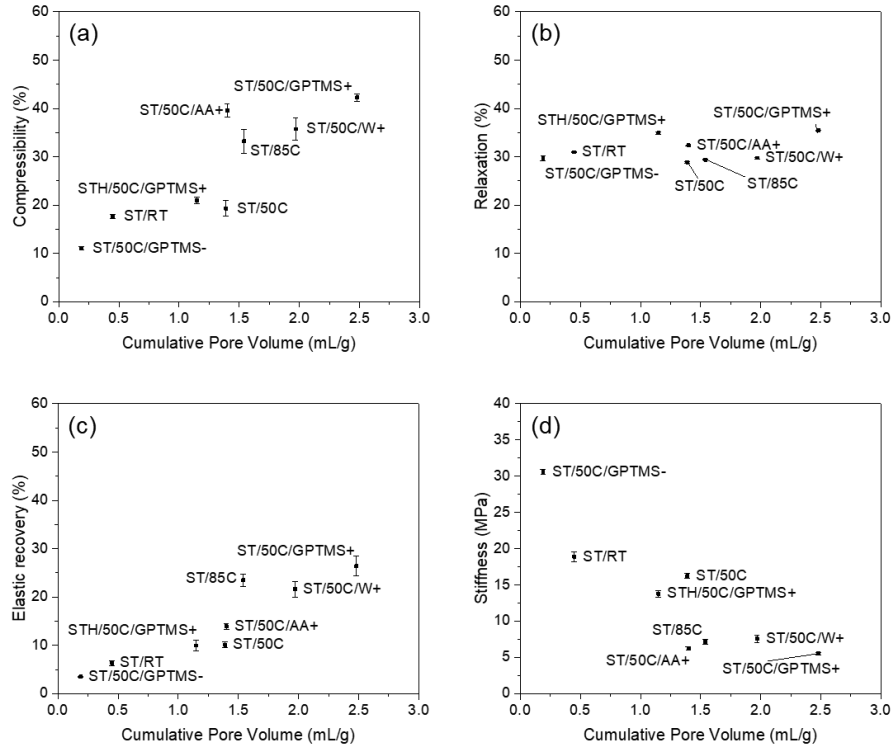


Figure 4.26. Effect of MICROSCAFS® cumulative pore volume in (a) compressibility, (b) relaxation, (c) elastic recovery, and (d) stiffness.

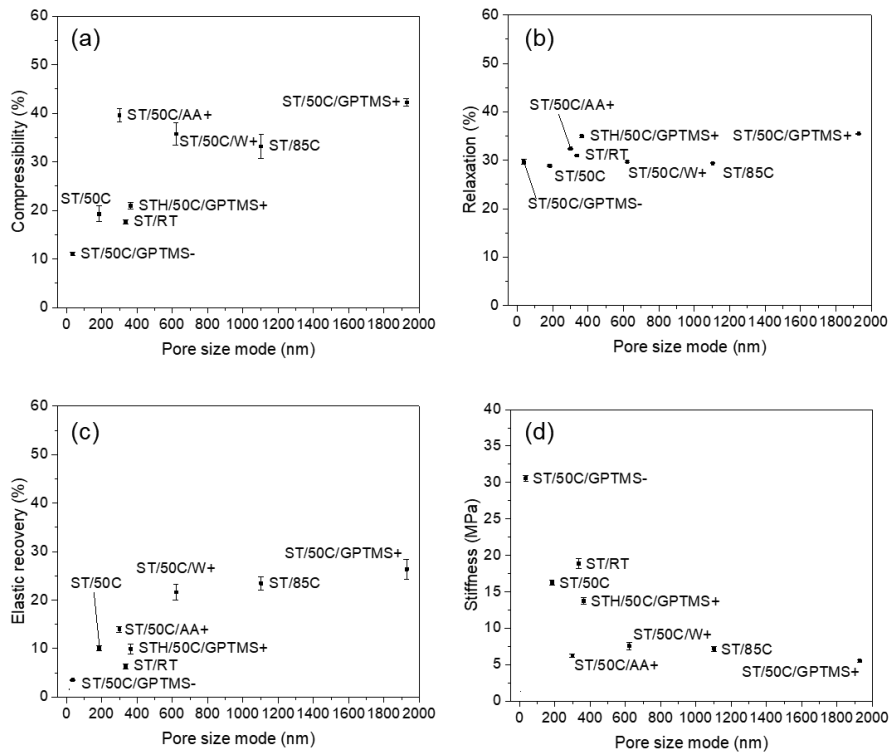


Figure 4.27. Effect of MICROSCAFS® pore size mode in (a) compressibility, (b) relaxation, (c) elastic recovery, and (d) stiffness.

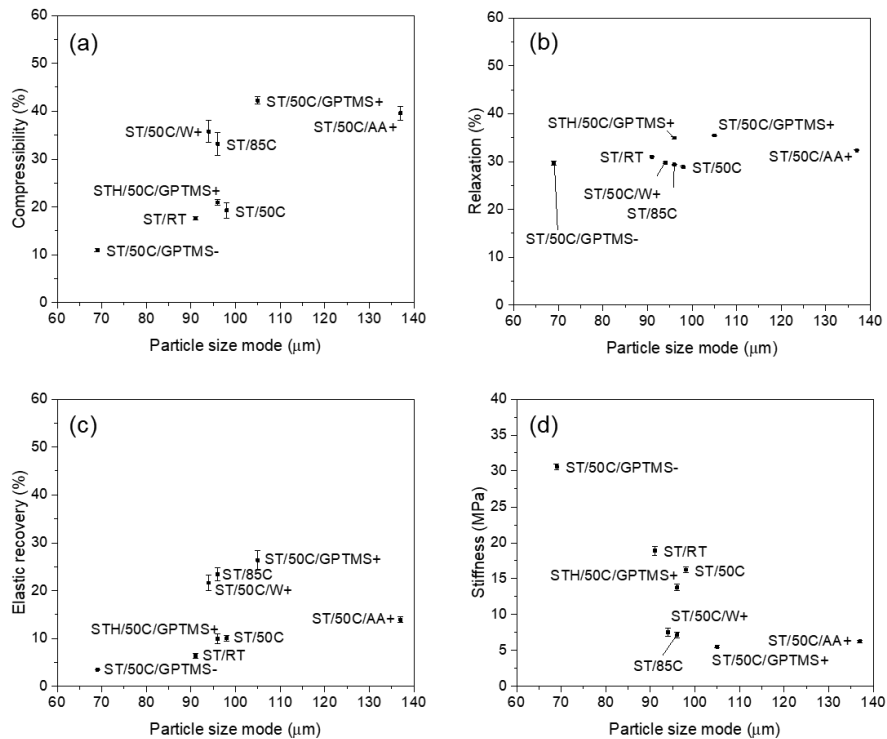


Figure 4.28. Effect of MICROSCAFS® particle size mode in (a) compressibility, (b) relaxation, (c) elastic recovery, and (d) stiffness.

Summarily, higher cumulative pore volumes and higher mode values of the pore size resulted in higher compressibility and elastic recovery, following an approximately linear trend. As for relaxation, no significant changes were observed, while stiffness decreases linearly for greater cumulative pore volumes, and exponentially for greater pore sizes. The effect of particle size, on the other hand, is not so evident in terms of MICROSCAFS® stiffness, because samples with similar particle size, but exhibiting different porosity, display different stiffness values.

These results show that by changing synthesis parameters, such as GPTMS/TEOS molar ratio, it is possible to finely tune the mechanical properties of the MICROSCAFS®, namely stiffness, compressibility, and elastic recovery. The recurrent lower stiffness observed in sample ST/50C/GPTMS+ is attributed to the higher quantity of GPTMS. Besides the larger macroporosity characteristic of this sample (Figure 4.25), the presence of more glycidloxypropyl groups, i.e., the higher number of organic fractions incorporated in the structure (more hybrid character) may also

play a role in reducing the stiffness and increasing compressibility and elastic recovery. On the contrary, the sample with a lower GPTMS/TEOS molar ratio and, thus, a higher quantity of TEOS exhibits the highest stiffness due to its more inorganic character, less disrupted 3D network, and denser structure (less macroporosity). A higher amount of TEOS confers a stiffer glass-like structure to the MICROSCAFS®.

All the MICROSCAFS®' additional calculated and graphical data can be found in Table 4.5 and Figure 4.29 to Figure 4.32.

Table 4.5. Mechanical parameters of the dried MICROSCAFS®.

Sample acronym	Compressibility (%)	Relaxation (%)	Stiffness (MPa)	Elastic recovery (%)
ST/RT	17.65 ± 0.40	30.96 ± 0.09	18.89 ± 0.65	6.34 ± 0.50
ST/50C	19.28 ± 1.61	28.86 ± 0.20	16.23 ± 0.37	10.07 ± 0.58
ST/85C	33.18 ± 2.42	29.38 ± 0.11	7.15 ± 0.35	23.47 ± 1.33
ST/50C/GPTMS-	11.01 ± 0.36	29.65 ± 0.20	30.59 ± 0.38	3.50 ± 0.05
ST/50C/GPTMS+	42.23 ± 0.77	35.44 ± 0.12	5.52 ± 0.16	26.38 ± 2.04
ST/50C/AA+	39.58 ± 1.43	32.35 ± 0.12	6.25 ± 0.21	13.94 ± 0.60
ST/50C/W+	35.73 ± 2.29	29.75 ± 0.16	7.55 ± 0.54	21.63 ± 1.60
STH/50C/GPTMS+	20.95 ± 0.64	34.93 ± 0.28	13.77 ± 0.48	9.95 ± 1.03

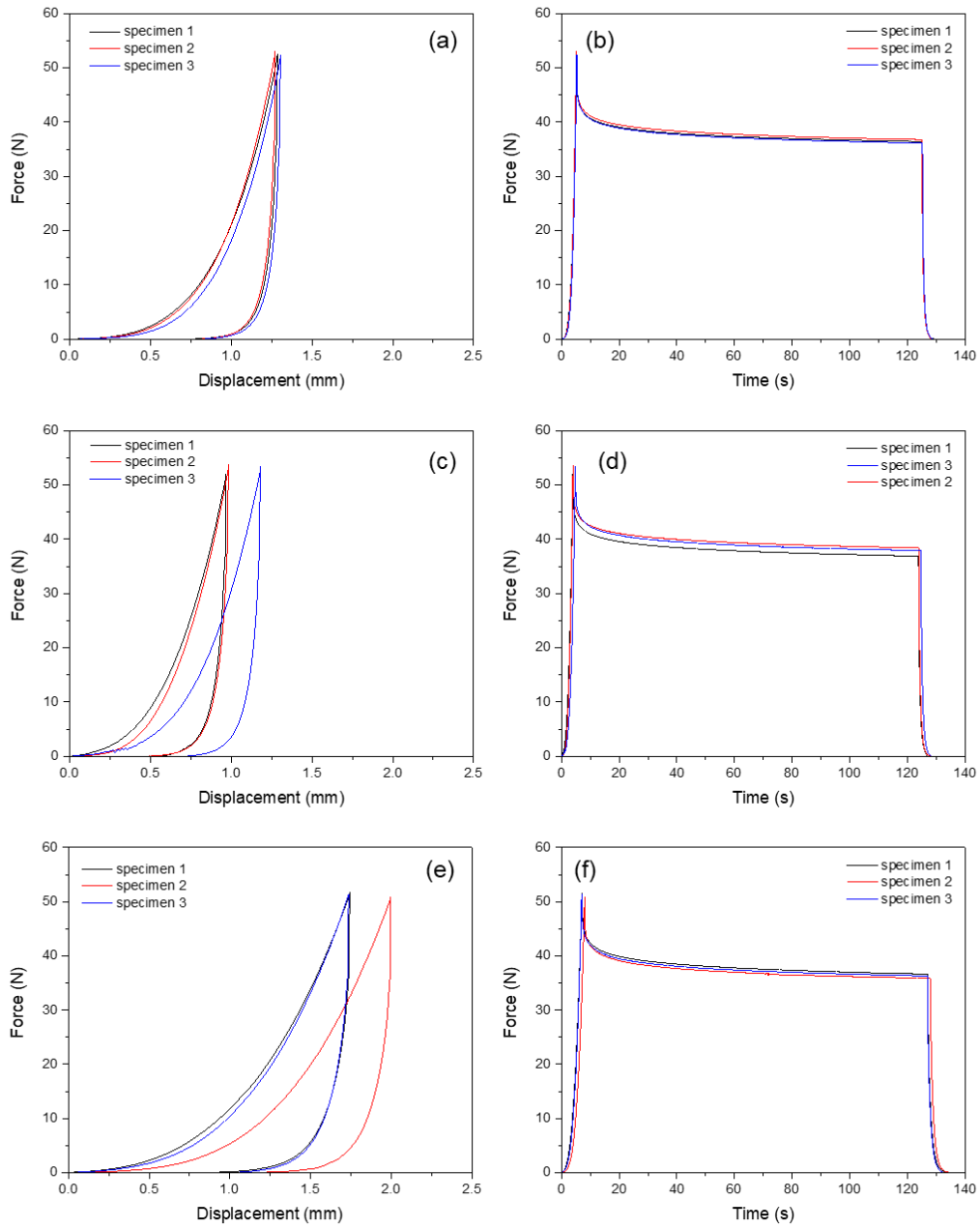


Figure 4.29. Compression and relaxation tests of (a, b) ST/RT, (c, d) ST/50C, and (e, f) ST/85C dried MICROSCAFS®.

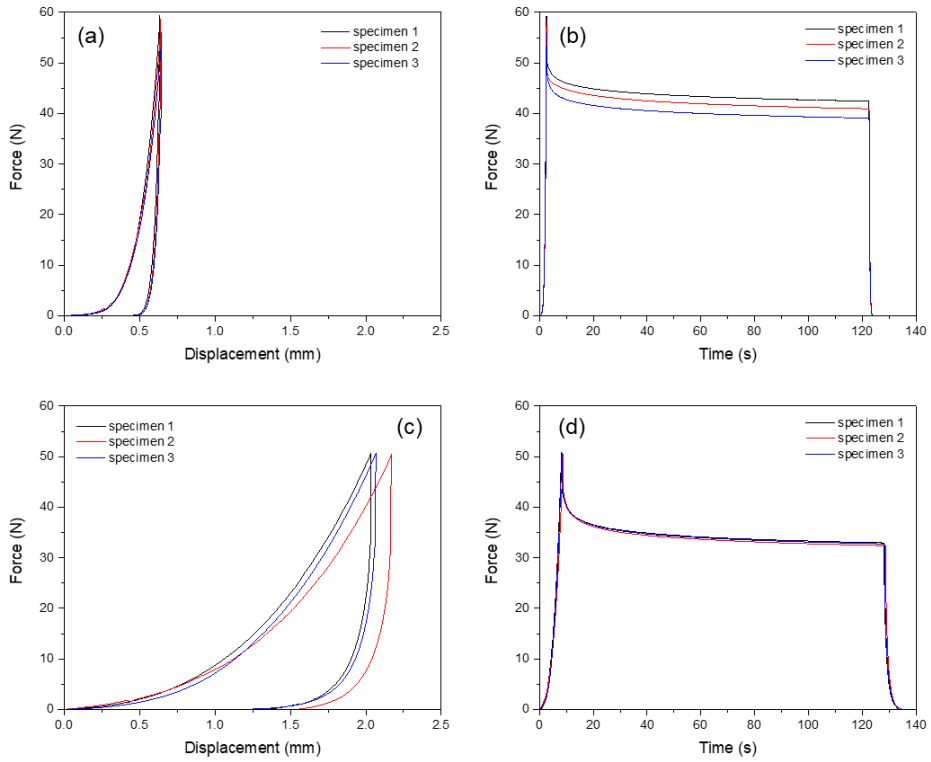


Figure 4.30. Compression and relaxation tests of (a, b) ST/50C/GPTMS-, (c, d) ST/50C/GPTMS+ dried MICROSCAFS®.

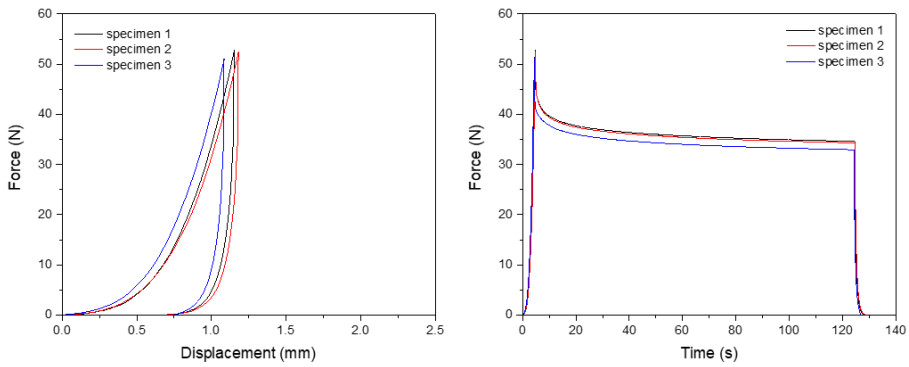


Figure 4.31. Compression and relaxation tests of STH/50C/GPTMS+ dried MICROSCAFS®.

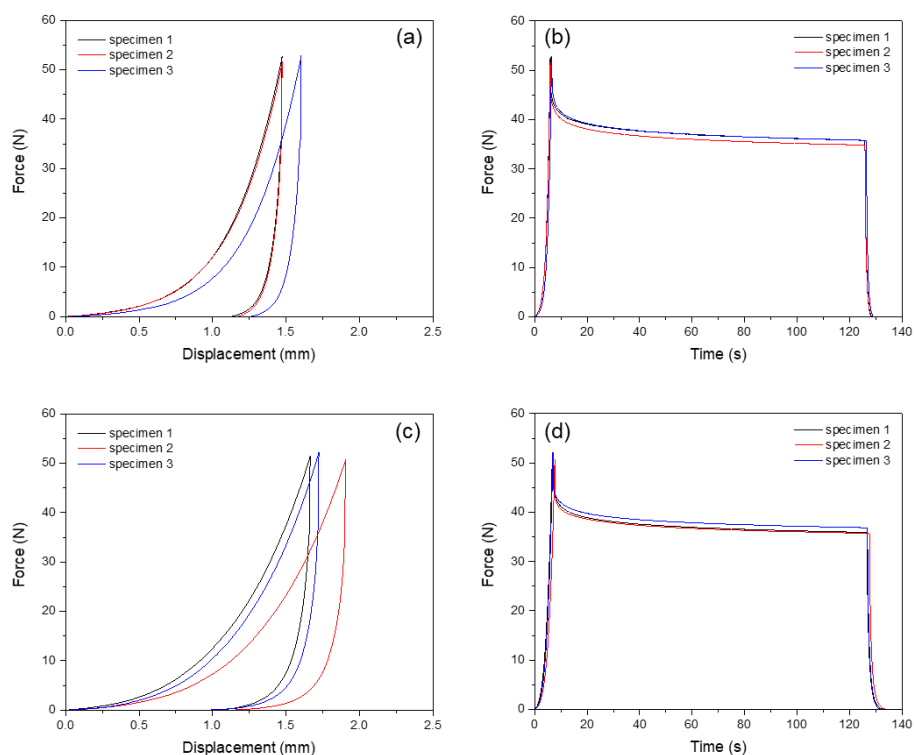


Figure 4.32. Compression and relaxation tests of (a, b) ST/50C/AA+, (c, d) ST/50C/W+ dried MICROSCAFS®.

4.1.4. Conclusion

This sub-chapter displays one of the main innovations of this thesis, which relies on the development of multicomponent oxide ST and STH MICROSCAFS®. A new method to reproducibly obtain these microspheres of tailored size, composition, interconnected macroporosity, and mechanical properties is herein described with success, despite the complexity of the simultaneous occurrence of phase separation and gelation in the confined space of emulsion droplets. The MICROSCAFS® display robust scaffolding properties, including thermal and chemical stability, making them an innovative multifunctional material for various applications.

Polymerization-induced phase separation applied to the sol-gel synthesis of the microspheres, where an emulsion is used as a soft template, was found to effectively control the morphological features and mechanical properties of ST and STH MICROSCAFS®. Such fine-tuning is achieved by a proper selection of the synthesis parameters and is expected to play a major role in terms of MICROSCAFS®

performance. To sum up, larger macroporosity (in most of the cases at the expense of some of the mesoporosity) and particle sizes were achieved by using a higher reaction temperature (85 °C), higher GPTMS/TEOS molar ratio (1.09), or lower TiPOT/CH₃COOH molar ratio (1:6). A higher W/O mass ratio (0.68:1) increased the pore size without effectively changing the particle size, while specific mixtures of surfactants (Span® 80 and Pluronic® P123, HLB=5.2) resulted in a drastic decrease of particle size. The composition and content of the silane precursors, defined by the GPTMS/TEOS molar ratio, had the greatest effect on the final interconnected macroporosity and particle size, yielding pores with size mode ranging from a few nanometers to a few microns in diameter and particle size modes ranging from 69 to 105 μm. Greater GPTMS content also increased the material's hybrid inorganic/organic character, enabling further functionalization reactions, if desired. The presence of Hf precursor (STH MICROSCAFS®) lead to smaller interconnected macroporosity, explained by the higher gelation rate induced by the Hf precursor.

Finally, a correlation between the size and amount of macropores and the mechanical properties of the MICROSCAFS® was established. Greater macroporosity generally leads to MICROSCAFS® displaying less stiffness, higher elastic recovery, and compressibility values up to 42%, for the more porous samples (68% open porosity).

In the end, it is now possible to precisely control the porosity and sizes of silica-based multicomponent MICROSCAFS®. Their potential for photocatalytic applications will be explored in the next chapter (Chapter 5), as well as the effect of their mechanical properties on their reusability and recyclability in photocatalytic tests.

4.2. Mechanistic study of the formation of multicomponent oxide MICROSCAFS[®] by cryo-SEM

4.2.1. Introduction

Despite the success of the previous experiments, the main phenomena happening inside the water droplets of the microemulsion, critical for the interconnected macroporosity generation, such as the way macromolecules assemble within the colloidal solution (sol) and the phase separation evolves, are still not completely understood. In this sub-chapter, combination of Cryo-SEM and EDS is shown as a viable methodology to provide the answers for the MICROSCAFS[®] formation inside the emulsion water droplets.

4.2.2. Experimental

4.2.2.1. Cryo-Scanning Electron Microscopy

Cryo-SEM images and EDS data were obtained using a high-resolution scanning electron microscope with X-Ray Microanalysis and Cryo-SEM experimental facilities, namely a JSM 6301F microscope, an INCA Energy 350 EDS spectrometer and an ALTO 2500 cryo-transfer system.

Aliquots from the reaction medium were taken at various stages of the MICROSCAFS[®] synthesis and rapidly cooled (by inserting them into sub-cooled nitrogen), then transferred under vacuum to the cold stage of the preparation chamber. The samples were subsequently broken and coated with Au/Pd by sputtering for 45 s before being placed into the SEM chamber and analyzed at a temperature of $-150\text{ }^{\circ}\text{C}$.

4.2.2.2. Further Characterization

A MSZ 5600 optical microscope (KRÜSS) was used to study the evolution of the emulsion and particle sizes during the different stages of the synthesis, as well as to evaluate the MICROSCAFS[®] size, shape and maturity (stiffness qualitatively assessed by punching or tearing with the point of a needle).

SEM images and EDS data were obtained using a Phenom ProX G6 benchtop SEM (ThermoScientific) with the aim of assessing the dried MICROSCAFS[®] morphology, including internal porosity. A 15 nm layer of gold-palladium was sputtered on the

samples before observation using a turbomolecular pumped coater Q150T ES (Quorum Technologies).

4.2.3. Results and Discussion

The ST and STH MICROSCAFS® synthesis protocol, described in 4.1.2.1, is herein divided into three stages, represented by the optical microscopy images of Figure 1. Stage 1 consists of the simultaneous preparation of the emulsion and of the precursors colloidal solutions (sol), Stage 2 (embryonic stage) starts with the incorporation of the sol into the previously prepared emulsion, and Stage 3 starts after the addition of the ammonia (NH_4^+) solution and ends when the MICROSCAFS®, in the gel form, are formed. The dried MICROSCAFS® were observed by SEM. Samples for cryo-SEM observation were prepared by taking an aliquot at these three different stages (Figure 4.33) and rapidly freezing it through immersion in liquid nitrogen, which was also complemented with EDS to study the chemical elemental composition at specific reaction times and locations in the samples (Table 4.6).

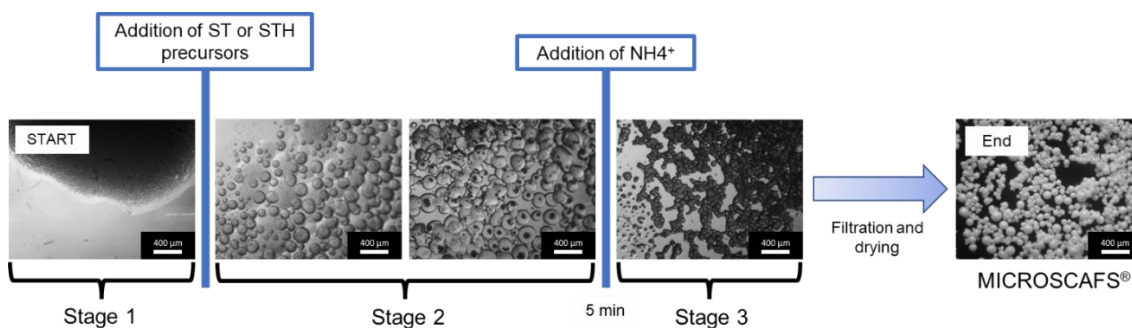


Figure 4.33. Different stages of the MICROSCAFS® synthesis process, observed by optical microscopy. Scale bar = 400 μm.

Table 4.6. EDS atomic concentrations of the different regions of the sample by cryo-SEM.

Cryo-SEM Image Region	Stage of the Synthesis	Atomic Concentration, %					
		C	O	Si	Cl	Ti	Hf
E1	Stage 1: Emulsion stage	92.8	7.2	-	-	-	-
E2		9.8	90.2	-	-	-	-
H1	Stage 1: Pre-hydrolysate (precursors colloidal solution, before adding to the emulsion)	35.2	46.5	14.8	-	3.5	-
H2		36.4	47.7	13.0	0.5	2.4	-
EH1	Stage 2: After addition of the pre-hydrolysate to the emulsion (embryonic stage)	24.4	43.1	24.1	-	8.4	-
EH2		26.7	48.2	21.6	-	3.5	-
EH3		29.7	65.6	2.9	1.1	0.2	0.5
EH4		96.4	3.6	-	-	-	-
EH5		29.8	60.1	6.4	1.4	1.5	0.8
EH6		19.8	73.4	5.1	-	0.9	0.8
G1	Stage 3: After addition of the ammonia solution to catalyze the gelation (final stage)	21.5	72.3	4.7	-	1.5	-
G2		94.8	5.2	-	-	-	-
G3		24.5	67.6	5	1.4	1.1	0.4
G4		92.8	7.2	-	-	-	-

The SE detector micrograph shows the topography of the W/O emulsion, the first step of the microsphere's synthesis process. As expected, the W/O emulsion displays water droplets rich in oxygen (ca. 90 at%) within the oil phase (decalin) of the emulsion. This latter one is rich in carbon (ca. 93 at%) (Figure 4.34a, regions E2 and E1, respectively).

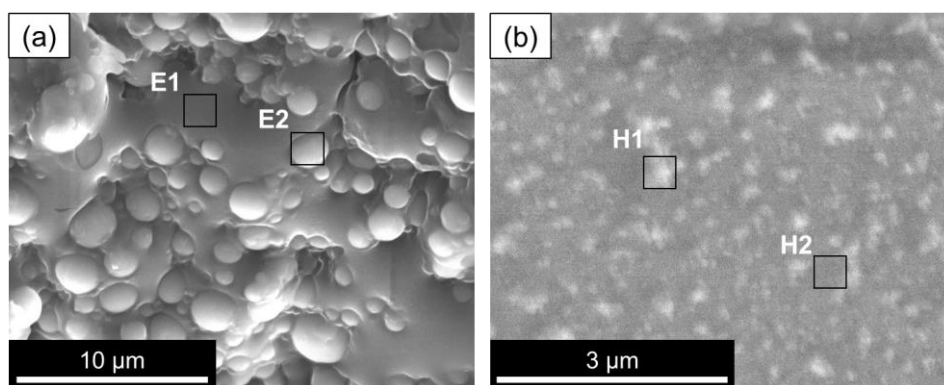


Figure 4.34. Cryo-SEM images of (a) W/O emulsion and (b) ST pre-hydrolysate (Stage 1).

In parallel to the emulsion, the pre-hydrolysate, a sol made from the metal precursors, such as TEOS, GPTMS, and TiPOT, was also observed by cryo-SEM. Figure 4.34b, in the BE mode, exhibits a silica–titania sol before being added to the emulsion, displaying oligomeric clusters represented by the whitish regions. The greyish regions (H2) also display the presence of Si and Ti, slightly less, however, than the whitish regions (H1), as well as some Cl due to the hydrolysis catalyst (HCl) employed in the synthesis. Also, in Figure 4.34b, the content of Ti is slightly higher compared to that of Si ($Ti/(Si + Ti) = 19\%$ in region H1 versus 16% for the darker region H2).

The addition of the pre-hydrolysate to the emulsion leads to some destabilization, namely droplet (aqueous phase) coalescence, which acts as a template for the MICROSCAFS® round shape. A sample of the aqueous phase of the emulsion, collected in the beginning of Stage 2, was observed by cryo-SEM in the SE mode. It is essentially composed of the added sol but a bit more diluted (lesser content of carbon atoms in both regions, EH1 and EH2) than the pre-hydrolysate, which confirms that the pre-hydrolysate (silanols, Si-OH) migrates to the water droplets of the emulsion due to its affinity with water. Also, the clusters (EH1) are found to increase in size, and they become richer in Si and Ti atoms, and poorer in C atoms, revealing the progress of hydrolysis and condensation reactions. As time proceeds, polymerization of silicate species occurs: first, it is the polymerization (condensation reactions) of monomers and oligomers containing Si-OH and Ti-OH groups to form particles and clusters (observed in Figure 4.35a) with Si-O-Si and Si-O-Ti bonds. This releases by-products such as alcohol and water. Second, further growth of the agglomerates and clusters occurs, as well as their linking into chains, and third, formation of networks that extend throughout the liquid medium proceeds, resulting in a gel. Since TiPOT is more reactive than the Si precursors employed, the polymerized clusters (condensation products, region EH1), which probably have higher molecular weight than the starting oligomers, are found to be richer in Ti atoms than the neighboring region EH2. Region EH1 of Figure 4.35a, shows an agglomerate of clusters exhibiting a $Ti/(Si + Ti) = 26\%$, while region EH2 exhibits $Ti/(Si + Ti) = 14\%$.

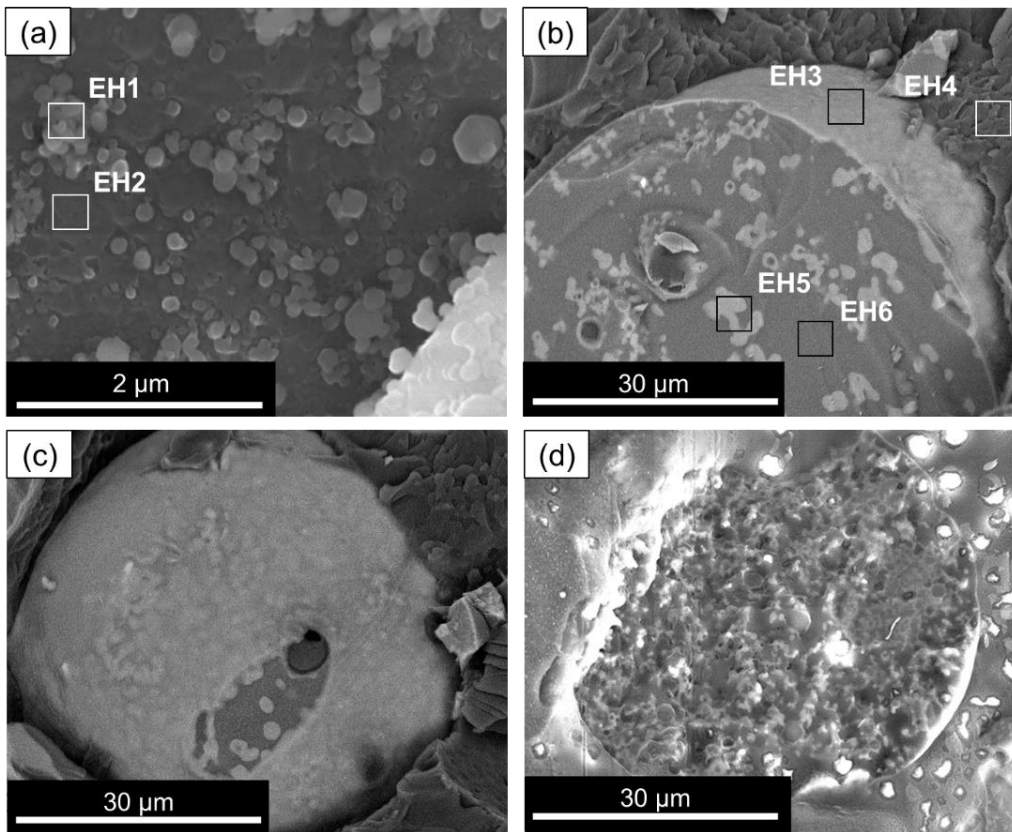


Figure 4.35. Cryo-SEM images of (a) ST oligomer clusters in the water phase, (b) STH MICROSCAFS[®] (cross-section) in the embryonic stage (BE mode), (c) STH MICROSCAFS[®] in the embryonic stage (BE mode), (d) ST MICROSCAFS[®] (cross-section) in the embryonic stage (SE mode) (Stage 2).

Figure 4.35b to d show microspheres in their embryonic stage taken at the end of Stage 2. The oligomeric clusters, present in the aqueous phase of the emulsion, are shown to accumulate at the water/oil interfaces (Figure 4.35b, region EH3, displaying the following relative atomic %: 80% Si, 6.6% Ti, 13.5% Hf), possibly to reduce the surface energy, explaining the presence of the thin layer that wraps the microspheres. It should be noted that this thin layer remains and is visible at the dried MICROSCAFS[®] (Figure 4.36, arrow). This is followed by the formation of polymerized skeleton domains by condensation reactions (Figure 4.35b, region EH5, displaying the following atomic % for an STH composition: 73.6% Si, 17% Ti, 9.2% Hf). The regions around these skeleton domains (Figure 4.35b, region EH6) are richer in oxygen, which reveals the presence of an aqueous phase around them, but also containing Si, Ti, and Hf atoms, probably oligomers or polymerized fractions of lower molecular weight (M_w) compared to that of the skeletons (Figure 4.35b, region EH5). This reveals the early occurrence of phase separation between the

water-rich phase and the polymerized fractions. With time, these oligomers or polymerized fractions of lower Mw join the formed skeletons, increasing the polymerized skeleton fraction within the microsphere, which grow by gelation, concomitantly with phase separation, until the microspheres attain their final morphology (Figure 4).

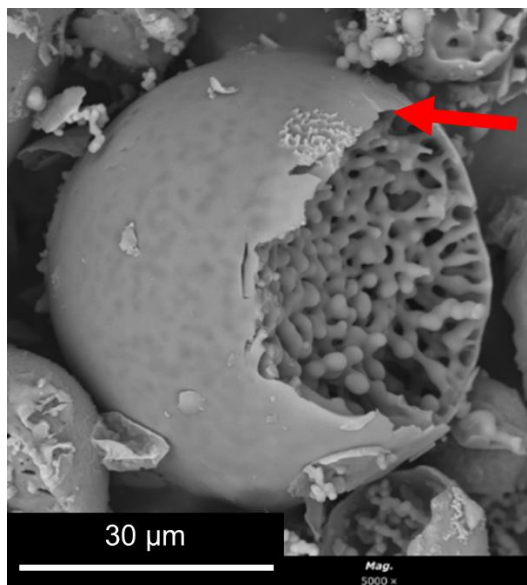


Figure 4.36. Example of a MICROSCAFS® final morphology.

Region EH4 shows that the zone involving the embryonic microspheres is richer in carbon, like region E1 in Figure 4.34a, confirming that the microspheres migrate to the oil phase once they start to form, surrounded by decalin (oil phase). In some cases, chlorine atoms are detected, which originate from the hafnium precursor or eventually from the pre-hydrolysis catalyst employed, HCl.

The addition of ammonia is found to catalyze the gelation process. Figure 5 shows wet gel MICROSCAFS® particles, after ammonia addition (Stage 3) for the ST composition (region G1, displaying particles with a relative atomic % of 76% Si and 23% Ti) and STH (region G3, displaying particles with a relative atomic percentage of 76.5% Si, 16% Ti and 6.5% Hf). The content of oxygen is relatively high (ca. 72%) in regions G1 and G3, which reveals that water from the initial aqueous phase and

resulting from polycondensation is entrapped inside the microspheres, namely in the water-rich phase, formed by phase separation.

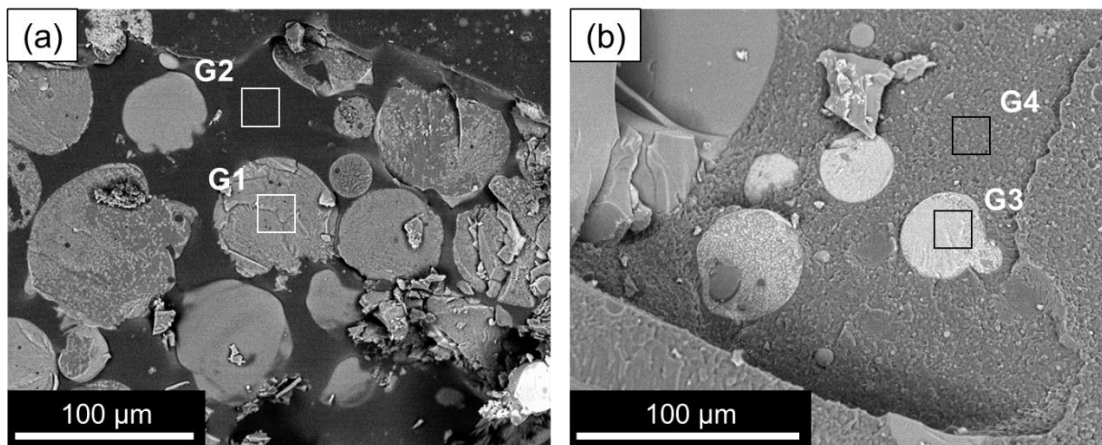


Figure 4.37. Cryo-SEM images of (a) ST and (b) STH MICROSCAFS[®] after the addition of ammonia (Stage 3).

Again, it is shown that the formed microspheres are in the oil phase (Figure 5, regions G2 and G4) since these zones are rich in carbon and sparse in oxygen, similar to the oil phase of the emulsion (Figure 4.34, region E1).

The water entrapped inside the microspheres is removed by drying/heat treatment after the microspheres are collected, filtered, and washed at the final stage of the MICROSCAFS[®] synthesis procedure.

With the help of the cryo-SEM characterization, the following mechanism is proposed for the formation of the multi-oxide MICROSCAFS[®] (Figure 4.38):

Step 1: the pre-hydrolyzed metal oxide precursors (sol) migrate to the water phase agglomerated droplets of the emulsion with the formation of oligomeric clusters (Figure 4.38a).

Step 2: accumulation of the oligomers at the water–oil interface, either by migration or kinetically trapping, and formation of a nanometric outer layer prior to the development of the internal interconnected gel skeleton, isolating the internal water/oligomer system from the outside (oil phase) and preventing particle coalescence (Figure 4.38b).

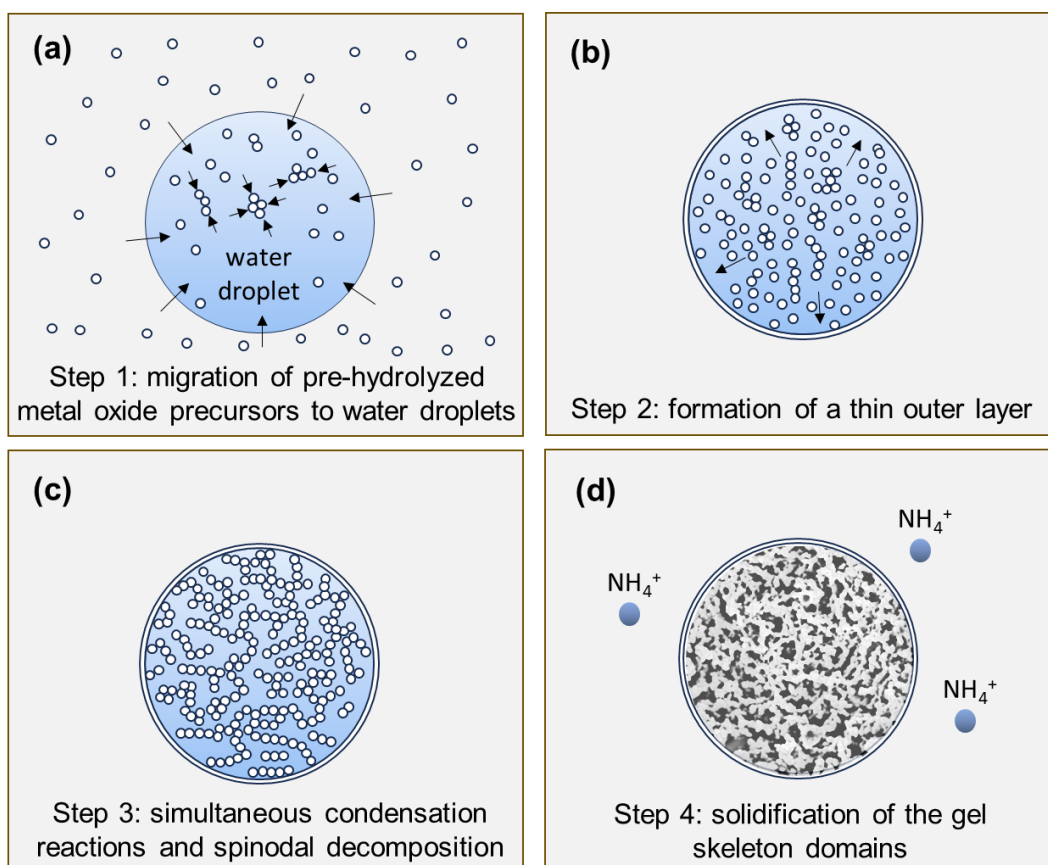


Figure 4.38. Formation mechanism of the multi-oxide MICROSCAFS®.

Step 3: condensation reactions lead to the formation of Si-O-Si, Si-O-Ti bonds at the expense of Si-OH and Ti-OH, with the formation of Si- and Ti-rich skeleton domains and their separation from the water phase inside the droplets (Figure 4.38c), typically by spinodal decomposition.

Step 4: concomitant phase separation and gelation with the system quickly maturing after the addition of the ammonia catalyst, producing the final MICROSCAFS® with interconnected macroporosity (Figure 4.38d). The typical mesoporosity observed in the MICROSCAFS® arises mainly from the binding of oligomeric clusters, forming the skeleton domains, while interconnected macroporosity is due to the phase separation process by spinodal decomposition. The size of the oligomeric clusters affects the size of the mesopores and can be influenced by the pH of the reaction medium, temperature, or the use of specific surfactants, such as the amphiphilic

Pluronic® P123. Post-synthesis procedures, based on solvent exchange, consist of another alternative.

It was demonstrated in the previous chapters that by changing the synthesis parameters, namely precursor content, temperature, pH, etc., it is possible to obtain either smaller or larger interconnected porosity and different particle sizes [39,42]. This is in line with the formation mechanism previously shown, where kinetics (hydrolysis and condensation reactions) and thermodynamics phenomena simultaneously occur. Also, the formation of a shell outside the system provides a more controlled, stable, and favorable environment inside the water droplets for the thermodynamics phenomenon (phase separation by spinodal decomposition) to occur. Phase separation onset and gelation times are therefore more controlled, allowing the fine tuning of the final porosity and particle sizes by changing the synthesis parameters.

4.2.4. Conclusion

Cryo-SEM complemented by EDS, SEM and optical microscopy proved to be an effective way to study the sol-gel chemistry of ST and STH compositions at their first stages, as well as the phase separation phenomenon which occurs in parallel, for the generation of multi-oxide microspheres with interconnected macroporosity. Highly magnified images of the emulsion that serves as a template for the MICROSCAFS® generation were observed, providing insight in the way the emulsion evolves during this synthesis. Oligomers were shown to homogeneously form within the aqueous phase (agglomerated droplets) of the emulsion and accumulate at the water-oil interface, explaining the presence of the thin layer that typically wraps the MICROSCAFS®. This was followed by formation and growth by gelation of skeleton domains, concomitantly to phase separation, until the microspheres achieve their final interconnected macroporous morphology. Cryo-SEM was essential to gain the first insight into the generation process of the MICROSCAFS®, elucidating their formation mechanism, proving to be critical for the optimization and development of advanced materials with tailored microstructures.

Chapter

5

Solar light-driven photocatalytic
water purification using
multicomponent oxide
MICROSCAFS®

The following chapter is based on the peer-reviewed article:

M. Vale, B.T. Barrocas, R.M.N. Serôdio, M.C. Oliveira, J.M. Lopes, A.C. Marques, Robust Photocatalytic MICROSCAFS® with Interconnected Macropores for Sustainable Solar-Driven Water Purification, Int J Mol Sci 25 (2024) 5958. <https://doi.org/10.3390/ijms25115958>.

5.1. Introduction

Water pollution is one of the biggest ecological problems that humanity currently faces. Synthetic dyes are used in many industries, such as textile processing, pharmaceutical sector, and food production, and approximately 80% of the resulting wastewaters are released untreated into the environment [196].

Water remediation is then one of the priorities in present-day scientific research. Among the explored methods for this purpose, heterogeneous photocatalysis offers many advantages, such as low cost, high flexibility of the process, the use of natural energy sources, relatively low quantity of required catalyst and, depending on the photocatalyst nature, high physical stability and recyclability of the materials employed, which make it an environmentally friendly technique [197–199]. However, the typical nanometric size of the photocatalysts, when used unsupported, in the powder form, makes complex their removal after the reaction, which is a significant drawback of this technique, being currently among the major limitations for the application of photocatalysis in a real-life scenario.

One solution for facilitating the photocatalysts recovery is their immobilization, preferably by grafting, into inert supports of relatively greater proportions. Binderless processes enable to overpass issues regarding the decrease of reactive sites due to hydrophobic effects and low surface area that result from organic or inorganic binders [200]. They are also preferred to achieve stable supported photocatalysts.

Undoped TiO₂ NPs, such as Aeroxide P25, is still a viable photocatalyst in today's standards, due to its low cost and high commercial availability. TiO₂ NPs have been supported in multiple materials like biochar [201], silica spheres [38], natural clays [202], cellulose nanofibrils [203], poly(methyl methacrylate) (PMMA) [204] and polyvinyl alcohol (PVA) films [205], and fly ash [206] to degrade MO. Additionally, TiO₂ aerogel was deposited over silica-coated bacterial nanocellulose scaffolds with fast photocatalytic degradation of methylene blue using UV-Vis light in a continuous flow reactor [207].

The majority of reported photocatalytic experiments is still made in batch conditions, which have some drawbacks if a real-life application is envisioned, like finite volume and non-continuous processing. Seldomly reported, the photocatalysts

are susceptible to mechanical stress and eventual fracture caused by the stirring in the batch reactor, generating smaller particles and higher surface area, which improves the photocatalytic performance in a false way, and jeopardizes the claimed easy removal of the photocatalysts after a test. Also, porosity data, like specific surface area and pore diameter, are not properly discussed or even totally or partially missing in some papers in the literature [208–216], neglecting possible synergies and effects granted by the catalytic supports, in what regards e.g. mass transfer. Concerning the particle size, most of the reported microspherical supports are usually very small ranging from 0.5 to 3 μm [212–215,217–219] which may impose problems and extra complexity and costs in a real-life application, in what regards the set-up and recovery aspects.

Lucchini et al. [203] have employed a continuous-flow reactor design, with total recirculation to a tank, consisting of a cylindrical PMMA cell topped by a quartz window, where the simulated sunlight impinges at a constant irradiance. The reactor chamber was filled with a cellulose nanofibrils (CNF)-based monolith loaded with synthesized TiO_2 NPs for the degradation of MO and paracetamol in liquid solution, which were made to circulate in a tube system connected to the bottom of the chamber and the tank. Then, in a previous study reported by Marques et al. [38], it was applied the same reactor design and procedure using photocatalytic silica microspheres, instead of a CNF monolith. These silica microspheres, namely S MICROSCAFS[®], were for the first time applied as supports for synthesized Trizma[®] functionalized TiO_2 NPs. Their inorganic nature provides them thermal and chemical stability.

In this chapter it is studied, in detail, the effect of pore and particle sizes of photocatalytic MICROSCAFS[®], in batch and continuous flow-type reactors, on the photocatalytic degradation of MO in aqueous solution (10 mg/L). ST MICROSCAFS[®] with variable sizes and porosity were loaded with well-known, commercial TiO_2 NPs using a simple binder-less process in which the NPs were at first physically entrapped inside the porosity of the MICROSCAFS[®], forming a layer on the surface and inner pores of the full particle, followed by a covalent binding promoted by heat treatment. A similar preparation was followed in a previous work, including additional gold NPs, but, contrary to the present work, only addressed a batch

reactor for photocatalysis experiments [220]. Moreover, a new kinetic model for the flow reactor is herein proposed, and the solar light-driven degradation of MO using the photocatalytic MICROSCAFS® is simulated using the proposed model and compared with experimental batch results. Finally, the MO degradation is followed by LC-HRMS/MS to identify and characterize its by-products, thus providing a deeper understanding of the degradation process.

5.2. Experimental

5.2.1. Preparation of the photocatalytic MICROSCAFS®

Four different ST MICROSCAFS® were prepared and studied in this work using the procedure explained in chapter 4.1.2.1. Table 5.1 lists the four different samples used in this chapter and corresponding variable synthesis parameters.

Table 5.1. MICROSCAFS®' synthesis parameters, which suffered variation.

Sample acronym	Volume of GPTMS (mL)	Volume of Span® 80 (mL)	Mass of Pluronic® P123 (g)
P-	10.4	6.0	0
P0 (reference)	13.8	6.0	0
P+	17.3	6.0	0
S-	13.8	7.7	2.3

Sample “P0” followed the procedure as described and was considered the reference in this chapter. Samples “P-” and “P+” were synthesized using lower (-25%) and higher (+25%) volume of GPTMS than the reference, respectively. Sample “S-” was synthesized using a higher amount of Span® 80 (+1.7 g) together with another surfactant, Pluronic® P-123 (HLB: 8, Sigma-Aldrich, USA), both added to the water phase of the emulsion.

All the four samples of MICROSCAFS® were used as a scaffolding or support to commercial Aeroxide® P25 Degussa TiO₂ NPs (Acros Organics, USA) using a wet impregnation method [38], forming the photocatalytic MICROSCAFS®. First, all the MICROSCAFS® were heat-treated for 30 min at 900 °C, to confer an inorganic nature to the support material and provide higher mechanical, chemical and thermal

stability during the final application. These particles are indicated by the acronym “HT” throughout this chapter. Sample S-/HT was sieved and the fraction between 25-45 μm of diameter was collected and used in the subsequent studies. All the other samples were sieved $<354 \mu\text{m}$ to ensure the absence of any agglomerate of MICROSCAFS[®] in the tests. Then, 372 mg of MICROSCAFS[®] were placed in 2.1 mL of a 62.5 mg mL⁻¹ aqueous dispersion of P25 TiO₂ NPs in a small glass vial, targeting at a loading of 26wt% relative to the total weight of MICROSCAFS[®] and P25 TiO₂ NPs. This dispersion was submitted to ultrasound sonication for 2 minutes, dried at 60 °C for 15 h, and finally subjected to a heat treatment at 500 °C for 1 hour. TiO₂ NPs are driven into the pores of the MICROSCAFS[®] by capillary action, and chemical bonds (e.g. Si-O-Ti) are formed during the subsequent heat treatment. These particles are indicated by the acronym “P25” throughout this chapter.

5.2.2. Characterization

The morphology and the elemental composition of the MICROSCAFS[®] were evaluated through SEM images and EDS data acquired using a Phenom ProX G6 benchtop SEM (ThermoScientific, USA). Internal porosity was observed on purposely broken particles. Prior to observation, a 15 nm gold–palladium layer was sputtered onto the samples using a turbomolecular pumped coater Q150T ES from Quorum Technologies (Lewes, UK). The MICROSCAFS[®] diameter was measured manually using the ImageJ software as previously reported [42]. The TEM images of the P25 TiO₂ NPs were obtained using a microscope (H8100, Hitachi, Japan) operating at 300 kV.

Dried, TiO₂ NPs loaded and unloaded MICROSCAFS[®] porosity was assessed by MIP using an Autopore IV 9500 Mercury Porosimeter (Micromeritics, USA) and N₂ adsorption/desorption isotherms using an ASAP 2010 adsorption analyzer (Micromeritics, USA), in the same fashion as described in chapter 4.1.2.2.

The chemical structure of the samples was assessed through Fourier-transform infrared spectroscopy (FTIR) using a Spectrum Two spectrometer (PerkinElmer, USA) coupled with a universal attenuated total reflectance (ATR) accessory (PerkinElmer, USA). The spectra were obtained at 4 cm⁻¹ resolution, and 8 scans of data accumulation.

The UV-Vis diffuse-reflectance spectra (UV-Vis DRS) was measured by a V-750 UV-Vis spectrophotometer (JASCO, USA) equipped with an integrating sphere and converted in absorption units (F_{KM}) using the Kubelka-Munk function, which is related to the diffuse reflectance by the expression $F_{KM}(R)=(1-R)^2/2R$ [221–223].

5.2.3. Photocatalytic tests

The photocatalytic MICROSCAFS® were tested in a batch and continuous flow reactor. The batch reactor was a 100 mL jacketed vessel connected to a water recirculatory bath at 19 °C. In each batch test 50 mg of photocatalytic MICROSCAFS® were dispersed in 50 mL of a MO (Fisher Chemical, USA). aqueous solution with an initial MO concentration of 10 mg/L and pH of 7, under magnetic stirring. The system was kept in the darkness for 1 hour, to study possible adsorption, following by illumination during 2 hours with a solar lamp. For this purpose, a Newport 94011A-ES LCS-100 solar simulator (Newport Corporation, USA) was employed, with a 100 W Xe lamp with reflector (Newport Corporation, USA). This solar simulator includes an AM1.5G air mass filter which provides Class A spectral performance based on current applicable standards. The solar lamp's distance from the solution's surface was adjusted to correspond to the intensity of 1 sun (1000 W/m²). The simulated solar light entered the reactor through a quartz window of 4 cm diameter (12.57 cm²) situated at the top of the reactor. Aliquots of 1 mL were taken every 20 minutes during the dark phase and every 15 minutes during the light phase and centrifuged. The MO solution concentration at each specific time was then determined by measuring the absorbance at 464 nm using a JASCO V-750 UV-Vis spectrophotometer (JASCO, USA). All the experiments were conducted for three replicates at 19 °C, and the mean results were reported.

Additionally, photocatalytic experiments (in batch) were carried out using distinct radical scavengers. Ethanol (EtOH, ≥99.8%, Fisher Chemical, USA) was employed as •OH scavenger in the photocatalysis reaction, ethylenediaminetetraacetic acid disodium salt dihydrate (EDTA, Panreac, Spain) was chosen as h⁺ quencher, and p-benzoquinone (BQ, Merck, Germany) was added to the system as O₂^{•-} scavenger. The MO photocatalytic experiments were performed using the same conditions described above while using separately 0.5 mM of each scavenger.

The flow tests were carried out using a set-up built to allow a continuous flow with recirculation to an intercalated tank (Figure 5.1).

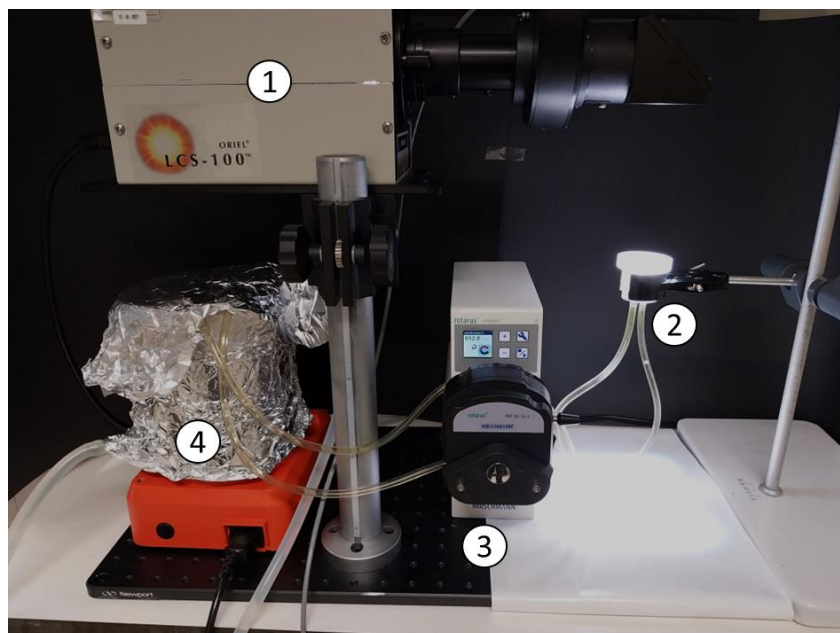


Figure 5.1. Continuous flow reactor with total recirculation to a tank. 1 – Solar simulator; 2 – Sample chamber (solar reactor); 3 – Peristaltic pump; 4 – MO solution stirred tank.

The photoreactor employed was adapted from the one previously reported [38,203]. This reactor comprises three separate acrylic pieces that, when assembled, form a chamber (solar reactor) where the photocatalytic MICROSCAFS[®] sample can be placed, and the solution can circulate throughout the sample. The top of this chamber displays a quartz window of 2 cm of diameter (3.14 cm²) of diameter on which the solar light will impinge, and the back contains the inlet and outlet of the circulating solution. 200 mg of photocatalytic MICROSCAFS[®] were inserted and compressed inside this chamber, around ~1.5 mm thick, resulting in a chamber volume of 0.47 cm³. A filter paper (1318 from FILTER-LAB[®], Spain) was placed at the back of the chamber, where the inlet and outlet of the circulating solution were placed, to prevent the MICROSCAFS[®] from exiting the chamber. The reactor was connected to a tank with two 78 cm long TYGON[®] hoses (Hirschmann Laborgeräte, Germany), and 200 mL of MO solution (10 mg/L) were made to circulate at a constant flow at 10 mL/min with the help of a Rotarus[®] standard 50 peristaltic

pump (Hirschmann Laborgeräte, Germany) during the tests. The reactor was exposed to a constant 1000 W/m^2 (1 sun) at the exterior surface of the quartz window over 6 hours, after 1 hour of darkness, to account for any possible adsorption. The concentration of the pollutant was checked every 30 minutes by measuring the absorbance at 464 nm of 1 mL MO aq. solution aliquots. The same solar simulator and reference solar cell from the batch tests were used. All the experiments were conducted for three replicates at $25 \text{ }^\circ\text{C}$, and the mean results were reported.

In the stability tests, six consecutive cycles were performed, by simply replacing, in the stirred tank, the degraded MO solution by a new one at 10 mg/L, and the corresponding MO degradation was recorded to examine the stability and reusability of the photocatalytic MICROSCAFS[®] at a catalyst/pollutant mass ratio of 23, pH of 7, under solar light (1 sun) exposure and $25 \text{ }^\circ\text{C}$.

5.2.4. Kinetics modeling of the photocatalytic performance

The kinetics for MO photocatalytic degradation was analyzed in batch and flow conditions. By assuming that it follows a first order transformation, with the reaction rate given by $r = kC_A$, the MO concentration evolution with the reaction time (t) can be described by Equation 5.1:

$$C_A = C_{A0}e^{-kt} \quad (5.1)$$

where k is the kinetic rate constant, C_A is the MO concentration inside the reactor at time t under light irradiation, and C_{A0} is the initial MO concentration before irradiation. The batch reactor is known to allow a good efficiency of mass transfer from the fluid to the surface of the solid photocatalyst, where the transformation takes place; for heterogeneous catalysis to occur, the MO pollutant dissolved in the liquid medium must contact and be adsorbed on the active sites of the photocatalyst. The constant k was determined by fitting Equation 5.1 to the experimental points of C_A as a function of time, using the sum of the squares deviations minimization method.

To model the experimental MO photodegradation system using a continuous flow set-up (continuous flow with recirculation to an intercalated tank), the following process flow diagram, shown in Figure 5.2, was employed, exhibiting the small continuous flow chamber (solar reactor) (2) with complete recirculation. The reactor, exposed to the solar simulator (3), is connected to the stirred tank (4) with 200 mL of volume in a closed circuit pumped by a peristaltic pump (1) at a constant volumetric flow rate of 10 mL/min.

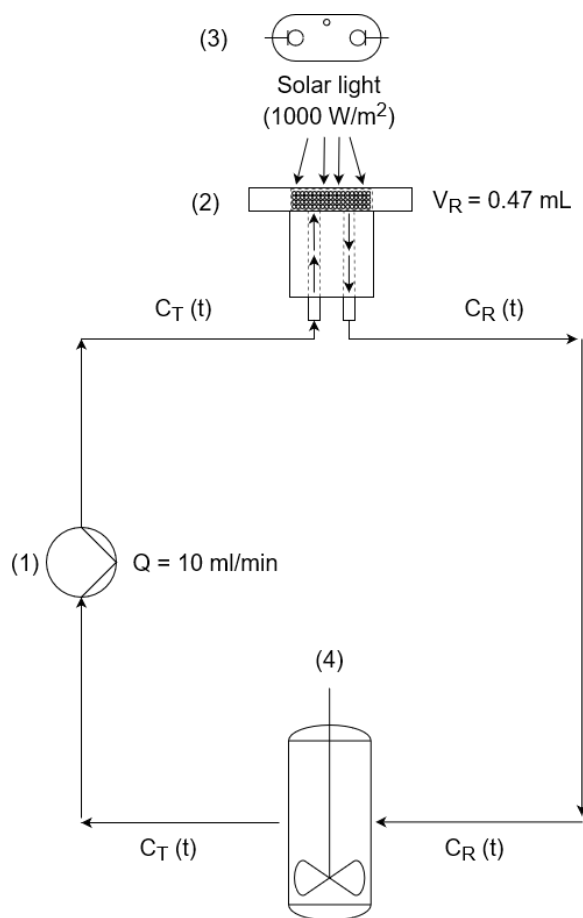


Figure 5.2. Process flow diagram of the flow reactor. (1) Peristaltic pump; (2) continuous flow chamber (solar reactor, side view) containing the photocatalytic MICROSCAFS®; (3) solar simulator (Xe lamp), and (4) stirred tank.

Homogeneous conditions were considered inside the solar reactor (chamber), which is a reasonable approximation when the conversion of the reactant, for each pass of a volume element of fluid through the reactor, is low. The inlet concentration of the solar reactor is the same as the outlet concentration of the tank (C_T(t)), while

the inlet concentration of the tank is equal to the outlet concentration of the solar reactor ($C_R(t)$), both changing over time.

After the peristaltic pump starts, the MO solution enters the reactor and flows throughout the photocatalytic MICROSCAFS[®] interparticle spaces and internal pores. It was considered that the flow solar reactor works in differential conditions, at constant flow and almost negligible concentration gradient inside, since the pollutant solution quickly flows through it (~ 2.8 s as mean residence time). The pollutant fluid stream leaving the reactor is mixed with the solution that remains behind in the dark, in the stirred tank (Figure 5.2).

The mass balance equations describing the transient behavior of the reactor, and of the tank where no reaction occurs, are given by Equations 5.2 and 5.3 respectively.

$$V_R \frac{dC_R(t)}{dt} = QC_T(t) - QC_R(t) - kC_R(t)W \quad (5.2)$$

$$V_T \frac{dC_T(t)}{dt} = QC_R(t) - QC_T(t) \quad (5.3)$$

where V_R is the volume of the flow reactor in L, V_T is the tank volume in L, Q is the volumetric flow in L/min, $C_R(t)$ is the MO concentration in the reactor (mg/L), $C_T(t)$ is the MO concentration in the tank (mg/L) and W is the mass of the photocatalytic MICROSCAFS[®] placed inside the reactor (200 mg). The kinetic rate constant, k , is the variable parameter of this mathematical model.

The simultaneous resolution (integration) of Equations 5.2 and 5.3 was accomplished using the Euler method, allowing the determination of the evolution of $C_R(t)$ and $C_T(t)$. Several integrations were carried out until the best value of k is reached (k_{app}), yielding the lowest sum of the squared deviations between the experimental and model $C_T(t)$ values.

5.2.5. Analytical methods for photocatalysis by-products determination

The transformation products (TPs) formed during the photocatalytic degradation of MO were analyzed by LC-HRMS/MS. The MO solutions were analyzed on an ultra high performance liquid chromatograph (UHPLC) Elute system interfaced with a QqTOF Impact II mass spectrometer equipped with an ESI source, operating in the negative mode (Bruker Daltonics, Germany). Chromatographic separation was carried out under gradient conditions using a RF-C18 Kinetex column 100 Å (150 mm × 2.1 mm, 2.6 µm particle size, Phenomenex). Detailed settings on LC-HRMS/MS settings were described in a previous work [220]. The TPs peak areas (A) were normalized with respect to MO at $t = 0$ minutes (A/A_0), and their variation as a function of irradiation time is shown in 3D bar graphs. The TPs are identified by HRMS based on their accurate m/z values released as deprotonated molecules ($[M-H]^-$), considering the accuracy and precision of the measurement parameters such as error (ppm) and mSigma. The molecular formulas were validated by extracting the ionic chromatograms from the raw data, and accurate mass isotopic patterns and fragmentation paths were evaluated, supporting the respective proposed chemical structures. Detailed equipment specifications and experimental protocol for calibration, data acquisition and processing are described elsewhere [224].

5.3. Results and discussion

5.3.1. Characterization of the MICROSCAFS® before and after heat treatment and photocatalyst (P25 TiO₂ NPs) loading

ST MICROSCAFS® composition are herein shown to be a versatile type of materials that can be obtained with high reproducibility via a relatively simple two-step, fast and low energy, adapted sol-gel process. Their final characteristics, like pore and particle diameter, and mechanical properties have been recently reported to be easily tuned by changing the synthesis parameters [42]. In this subchapter, the effect of pores size and particles diameter on the photocatalytic performance of TiO₂ NPs loaded MICROSCAFS® was studied.

All the MICROSCAFS® particle size distributions before and after calcination (HT) are shown in Figure 5.3, obtained from the SEM images present in Figure 5.4.

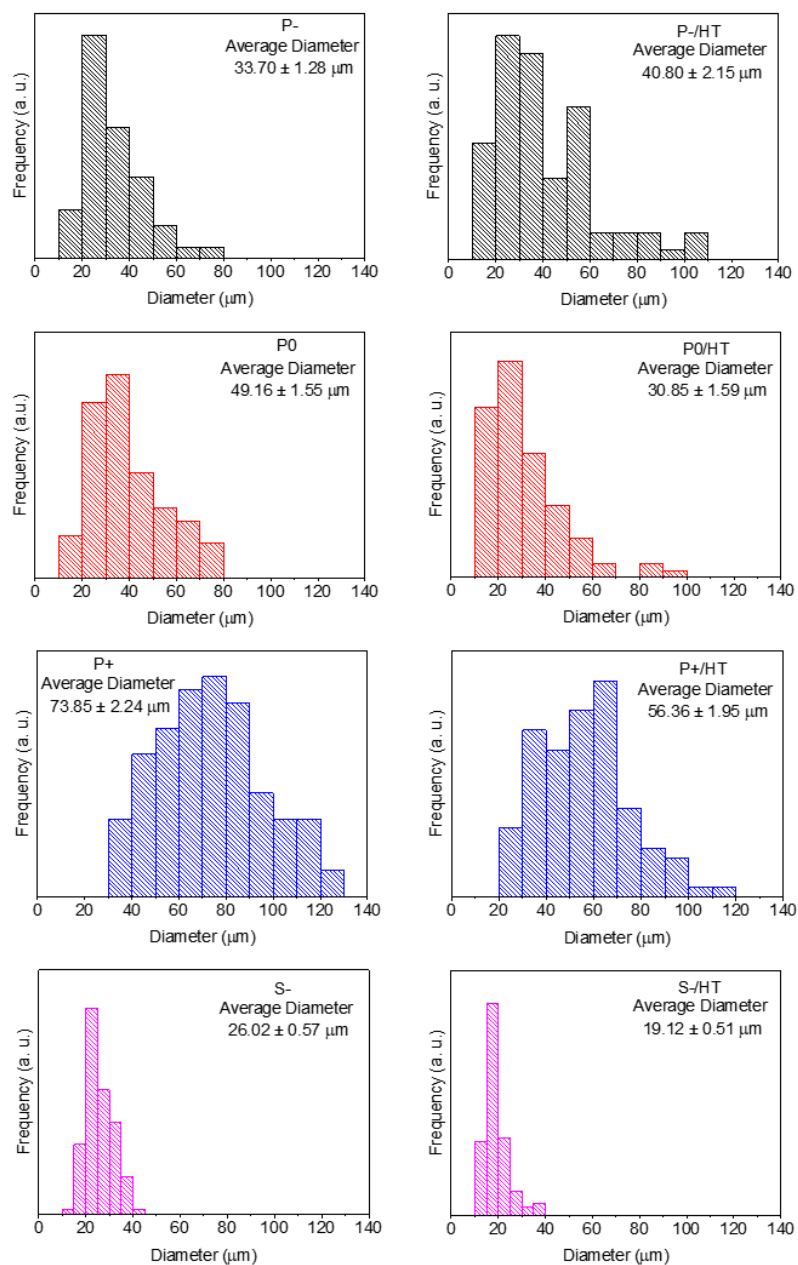


Figure 5.3. Particle size distributions of the ST MICROSCAFS® before and after HT (calcination) at 900 °C during 30 min.

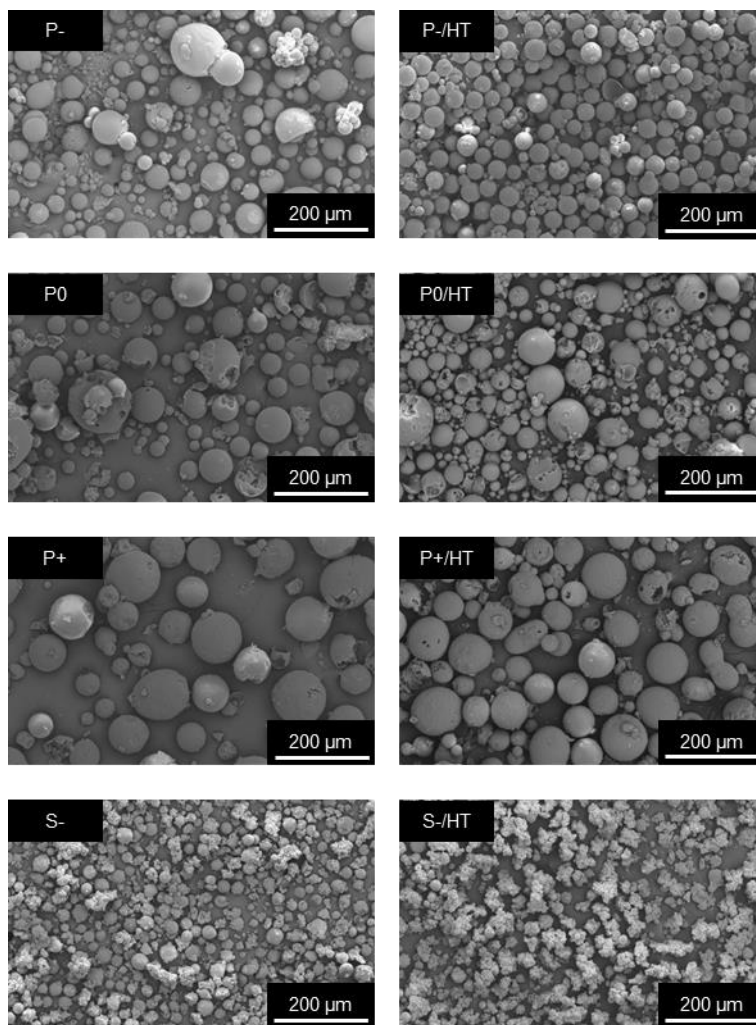


Figure 5.4. SEM images of the MICROSCAFS® used for the particle size distributions, before (left column) and after (right column) being heat treated at 900 °C for 30 minutes.

The average particle diameter tends to increase with the quantity of GPTMS, and the span or the dispersion was found to decrease, particularly when using +25% GPTMS (Table 5.2).

Table 5.2. Particle size distribution data of the treated and non-heat-treated MICROSCAFS®.

Sample acronym	D (0.1), μm	D (0.5), μm	D (0.9), μm	Span
P-	20.16	29.61	50.56	1.03
P0	22.58	33.99	65.36	1.26
P+	43.68	72.29	107.52	0.88
S-	19.02	24.50	34.13	0.62
P-/HT	18.62	34.29	72.86	1.58
P0/HT	16.24	26.23	50.99	1.32
P+/HT	31.88	56.12	83.87	0.93
S-/HT	14.29	17.90	25.07	0.60

GPTMS precursor slows the condensation reaction of the titania and silica precursors due to steric hindrance caused by the relatively big aliphatic chain. This might provide a steady formation of siloxanes and Si-O-Ti bonds inside the water droplets of the emulsion, producing particles with lower size dispersions. The diameters of S- particles were mostly within the range of 20 to 40 μm , which was expected due to the sieving procedure applied in this particular sample. As expected, after the first HT, most of the samples decreased in size, with sample P- being the only exception. Despite a non-linear change in the average diameter, the particle diameter mode did not change, meaning that the HT had no significant effect on its size, and the difference in the distribution might be due to sampling heterogeneity. This fact is linked to the lower porosity of the P- samples, demonstrated below, so that there are less pores to collapse during calcination.

Optical microscopy photographs of the P25 TiO_2 NPs loaded and unloaded MICROSCAFS® used in this work are presented in Figure 5.5. A concentration of P25 TiO_2 NPs equal to 23 wt% was achieved in most samples, except for sample P-/HT/P25, where such concentration corresponds to 25 wt%, being very close to the nominal concentration at 26 wt%. The different colors of the MICROSCAFS® after the HT are a direct result of the internal porosity of the samples, dictated by the different content of TEOS and GPTMS (Figure 5.5). Spheres with smaller pore sizes, namely P- sample, exhibit a darker color because of the entrapment, inside the pore network, of generated gases resulting from organics degradation.

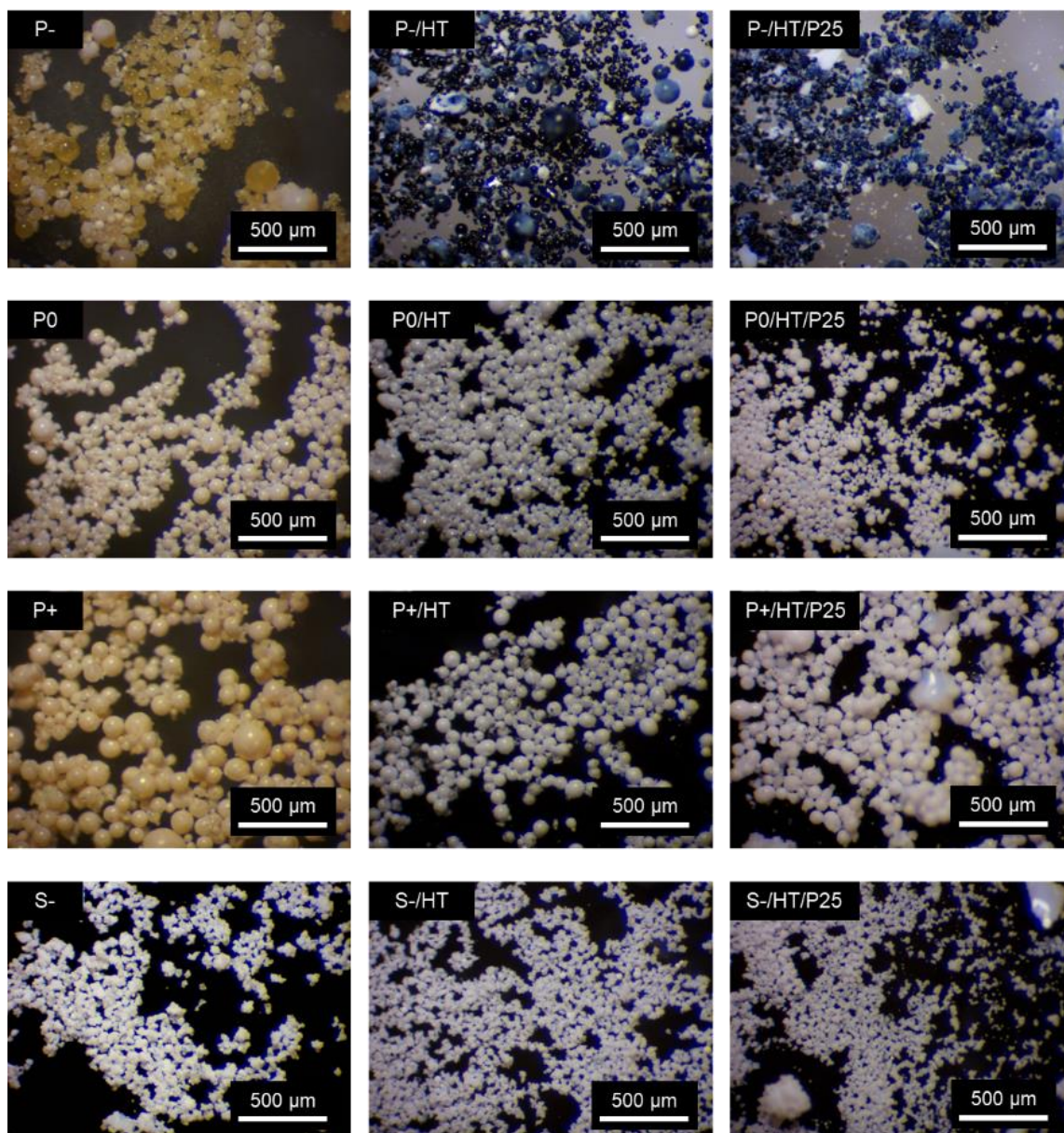


Figure 5.5. Optical microscopy photographs of the MICROSCAFS® in three subsequent stages: 1 (first column) – dried MICROSCAFS®; 2 - (second column) MICROSCAFS® after being heat treated at 900 °C for 30 minutes; 3 (third column) – MICROSCAFS® after being loaded with the P25 TiO₂ NPs.

The porosity exhibited by the dried, heat-treated and TiO₂ NPs loaded MICROSCAFS® was analyzed using SEM, MIP (Figure 5.6) and N₂ adsorption-desorption isotherms (Figure 5.7).

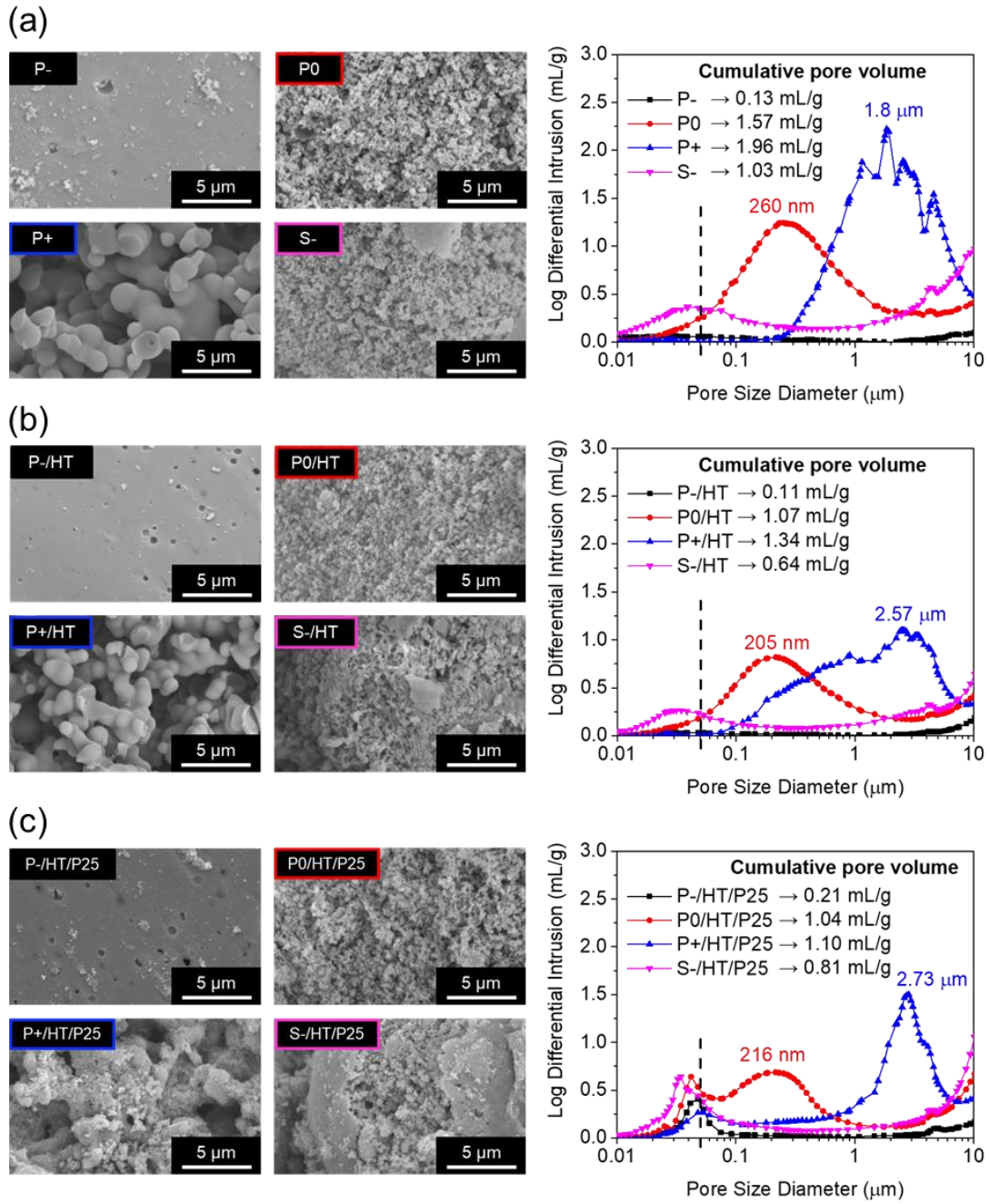


Figure 5.6. SEM images of the internal porosity (left), and corresponding MIP pore size distributions (right) of the MICROSCAFS® (a) dried at 45 °C, (b) heat-treated at 900 °C and (c) loaded with P25 TiO₂ NPs and heat-treated at 500 °C.

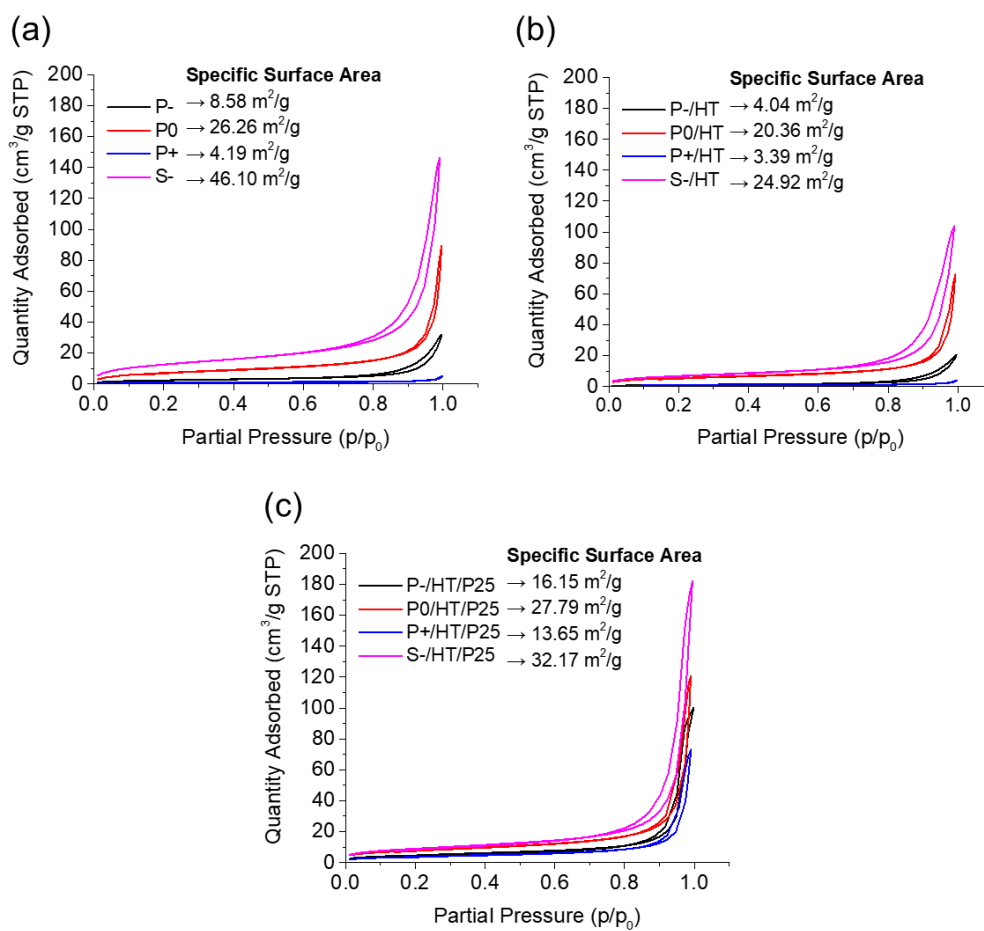


Figure 5.7. N₂ adsorption-desorption isotherms of the MICROSCAFS® (a) dried at 45 °C, (b) heat-treated at 900 °C and (c) loaded with P25 TiO₂ NPs.

A higher quantity of GPTMS precursor yielded spherical particles with significantly greater macropore size and cumulative pore volume (Figure 5.6a), which means that the domains of the separated phases, oxide-based xerogel-rich phase (containing Si-O-Si, Si-O-Ti and Ti-O-Ti bonds) and water-rich phase, are larger. The presence of GPTMS simultaneously affected the phase separation and condensation processes, without requiring any phase separation inducer [42]. The N₂ adsorption isotherms of all the dried MICROSCAFS® were of type III (IUPAC classification) further corroborating, in the present case, their macroporous morphology, exhibiting specific surface areas (SSA) that ranged from 4.19 to 46.10 m²/g (Figure 5.7a). Samples S- and P0 exhibit the largest SSA, suggesting the presence of mesopores, which is in agreement with the findings from MIP (Figure 5.6a). They were both prepared with the same amount of GPTMS, however sample S- shows less

macropores, probably because of the larger amount of surfactants (10 g), which might contribute to the disruption of the phase separation due to lower interfacial tension, breaking the skeleton particles as the macropores domains were forming. The presence of Pluronic® P123 is also responsible for the formation of mesopores. Additionally, this sample is found to consist of smaller particles with a rough and fragmented morphology (Figure 5.4 and Figure 5.5). As expected, after the HT at 900 °C for 30 min, the pore diameters and cumulative pore volumes, as well as the SSA, decreased in almost all the samples, suggesting the occurrence of some sintering or pore collapse, however, the presence of meso and macropores is retained (Figure 5.6b). On the other hand, the loading with P25 TiO₂ NPs resulted in the appearance of a peak at the mesoporosity range, between 30 and 50 nm (Figure 5.6c), and an increment of the SSA (Figure 5.7c) and did not significantly affect macroporosity. The employed P25 TiO₂ NPs have an average diameter of about 27.4 ± 0.9 nm (Figure 5.8) so that the interparticle spaces contribute to the mesoporosity exhibited by the TiO₂ NPs loaded MICROSCAFS®.

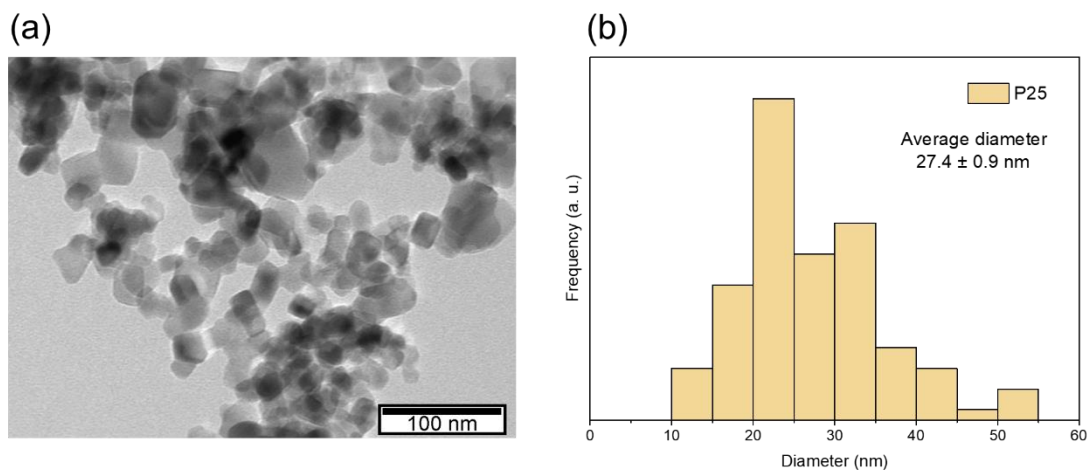


Figure 5.8. TEM image of the P25 TiO₂ NPs (a) and their respective particle size distribution (b).

As for elemental composition, EDS data in Table 5.3 revealed that P+ sample is the one with a Si and Ti at. % closer to the nominal Si and Ti precursor molar ratio of 80/20.

Table 5.3. EDS atomic concentration data of the MICROSCAFS®. Ti/Si is the atomic % ratio.

Sample acronym	EDS atomic concentration (%)			Ti/Si
	O	Si	Ti	
P-	67.37 ± 0.59	25.68 ± 0.73	6.94 ± 0.31	0.272 ± 0.017
P0	67.53 ± 0.44	25.04 ± 0.60	7.43 ± 0.31	0.298 ± 0.018
P+	63.95 ± 0.35	27.94 ± 0.27	8.11 ± 0.10	0.290 ± 0.002
S-	62.00 ± 0.35	34.4 ± 0.2	3.6 ± 0.2	0.106 ± 0.005
P-/HT	61.22 ± 0.23	30.50 ± 0.08	8.28 ± 0.26	0.272 ± 0.009
P0/HT	60.32 ± 0.03	30.38 ± 0.07	9.29 ± 0.05	0.306 ± 0.002
P+/HT	60.25 ± 0.19	30.31 ± 0.21	9.43 ± 0.14	0.311 ± 0.006
S-/HT	60.24 ± 0.20	32.97 ± 0.07	6.78 ± 0.005	0.206 ± 0.005
P-/HT/P25	70.26 ± 0.84	12.51 ± 0.57	17.17 ± 0.89	1.40 ± 0.11
P0/HT/P25	69.05 ± 0.30	16.52 ± 0.29	14.44 ± 0.30	0.88 ± 0.03
P+/HT/P25	71.17 ± 0.26	18.00 ± 0.75	10.84 ± 0.73	0.62 ± 0.07
S-/HT/P25	74.31 ± 0.57	17.79 ± 0.61	7.89 ± 0.27	0.45 ± 0.03

Also, it is clear that MICROSCAFS® present higher Ti/Si at. % ratios after loading with the P25 TiO₂ NPs, as expected. Interestingly, P+ sample, the one exhibiting large interconnected macroporosity, has less loading of TiO₂ NPs, given by the lower Ti/Si at. % ratio, compared to P- and P0 samples, for the same loading conditions. This might be due to the facilitated flow of the TiO₂ NPs dispersion throughout the large pores, and therefore, less clogging of the pores, which may be beneficial for the wastewater flow throughout the MICROSCAFS® in the photocatalytic tests.

The FTIR spectra of the MICROSCAFS® after drying at 45 °C (Figure 5.9a and Figure 5.9b) contain multiple bands characteristic of the oxides network, but also of other organic compounds from the reactional mixture, including some residues of precursors (alkoxides), surfactant and decalin. The band at 1267 cm⁻¹ is characteristic of the epoxy group of the GPTMS [163,225], however the bands at 906 and 850 cm⁻¹, ascribed to C–O and C–O–C stretching of the GPTMS' epoxy are hard to detect because they might be hidden by the intense band at 915 cm⁻¹ (Si–OH, or Si–O– from Si–O–Ti units). After the heat treatment at 900 °C (Figure 5.9c and d), the

organic groups completely disappeared. The intensity of the band at around 934 cm^{-1} , which includes the silanol (OH groups) vibrations, becomes lower, probably because of the OH elimination during heat treatment and some degree of phase separation, i.e. Si-O-Ti conversion to Si-O-Si and Ti-O-Ti links. An intense band at 1065 cm^{-1} is related to Si-O-Si asymmetric stretching vibration. After loading with P25 TiO₂ NPs (Figure 5.9e and f) the $I(\text{Ti-O-Ti}, 450\text{ cm}^{-1})/I(\text{Si-O-Si}, 1065\text{ cm}^{-1})$ ratio increased in all samples (Table 5.4), as expected, meaning that higher amount of titania is present in the photocatalytic MICROSCAFS[®]. Again, the higher the pore size (P+/HT/P25), the lower the amount of Ti (TiO₂), corroborating the EDS results (Table 5.2).

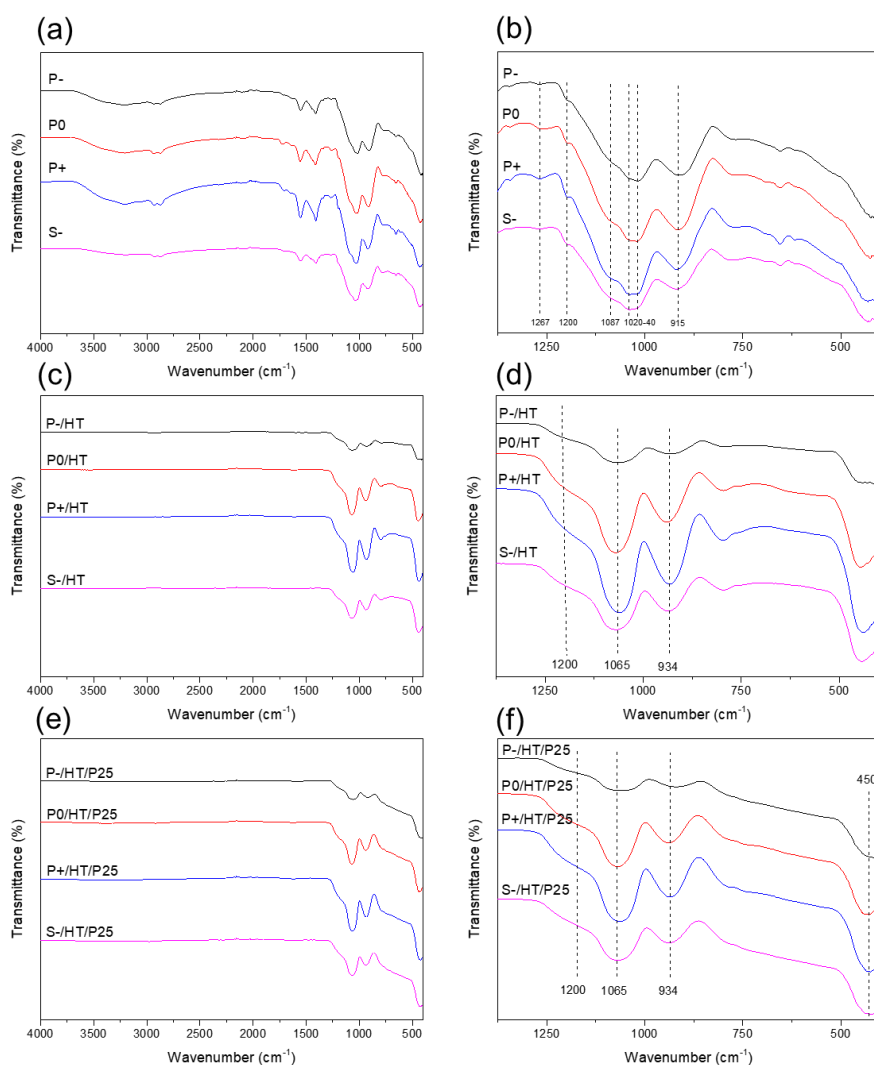


Figure 5.9. ATR-FTIR spectra of all the MICROSCAFS[®] (a, c and e) and it's respective zoom between 1500 and 400 cm^{-1} (b, d and f).

Table 5.4. FTIR band intensity ratio $\frac{I_{Ti-O-Ti}}{I_{Si-O-Si}}$.

Sample	$\frac{I_{450\text{ cm}^{-1}}}{I_{1065\text{ cm}^{-1}}}$
P-/HT	1.04
P0/HT	0.80
P+/HT	1.28
S-/HT	1.20
P-/HT/P25	3.60
P0/HT/P25	1.60
P+/HT/P25	1.48
S-/HT/P25	1.87

5.3.2. Photocatalytic studies on the TiO₂ NPs loaded MICROSCAFS®

Photolysis of MO resulted in no degradation over the 2 hours of light exposure, whereas the photocatalytic P25 TiO₂ NPs (non-supported) were able to fully degrade the pollutant in the same period (Figure 5.10a). No adsorption was detected for the photocatalytic NPs, neither for the heat-treated unloaded MICROSCAFS®. Also, these latter ones exhibited no significant photocatalytic activity (Figure 5.10a).

Regarding the loaded MICROSCAFS®, photocatalytic degradation data using the batch reactor showed that overall, larger pores proved to be better, with sample P+/HT/P25 degrading 87% of the MO dye in 2 hours of exposure to simulated solar light (Figure 5.10b). Larger interconnected pores improved the accessibility and the diffusion of both the reactants and products to and from the active sites, speeding up the reaction and promoting the photocatalytic degradation of MO species.

The MO UV-Vis spectra had two major absorption bands, around 464 and 271 nm, which are from the aromatic ring in the MO molecule (Figure 5.10c) [226]. UV-Vis absorption spectra intensity at ~464 nm decreased as the reaction proceeded during light exposure, suggesting some degree of degradation. The characteristic orange color of the solution clearly faded over time with the exposure to the simulated solar light, proving the photocatalytic MICROSCAFS®'s efficacy (Figure 5.10d).

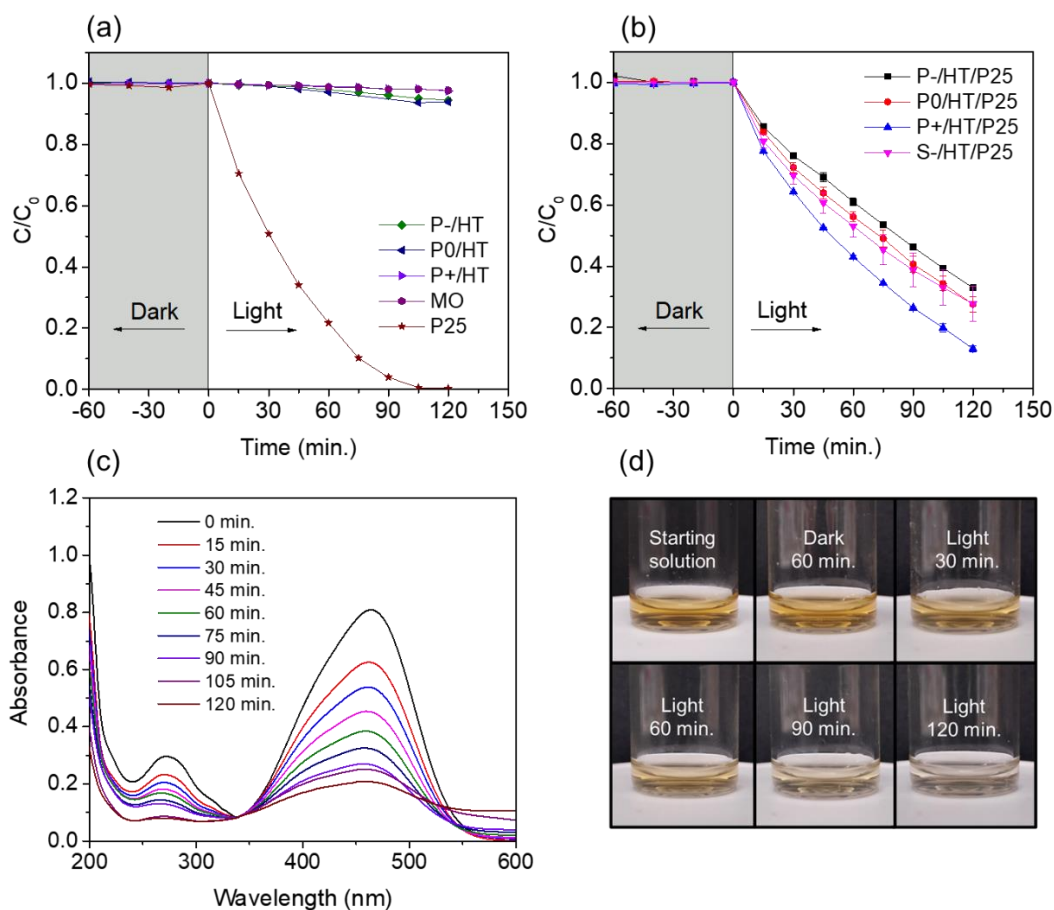


Figure 5.10. (a) Plots of C/C_0 versus time of the heat-treated unloaded MICROSCAFS[®], i.e. without photocatalyst (P-/HT, P0/HT and P+/HT), P25 TiO₂ NPs and photolysis of the MO dye; (b) Plots of C/C_0 versus time of the photocatalytic P25 TiO₂ NPs loaded MICROSCAFS[®]; (c) UV-vis spectra of MO solution aliquots taken during the light phase of a P+/HT/P25 experiment; (d) Photos of MO solution aliquots at the starting of the illumination and after 120 minutes when using the P+/HT/P25. Experiments done in batch conditions at 19 °C, pH = 7, mass(TiO₂ NPs)/mass(MO) = 23, 50 mL of 10 mg/L MO aq. solution, 50 mg of P25 TiO₂ NPs loaded MICROSCAFS[®] (11 – 12.5 mg TiO₂), irradiance = 1000 W m⁻² (1 sun).

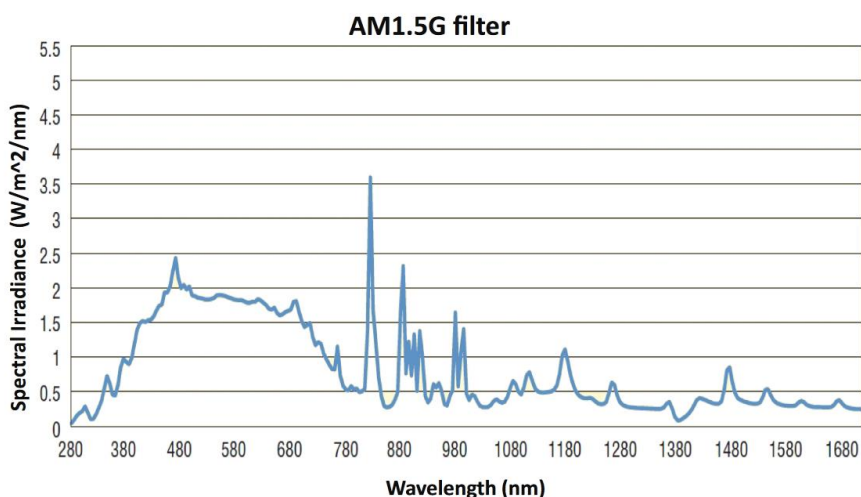


Figure 5.11. Spectral output of LCS-100 Solar Simulator with standard AM1.5G filter.

The presence of silica in the MICROSCAFS[®] hindered the absorption of the photocatalyst (Figure 5.12).

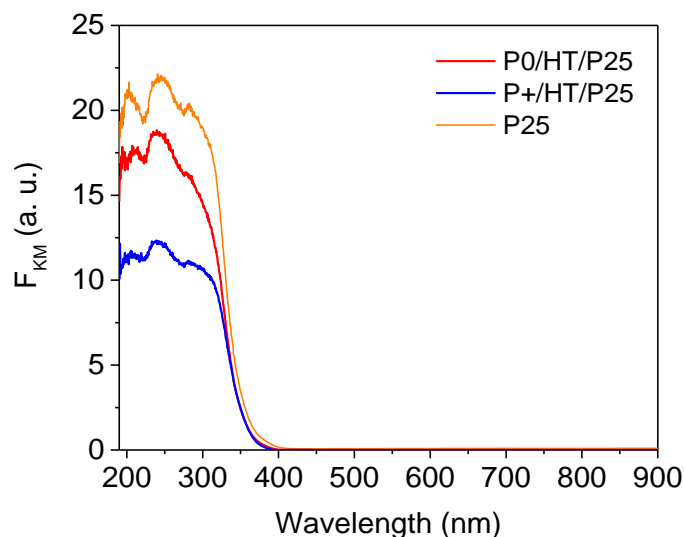


Figure 5.12. Kubelka-Munk transformed UV-Vis DRS absorption spectra of the P25 TiO₂ NPs loaded MICROSCAFS[®] and P25 TiO₂ NPs.

Its effect was higher for sample P+/HT/P25 sample which had the highest amount of Si atoms by EDS (Table 5.3). Silicon dioxide is known for its wide bandgap of 9 eV, which plays the effect of an energetic barrier for the solar radiation (in particular visible light), thus not generating excited electrons and holes and therefore no photocatalytic activity [227]. However, the photocatalytic activity exhibited by sample P+/HT/P25 was the highest demonstrating that other factors such as the presence of wider and interconnected pores, played an important role in the achievement of higher photocatalytic activities. The presence of pores has been reported to increase the absorbance of the light in aerogels [228]. In this case, it has been reported that the pore network traps the photons, which then diffuse over a few millimeters and thus increase the probability of the light to be absorbed. A similar effect might be happening with the reported MICROSCAFS[®]. Compared to a dense bead, the macroporous network extends the pathway of the photons, increasing their probability to be absorbed by TiO₂ NPs located in the inner surface of the pores, thus yielding higher photocatalytic activities. Regarding the tests in the

continuous flow reactor, the same parameters (pH, irradiance, temperature, and photocatalyst/pollutant mass ratio) were employed and indeed, the same tendency was observed as in the batch reactor: the greater the interconnected pores size (P+/HT/P25), the higher the pollutant (MO) degradation. MO suffers a 29% degradation within 6 hours (Figure 5.13a) using P+/HT/P25 as photocatalyst.

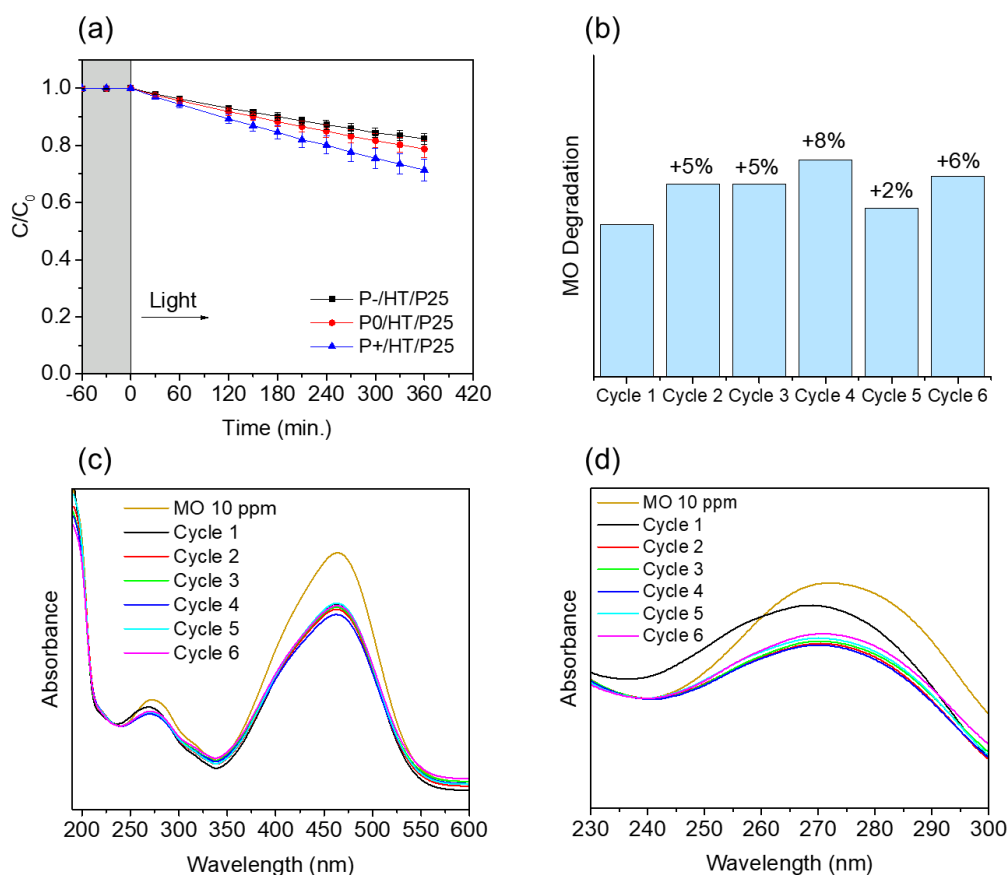


Figure 5.13. (a) Plots of C/C_0 versus time of the P25 TiO₂ NPs loaded MICROSCAFS® using a continuous flow set-up; (b) MO degradation evolution achieved for 6 consecutive cycles with solar light irradiation for 6 hours using sample P+/HT/P25; (c) UV-Vis spectra of the final MO solution after each cycle in the range of 190 to 600 nm; (d) UV-Vis spectra of the final MO solution after each cycle in the range of 230 to 300 nm. Experiments done in flow conditions at 19 °C, pH = 7, mass (P25 TiO₂ NPs)/mass (MO) = 23, 200 mL of 10 mg/L MO aq. solution, 200 mg of P25 TiO₂ NPs loaded MICROSCAFS® (46-50 mg TiO₂), volumetric flow = 10 mL min⁻¹, irradiance = 1000 W m⁻² (1 sun).

It should be noted that the reaction was significantly slower than that in the batch reactor, which is explained by the different reactor designs. First, the flow reactor allows for a much smaller exposure area (3.14 cm²) to solar light than the batch reactor (12.57 cm²). In the flow reactor, the pollutant solution passes under the

quartz glass, inside the chamber, going through the thin layer of porous photocatalytic MICROSCAFS® (Figure 5.14).

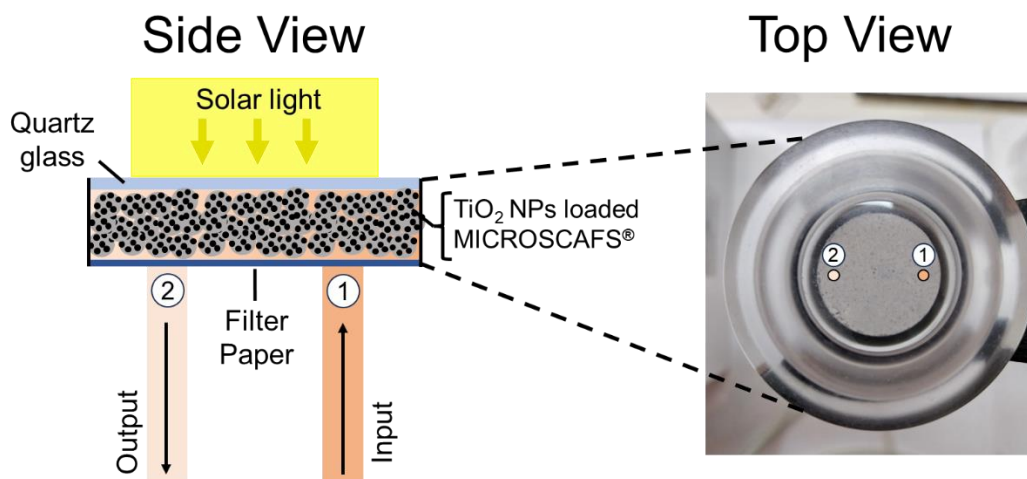


Figure 5.14. Side and top views of the continuous flow reactor's sample chamber. The arrows indicate the direction of the flow of the MO solution and the color it's concentration.

Despite the thin layer of MICROSCAFS®, of only 1.5 mm thickness, the particles at the top, closer to the quartz glass, are more exposed to the solar light than the particles beneath, whereas in the batch reactor, all the particles are constantly exposed to the light, in a free flow fashion. In contrast, in batch, all the MO solution is in permanent contact with the light and photocatalyst over the full extent of the reaction. Moreover, the fraction of the MO solution exposed to the solar light in the flow set-up, and therefore partially degraded, returns to the intercalated tank, that contains MO solution in a higher concentration. On the other hand, the continuous flow system is somewhat similar to a real case scenario, and greatly facilitates and enables the recyclability of the photocatalytic MICROSCAFS®, preserving their mechanical integrity during numerous cycles (does not involve stirring) and their easy removal/collection. Figure 5.15 shows samples P-/HT/P25 and P+/HT/P25 after a photocatalytic test in flow and batch set-ups.

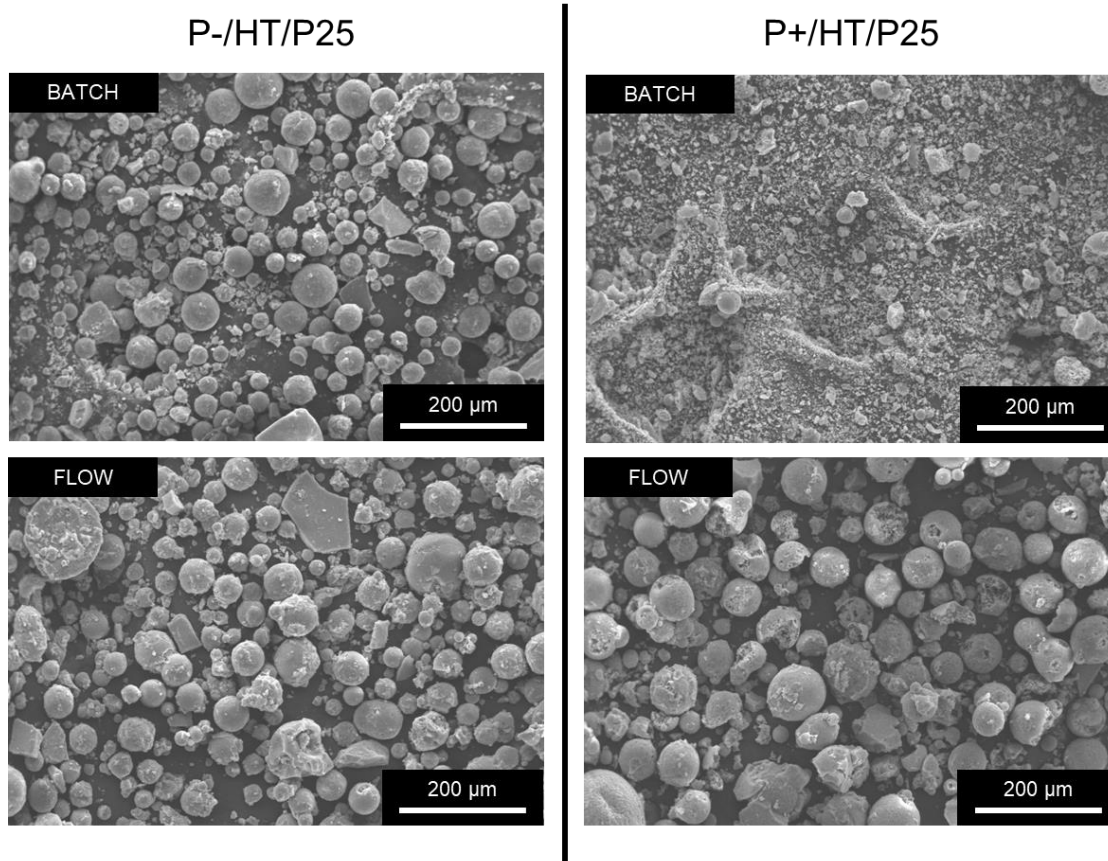


Figure 5.15. SEM images of the P-/HT/P25 (left column) and P+/HT/P25 (right column) photocatalytic MICROSCAFS® after one cycle in batch and in flow.

Compared to the SEM images of Figure 5.4, the denser (stiffer [42]) sample, P-/HT/P25, is fully preserved whatever the set-up employed for photocatalysis, whereas the largely porous P+/HT/P25 MICROSCAFS® are fully preserved after the continuous flow tests but tend to fracture when stirring at a high rate is applied. The higher compressibility, or flexibility, of the P+/HT/P25 spheres did not influence the result of the photocatalytic reaction because the same trend occurred both in batch and in flow. Sample S-/HT/P25 was not studied in the flow reactor due to its relatively small particle diameter, which clogged the filter employed in the experiment.

As observed in Figure 5.13b, the final degradation of MO with P+/HT/P25 increased slightly after the first cycle and stayed relatively stable during the subsequent five tested flow cycles. The UV-Vis absorbance spectra in Figure 5.13c and d were very similar from the 2nd cycle onward, whereas in the 1st cycle, not only the 271 nm band

absorbance is higher, but it is shifted to lower wavelengths, suggesting a (minor) release of TiO₂ NPs, probably those in excess and not covalently bonded to the MICROSCAFS® surface. Also, the lower MO degradation achieved in the 1st cycle might have been due to some congestion of the pores of the P+/HT/P25 sample (Figure 5.13b), which after the 1st cycle does not happen anymore due to the release of the NPs in excess. In this sense, a better flow throughout the MICROSCAFS® and more access to active sites is promoted, leading to the observed better performance after the 1st cycle. On the other hand, variability issues cannot be disregarded, and such difference in MO degradation for the various cycles could be simply within the error of the analyses. Finally, the flow reactor was more suitable for the recyclability studies than the batch reactor since the same particles stayed inside the reactor in every cycle without the need for any separation process, like centrifugation or filtration, which avoided the loss of some photocatalyst mass inherent to these separation processes.

5.3.3. Kinetic studies

The kinetics of MO degradation was assessed using a small laboratory batch reactor with stirring, in which the approximation to perfect mixing inside the reactor, is considered very reasonable. The MO concentration evolution with the reaction time (t) is fitted by Equation 5.1, stated in the experimental section of this chapter. The results of the corresponding adjustments are shown in Figure 5.16, where the quality of all the fittings reinforces the fact that the degradation of MO occurs according to a first-order reaction ($A \rightarrow B$).

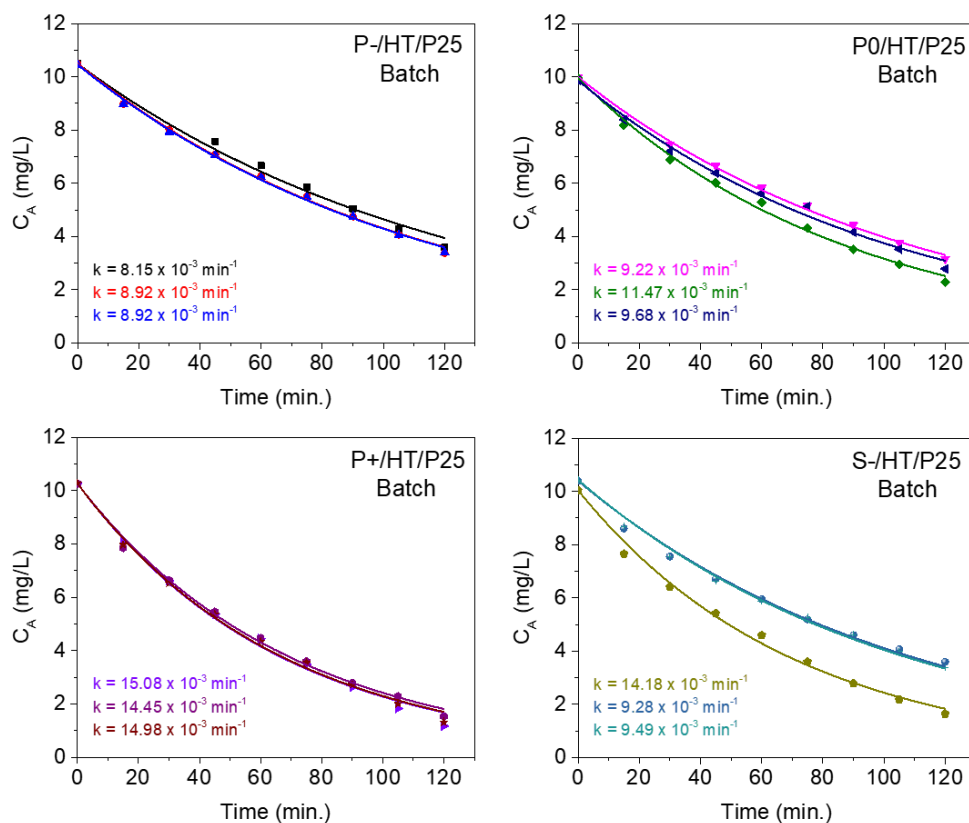


Figure 5.16. Adjusted kinetic models in batch using the photocatalytic MICROSCAFS® with different porosities and size. Kinetic rate constant values (k) are indicated for each case.

It is worth noting that the P+/HT/P25 sample shows the highest reproducibility among all the photocatalytic MICROSCAFS®. This is possibly due to the large pore size, which possibly enabled well-distributed and dispersed photocatalytic NPs and ensured a good flow of the pollutant solution, increasing the contact between active sites and pollutant species and avoiding the formation of concentration gradients.

Regarding the continuous flow set-up, whose diagram is shown in Figure 5.2, and taking into account the considerations well-described in the experimental section, the modeling and fitting of the MO concentration evolution with the reaction time (t) was carried-out, using Equations 5.2 and 5.3.

The best adjusted models of the flow reactor are displayed in Figure 5.17 in triplicate for the photocatalytic MICROSCAFS® with different porosities.

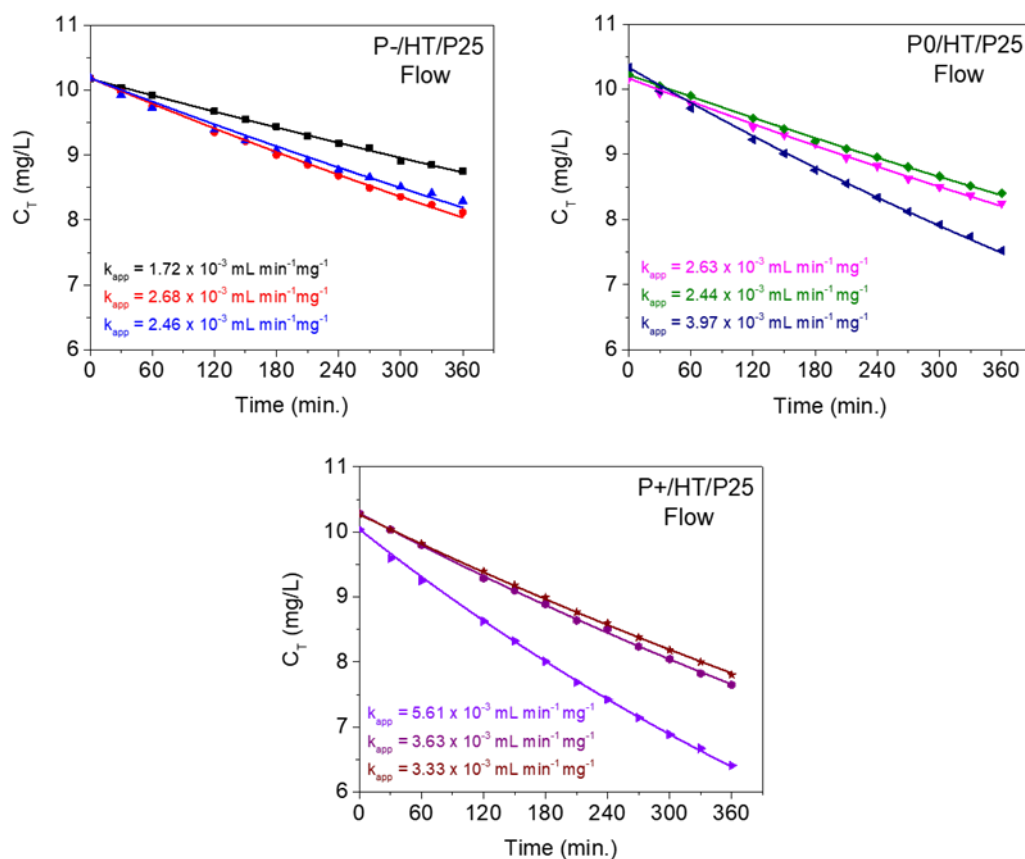


Figure 5.17. Adjusted kinetic models of the flow reactor using the photocatalytic MICROSCAFS® with different porosities, and a constant tank volume of 200 mL. Apparent flow (adjusted) kinetic rate constant values (k_{app}) are indicated for each case.

Table 5.5 lists the average kinetic rate constant values, obtained from experiments in batch conditions, and the average apparent flow (adjusted) kinetic rate constant values, obtained from experiments in flow conditions for the photocatalysts under study. The constant obtained from the batch reaction studies (min^{-1}) was multiplied by the reactor volume (50 mL) and divided by the mass of active phase (11.5 mg) to be comparable with the apparent flow kinetic rate constants (expressed in $\text{mL min}^{-1} \text{mg}^{-1}$). In this way the kinetic constants better characterize the activity of the catalyst.

Table 5.5. Average kinetic rate constants and apparent flow reactor rate constants of the photocatalytic MICROSCAFS®.

Sample acronym	Average kinetic rate constant k (mL min ⁻¹ mg ⁻¹)	Average apparent flow reaction rate constant k_{app} (mL min ⁻¹ mg ⁻¹)
P-/HT/P25	$(3.47 \pm 0.1) \times 10^{-2}$	$(2.28 \pm 0.3) \times 10^{-3}$
P0/HT/P25	$(4.40 \pm 0.3) \times 10^{-2}$	$(3.01 \pm 0.5) \times 10^{-3}$
P+/HT/P25	$(6.45 \pm 0.08) \times 10^{-2}$	$(4.19 \pm 0.7) \times 10^{-3}$
S-/HT/P25	$(4.99 \pm 0.7) \times 10^{-2}$	n. a.

The MO degradation graphs from the flow reactor modeling (Figure 5.17) clearly show that the adjusted model is able to describe very well the experimental data during the timeframe of the experiment (6 hours of reaction). In this case, the fitting process shows that the apparent velocity constant values, k_{app} , are lower than those (k) obtained at the batch experiment (Table 5.5), which is also in agreement with Figure 5.10b and Figure 5.13a.

Since the reaction in study is a photocatalytic heterogeneous transformation, the reactant has to be adsorbed onto the active sites of the solid surface of the photocatalyst and, simultaneously, the available light and effective irradiance at the solid surface is also essential for the reaction to proceed. There is probably a lower efficiency of mass transfer of the reactant from the fluid to the solid surface and a less favored interaction of the radiation with the active sites of the catalyst in the continuous flow set-up, when compared to the batch set-up. The photocatalytic MICROSCAFS® are densely packed inside the flow reactor chamber, whereas, in batch, they are free-flowing and well dispersed, facilitating their exposure to solar radiation. Also, the surface area exposed to the simulated solar light is much less than in the batch set-up. Thus, despite the benefit of the flow set-up for real-life applications, the observed reaction rate for the photocatalytic heterogeneous transformation is expected to be reduced, when compared to the batch set-up. A design optimization of the reactor targeting a larger surface area of exposure to solar light might approximate the flow reactor performance to that of the batch reactor.

A full degradation of the MO species present in solution was achieved for ca. 50 hours using the continuous flow set-up, which is slightly less than the model (Figure 5.18). This fact suggests that other effects not considered in the model might become

relevant, particularly the effect of MO solution volume, which is made to decrease along the experiment due to removing aliquots, to ca. 13% of the initial volume, and possibly some evaporation. Additionally, the circular shape of the reactor chamber might be less favorable than, for instance, the well-known tubular reactors, these latter ones promoting better contact between the solid photocatalyst and liquid pollutant solution. Therefore, the probability for concentration gradients generation inside the flow reactor chamber might be considerable. For longer reaction times these effects might be significant, having a cumulative effect.

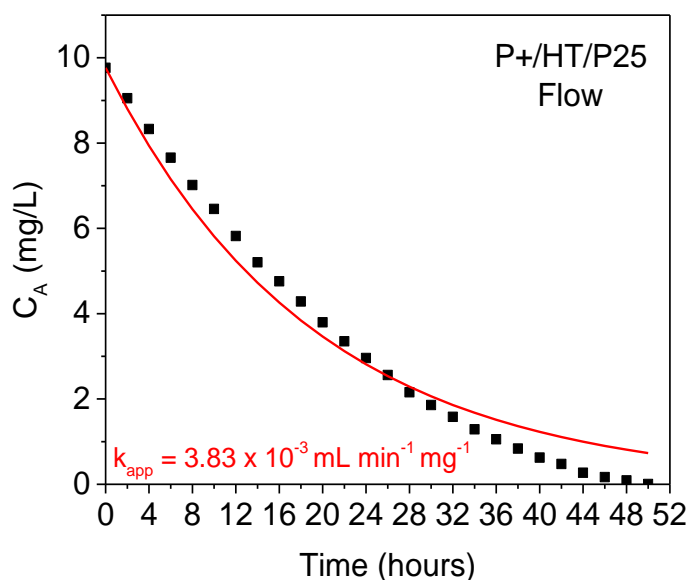


Figure 5.18. Adjusted kinetic model of a complete MO degradation using the continuous flow reactor.

Table 5.6 compiles various supported photocatalyst systems in the literature and the corresponding rate constant values factorized to the reactor volume and mass of the active phase. The relevant experimental conditions are described as well. It was only taken into consideration literature works where the photocatalytic MO degradation was carried out using supported TiO₂ NPs [38,201–206,229].

Table 5.6. Experimental conditions, MO degradation and kinetic rate constants (k or k_{app}) of supported TiO₂ photocatalyst – comparison of the present study with the literature.

Supported photocatalyst system	Radiation source	Reactor type and pH	Reactor volume and initial concentration of MO solution	Photocatalyst/pollutant mass ratio	MO degradation at 464 nm	k (batch) or k_{app} (flow) (mL min ⁻¹ mg ⁻¹)	Ref., year
P25 TiO ₂ NPs supported in SiO ₂ -TiO ₂ MICROSCAFS® (11.5 mg batch; 46 mg flow) (23 wt% loading)	Solar simulator Xe lamp, 100 W, 1000 W/m ² (1 sun)	Batch pH=7	50 mL, 10 mg/L	23	87% in 120 min.	$(6.45 \pm 0.08) \times 10^{-2}$	Present study
		Flow pH=7	0.47 mL, 10 mg/L	23	29% in 360 min.	$(4.19 \pm 0.7) \times 10^{-3}$	
Commercial anatase TiO ₂ (11 mg, 2-3 μm) supported in biochar (75% wt% loading)	Hg lamp, 500 W	Batch pH = 6.3	30 mL, 60 mg/L	6	~99% in 60 min.	1.39×10^{-1}	[201], 2023
Synthesized anatase TiO ₂ (66 mg) supported in SiO ₂ MICROSCAFS®, (22 wt% loading)	Solar simulator Xe lamp, 100 W, 1000 W/m ² (1 sun)	Flow pH=7	100 mL, 20 mg/L	33	30% in 375 min.	1.36×10^{-3}	[38], 2021
Synthesized anatase TiO ₂ (2 mg) supported on natural clays (~11 wt% loading)	Xe lamp, 500 W	Batch pH=n/d	20 mL, 10 mg/L	10	90% in 150 min.	1.20×10^{-1}	[202], 2019
Synthesized anatase TiO ₂ (19 mg) supported on cellulose nanofibrils (17 wt% loading)	Solar simulator Xe lamp, 100 W, 1000 W/m ² (1 sun)	Flow pH=7	100 mL, 20 mg/L	10	21% in 200 min.	5.79×10^{-3}	[203], 2018
P25 TiO ₂ (16 mg) supported in porous PMMA wafers (loading n/d)	UV-LED	Batch pH = n/d	60 mL, 10 mg/L	27	28% in ~30 min.	4.08×10^{-2}	[204], 2015
P25 TiO ₂ (50 mg) supported on fly ash (25 wt% loading)	Black light lamps, 320-440 nm	Batch pH=8.5	200 mL, 3.27 mg/L	76	50% in 170 min.	6.40×10^{-3}	[206], 2014
Anatase TiO ₂ layer (~9.8 mg) deposited on 500 nm SiO ₂ spheres, (10 wt% loading)	Xe lamp, 300 W	Batch pH=n/d	90 mL, 20 mg/L	5	90% in 120 min.	1.65×10^{-1}	[229], 2012
P25 TiO ₂ (10 mg) supported on a PVA film (loading n/d)	UV 300 nm lamps, 6x8 W, 90 ± 10 μW/cm ²	Batch pH=n/d	10 mL, 15 mg/L	67	~100% in 300 min.	1.30×10^{-2}	[205], 2012

It was found that the k_{app} achieved in the current work, for continuous flow experiments, was higher than that achieved for SiO₂ MICROSCAFS® ($(4.19 \pm 0.7) \times 10^{-3}$ vs. 1.36×10^{-3}) [38], even for a smaller photocatalyst/pollutant mass ratio (23 vs. 33). It is suggested that the small extra amount of TiO₂ already present in the SiO₂-TiO₂ MICROSCAFS® of the current work might contribute to a more efficient photocatalytic process, as well as the larger interconnected macropores which have a size distribution peaked at $\sim 1.95 \mu\text{m}$ (almost 20 times higher than the reported for SiO₂ MICROSCAFS®). Also, as an extra variable, SiO₂ MICROSCAFS® had been loaded with synthesized TiO₂ NPs (anatase) and not P25 TiO₂ NPs, contrary to SiO₂-TiO₂ MICROSCAFS® where P25 TiO₂ NPs were employed. Ljubas et al. have reported higher photocatalytic activity achieved by P25 TiO₂ than anatase [230]. Compared to a work which used a similar continuous flow reactor and cellulose nanofibrils supports [203], the MICROSCAFS® are still behind, possibly because of their lower transparency to the UV-Vis radiation. However, in what regards chemical and mechanical resistance and durability, MICROSCAFS®, due to their inorganic nature, are expected to display a better performance.

Notably, the present work fits the experimental photocatalytic behavior in flow using the equations for the specific employed continuous flow set-up, which is a more accurate methodology to calculate k_{app} , than using a batch reactor as a model. Another best practice of the present work is the type of solar source and conditions employed. The 1 sun AM 1.5G reference spectrum was used as standard for the photocatalytic tests in this work. Also, full experimental conditions under which the photocatalytic tests were carried out were revealed, with special attention for the active area of the device, the calibration protocol and properties of the illumination including spectral irradiance and intensity. Other works herein referred for comparison used unfiltered Hg lamps or even UV lamps, not mimicking sunlight, which does not really comply with the critical need of using solar light in a real application, to minimize energy consumption. Some other works [202,229] used Xe lamps without filters, which emit more UV radiation than the present work lamp, which might explain the higher degradations and photocatalytic activities reported for TiO₂ NPs. P25 TiO₂ when immobilized on a PVA film [205] has demonstrated higher activity than the present work, however the photocatalyst/pollutant mass ratio was three times higher, a UV radiation source was used and pH value was

not disclosed, which is known to greatly affect the photocatalysis activity, with acidic media being more favorable in this case. For instance, works [201,202,204,206,229], where a batch set-up was employed, did not refer experimental conditions, such as the irradiance, which is crucial to compare results. Nevertheless, it is worth noting that the present work photocatalyst still yielded higher reaction rate constant than some UV-irradiated batch systems [204,206]. Systematic computational investigations on TiO₂ NPs [231], have revealed that thermal annealing leads to amorphization (disorder) of the anatase NPs' surface, inducing valence band edge broadening and higher photoactivities. In this work, besides thermal annealing at 500 °C, P25 TiO₂ NPs are grafted to the silica-titania MICROSCAFS[®] and, therefore, in very close contact with amorphous, low coordination, titania species existent in the MICROSCAFS[®]. This, together with the wide and interconnected macropores characteristic of the MICROSCAFS[®], might suggest a reason for the relevant photocatalytic MICROSCAFS[®] activity, achieved in the present work, when exposed to solar radiation, which includes only a very small fraction of UV radiation.

5.3.4. Study of the by-products from photocatalytic MO degradation

The TPs formed during the photocatalytic degradation of MO using sample P0/HT/P25 were analyzed by LC-HRMS/MS. Figure 5.19 shows the formation of MO TPs over irradiation time in the presence of the photocatalytic MICROSCAFS[®] P0/HT/P25 using a batch (Figure 5.19a) and flow (Figure 5.19b) reactor. The analysis was carried out up to a solar exposure time of 120 min (batch) and 360 min (continuous flow), which corresponds to a partial MO degradation at 72 % and 27 %, respectively (by UV-Vis).

5 and 2 by-products were identified, using the batch and flow reactor, respectively, whose chemical structure is included in Table 5.7, in agreement with a degradation mechanism proposed in the literature [232–235]. As can be seen in Table 5.7, five by-products were identified. Two of them (TP320-a and TP320-b) are isomers and are formed because the MO molecular structure contains two benzene groups, and the addition of a hydroxyl radical can occur in two positions.

Figure 5.19a shows that MO degradation (in the batch reactor) starts with its partial conversion to the compounds TP290 and TP320-a, following a similar pattern to a

previously reported one [220], whose amount starts to decrease after around 60 min of exposure to simulated solar light. The formation of these by-products, TP320-a and TP290, occurs due to the addition of a hydroxyl radical at a benzene group of MO, and to the cleavage of a methyl in the dimethylamine group of MO, respectively. After 30 min of irradiation the formation of the compounds TP306 and TP320-b were detected, due to the cleavage of a methyl in the dimethylamine group of TP320-a, and isomerization of TP320-a, respectively. In the meantime, the loss of both methyl of the dimethylamine group of MO occurs, and the formation of the compound TP276 was observed. It should be noted that the formation of the compounds TP320-b and TP276 was in a very small amount. Although it was not possible to remove all the TPs, a decrease was observed after around 60 min of irradiation. After 120 min of irradiation, residual MO species were still identified, which were expected because of the incomplete MO degradation at this stage, together with the just mentioned 5 TPs in solution. Therefore, a longer irradiation time will be necessary to achieve the complete degradation of both MO and by-products.

As for the flow reactor results Figure 5.19b, it should be noted that only the initial stages of MO degradation are being analyzed, i.e. until 27% MO degradation. In this case MO degradation was found to be slower than in batch conditions, which might explain the lower number of TPs (TP290, TP320-a and TP276) identified in this case. So, it is found to begin with MO's conversion to compound TP290, followed by the formation of compound TP320-a after 120 min of irradiation. After 150 min of irradiation compound TP276 appears in a very small amount. All the TPs start to decrease in amount after 270 min of irradiation. After 360 min of irradiation, which corresponds to 27% MO degradation (by UV-Vis), TPs and MO species are still present in solution, as expected, suggesting that a longer irradiation period is required for the complete degradation of MO. Comparing the same level of MO degradation at 27%, determined by UV-Vis spectroscopy, i.e. 30 min (batch) and 360 min (flow), a similar trend is observed, with the same TPs being identified, except for TP306 (that appears just in batch). Finally, regarding toxicity, Ecological Structure Activity Relationships (ECOSAR) analysis demonstrated that both TP290 and TP276 are less toxic to green algae [236].

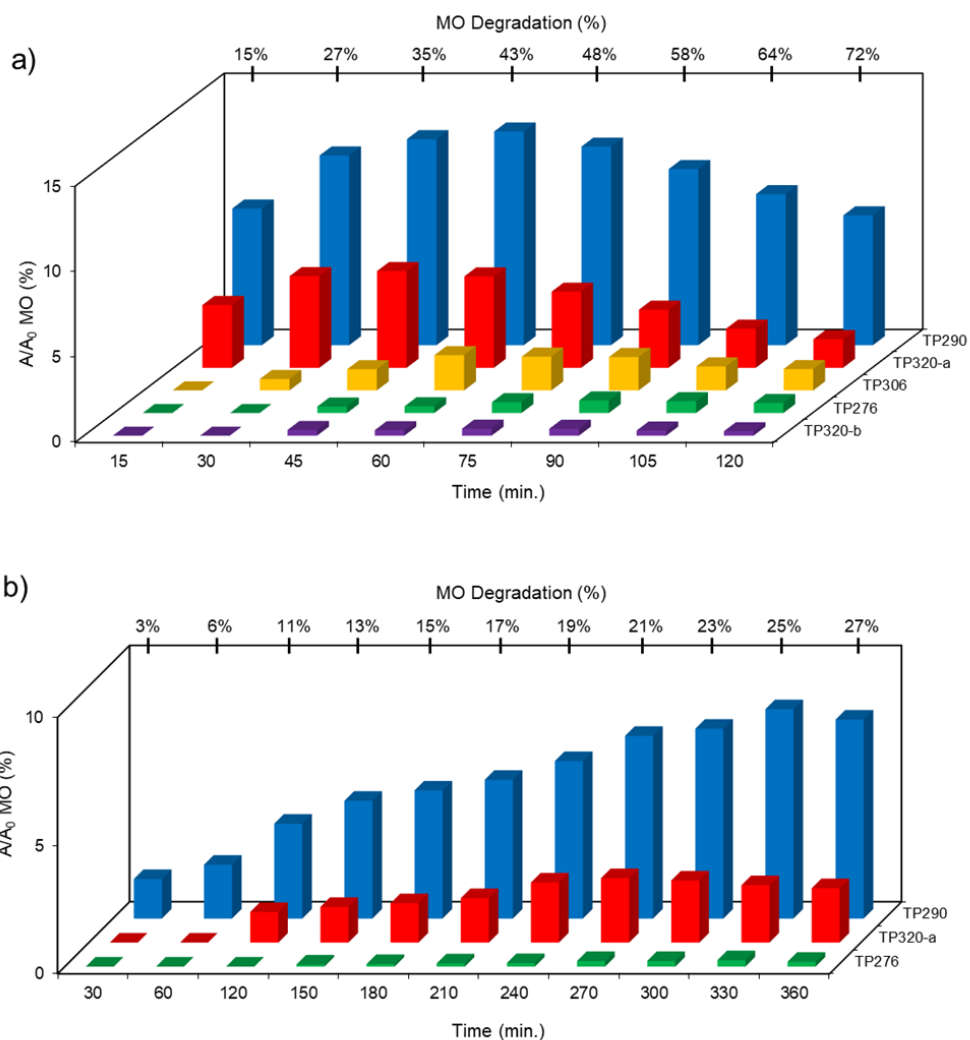
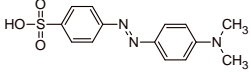
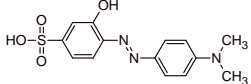
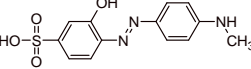
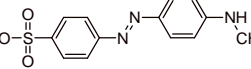
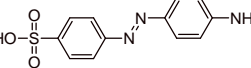
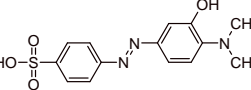


Figure 5.19. TPs identification of MO photocatalytic degradation, during 120 and 360 min using P0/HT/P25 MICROSCAFS® on the (a) batch and (b) flow reactor, respectively. MO degradation values (%) were obtained by UV-Vis spectroscopy.

Table 5.7. LC-HRMS/MS identification of MO and their degradation by-products.

Compound	Structure	t_R (min)	Proposed Empirical Formula	[M-H] ⁻ [m/z (Δ ppm) mSigma]
MO		9.5	C ₁₄ H ₁₅ N ₃ O ₃ S	[304.0770 (-2.9; 6.5)]
TP320-a		10.9	C ₁₄ H ₁₅ N ₃ O ₄ S	[320.0722 (-3.7; 9.2)]
TP306		9.0	C ₁₃ H ₁₃ N ₃ O ₄ S	[306.0562 (-2.7; 12.5)]
TP290		7.8	C ₁₃ H ₁₃ N ₃ O ₃ S	[290.0614 (-3.2; 10.5)]
TP276		5.8	C ₁₂ H ₁₁ N ₃ O ₃ S	[276.0453 (-3.2; 21.6)]
TP320-b		3.9	C ₁₄ H ₁₅ N ₃ O ₄ S	[320.0712 (-0.2; 9.7)]

5.3.5. Scavenger's study on the photocatalytic MICROSCAFS® and photocatalysis mechanistic study

To go further in this study and to analyze whether the MO photocatalytic degradation takes place via oxygen radical species, such as O₂^{•-}, •OH or via direct positive holes (h⁺) or electron (e⁻) transfer, radical scavengers like BQ, EtOH, and EDTA, were added to the reaction media during irradiation. Considering the photocatalytic performance results discussed above, the P+/HT/P25 sample was chosen for this study. BQ, EtOH and EDTA, here used as O₂^{•-}, •OH and h⁺ scavengers, respectively.

As can be observed in Figure 5.20 the presence of the three scavengers has distinct influence on MO removal. The obtained results revealed that using ethanol, an •OH scavenger, no significant differences in the pollutant removal were observed. On the other hand, the most pronounced photodegradation suppression can be seen when BQ was added to the MO solution. The addition of this well-known O₂^{•-} scavenger, during MO photocatalytic degradation reduced around 49% of MO removal

(absolute value). On the other hand, the degradation of MO was enhanced in the presence of EDTA. When EDTA (h^+ scavenger) was added to the system an increase of 22% (absolute value) of MO removal was obtained comparing with the degradation of MO without a presence of scavengers. Similar results were already published by Liu et. al. [237] when used EDTA as a scavenger in the degradation of dyes. This obtained result can be justified due to the fact that EDTA is as h^+ scavenger and also an e^- donor [238]. In fact, the presence of EDTA in the photocatalytic degradation of MO, will reduce the recombination of the e^-/h^+ , since the EDTA was used as a scavenger to quench h^+ , and consequently more e^- can react with the O_2 in the surface to produce $O_2^{\bullet-}$. Furthermore, the superoxide radicals, $O_2^{\bullet-}$, seem to be the main oxidant species involved in this photocatalytic process. Therefore, in the presence of EDTA, more e^- are available in the system to do the $O_2/O_2^{\bullet-}$ reduction in the conduction band, enhancing the MO degradation under solar irradiation. Within these results, it is plausible to conclude that MO degradation does not take place directly through $\bullet OH$ and h^+ but the $O_2^{\bullet-}$ are the main oxidant species involved in this photocatalytic process.

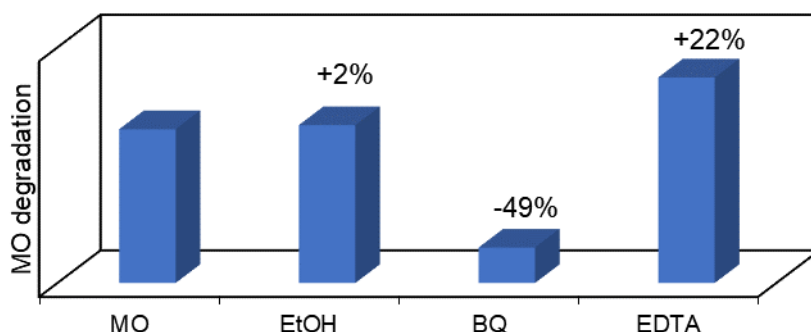


Figure 5.20. MO degradation evolution after 120 min. of irradiation using P+/HT/P25 as catalyst, when in the presence of selected scavengers: EtOH, BQ and EDTA to quench $\bullet OH$, $O_2^{\bullet-}$, and h^+ , respectively.

Supported in the above discussed data, a mechanism for the solar light activation of the P+/HT/P25 MICROSCAFS[®] is proposed in Figure 5.21. When the MICROSCAFS[®] is exposed to solar radiation with energy enough to promote the photogeneration of charge carriers, e^- and h^+ will be generated in the conduction band (CB) and valence band (VB), respectively. The excited electrons in the CB will react with the adsorbed

O_2 and reduce them in $O_2^{\bullet-}$, this superoxide radical play an active role in the photodegradation of MO as concluded by the scavenger's study, and also contribute to increase the lifetime of the charge carriers. Furthermore, the $O_2^{\bullet-}$ can also produce H_2O_2 as a consequence of the O_2 photo-reduction that also enhance the photodegradation of MO. On the other hand, in the VB the photogenerated h^+ react with either the adsorbed H_2O or OH^- , resulting in the formation of $\bullet OH$ radicals. These reactive species do not play an active role in this photodegradation system, however, these $\bullet OH$ radicals are responsible for the formation of two TPs detected by HRMS, the isomers TP320-a and TP320-b, formed due to hydroxylation of the MO. In a previous work it was observed that the hydroxylation of the antidepressant amitriptyline formed three isomers, during their photocatalytic degradation, due to the addition of hydroxyl radicals in different positions on the amitriptyline molecule [239]. Similar results were also published, during the photodegradation of several compounds, such as sulfaclozine, sulfonamides and sulfachloropyridazine, reporting that the photocatalytic degradation of the studied pollutants starts with their hydroxylation, due to the addition of $\bullet OH$ to the aniline ring [240–243].

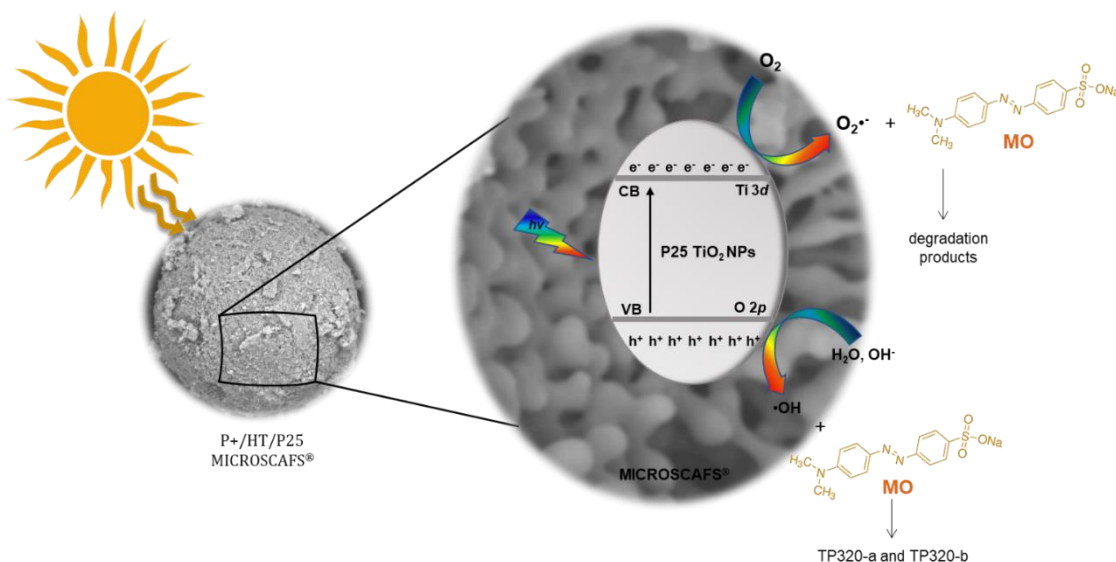


Figure 5.21. Photoactivation mechanism proposed for P+/HT/P25 MICROSCAFS® used as catalyst for the photodegradation of MO under solar light irradiation.

5.4. Conclusion

ST MICROSCAFS[®] with different scales of pore sizes and particle size diameters were successfully developed with high reproducibility using an adapted sol-gel method, involving polymerization-induced phase separation. They were loaded with commercial photocatalytic P25 TiO₂ NPs, whose immobilization within the MICROSCAFS[®] was promoted by HT at 500 °C. MICROSCAFS[®] characteristics, mainly macropore size, directly affected the photocatalytic performance in what regards the organic dye MO degradation. MICROSCAFS[®] with greater interconnected pore sizes exhibited higher photocatalytic activity both in batch and in flow set-ups. Their engineered macroporous network favors mass transport, and therefore the flow of the pollutant solution throughout the pores, confers higher accessibility of the pollutant molecules to the active sites, and provides conditions to spread the photons' pathway inside the pore channels. The size of the particles appears to be not so important as the size of the pores. MICROSCAFS[®] are herein shown to be a viable solution for environmental remediation (e.g. wastewater purification), using straightforward flow conditions, does not requiring any separation step, like centrifugation or filtration, which otherwise would be very expensive on an industrial scale, or of high complexity in remote areas such as rural villages. A modeling study of a flow set-up was developed and tested, which yields more accurate results and successfully predicts the reaction evolution. There are other works from the literature that have reported higher degradation rates than the present work, however the employed photocatalyst/pollutant ratio was generally higher and/or they used UV light (instead of solar light) which gives rise to high photo-efficiency, or relevant information on the experimental conditions was missing. This process used solar light as the light source, which has only ~5% UV. Finally, the design of a new larger scale flow reactor, with higher photocatalyst/pollutant/light contact, is promising to further enhance photocatalytic activity and allowing the application of this system in an industrial scale, providing a viable solution for the global water pollution problem.

Chapter

Conclusions and Future Work

6

6.1. Conclusions

The production of tailored porous materials with controlled pore size, shape, and morphology (pore interconnectivity) is a relevant research topic in the materials and chemistry domains due to their high potential for sustainable and innovative applications in the fields of catalysis, chromatography, controlled release, scaffolds for biomedical applications, sensing, energy storage, and conversion, sorption, and separation.

During the past 30 years, many authors have reported on the development of single- and multicomponent oxide and non-oxide macroporous monoliths relying on a process called polymerization-induced phase separation, which occurs during a sol-gel reaction. The increasingly hydrophobic gel separates from the liquid media during a sol-gel reaction, and by varying the reaction parameters, conditions, and precursors, different porosities can be obtained, provided a phase separation agent, like a polymeric additive, is present. This chemical additive, which might take many forms and display multiple affinities toward different chemicals, is always present in these works, with virtually no reports using sol-gel processes with inherent phase separation. Moreover, despite the published works on monoliths, reports on macroporous microspheres using the polymerization-induced phase separation are very rare, and a complete systematic study of their development was still lacking in the literature. Microspheres present some advantages when comparing to monoliths since they might adapt to any reactor shape and size and exhibit higher mechanical robustness, and thus, their study and development are of high interest.

This thesis aims to present a more straightforward and quicker method to create macroporous microspheres, registered as MICROSCAFS[®], that dispense phase separation inducers, using a systematic approach, while providing a complete morphological, chemical and mechanical characterization and exploring their application in solar light-driven photocatalysis for water purification.

Chapter 3 details the successful development of silica (S) MICROSCAFS[®] with varying particle size and pore diameter as an introductory study. By varying synthesis parameters like hydrolysis time, amount of hydrolysis catalyst and amount of surfactant the porosity and particle size were found to change. Increased HCl

concentration or hydrolysis time led to a general rise in pore size, attributed to higher viscosity in the Si precursor solution, (longer-chain oligomers). Microspheres with particle size mode ranging from 26 to 130 μm were obtained and MIP and N_2 adsorption/desorption analysis indicated that all obtained microspheres were predominantly macroporous, exhibiting low specific surface areas ranging from 2.46 to 14.51 m^2/g and pore size modes ranging from 164 to 405 nm, also including a smaller number of mesopores.

NMR data established that most epoxy rings of GPTMS opened during microsphere synthesis, acting as inherent gelation and phase separation promoters, eliminating the need for additional chemicals. FTIR-ATR spectra analysis of microspheres dried at 150 $^\circ\text{C}$ revealed its hybrid character, with some epoxy rings remaining unopened during synthesis, allowing the possibility of grafting selected chemical species for specific applications. Conversely, heat-treated microspheres at 700 $^\circ\text{C}$ were composed of fully inorganic material, displaying macropores and influencing Si-O-Si FTIR bands with mixed Q and T Si units. This chapter introduces the possibility of producing hybrid silica-based MICROSCAFS[®] and inorganic silica-based MICROSCAFS[®] without pore-forming agents.

Chapter 4 presented a novel approach to consistently produce multioxide ST and STH MICROSCAFS[®] with customizable size, and interconnected macroporosity, and consequently, different mechanical properties. The addition of alkaline catalyst combined with the titania precursor at constant temperature reduced the reaction time by 4.5h, when compared to the synthesis of S MICROSCAFS[®]. and increased the reproducibility, when compared to the method reported in chapter 3.

The manipulation of reaction conditions such as a higher temperature (85 $^\circ\text{C}$), an elevated GPTMS/TEOS molar ratio (1.09), or a lower TiPOT/ CH_3COOH molar ratio (1:6) led to larger macropores (in some cases at the expense of mesopores) and particle sizes. A higher W/O mass ratio (0.68:1) increased the pore size without significantly altering particle size, while specific surfactant mixtures (Span[®] 80 and Pluronic[®] P123, HLB=5.2) resulted in a considerable reduction in particle size. The composition, particularly the GPTMS/TEOS molar ratio, significantly influenced interconnected macroporosity and particle size, yielding pore size modes ranging from a few nanometers to 1.9 μm in diameter and particle sizes modes from 69 to

105 μm . Higher GPTMS content imparted a more pronounced hybrid inorganic/organic character, facilitating further functionalization reactions. The inclusion of Hf precursor (STH MICROSCAFS[®]) lead to a reduction in interconnected macroporosity, attributed to the accelerated gelation induced by the Hf precursor.

Furthermore, a correlation between the size and quantity of macropores and the mechanical properties of MICROSCAFS[®] has been established. Increased macroporosity generally resulted in MICROSCAFS[®] exhibiting lower stiffness, higher elastic recovery, and compressibility values, reaching up to 42% for the more porous samples (68% open porosity).

The synergy of cryo-SEM, coupled with EDS, SEM, and optical microscopy, emerged as a powerful methodology for stabilising the formation mechanism of the ST and STH MICROSCAFS[®]. The oligomers present within the aqueous phase (agglomerated droplets) of the emulsion accumulated at the water–oil interface and formed the characteristic thin layer enveloping MICROSCAFS[®]. Subsequent stages involved the growth and gelation of skeleton domains concurrently with phase separation, culminating in the attainment of the final interconnected macroporous morphology of the microspheres.

In Chapter 5, ST MICROSCAFS[®] with different pores and particle sizes were tested as a support to commercial photocatalytic NPs and applied in the degradation of MO organic dye, as a case study, using a batch and a flow reactor under simulated solar light. The ST MICROSCAFS exhibited particle sizes ranging from $26.02 \pm 0.57 \mu\text{m}$ to $73.85 \pm 2.24 \mu\text{m}$ and pore size modes ranging from a very few nm to $1.8 \mu\text{m}$. Commercial P25 TiO₂ NPs were successfully loaded into the MICROSCAFS using a wet impregnation method involving calcination. MO was successfully degraded through solar light photocatalysis in aqueous media, reaching degradations as high as 87% after 2 hours in batch and 29%, after 6 hours, in flow. In both reactor types, larger pores improved photocatalytic degradation, enhancing the accessibility and diffusion of reactants and products to and from the active sites. The lower degradation observed in flow was caused by the limited exposure to light of the MO solution; however, it proved to be instrumental in studying the recyclability of these particles since they were fully preserved after each cycle, exhibiting almost constant photocatalytic activities after at least 6 cycles in flow. The batch and flow

photocatalytic reactions were analyzed by LC-HRMS/MS, and up to 5 degradation by-products were generated, possibly involving lower toxicity than the original pollutant species. Finally, the reaction kinetics of both systems was studied, revealing a higher kinetic rate constant for the photocatalytic MICROSCAFS® even higher than in some of the works that used UV light. A new flow reactor model was designed and applied successfully, predicting the concentration of MO with great accuracy in the studied first 6 hours of light exposure.

In the final analysis, MICROSCAFS® demonstrated good applicability as a catalytic support in the realm of photocatalysis. Interconnected macropores, which are normally not explored in the literature, posed as an important feature of these materials, improving the flow of the pollutant solution and thus the contact with the photocatalyst. Notably, their utilization in conjunction with a continuous flow-type reactor addressed a prevalent challenge in the field - the separation issue commonly associated with nanoparticles used in batch processes. In practice, MICROSCAFS® exhibited effective degradation of MO dye across multiple cycles without any physical/chemical deterioration.

This successful application places MICROSCAFS® as an innovative material with the versatility to be tailored for diverse applications, from environmental remediation to catalysis or biomedical applications.

6.2. Future Work

A new and more precise MIP technique, namely differential scanning porosimetry (DSP), would be of interest, because it can give more information about the interconnected pore network of porous materials. This technique distinguishes the access channels' volume and size (pore throats) from the internal junction void volume (pore cavities) instead of using the simple bundle of cylindrical capillaries mode and is present in the most recent porosimeters.

Regarding photocatalysis experiments, new photocatalytic NPs with more capability for visible light harvesting than TiO₂ NPs could be tested. The idea is to use even less amount of photocatalytic NPs immobilized within the MICROSCAFS®. Using the MICROSCAFS® as microreactors for the *in-situ* synthesis of photocatalytic NPs, either

by traditional wet chemistry sol-gel techniques, or by the use of a microwave reactor is envisaged in the following of this thesis. Exploring other compositions for the MICROSCAFS® is also interesting, especially if one wants to increase their transparency in the visible range and decrease their band gap energy.

The photocatalytic continuous flow reactor model could be improved for a higher degradation yield. The reactor chamber might be a serpentine tube where the photocatalytic MICROSCAFS® would fill it, increasing the area exposed to the sunlight. Also, studies using other pollutants, like pharmaceuticals, might yield more data for future applications. Performing those tests using real water matrices is also very relevant, because it could lead to different results in terms of photocatalysis performance. Scale-up trials using real water matrices, under natural sunlight conditions, are the ultimate goal to transfer this new technology into a real wastewater purification set-up, further increasing its environmental remediation impact.

Chapter

References

7

- [1] M.H. Sun, S.Z. Huang, L.H. Chen, Y. Li, X.Y. Yang, Z.Y. Yuan, B.L. Su, Applications of hierarchically structured porous materials from energy storage and conversion, catalysis, photocatalysis, adsorption, separation, and sensing to biomedicine, *Chem Soc Rev* 45 (2016) 3479–3563. <https://doi.org/10.1039/c6cs00135a>.
- [2] S. Wang, M.M. Falk, A. Rashad, M.M. Saad, A.C. Marques, R.M. Almeida, M.K. Marei, H. Jain, Evaluation of 3D nano-macro porous bioactive glass scaffold for hard tissue engineering, *J Mater Sci Mater Med* 22 (2011) 1195–1203. <https://doi.org/10.1007/s10856-011-4297-4>.
- [3] A.C. Marques, R.M. Almeida, A. Thiema, S. Wang, M. Falk, H. Jain, Sol-gel-derived glass scaffold with high pore interconnectivity and enhanced bioactivity, *J Mater Res* 24 (2009) 3495–3502. <https://doi.org/10.1557/jmr.2009.0440>.
- [4] A.C. Marques, H. Jain, C. Kiely, K. Song, C.J. Kiely, R.M. Almeida, Nano/macroporous monolithic scaffolds prepared by the sol-gel method, *J Solgel Sci Technol* 51 (2009) 42–47. <https://doi.org/10.1007/s10971-009-1960-z>.
- [5] H. Wang, I. Sung, L.I. Xiaodong, D. Kim, Fabrication of porous SiC ceramics with special morphologies by sacrificing template method, *Journal of Porous Materials* 11 (2004) 265–271. <https://doi.org/10.1023/B:JOP0.0000046353.24308.86>.
- [6] H. Wang, X.D. Li, J.S. Yu, D.P. Kim, Fabrication and characterization of ordered macroporous PMS-derived SiC from a sacrificial template method, *J Mater Chem* 14 (2004) 1383–1386. <https://doi.org/10.1039/b313405a>.
- [7] H. Wan, J. Jiang, J. Yu, K. Xu, L. Miao, L. Zhang, H. Chen, Y. Ruan, NiCo₂S₄ porous nanotubes synthesis via sacrificial templates: High-performance electrode materials of supercapacitors, *CrystEngComm* 15 (2013) 7649–7651. <https://doi.org/10.1039/c3ce41243a>.

- [8] X. He, X. Zhou, B. Su, 3D interconnective porous alumina ceramics via direct protein foaming, *Mater Lett* 63 (2009) 830–832. <https://doi.org/10.1016/j.matlet.2008.12.021>.
- [9] S. Barg, C. Soltmann, M. Andrade, D. Koch, G. Grathwohl, Cellular ceramics by direct foaming of emulsified ceramic powder suspensions, *Journal of the American Ceramic Society* 91 (2008) 2823–2829. <https://doi.org/10.1111/j.1551-2916.2008.02553.x>.
- [10] F. Li, Z. Kang, X. Huang, X.G. Wang, G.J. Zhang, Preparation of zirconium carbide foam by direct foaming method, *J Eur Ceram Soc* 34 (2014) 3513–3520. <https://doi.org/10.1016/j.jeurceramsoc.2014.05.029>.
- [11] L. Ren, Y.P. Zeng, D. Jiang, Fabrication of Gradient Pore TiO₂ Sheets by a Novel Freeze–Tape-Casting Process, *Journal of the American Ceramic Society* 90 (2007) 3001–3004. <https://doi.org/10.1111/j.1551-2916.2007.01833.x>.
- [12] Z.Y. Deng, H.R. Fernandes, J.M. Ventura, S. Kannan, J.M.F. Ferreira, Nano-TiO₂-Coated Unidirectional Porous Glass Structure Prepared by Freeze Drying and Solution Infiltration, *Journal of the American Ceramic Society* 90 (2007) 1265–1268. <https://doi.org/10.1111/j.1551-2916.2007.01602.x>.
- [13] T. Fukasawa, Z.Y. Deng, M. Ando, T. Ohji, Y. Goto, Pore structure of porous ceramics synthesized from water-based slurry by freeze-dry process, *J Mater Sci* 36 (2001) 2523–2527. <https://doi.org/10.1023/A:1017946518955>.
- [14] K. Araki, J.W. Halloran, Porous ceramic bodies with interconnected pore channels by a novel freeze casting technique, *Journal of the American Ceramic Society* 88 (2005) 1108–1114. <https://doi.org/10.1111/j.1551-2916.2005.00176.x>.
- [15] K. Kajihara, S. Kuwatani, R. Maehana, K. Kanamura, Macroscopic Phase Separation in a Tetraethoxysilane–Water Binary Sol–Gel System, *Bull. Chem. Soc. Jpn* 82 (2009) 1470. <https://doi.org/10.1246/bcsj.82.1470>.
- [16] K. Nakanishi, N. Soga, Phase Separation in Gelling Silica–Organic Polymer Solution: Systems Containing Poly(sodium styrenesulfonate), *Journal of the*

- American Ceramic Society 74 (1991) 2518–2530.
<https://doi.org/10.1111/j.1151-2916.1991.tb06794.x>.
- [17] K. Nakanishi, H. Komura, R. Takahashi, N. Soga, Phase Separation in Silica Sol-Gel System Containing Poly(ethylene oxide). I. Phase Relation and Gel Morphology, *Bull Chem Soc Jpn* 67 (1994) 1327–1335.
<https://doi.org/10.1246/bcsj.67.1327>.
- [18] R. Takahashi, S. Sato, T. Sodesawa, T. Azuma, Silica with Bimodal Pores for Solid Catalysts Prepared from Water Glass, *J Solgel Sci Technol* 31 (2004) 373–376.
<https://doi.org/10.1023/B:JSST.0000048020.53138.83>.
- [19] H. Kaji, K. Nakanishi, N. Soga, Polymerization-induced phase separation in silica sol-gel systems containing formamide, *J Solgel Sci Technol* 1 (1993) 35–46. <https://doi.org/10.1007/BF00486427>.
- [20] A. Feinle, M.S. Elsaesser, N. Hüsing, Sol-gel synthesis of monolithic materials with hierarchical porosity, *Chem Soc Rev* 45 (2016) 3377–3399.
<https://doi.org/10.1039/c5cs00710k>.
- [21] K. Nakanishi, Macroporous Morphology Control by Phase Separation, in: L. Klein, M. Aparicio, A. Jitiano (Eds.), *Handbook of Sol-Gel Science and Technology*, Springer International Publishing, Switzerland, 2016: pp. 1–32.
https://doi.org/10.1007/978-3-319-19454-7_25-1.
- [22] W.W. Cai, H. Yang, X.Z. Guo, A facile one-step route to synthesize titania hollow microspheres with incontinuous multicavities, *Chinese Chemical Letters* 25 (2014) 441–446. <https://doi.org/10.1016/j.ccllet.2013.12.002>.
- [23] L.M. Yang, Y.J. Wang, Y.W. Sun, G.S. Luo, Y.Y. Dai, Synthesis of micrometer-sized hard silica spheres with uniform mesopore size and textural pores, *J Colloid Interface Sci* 299 (2006) 823–830.
<https://doi.org/10.1016/j.jcis.2006.02.043>.
- [24] Z.G. Shi, Y.Q. Feng, Synthesis and characterization of hierarchically porous silica microspheres with penetrable macropores and tunable mesopores, *Microporous and Mesoporous Materials* 116 (2008) 701–704.
<https://doi.org/10.1016/j.micromeso.2008.05.010>.

- [25] J. Li, L. Xu, Z. guo Shi, Waxberry-like hierarchically porous ethyl-bridged hybrid silica microsphere: A substrate for enzyme catalysis and high-performance liquid chromatography, *J Chromatogr A* 1587 (2019) 79–87. <https://doi.org/10.1016/j.chroma.2018.11.073>.
- [26] J.X. Wei, Z.G. Shi, F. Chen, Y.Q. Feng, Q.Z. Guo, Synthesis of penetrable macroporous silica spheres for high-performance liquid chromatography, *J Chromatogr A* 1216 (2009) 7388–7393. <https://doi.org/10.1016/j.chroma.2009.04.066>.
- [27] T. Long, Q.Z. Guo, L.Y. Xu, Fast separation of sulfanilamides using macroporous silica spheres as the separation media, *J Liq Chromatogr Relat Technol* 34 (2011) 1391–1398. <https://doi.org/10.1080/10826076.2011.572212>.
- [28] C. ru Yin, L. yun Ma, J. geng Huang, L. Xu, Z. guo Shi, Fast profiling ecotoxicity and skin permeability of benzophenone ultraviolet filters using biopartitioning micellar chromatography based on penetrable silica spheres, *Anal Chim Acta* 804 (2013) 321–327. <https://doi.org/10.1016/j.aca.2013.10.040>.
- [29] L. Ma, J. Li, J. Zhao, H. Liao, L. Xu, Z.G. Shi, Penetrable silica microspheres for immobilization of bovine serum albumin and their application to the study of the interaction between imatinib mesylate and protein by frontal affinity chromatography, *Anal Bioanal Chem* 408 (2016) 805–814. <https://doi.org/10.1007/s00216-015-9163-7>.
- [30] T. Qiao, L. yun Ma, X. Wang, Z.G. Shi, The flow-through silica as the matrix to immobilize gold nanoparticles for HPLC applications, *J Liq Chromatogr Relat Technol* 41 (2018) 107–113. <https://doi.org/10.1080/10826076.2017.1421552>.
- [31] X. jing Mao, J. Li, D. Liu, T. Qiao, L. Ma, X. Sun, L. Xu, Z. guo Shi, Flow-through silica: A potential matrix for fast chromatographic enantioseparation with high enantioselectivity, *Talanta* 178 (2018) 583–587. <https://doi.org/10.1016/j.talanta.2017.09.093>.

- [32] Z.G. Shi, Q.Z. Guo, Y.T. Liu, Y.X. Xiao, L. Xu, Drug delivery devices based on macroporous silica spheres, *Mater Chem Phys* 126 (2011) 826–831. <https://doi.org/10.1016/j.matchemphys.2010.12.035>.
- [33] L.Y. Xu, Y.Y. Huang, T. Long, Z.G. Shi, Synthesis of macroporous silica spheres for drug delivery, *Materials and Manufacturing Processes* 28 (2013) 626–630. <https://doi.org/10.1080/10426914.2013.773014>.
- [34] T. Ataei-Germi, A. Nematollahzadeh, Bimodal porous silica microspheres decorated with polydopamine nano-particles for the adsorption of methylene blue in fixed-bed columns, *J Colloid Interface Sci* 470 (2016) 172–182. <https://doi.org/10.1016/j.jcis.2016.02.057>.
- [35] Q. Guo, L. Hu, C. Fan, Y. Zhang, Q. Zhang, Perforative silica microsphere-modified phenolphthalein-based poly(arylene ether sulfone) composites: tensile and thermal properties, *Iranian Polymer Journal (English Edition)* 27 (2018) 611–619. <https://doi.org/10.1007/s13726-018-0637-2>.
- [36] R. Wang, H. Yang, K. Xue, Y. Zhao, X. Guo, Facile Synthesis and Chiral Separation of Chiral Mesoporous Silica Microspheres, *J Chromatogr Sci* 55 (2017) 736–741. <https://doi.org/10.1093/chromsci/bmx028>.
- [37] Y. Zhang, X. Qiao, J. Wan, L.A. Wu, B. Chen, X. Fan, Facile synthesis of monodisperse YAG:Ce³⁺ microspheres with high quantum yield via an epoxide-driven sol-gel route, *J Mater Chem C Mater* 5 (2017) 8952–8957. <https://doi.org/10.1039/c7tc02909h>.
- [38] A.C. Marques, M. Vale, D. Vicente, M. Schreck, E. Tervoort, M. Niederberger, Porous Silica Microspheres with Immobilized Titania Nanoparticles for In-Flow Solar-Driven Purification of Wastewater, *Global Challenges* 5 (2021) 2000116. <https://doi.org/10.1002/gch2.202000116>.
- [39] M. Vale, M. V. Loureiro, M.J. Ferreira, A.C. Marques, Silica-based microspheres with interconnected macroporosity by phase separation, *J Solgel Sci Technol* 95 (2020) 746–759. <https://doi.org/10.1007/s10971-020-05257-4>.

- [40] A.C. Marques, M. Vale, Macroporosity Control by Phase Separation in Sol-Gel Derived Monoliths and Microspheres, *Materials* 14 (2021) 4247. <https://doi.org/10.3390/ma14154247>.
- [41] M. V. Loureiro, M. Vale, A. De Schrijver, J.C. Bordado, E. Silva, A.C. Marques, Hybrid custom-tailored sol-gel derived microscaffold for biocides immobilization, *Microporous and Mesoporous Materials* 261 (2018) 252–258. <https://doi.org/10.1016/j.micromeso.2017.10.056>.
- [42] M. Vale, S. Orišková, A. Mariquito, L. Reis, M. Pinto, A.C. Marques, Multicomponent oxide microspheres with designed macroporosity (MICROSCAFS®): a customized platform for chemicals immobilization, *RSC Adv* 13 (2023) 12951–12965. <https://doi.org/10.1039/D3RA00895A>.
- [43] M. Vale, A.C. Marques, Mechanistic Study of the Formation of Multicomponent Oxide Porous Microspheres (MICROSCAFS®) by Cryo-Scanning Electron Microscopy, *Gels* 9 (2023) 704. <https://doi.org/10.3390/gels9090704>.
- [44] C.J. Brinker, G.W. Scherer, *Sol-gel science: the physics and chemistry of sol-gel processing*, 1st Edition, Academic Press, San Diego, US, 1990.
- [45] D. Levy, M. Zayat, eds., *The Sol-Gel Handbook: Synthesis, Characterization, and Applications*, 1st Edition, Wiley-VCH, Weinheim, Germany, 2015.
- [46] K.-H. Nam, T.-H. Lee, B.-S. Bae, M. Popall, Condensation reaction of 3-(methacryloxypropyl)-trimethoxysilane and diisobutylsilanediol in non-hydrolytic sol-gel process, *J Solgel Sci Technol* 39 (2006) 255–260. <https://doi.org/10.1007/s10971-006-7884-y>.
- [47] E.D. Siggia, Late stages of spinodal decomposition in binary mixtures, *Phys Rev A (Coll Park)* 20 (1979) 595–605. <https://doi.org/10.1103/PhysRevA.20.595>.
- [48] S.W. Koch, R.C. Desai, F.F. Abraham, Dynamics of phase separation in two-dimensional fluids: Spinodal decomposition, *Phys Rev A (Coll Park)* 27 (1983) 2152–2167. <https://doi.org/10.1103/PhysRevA.27.2152>.

- [49] R. Shimizu, H. Tanaka, A novel coarsening mechanism of droplets in immiscible fluid mixtures, *Nat Commun* 6 (2015) 7407. <https://doi.org/10.1038/ncomms8407>.
- [50] M. Tateno, H. Tanaka, Power-law coarsening in network-forming phase separation governed by mechanical relaxation, *Nat Commun* 12 (2021) 912. <https://doi.org/10.1038/s41467-020-20734-8>.
- [51] J.W. Cahn, Phase separation by spinodal decomposition in isotropic systems, *J Chem Phys* 42 (1965) 93–99. <https://doi.org/10.1063/1.1695731>.
- [52] M.L. Huggins, Solutions of long chain compounds, *J Chem Phys* 9 (1941) 440. <https://doi.org/10.1063/1.1750930>.
- [53] M.L. Huggins, Some properties of solutions of long-chain compounds, *Journal of Physical Chemistry* 46 (1942) 151–158. <https://doi.org/10.1021/j150415a018>.
- [54] P.J. Flory, Thermodynamics of high polymer solutions, *J Chem Phys* 10 (1942) 51–61. <https://doi.org/10.1063/1.1723621>.
- [55] M.L. Huggins, The Viscosity of Dilute Solutions of Long-Chain Molecules. IV. Dependence on Concentration, *J Am Chem Soc* 64 (1942) 2716–2718. <https://doi.org/10.1021/ja01263a056>.
- [56] M. Rubinstein, R.H. Colby, *Polymer Physics*, 1st Edition, Oxford University Press, USA, 2003.
- [57] K. Nakanishi, Pore Structure Control of Silica Gels Based on Phase Separation, *Journal of Porous Materials* 4 (1997) 67–112. <https://doi.org/10.1023/A:1009627216939>.
- [58] D.W. Schaefer, K.D. Keefer, Structure of Soluble Silicates, *MRS Online Proceedings Library* 32 (2011) 1. <https://doi.org/10.1557/PROC-32-1>.
- [59] K. Nakanishi, N. Soga, H. Matsuoka, N. Ise, Small-Angle X-ray Scattering Study of Gelling Silica–Organic Polymer Solution: Systems Containing Poly(Sodium Styrenesulfonate), *Journal of the American Ceramic Society* 75 (1992) 971–975. <https://doi.org/10.1111/j.1151-2916.1992.tb04168.x>.

- [60] K. Nakanishi, N. Soga, Phase separation in silica sol-gel system containing polyacrylic acid I. Gel formation behavior and effect of solvent composition, *J Non Cryst Solids* 139 (1992) 1–13. [https://doi.org/10.1016/S0022-3093\(05\)80800-2](https://doi.org/10.1016/S0022-3093(05)80800-2).
- [61] K. Nakanishi, N. Soga, Phase separation in silica sol-gel system containing polyacrylic acid II. Effects of molecular weight and temperature, *J Non Cryst Solids* 139 (1992) 14–24. [https://doi.org/10.1016/S0022-3093\(05\)80801-4](https://doi.org/10.1016/S0022-3093(05)80801-4).
- [62] K. Nakanishi, N. Soga, Phase separation in silica sol-gel system containing polyacrylic acid. III. Effect of catalytic condition, *J Non Cryst Solids* 142 (1992) 36–44. [https://doi.org/10.1016/S0022-3093\(05\)80004-3](https://doi.org/10.1016/S0022-3093(05)80004-3).
- [63] K. Nakanishi, N. Soga, Phase separation in silica sol-gel system containing polyacrylic acid. IV. Effect of chemical additives, *J Non Cryst Solids* 142 (1992) 45–54. [https://doi.org/10.1016/S0022-3093\(05\)80005-5](https://doi.org/10.1016/S0022-3093(05)80005-5).
- [64] G. Hasegawa, T. Yano, H. Akamatsu, K. Hayashi, K. Nakanishi, Variation of meso- and macroporous morphologies in resorcinol–formaldehyde (RF) gels tailored via a sol–gel process combined with soft-templating and phase separation, *J Solgel Sci Technol* 95 (2020) 801–812. <https://doi.org/10.1007/s10971-020-05236-9>.
- [65] K. Nakanishi, T. Nagakane, N. Soga, Designing Double Pore Structure in Alkoxy-Derived Silica Incorporated with Nonionic Surfactant, *Journal of Porous Materials* 5 (1998) 103–110. <https://doi.org/10.1023/A:1009633102016>.
- [66] K. Nakanishi, Y. Yamasaki, H. Kaji, N. Soga, T. Inoue, N. Nemoto, Phase separation kinetics in silica sol-gel system containing polyethylene oxide. I. Initial stage - Code: C7, *J Solgel Sci Technol* 2 (1994) 227–31. <https://doi.org/10.1007/BF00486246>.
- [67] K. Nakanishi, N. Soga, Phase Separation in Silica Sol-Gel System Containing Poly(ethylene oxide) II. Effects of Molecular Weight and Temperature, *Bull Chem Soc Jpn* 70 (1997) 587–592. <https://doi.org/10.1246/bcsj.70.587>.
- [68] R. Meinus, K. Hormann, R. Hakim, U. Tallarek, B.M. Smarsly, Synthesis and morphological characterization of phenyl-modified macroporous-

- mesoporous hybrid silica monoliths, *RSC Adv* 5 (2015) 20283–20294. <https://doi.org/10.1039/c4ra16519e>.
- [69] Y. Sato, K. Nakanishi, K. Hirao, H. Jinnai, M. Shibayama, Y.B. Melnichenko, G.D. Wignall, Formation of ordered macropores and templated nanopores in silica sol-gel system incorporated with EO-PO-EO triblock copolymer, *Colloids Surf A Physicochem Eng Asp* 187–188 (2001) 117–122. [https://doi.org/10.1016/S0927-7757\(01\)00626-4](https://doi.org/10.1016/S0927-7757(01)00626-4).
- [70] K. Nakanishi, T. Amatani, S. Yano, T. Kodaira, Multiscale templating of siloxane gels via polymerization-induced phase separation, *Chemistry of Materials* 20 (2008) 1108–1115. <https://doi.org/10.1021/cm702486b>.
- [71] K. Nakanishi, Y. Sato, Y. Ruyat, K. Hirao, Supramolecular templating of mesopores in phase-separating silica Sol-Gels incorporated with cationic surfactant, *J Solgel Sci Technol* 26 (2003) 567–570. <https://doi.org/10.1023/A:1020767820079>.
- [72] J.H. Smått, S. Schunk, M. Lindén, Versatile double-templating synthesis route to silica monoliths exhibiting a multimodal hierarchical porosity, *Chemistry of Materials* 15 (2003) 2354–2361. <https://doi.org/10.1021/cm0213422>.
- [73] K. Nakanishi, T. Yamato, K. Hirao, Phase Separation in Alkylene-Bridged Polysilsesquioxane Sol-Gel Systems, *MRS Online Proceedings Library* 726 (2011) 97. <https://doi.org/10.1557/PROC-726-Q9.7>.
- [74] A. Itagaki, K. Nakanishi, K. Hirao, Phase separation in sol-gel system containing mixture of 3- and 4-functional alkoxysilanes, *J Solgel Sci Technol* 26 (2003) 153–156. <https://doi.org/10.1023/A:1020770209234>.
- [75] H. Dong, J.D. Brennan, Controlling the morphology of methylsilsesquioxane monoliths using a two-step processing method, *Chemistry of Materials* 18 (2006) 541–546. <https://doi.org/10.1021/cm051900n>.
- [76] K. Kanamori, Y. Kodera, G. Hayase, K. Nakanishi, T. Hanada, Transition from transparent aerogels to hierarchically porous monoliths in polymethylsilsesquioxane sol-gel system, *J Colloid Interface Sci* 357 (2011) 336–344. <https://doi.org/10.1016/j.jcis.2011.02.027>.

- [77] S. Tao, Y. Wang, Y. An, Superwetting monolithic SiO₂ with hierarchical structure for oil removal, *J Mater Chem* 21 (2011) 11901–11907. <https://doi.org/10.1039/c1jm12141c>.
- [78] M. Kurahashi, K. Kanamori, K. Takeda, H. Kaji, K. Nakanishi, Role of block copolymer surfactant on the pore formation in methylsilsesquioxane aerogel systems, *RSC Adv* 2 (2012) 7166–7173. <https://doi.org/10.1039/c2ra20799k>.
- [79] N. Huesing, C. Raab, V. Torma, A. Roig, H. Peterlik, Periodically mesostructured silica monoliths from diol-modified silanes, *Chemistry of Materials* 15 (2003) 2690–2692. <https://doi.org/10.1021/cm034036c>.
- [80] D. Brandhuber, V. Torma, C. Raab, H. Peterlik, A. Kulak, N. Hüsing, Glycol-modified silanes in the synthesis of mesoscopically organized silica monoliths with hierarchical porosity, *Chemistry of Materials* 17 (2005) 4262–4271. <https://doi.org/10.1021/cm048483j>.
- [81] H. Zhong, J. Liu, P. Wang, J. Yang, Q. Yang, Inorganic salt aided synthesis of monolithic silica with meso/macro hierarchical structure, *Microporous and Mesoporous Materials* 123 (2009) 63–70. <https://doi.org/10.1016/j.micromeso.2009.03.024>.
- [82] S. Sharma, S. Basu, Highly reusable visible light active hierarchical porous WO₃/SiO₂ monolith in centimeter length scale for enhanced photocatalytic degradation of toxic pollutants, *Sep Purif Technol* 231 (2020) 115916. <https://doi.org/10.1016/j.seppur.2019.115916>.
- [83] K. Nakanishi, S. Motowaki, N. Soga, Preparation of SiO₂-TiO₂ Gels with Controlled Pore Structure via Sol-Gel Route, *Bull Inst Chem Res Kyoto Univ* 70 (1992) 144–151.
- [84] O. Ruzimuradov, S. Nurmanov, Y. Kodani, R. Takahashi, I. Yamada, Morphology and dispersion control of titania-silica monolith with macro-meso pore system, *J Solgel Sci Technol* 64 (2012) 684–693. <https://doi.org/10.1007/s10971-012-2903-7>.

- [85] H. Yang, Z. Liu, H. Gao, Z. Xie, Synthesis and characterization of hierarchical titania-silica monolith, *Catal Today* 216 (2013) 90–94. <https://doi.org/10.1016/j.cattod.2013.05.025>.
- [86] R. Takahashi, K. Nakanishi, N. Soga, Phase Separation Process of Polymer - Incorporated Silica-Zirconia Sol-Gel System, *J Solgel Sci Technol* 8 (1997) 71–76. <https://doi.org/10.1007/BF02436820>.
- [87] R. TAKAHASHI, K. Nakanishi, N. Soga, Morphology Control of Macroporous Silica-Zirconia Gel Based on Phase Separation, *Journal of the Ceramic Society of Japan* 106 (1998) 772–777. <https://doi.org/10.2109/jcersj.106.772>.
- [88] R. Takahashi, S. Sato, T. Sodesawa, K. Suzuki, M. Tafu, K. Nakanishi, N. Soga, Phase Separation in Sol-Gel Process of Alkoxide-Derived Silica-Zirconia in the Presence of Polyethylene Oxide, *Journal of the American Ceramic Society* 84 (2004) 1968–1976. <https://doi.org/10.1111/j.1151-2916.2001.tb00944.x>.
- [89] R. Takahashi, S. Sato, T. Sodesawa, M. Yabuki, Silica-alumina catalyst with bimodal pore structure prepared by phase separation in sol-gel process, *J Catal* 200 (2001) 197–202. <https://doi.org/10.1006/jcat.2001.3196>.
- [90] J. Wu, X. Li, W. Du, C. Dong, L. Li, Preparation and characterization of bimodal porous alumina-silica and its application to removal of basic nitrogen compounds from light oil, *J Mater Chem* 17 (2007) 2233–2240. <https://doi.org/10.1039/b612501h>.
- [91] H. Yang, Q. Liu, Z. Liu, H. Gao, Z. Xie, Controllable synthesis of aluminosilica monoliths with hierarchical pore structure and their catalytic performance, *Microporous and Mesoporous Materials* 127 (2010) 213–218. <https://doi.org/10.1016/j.micromeso.2009.07.016>.
- [92] S. Murai, K. Fujita, K. Nakanishi, K. Hirao, Morphology control of phase-separation-induced alumina-silica macroporous gels for rare-earth-doped scattering media, *Journal of Physical Chemistry B* 108 (2004) 16670–16676. <https://doi.org/10.1021/jp0481658>.
- [93] X. Guo, W. Li, K. Nakanishi, K. Kanamori, Y. Zhu, H. Yang, Preparation of mullite monoliths with well-defined macropores and mesostructured skeletons via

- the sol-gel process accompanied by phase separation, *J Eur Ceram Soc* 33 (2013) 1967–1974. <https://doi.org/10.1016/j.jeurceramsoc.2013.02.018>.
- [94] N. Nakamura, R. Takahashi, S. Sato, T. Sodesawa, S. Yoshida, Ni/SiO₂ catalyst with hierarchical pore structure prepared by phase separation in sol-gel process, *Physical Chemistry Chemical Physics* 2 (2000) 4983–4990. <https://doi.org/10.1039/b006378i>.
- [95] M. Zheng, T. Zhao, W. Xu, F. Li, Y. Yang, Preparation and characterization of CuO/SiO₂ and NiO/SiO₂ with bimodal pore structure by sol-gel method, *J Solgel Sci Technol* 39 (2006) 151–157. <https://doi.org/10.1007/s10971-006-9172-2>.
- [96] A.C. Marques, H. Jain, R.M. Almeida, Sol-gel derived nano/macroporous scaffolds, *Physics and Chemistry of Glasses: European Journal of Glass Science and Technology Part B* 48 (2007) 65–68.
- [97] X. Guo, K. Nakanishi, K. Kanamori, Y. Zhu, H. Yang, Preparation of macroporous cordierite monoliths via the sol-gel process accompanied by phase separation, *J Eur Ceram Soc* 34 (2014) 817–823. <https://doi.org/10.1016/j.jeurceramsoc.2013.08.016>.
- [98] M. Sun, T. Zhao, Z. Li, Z. Ma, J. Wang, F. Li, Sol-gel synthesis of macroporous Al₂O₃-SiO₂-TiO₂ monoliths via phase separation route, *Ceram Int* 42 (2016) 15926–15932. <https://doi.org/10.1016/j.ceramint.2016.07.068>.
- [99] S. Murai, K. Fujita, K. Nakanishi, K. Hirao, Direct observation of the spatial distribution of samarium ions in alumina-silica macroporous monoliths by laser scanning confocal microscopy, *J Alloys Compd* 408–412 (2006) 831–834. <https://doi.org/10.1016/j.jallcom.2005.01.085>.
- [100] K. Fujita, J. Konishi, K. Nakanishi, K. Hirao, Strong light scattering in macroporous TiO₂ monoliths induced by phase separation, *Appl Phys Lett* 85 (2004) 5595–5597. <https://doi.org/10.1063/1.1823596>.
- [101] J. Konishi, K. Fujita, K. Nakanishi, K. Hirao, Phase-separation-induced titania monoliths with well-defined macropores and mesostructured framework

- from colloid-derived sol-gel systems, *Chemistry of Materials* 18 (2006) 864–866. <https://doi.org/10.1021/cm052155h>.
- [102] J. Konishi, K. Fujita, K. Nakanishi, K. Hirao, Monolithic TiO₂ with controlled multiscale porosity via a template-free sol-gel process accompanied by phase separation, *Chemistry of Materials* 18 (2006) 6069–6074. <https://doi.org/10.1021/cm0617485>.
- [103] G. Hasegawa, K. Kanamori, K. Nakanishi, T. Hanada, Facile Preparation of Hierarchically Porous TiO₂ Monoliths, *Journal of the American Ceramic Society* 93 (2010) 3110–3115. <https://doi.org/10.1111/j.1551-2916.2010.03831.x>.
- [104] G. Hasegawa, K. Morisato, K. Kanamori, K. Nakanishi, New hierarchically porous titania monoliths for chromatographic separation media, *J Sep Sci* 34 (2011) 3004–3010. <https://doi.org/10.1002/jssc.201100538>.
- [105] J. Konishi, K. Fujita, K. Nakanishi, K. Hirao, K. Morisato, S. Miyazaki, M. Ohira, Sol-gel synthesis of macro-mesoporous titania monoliths and their applications to chromatographic separation media for organophosphate compounds, *J Chromatogr A* 1216 (2009) 7375–7383. <https://doi.org/10.1016/j.chroma.2009.06.016>.
- [106] W. Li, X. Guo, Y. Zhu, Y. Hui, K. Kanamori, K. Nakanishi, Sol-gel synthesis of macroporous TiO₂ from ionic precursors via phase separation route, *J Solgel Sci Technol* 67 (2013) 639–645. <https://doi.org/10.1007/s10971-013-3123-5>.
- [107] S. Backlund, J. Smått, J.B. Rosenholm, M. Lindén, Template-Free Sol-Gel Synthesis of Hierarchically Macro- and Mesoporous Monolithic TiO₂, *J Dispers Sci Technol* 28 (2007) 115–119. <https://doi.org/10.1080/01932690600992662>.
- [108] G. Hasegawa, K. Kanamori, K. Nakanishi, T. Hanada, Facile preparation of transparent monolithic titania gels utilizing a chelating ligand and mineral salts, *J Solgel Sci Technol* 53 (2010) 59–66. <https://doi.org/10.1007/s10971-009-2056-5>.

- [109] J. Konishi, K. Fujita, S. Oiwa, K. Nakanishi, K. Hirao, Crystalline ZrO₂ monoliths with well-defined macropores and mesostructured skeletons prepared by combining the alkoxy-derived sol-gel process accompanied by phase separation and the solvothermal process, *Chemistry of Materials* 20 (2008) 2165–2173. <https://doi.org/10.1021/cm703351d>.
- [110] Y. Tokudome, K. Fujita, K. Nakanishi, K. Miura, K. Hirao, Synthesis of monolithic Al₂O₃ with well-defined macropores and mesostructured skeletons via the sol-gel process accompanied by phase separation, *Chemistry of Materials* 19 (2007) 3393–3398. <https://doi.org/10.1021/cm063051p>.
- [111] L.A. Wu, X. Jiang, S. Wu, R. Yao, X. Qiao, X. Fan, Synthesis of monolithic zirconia with macroporous bicontinuous structure via epoxide-driven sol-gel process accompanied by phase separation, *J Solgel Sci Technol* 69 (2014) 1–8. <https://doi.org/10.1007/s10971-013-3157-8>.
- [112] X. Guo, J. Song, Y. Lvlin, K. Nakanishi, K. Kanamori, H. Yang, Preparation of macroporous zirconia monoliths from ionic precursors via an epoxide-mediated sol-gel process accompanied by phase separation, *Sci Technol Adv Mater* 16 (2015). <https://doi.org/10.1088/1468-6996/16/2/025003>.
- [113] X. Guo, J. Song, J. Ren, F. Yang, K. Kanamori, K. Nakanishi, Facile preparation of well-defined macroporous yttria-stabilized zirconia monoliths via sol-gel process accompanied by phase separation, *Journal of Porous Materials* 23 (2016) 867–875. <https://doi.org/10.1007/s10934-016-0143-x>.
- [114] X. Guo, Z. Wang, J. Song, H. Yang, Sol-gel synthesis of macroporous barium zirconate monoliths from ionic precursors via a phase separation route, *Journal of Physics and Chemistry of Solids* 102 (2017) 105–109. <https://doi.org/10.1016/j.jpcs.2016.11.012>.
- [115] Y. Kido, G. Hasegawa, K. Kanamori, K. Nakanishi, Porous chromium-based ceramic monoliths: Oxides (Cr₂O₃), nitrides (CrN), and carbides (Cr₃C₂), *J Mater Chem A Mater* 2 (2014) 745–752. <https://doi.org/10.1039/c3ta13725b>.

- [116] Y. Kido, K. Nakanishi, A. Miyasaka, K. Kanamori, Synthesis of monolithic hierarchically porous iron-based xerogels from iron(III) salts via an epoxide-mediated sol-gel process, *Chemistry of Materials* 24 (2012) 2071–2077. <https://doi.org/10.1021/cm300495j>.
- [117] X. Lu, K. Kanamori, K. Nakanishi, Synthesis of hierarchically porous MgO monoliths with continuous structure via sol-gel process accompanied by phase separation, *J Solgel Sci Technol* 89 (2019) 29–36. <https://doi.org/10.1007/s10971-018-4682-2>.
- [118] X. Guo, L. Ding, J. Ren, H. Yang, Preparation of macroporous Li₂ZrO₃ monoliths via an epoxide-mediated sol-gel process accompanied by phase separation, *Journal of Porous Materials* 24 (2017) 1319–1326. <https://doi.org/10.1007/s10934-017-0373-6>.
- [119] J. Herwig, J. Titus, J. Kullmann, N. Wilde, T. Hahn, R. Glaser, D. Enke, Hierarchically structured porous spinels via an epoxide-mediated sol-gel process accompanied by polymerization-induced phase separation, *ACS Omega* 3 (2018) 1201–1212. <https://doi.org/10.1021/acsomega.7b01621>.
- [120] S. Wang, W. Li, S. Wang, J. Jiang, Z. Chen, Synthesis of well-defined hierarchical porous La₂Zr₂O₇ monoliths via non-alkoxide sol-gel process accompanied by phase separation, *Microporous and Mesoporous Materials* 221 (2016) 32–39. <https://doi.org/10.1016/j.micromeso.2015.08.031>.
- [121] X. Guo, P. Yin, W. Lei, H. Yang, K. Kanamori, K. Nakanishi, Synthesis and characterization of monolithic ZnAl₂O₄ spinel with well-defined hierarchical pore structures via a sol-gel route, *J Alloys Compd* 727 (2017) 763–770. <https://doi.org/10.1016/j.jallcom.2017.08.172>.
- [122] M. Sun, T. Zhao, Z. Ma, Z. Li, Facile preparation of macro-mesoporous zirconium titanate monoliths via a sol-gel reaction accompanied by phase separation, *J Mater Res* 34 (2019) 4066–4075. <https://doi.org/10.1557/jmr.2019.280>.
- [123] X. Lu, K. Kanamori, K. Nakanishi, Preparation of zinc oxide with a three-dimensionally interconnected macroporous structure via a sol-gel method

- accompanied by phase separation, *New Journal of Chemistry* 43 (2019) 11720–11726. <https://doi.org/10.1039/c9nj02373a>.
- [124] A.E. Gash, J.H. Satcher, R.L. Simpson, Monolithic nickel(II)-based aerogels using an organic epoxide: The importance of the counterion, *J Non Cryst Solids* 350 (2004) 145–151. <https://doi.org/10.1016/j.jnoncrysol.2004.06.030>.
- [125] X. Lu, K. Kanamori, K. Nakanishi, Hierarchically porous monoliths based on low-valence transition metal (Cu, Co, Mn) oxides: gelation and phase separation, *Natl Sci Rev* 7 (2020) 1656–1666. <https://doi.org/10.1093/nsr/nwaa103>.
- [126] Y. Kido, K. Nakanishi, K. Kanamori, Sol-gel synthesis of zinc ferrite-based xerogel monoliths with well-defined macropores, *RSC Adv* 3 (2013) 3661–3666. <https://doi.org/10.1039/c3ra22481c>.
- [127] M. Li, N. Zhou, X. Luo, G. Zhang, Z. Xie, L. Xu, P. Liu, Macroporous MgO monoliths prepared by sol-gel process with phase separation, *Ceram Int* 42 (2016) 16368–16373. <https://doi.org/10.1016/j.ceramint.2016.07.011>.
- [128] F. Wang, Y. Sun, X. Guo, D. Li, H. Yang, Preparation and graft modification of hierarchically porous ferriferrous oxide for heavy metal ions adsorption, *J Solgel Sci Technol* 96 (2020) 360–369. <https://doi.org/10.1007/s10971-020-05350-8>.
- [129] F. Liu, D. Feng, H. Yang, X. Guo, Preparation of macroporous transition metal hydroxide monoliths via a sol-gel process accompanied by phase separation, *Sci Rep* 10 (2020) 4331. <https://doi.org/10.1038/s41598-020-61195-9>.
- [130] W. Li, Y. Zhu, X. Guo, K. Nakanishi, K. Kanamori, H. Yang, Preparation of a hierarchically porous AlPO₄ monolith via an epoxide-mediated sol-gel process accompanied by phase separation, *Sci Technol Adv Mater* 14 (2013) 045007. <https://doi.org/10.1088/1468-6996/14/4/045007>.
- [131] Y. Zhu, K. Kanamori, N. Moitra, K. Kadono, S. Ohi, N. Shimobayashi, K. Nakanishi, Metal zirconium phosphate macroporous monoliths: Versatile synthesis, thermal expansion and mechanical properties, *Microporous and*

- Mesoporous Materials 225 (2016) 122–127.
<https://doi.org/10.1016/j.micromeso.2015.12.002>.
- [132] O. Ruzimuradov, G. Hasegawa, K. Kanamori, K. Nakanishi, Preparation of hierarchically porous nanocrystalline CaTiO₃, SrTiO₃ and BaTiO₃ perovskite monoliths, *Journal of the American Ceramic Society* 94 (2011) 3335–3339.
<https://doi.org/10.1111/j.1551-2916.2011.04613.x>.
- [133] X. Guo, W. Zhu, X. Cai, S. Liu, H. Yang, Preparation of monolithic aluminium titanate with well-defined macropores via a sol-gel process accompanied by phase separation, *Mater Des* 83 (2015) 314–319.
<https://doi.org/10.1016/j.matdes.2015.06.055>.
- [134] X. Lu, K. Kanamori, G. Hasegawa, K. Nakanishi, Preparation of hierarchically porous spinel CoMn₂O₄ monoliths via sol-gel process accompanied by phase separation, *Journal of the American Ceramic Society* 104 (2020) 2449–2459.
<https://doi.org/10.1111/jace.17662>.
- [135] W. Zhu, H. Yang, K. Nakanishi, K. Kanamori, X. Guo, Sol-gel synthesis of nanocrystal-constructed hierarchically porous TiO₂ based composites for lithium ion batteries, *RSC Adv* 5 (2015) 24803–24813.
<https://doi.org/10.1039/c5ra03491d>.
- [136] G. Hasegawa, K. Kanamori, T. Kiyomura, H. Kurata, T. Abe, K. Nakanishi, Hierarchically Porous Carbon Monoliths Comprising Ordered Mesoporous Nanorod Assemblies for High-Voltage Aqueous Supercapacitors, *Chemistry of Materials* 28 (2016) 3944–3950.
<https://doi.org/10.1021/acs.chemmater.6b01261>.
- [137] J. Schoiber, C. Koczwarra, S. Rumswinkel, L. Whitmore, C. Prehal, F. Putz, M.S. Elsaesser, O. Paris, N. Hüsing, A Facile One-Pot Synthesis of Hierarchically Organized Carbon/TiO₂ Monoliths with Ordered Mesopores, *Chempluschem* 86 (2021) 275–283. <https://doi.org/10.1002/cplu.202000740>.
- [138] Y. Hara, K. Kanamori, K. Nakanishi, Self-Assembly of Metal–Organic Frameworks into Monolithic Materials with Highly Controlled Trimodal Pore

- Structures, *Angewandte Chemie International Edition* 58 (2019) 19047–19053. <https://doi.org/10.1002/anie.201911499>.
- [139] K. Kato, A. Tsuzuki, Y. Torii, H. Taoda, T. Kato, Y. Butsugan, Morphology of thin anatase coatings prepared from alkoxide solutions containing organic polymer, affecting the photocatalytic decomposition of aqueous acetic acid, *J Mater Sci* 30 (1995) 837–841. <https://doi.org/10.1007/BF00356349>.
- [140] K. Kajihara, T. Yao, Macroporous morphology of the titania films prepared by a sol-gel dip-coating method from the system containing poly(ethylene glycol): effects of molecular weight and dipping temperature, *J Solgel Sci Technol* 19 (2000) 219–222. <https://doi.org/10.1023/A:1008736305330>.
- [141] S. Li, M. Li, A. Tao, M. Song, B. Wang, J. Niu, F. Yu, Y. Wu, Synthesis of a bicontinuous structured SrTiO₃ porous film with significant photocatalytic activity by controlling phase separation process, *J Solgel Sci Technol* 94 (2020) 288–297. <https://doi.org/10.1007/s10971-020-05271-6>.
- [142] M. Yanagisawa, S. Nigorikawa, T. Sakaue, K. Fujiwara, M. Tokita, Multiple patterns of polymer gels in microspheres due to the interplay among phase separation, wetting, and gelation, *Proc Natl Acad Sci U S A* 111 (2014) 15894–15899. <https://doi.org/10.1073/pnas.1416592111>.
- [143] X. Guo, Q. Zhang, X. Ding, Q. Shen, C. Wu, L. Zhang, H. Yang, Synthesis and application of several sol-gel-derived materials via sol-gel process combining with other technologies: a review, *J Solgel Sci Technol* 79 (2016) 328–358. <https://doi.org/10.1007/s10971-015-3935-6>.
- [144] T. Guo, C. Wang, L. Dong, J. Lü, T. Liang, Effect of Al₂O₃ on the Process Performance of ZrO₂ Microspheres, *Journal Wuhan University of Technology, Materials Science Edition* 35 (2020) 841–846. <https://doi.org/10.1007/s11595-020-2328-z>.
- [145] J.H. Smått, N. Schüwer, M. Järn, W. Lindner, M. Lindén, Synthesis of micrometer sized mesoporous metal oxide spheres by nanocasting, *Microporous and Mesoporous Materials* 112 (2008) 308–318. <https://doi.org/10.1016/j.micromeso.2007.10.003>.

- [146] Y. Luan, Y.W. Xue, Z.G. Shi, Synthesis of hierarchically macro/meso/microporous carbon spheres and its application in fast rechargeable electric double layer capacitor, *Mater Lett* 88 (2012) 30–32. <https://doi.org/10.1016/j.matlet.2012.08.046>.
- [147] L. Lu, F. Teng, SenTapas, D. Qi, L. Wang, J. Zhang, Synthesis of visible-light driven $\text{Cr}_x\text{O}_y\text{-TiO}_2$ binary photocatalyst based on hierarchical macro-mesoporous silica, *Appl Catal B* 163 (2015) 9–15. <https://doi.org/10.1016/j.apcatb.2014.06.024>.
- [148] D. Grosso, G.J.D.A.A. Soler Illia, E.L. Crepaldi, B. Charleux, C. Sanchez, Nanocrystalline transition-metal oxide spheres with controlled multi-scale porosity, *Adv Funct Mater* 13 (2003) 37–42. <https://doi.org/10.1002/adfm.200390002>.
- [149] J. Shen, H. Yang, Q. Shen, Y. Feng, Synthesis of 3D micro- and nano-hierarchical structure InVO_4 porous microspheres with improved visible-light photocatalytic activities, *J Mater Sci* 48 (2013) 7574–7580. <https://doi.org/10.1007/s10853-013-7573-5>.
- [150] Q. Shen, Z. You, Y. Yu, T. Qin, Y. Su, H. Wang, C. Wu, F. Zhang, H. Yang, A Carbon Quantum Dots/Porous InVO_4 Microsphere Composite with Enhanced Photocatalytic Activity, *Eur J Inorg Chem* 2018 (2018) 1080–1086. <https://doi.org/10.1002/ejic.201701325>.
- [151] J. He, C. Yang, X. Xiong, B. Jiang, Preparation and characterization of monodisperse porous silica microspheres with controllable morphology and structure, *J Polym Sci A Polym Chem* 50 (2012) 2889–2897. <https://doi.org/10.1002/pola.26066>.
- [152] C. Teng, J. He, L. Zhu, L. Ren, J. Chen, M. Hong, Y. Wang, Fabrication and Characterization of Monodisperse Magnetic Porous Nickel Microspheres as Novel Catalysts, *Nanoscale Res Lett* 5 (2015) 8952. <https://doi.org/10.1186/s11671-015-1088-8>.
- [153] J. He, J. Chen, L. Ren, Y. Wang, C. Teng, M. Hong, J. Zhao, B. Jiang, Fabrication of monodisperse porous zirconia microspheres and their phosphorylation for

- friedel-crafts alkylation of indoles, *ACS Appl Mater Interfaces* 6 (2014) 2718–2725. <https://doi.org/10.1021/am405202d>.
- [154] H. Mori, H. Yamashita, K. Nakamura, T. Maekawa, Synthesis of Spherical Porous Silica Particles, *Journal of the Ceramic Society of Japan* 101 (1993) 1180–1183. <https://doi.org/10.2109/jcersj.101.1180>.
- [155] H. Yang, Y. Xie, G. Hao, W. Cai, X. Guo, Preparation of porous alumina microspheres via an oil-in-water emulsion method accompanied by a sol-gel process, *New Journal of Chemistry* 40 (2016) 589–595. <https://doi.org/10.1039/c5nj02509e>.
- [156] X. Guo, G. Hao, Y. Xie, W. Cai, H. Yang, Preparation of porous zirconia microspheres via emulsion method combined with phase separation, *J Solgel Sci Technol* 76 (2015) 651–657. <https://doi.org/10.1007/s10971-015-3817-y>.
- [157] M. V. Loureiro, M. Vale, A. De Schrijver, J.C. Bordado, E. Silva, A.C. Marques, Hybrid custom-tailored sol-gel derived microscaffold for biocides immobilization, *Microporous and Mesoporous Materials* 261 (2018) 252–258. <https://doi.org/10.1016/j.micromeso.2017.10.056>.
- [158] M. V. Loureiro, R. Ciriminna, M.J. Lourenço, L.F. Santos, A. De Schrijver, J.C. Bordado, M. Pagliaro, A.C. Marques, Organically-modified silica based microspheres for self-curing polyurethane one component foams, *Microporous and Mesoporous Materials* 244 (2017) 244–250. <https://doi.org/10.1016/j.micromeso.2016.10.039>.
- [159] A.C. Marques, M. V. Loureiro, M.J. Lourenço, A. De Schrijver, J.C. Bordado, Amino surface functionalized microcapsules as curing agents for polyurethane foams, *Materials and Manufacturing Processes* 32 (2017) 1304–1309. <https://doi.org/10.1080/10426914.2017.1291950>.
- [160] M. V. Loureiro, M.J. Lourenço, A. De Schrijver, L.F. Santos, J.C. Bordado, A.C. Marques, Amino-silica microcapsules as effective curing agents for polyurethane foams, *J Mater Sci* 52 (2017) 5380–5389. <https://doi.org/10.1007/s10853-017-0782-6>.

- [161] J. Schindelin, I. Arganda-Carreras, E. Frise, V. Kaynig, M. Longair, T. Pietzsch, S. Preibisch, C. Rueden, S. Saalfeld, B. Schmid, J.Y. Tinevez, D.J. White, V. Hartenstein, K. Eliceiri, P. Tomancak, A. Cardona, Fiji: An open-source platform for biological-image analysis, *Nat Methods* 9 (2012) 676–682. <https://doi.org/10.1038/nmeth.2019>.
- [162] J. Le Bideau, M.Y. Miah, A. Vioux, F. Fajula, A. Galarneau, Bimodal porous silica monoliths obtained by phase separation in non-aqueous media, *J Mater Chem* 20 (2010) 964–971. <https://doi.org/10.1039/b918412k>.
- [163] M. V. Loureiro, R. Ciriminna, M.J. Lourenço, L.F. Santos, A. De Schrijver, J.C. Bordado, M. Pagliaro, A.C. Marques, Organically-modified silica based microspheres for self-curing polyurethane one component foams, *Microporous and Mesoporous Materials* 244 (2017) 244–250. <https://doi.org/10.1016/j.micromeso.2016.10.039>.
- [164] L. Gabrielli, L. Russo, A. Poveda, J.R. Jones, F. Nicotra, J. Jiménez-Barbero, L. Cipolla, Epoxide opening versus silica condensation during sol-gel hybrid biomaterial synthesis, *Chemistry - A European Journal* 19 (2013) 7856–7864. <https://doi.org/10.1002/chem.201204326>.
- [165] K. Nakanishi, N. Soga, Phase Separation in Gelling Silica–Organic Polymer Solution: Systems Containing Poly(sodium styrenesulfonate), *Journal of the American Ceramic Society* 74 (1991) 2518–2530. <https://doi.org/10.1111/j.1151-2916.1991.tb06794.x>.
- [166] H. Kaji, K. Nakanishi, N. Soga, Polymerization-induced phase separation in silica sol-gel systems containing formamide, *J Solgel Sci Technol* 1 (1993) 35–46. <https://doi.org/10.1007/BF00486427>.
- [167] K.S.W. Sing, D.H. Everett, R.A.W. Haul, L. Moscou, R.A. Pierotti, J. Rouquerol, T. Siemieniewska, Reporting Physisorption Data for Gas/Solid Systems with Special Reference to the Determination of Surface Area and Porosity, *Pure and Applied Chemistry* 57 (1985) 603–619. <https://doi.org/10.1351/pac198557040603>.

- [168] A.C. Marques, R.M. Almeida, A. Thiema, S. Wang, M.M. Falk, H. Jain, Sol-gel-derived glass scaffold with high pore interconnectivity and enhanced bioactivity, *J Mater Res* 24 (2009) 3495–3502. <https://doi.org/10.1557/jmr.2009.0440>.
- [169] A.C. Marques, H. Jain, C. Kiely, K. Song, C.J. Kiely, R.M. Almeida, Nano/macroporous monolithic scaffolds prepared by the sol-gel method, *J Solgel Sci Technol* 51 (2009) 42–47. <https://doi.org/10.1007/s10971-009-1960-z>.
- [170] X. Guo, R. Wang, H. Yu, Y. Zhu, K. Nakanishi, K. Kanamori, H. Yang, Spontaneous preparation of hierarchically porous silica monoliths with uniform spherical mesopores confined in a well-defined macroporous framework, *Dalton Transactions* 44 (2015) 13592–13601. <https://doi.org/10.1039/c5dt01672j>.
- [171] A. Feinle, M.S. Elsaesser, N. Hüsing, Hierarchical Organization in Monolithic Sol-Gel Materials, in: L. Klein, M. Aparicio, A. Jitianu (Eds.), *Handbook of Sol-Gel Science and Technology*, Springer International Publishing, Switzerland, 2016: pp. 1–49. https://doi.org/10.1007/978-3-319-19454-7_127-1.
- [172] S. Gheorghiu, M.O. Coppens, Optimal Bimodal Pore Networks for Heterogeneous Catalysis, *AIChE Journal* 50 (2004) 812–820. <https://doi.org/10.1002/aic.10076>.
- [173] J. Gallardo, A. Durán, D. Di Martino, R.M. Almeida, Structure of inorganic and hybrid SiO₂ sol-gel coatings studied by variable incidence infrared spectroscopy, *J Non Cryst Solids* 298 (2002) 219–225. [https://doi.org/10.1016/S0022-3093\(02\)00921-3](https://doi.org/10.1016/S0022-3093(02)00921-3).
- [174] R.M. Almeida, A.C. Marques, Characterization of Sol-Gel Materials by Infrared Spectroscopy, in: L. Klein, M. Aparicio, A. Jitianu (Eds.), *Handbook of Sol-Gel Science and Technology*, Springer International Publishing, Switzerland, 2016: pp. 1–31. https://doi.org/10.1007/978-3-319-19454-7_33-1.
- [175] R.M. Almeida, C.G. Pantano, Structural investigation of silica gel films by infrared spectroscopy, *J Appl Phys* 68 (1990) 4225–4232. <https://doi.org/10.1063/1.346213>.

- [176] F.L. Galeener, Band limits and the vibrational spectra of tetrahedral glasses, *Phys Rev B* 19 (1979) 4292–4297. <https://doi.org/10.1103/PhysRevB.19.4292>.
- [177] R.M. Almeida, C.G. Pantano, Structural investigation of silica gel films by infrared spectroscopy, *J Appl Phys* 68 (1990) 4225–4232. <https://doi.org/10.1063/1.346213>.
- [178] X. Zhu, Y. Yang, Z. Zheng, B. Xiang, X. Cui, Multiwave rheology and dynamic light scattering characterizations for a two-step sol-gel transition of tetraethoxysilane hydrolysis and condensation, *J Solgel Sci Technol* 88 (2018) 255–262. <https://doi.org/10.1007/S10971-018-4788-6/FIGURES/5>.
- [179] B. H. Stuart, *Infrared Spectroscopy: Fundamentals and Applications*, 1st Edition, John Wiley & Sons Ltd, West Sussex, England, 2004.
- [180] R.M. Almeida, Spectroscopy and Structure of Sol-Gel Systems, *Journal of Sol-Gel Science and Technology* 1998 13:1 13 (1998) 51–59. <https://doi.org/10.1023/A:1008643019875>.
- [181] R.M. Almeida, P.J. Morais, A.C. Marques, Planar waveguides for integrated optics prepared by sol-gel methods, *Philosophical Magazine B* 82 (2002) 707–719. <https://doi.org/10.1080/13642810208224361>.
- [182] S.-L. Chen, P. Dong, G.-H. Yang, J.-J. Yang, Kinetics of Formation of Monodisperse Colloidal Silica Particles through the Hydrolysis and Condensation of Tetraethylorthosilicate, *Ind Eng Chem Res* 35 (1996) 4487–4493. <https://doi.org/10.1021/ie9602217>.
- [183] C. Wang, J. Wang, C.B. Park, Y.-W. Kim, Cross-linking behavior of a polysiloxane in preceramic foam processing, *J Mater Sci* 39 (2004) 4913–4915. <https://doi.org/10.1023/B:JMSC.0000035335.92101.7c>.
- [184] S.Y. Kim, D.G. Choi, S.M. Yang, Rheological analysis of the gelation behavior of tetraethylorthosilane/ vinyltriethoxysilane hybrid solutions, *Korean Journal of Chemical Engineering* 2002 19:1 19 (2002) 190–196. <https://doi.org/10.1007/BF02706894>.

- [185] Y. Sun, Y. Fang, A. Chen, Q. You, C. Dai, R. Cheng, Y. Liu, Gelation Behavior Study of a Resorcinol–Hexamethyleneteramine Crosslinked Polymer Gel for Water Shut-Off Treatment in Low Temperature and High Salinity Reservoirs, *Energies (Basel)* 10 (2017) 913. <https://doi.org/10.3390/en10070913>.
- [186] E. Katoueizadeh, M. Rasouli, S.M. Zebarjad, A comprehensive study on the gelation process of silica gels from sodium silicate, *Journal of Materials Research and Technology* 9 (2020) 10157–10165. <https://doi.org/10.1016/J.JMRT.2020.07.020>.
- [187] A.B. Giasuddin, D.W. Britt, Monitoring Silane Sol-Gel Kinetics with In-Situ Optical Turbidity Scanning and Dynamic Light Scattering, *Molecules* 24 (2019) 2931. <https://doi.org/10.3390/molecules24162931>.
- [188] R.M. Almeida, A.C. Marques, Characterization of Sol-Gel Materials by Infrared Spectroscopy, in: L. Klein, M. Aparicio, A. Jitianu (Eds.), *Handbook of Sol-Gel Science and Technology*, Springer International Publishing, Cham, 2018: pp. 1121–1151. https://doi.org/10.1007/978-3-319-32101-1_33.
- [189] R. Parra, M.S. Góes, M.S. Castro, E. Longo, P.R. Bueno, J.A. Varela, Reaction Pathway to the Synthesis of Anatase via the Chemical Modification of Titanium Isopropoxide with Acetic Acid, *Chemistry of Materials* 20 (2008) 143–150. <https://doi.org/10.1021/cm702286e>.
- [190] R. Pal, Rheology of simple and multiple emulsions, *Curr Opin Colloid Interface Sci* 16 (2011) 41–60. <https://doi.org/10.1016/J.COCIS.2010.10.001>.
- [191] R. Pal, Shear Viscosity Behavior of Emulsions of Two Immiscible Liquids, *J Colloid Interface Sci* 225 (2000) 359–366. <https://doi.org/10.1006/JCIS.2000.6776>.
- [192] F. Goodarzi, S. Zendehboudi, A Comprehensive Review on Emulsions and Emulsion Stability in Chemical and Energy Industries, *Can J Chem Eng* 97 (2019) 281–309. <https://doi.org/10.1002/CJCE.23336>.
- [193] D.S. Kolotova, Y.A. Kuchina, L.A. Petrova, N.G. Voron'ko, S.R. Derkach, Rheology of Water-in-Crude Oil Emulsions: Influence of Concentration and

- Temperature, Colloids and Interfaces 2 (2018) 64.
<https://doi.org/10.3390/colloids2040064>.
- [194] A.A. Issa, A.S. Luyt, Kinetics of Alkoxysilanes and Organoalkoxysilanes Polymerization: A Review, Polymers (Basel) 11 (2019) 537.
<https://doi.org/10.3390/POLYM11030537>.
- [195] D.A. Neumayer, E. Cartier, Materials characterization of ZrO₂-SiO₂ and HfO₂-SiO₂ binary oxides deposited by chemical solution deposition, J Appl Phys 90 (2001) 1801. <https://doi.org/10.1063/1.1382851>.
- [196] J. Lin, W. Ye, M. Xie, D.H. Seo, J. Luo, Y. Wan, B. Van der Bruggen, Environmental impacts and remediation of dye-containing wastewater, Nat Rev Earth Environ 4 (2023) 785-803. <https://doi.org/10.1038/s43017-023-00489-8>.
- [197] A. Saravanan, V.C. Deivayanai, P.S. Kumar, G. Rangasamy, R. V Hemavathy, T. Harshana, N. Gayathri, K. Alagumalai, A detailed review on advanced oxidation process in treatment of wastewater: Mechanism, challenges and future outlook, Chemosphere 308 (2022) 136524.
<https://doi.org/https://doi.org/10.1016/j.chemosphere.2022.136524>.
- [198] A. Mancuso, G. Iervolino, Synthesis and Application of Innovative and Environmentally Friendly Photocatalysts: A Review, Catalysts 12 (2022) 1074.
<https://doi.org/10.3390/catal12101074>.
- [199] M.A. Rauf, S.S. Ashraf, Fundamental principles and application of heterogeneous photocatalytic degradation of dyes in solution, Chemical Engineering Journal 151 (2009) 10-18.
<https://doi.org/https://doi.org/10.1016/j.cej.2009.02.026>.
- [200] S. Park, G.R. Choi, J.C. Lee, Y.C. Kim, D. Oh, S. Cho, J.-H. Lee, Organic and inorganic binder-coating properties for immobilization of photocatalytic ZnO nanopowders, Research on Chemical Intermediates 36 (2010) 819-825.
<https://doi.org/10.1007/s11164-010-0186-6>.
- [201] Y. Jiang, A. Liu, Cornstalk biochar-TiO₂ composites as alternative photocatalyst for degrading methyl orange, Environmental Science and Pollution Research 30 (2023) 31923-31934. <https://doi.org/10.1007/s11356-022-24490-8>.

- [202] A. Wu, D. Wang, C. Wei, X. Zhang, Z. Liu, P. Feng, X. Ou, Y. Qiang, H. Garcia, J. Niu, A comparative photocatalytic study of TiO₂ loaded on three natural clays with different morphologies, *Appl Clay Sci* 183 (2019) 105352. <https://doi.org/https://doi.org/10.1016/j.clay.2019.105352>.
- [203] M.A. Lucchini, E. Lizundia, S. Moser, M. Niederberger, G. Nyström, Titania-Cellulose Hybrid Monolith for In-Flow Purification of Water under Solar Illumination, *ACS Appl Mater Interfaces* 10 (2018) 29599–29607. <https://doi.org/10.1021/acsami.8b09735>.
- [204] B.D. Stewart, L.G. Andrews, B.S. Pelletier, C.A. Daly, J.E. Boyd, Porous PMMA-titania composites: A step towards more sustainable photocatalysis, *Journal of Water Process Engineering* 8 (2015) 179–185. <https://doi.org/https://doi.org/10.1016/j.jwpe.2015.10.007>.
- [205] P. Lei, F. Wang, X. Gao, Y. Ding, S. Zhang, J. Zhao, S. Liu, M. Yang, Immobilization of TiO₂ nanoparticles in polymeric substrates by chemical bonding for multi-cycle photodegradation of organic pollutants, *J Hazard Mater* 227–228 (2012) 185–194. <https://doi.org/https://doi.org/10.1016/j.jhazmat.2012.05.029>.
- [206] A.N. Ökte, D. Karamanis, D. Tuncel, Dual functionality of TiO₂-flyash nanocomposites: Water vapor adsorption and photocatalysis, *Catal Today* 230 (2014) 205–213. <https://doi.org/https://doi.org/10.1016/j.cattod.2014.01.031>.
- [207] T.C. Almeida da Silva, L. Marchiori, B. Oliveira Mattos, S. Ullah, H. da S. Barud, R. Romano Domenegueti, H.D. Rojas-Mantilla, M.V. Boldrin Zanoni, U.P. Rodrigues-Filho, E.P. Ferreira-Neto, S.J.L. Ribeiro, Designing Highly Photoactive Hybrid Aerogels for In-Flow Photocatalytic Contaminant Removal Using Silica-Coated Bacterial Nanocellulose Supports, *ACS Appl Mater Interfaces* 15 (2023) 23146–23159. <https://doi.org/10.1021/acsami.3c02008>.
- [208] Y. Hu, H. Dong, A.R. Tapa, J. Shamsi, J.S. Shayeh, A. Trokourey, B. Liu, X. Zhao, Y. Xie, NaBr-Assisted Aqueous Synthesis of Perovskite-Embedded PbBr(OH) Hierarchical Nanostructures for Dye Photodegradation, *ACS Appl Nano Mater* 6 (2023) 2538–2548. <https://doi.org/10.1021/acsanm.2c04900>.

- [209] J. Wu, K. Ke, N. Qin, E. Lin, Z. Kang, D. Bao, Magnetically retrievable Fe₃O₄@SiO₂@ZnO piezo-photocatalyst: Synthesis and multiple catalytic properties, *J Colloid Interface Sci* 636 (2023) 167–175. <https://doi.org/https://doi.org/10.1016/j.jcis.2023.01.009>.
- [210] G. Sun, N. Li, S. Zuo, W. Shen, M. Wu, Q. Li, M. Shi, J. Ma, Piezo-photocatalysis over phase-engineered MoSe₂ modified Bi₂WO₆ hierarchical microspheres: Utilizing piezoelectric effect to enhance photocatalytic performance, *Ceram Int* 48 (2022) 37242–37252. <https://doi.org/https://doi.org/10.1016/j.ceramint.2022.08.302>.
- [211] J. Wang, M. Sgarzi, Z. Němečková, J. Henych, N. Licciardello, G. Cuniberti, Reusable and Antibacterial Polymer-Based Nanocomposites for the Adsorption of Dyes and the Visible-Light-Driven Photocatalytic Degradation of Antibiotics, *Global Challenges* 6 (2022) 2200076. <https://doi.org/https://doi.org/10.1002/gch2.202200076>.
- [212] M. Imran, W. Ashraf, A.K. Hafiz, M. Khanuja, Synthesis and Performance Analysis of Photocatalytic Activity of ZnIn₂S₄ Microspheres Synthesized Using a Low-Temperature Method, *ACS Omega* 7 (2022) 22987–22996. <https://doi.org/10.1021/acsomega.2c00945>.
- [213] M. Qin, K. Jin, X. Li, R. Wang, Y. Zhao, H. Wang, Bi nanosphere-decorated oxygen-vacancy BiOBr hollow microspheres with exposed (110) facets to enhance the photocatalytic performance for the degradation of azo dyes, *New Journal of Chemistry* 46 (2022) 12410–12418. <https://doi.org/10.1039/D2NJ02076A>.
- [214] J. Kim, S. Jo, W. Lee, J. Lim, T. Seung Lee, Moving photocatalyst of a titanium dioxide-based micromotor asymmetrically decorated with conjugated polymer dots, *Mater Des* 219 (2022) 110743. <https://doi.org/https://doi.org/10.1016/j.matdes.2022.110743>.
- [215] X. Li, S. Raza, C. Liu, Preparation of titanium dioxide modified biomass polymer microspheres for photocatalytic degradation of rhodamine-B dye and tetracycline, *J Taiwan Inst Chem Eng* 122 (2021) 157–167. <https://doi.org/https://doi.org/10.1016/j.jtice.2021.04.040>.

- [216] H. Liang, S. Wang, Y. Lu, P. Ren, G. Li, F. Yang, Y. Chen, Highly efficient and cheap treatment of dye by graphene-doped TiO₂ microspheres, *Water Science and Technology* 83 (2020) 223–232. <https://doi.org/10.2166/wst.2020.545>.
- [217] J. He, Q. Liu, Y. Zhang, X. Zhao, G. Zhang, B. Xiao, K. Fu, In situ synthesis of the mesoporous C–TiO₂ microspheres derived from partial hydrolysis tetrabutyl titanate for enhanced photocatalytic degradation under visible light, *Mater Res Bull* 161 (2023) 112168. <https://doi.org/10.1016/j.materresbull.2023.112168>.
- [218] X. Feng, L. Gu, N. Wang, Q. Pu, G. Liu, Fe/N co-doped nano-TiO₂ wrapped mesoporous carbon spheres for synergetically enhanced adsorption and photocatalysis, *J Mater Sci Technol* 135 (2023) 54–64. <https://doi.org/10.1016/j.jmst.2022.06.038>.
- [219] X. Ren, X. Zhang, R. Guo, X. Li, Y. Peng, X. Zhao, X. Pu, Hollow mesoporous g-C₃N₄/Ag₂CrO₄ photocatalysis with direct Z-scheme: Excellent degradation performance for antibiotics and dyes, *Sep Purif Technol* 270 (2021) 118797. <https://doi.org/10.1016/j.seppur.2021.118797>.
- [220] S.M. Fernandes, B.T. Barrocas, J.V. Nardeli, M.F. Montemor, E. Maças, M.C. Oliveira, C.C.C.R. de Carvalho, A. Lauria, M. Niederberger, A.C. Marques, Maximizing photocatalytic efficiency with minimal amount of gold: Solar-driven TiO₂ photocatalysis supported by MICROSCAFS® for facile catalyst recovery, *J Environ Chem Eng* 12 (2024) 112043. <https://doi.org/10.1016/j.jece.2024.112043>.
- [221] S. Landi, I.R. Segundo, E. Freitas, M. Vasilevskiy, J. Carneiro, C.J. Tavares, Use and misuse of the Kubelka-Munk function to obtain the band gap energy from diffuse reflectance measurements, *Solid State Commun* 341 (2022) 114573. <https://doi.org/10.1016/j.ssc.2021.114573>.
- [222] P. Makuła, M. Pacia, W. Macyk, How To Correctly Determine the Band Gap Energy of Modified Semiconductor Photocatalysts Based on UV–Vis Spectra, *J Phys Chem Lett* 9 (2018) 6814–6817. <https://doi.org/10.1021/acs.jpcllett.8b02892>.

- [223] B. Barrocas, L.D. Chiavassa, M. Conceição Oliveira, O.C. Monteiro, Impact of Fe, Mn co-doping in titanate nanowires photocatalytic performance for emergent organic pollutants removal, *Chemosphere* 250 (2020) 126240. <https://doi.org/https://doi.org/10.1016/j.chemosphere.2020.126240>.
- [224] B.T. Barrocas, M.C. Oliveira, H.I.S. Nogueira, S. Fateixa, O.C. Monteiro, Ruthenium-Modified Titanate Nanowires for the Photocatalytic Oxidative Removal of Organic Pollutants from Water, *ACS Appl Nano Mater* 2 (2019) 1341–1349. <https://doi.org/10.1021/acsnm.8b02215>.
- [225] A.C. Marques, M. V. Loureiro, M.J. Lourenço, A. De Schrijver, J.C. Bordado, Amino surface functionalized microcapsules as curing agents for polyurethane foams, *Materials and Manufacturing Processes* 32 (2017) 1304–1309. <https://doi.org/10.1080/10426914.2017.1291950>.
- [226] N. Nagar, V. Devra, A kinetic study on the degradation and biodegradability of silver nanoparticles catalyzed Methyl Orange and textile effluents, *Heliyon* 5 (2019) e01356. <https://doi.org/https://doi.org/10.1016/j.heliyon.2019.e01356>.
- [227] D. Benz, H. Van Bui, H.T. Hintzen, M.T. Kreutzer, J.R. van Ommen, Mechanistic insight into the improved photocatalytic degradation of dyes for an ultrathin coating of SiO₂ on TiO₂ (P25) nanoparticles, *Chemical Engineering Journal Advances* 10 (2022) 100288. <https://doi.org/https://doi.org/10.1016/j.cej.2022.100288>.
- [228] A.L. Luna, F. Matter, M. Schreck, J. Wohllwend, E. Tervoort, C. Colbeau-Justin, M. Niederberger, Monolithic metal-containing TiO₂ aerogels assembled from crystalline pre-formed nanoparticles as efficient photocatalysts for H₂ generation, *Appl Catal B* 267 (2020) 118660. <https://doi.org/10.1016/j.apcatb.2020.118660>.
- [229] P.A. Williams, C.P. Ireland, P.J. King, P.A. Chater, P. Boldrin, R.G. Palgrave, J.B. Claridge, J.R. Darwent, P.R. Chalker, M.J. Rosseinsky, Atomic layer deposition of anatase TiO₂ coating on silica particles: growth, characterization and evaluation as photocatalysts for methyl orange degradation and hydrogen

- production, *J Mater Chem* 22 (2012) 20203–20209.
<https://doi.org/10.1039/C2JM33446A>.
- [230] D. Ljubas, G. Smoljanić, H. Juretić, Degradation of Methyl Orange and Congo Red dyes by using TiO₂ nanoparticles activated by the solar and the solar-like radiation, *J Environ Manage* 161 (2015) 83–91.
<https://doi.org/https://doi.org/10.1016/j.jenvman.2015.06.042>.
- [231] Á. Morales-García, A. Macià Escatllar, F. Illas, S.T. Bromley, Understanding the interplay between size, morphology and energy gap in photoactive TiO₂ nanoparticles, *Nanoscale* 11 (2019) 9032–9041.
<https://doi.org/10.1039/C9NR00812H>.
- [232] R. Comparelli, E. Fanizza, M.L. Curri, P.D. Cozzoli, G. Mascolo, R. Passino, A. Agostiano, Photocatalytic degradation of azo dyes by organic-capped anatase TiO₂ nanocrystals immobilized onto substrates, *Appl Catal B* 55 (2005) 81–91. <https://doi.org/https://doi.org/10.1016/j.apcatb.2004.07.011>.
- [233] S. Kokilavani, I.A. Alaraidh, M.K. Okla, P. Chandran, A. Mohebaldin, W. Soufan, A.A. AL-ghamdi, M.A. Abdel-Maksoud, H. AbdElgawad, A.M. Thomas, L.L. Raju, S. Sudheer Khan, Efficient photocatalytic degradation of methyl orange and malachite green by Ag₃PO₄ decorated BiOBr nanoflower under visible light: Performance evaluation, mechanism insights and toxicology of the by-products, *J Alloys Compd* 909 (2022) 164703.
<https://doi.org/https://doi.org/10.1016/j.jallcom.2022.164703>.
- [234] R.A. Putri, S. Safni, N. Jamarun, U. Septiani, M.-K. Kim, K. Zoh, Kinetics studies on photodegradation of methyl orange in the presence of C-N-codoped TiO₂ catalyst, *Egypt J Chem* 62 (2019) 563–575.
<https://doi.org/10.21608/ejchem.2019.14543.1883>.
- [235] C. Baiocchi, M.C. Brussino, E. Pramauro, A.B. Prevot, L. Palmisano, G. Marci, Characterization of methyl orange and its photocatalytic degradation products by HPLC/UV-VIS diode array and atmospheric pressure ionization quadrupole ion trap mass spectrometry, *Int J Mass Spectrom* 214 (2002) 247–256. [https://doi.org/https://doi.org/10.1016/S1387-3806\(01\)00590-5](https://doi.org/https://doi.org/10.1016/S1387-3806(01)00590-5).

- [236] S. Kokilavani, I.A. Alaraidh, M.K. Okla, P. Chandran, A. Mohebaldin, W. Soufan, A.A. AL-ghamdi, M.A. Abdel-Maksoud, H. AbdElgawad, A.M. Thomas, L.L. Raju, S. Sudheer Khan, Efficient photocatalytic degradation of methyl orange and malachite green by Ag₃PO₄ decorated BiOBr nanoflower under visible light: Performance evaluation, mechanism insights and toxicology of the by-products, *J Alloys Compd* 909 (2022) 164703. <https://doi.org/https://doi.org/10.1016/j.jallcom.2022.164703>.
- [237] T. Liu, L. Wang, X. Lu, J. Fan, X. Cai, B. Gao, R. Miao, J. Wang, Y. Lv, Comparative study of the photocatalytic performance for the degradation of different dyes by ZnIn₂S₄: adsorption, active species, and pathways, *RSC Adv.* 7 (2017) 12292–12300. <https://doi.org/10.1039/C7RA00199A>.
- [238] A. Mills, G. Williams, Methyl orange as a probe of the semiconductor–electrolyte interfaces in CdS suspensions, *J. Chem. Soc., Faraday Trans. 1* 83 (1987) 2647–2661. <https://doi.org/10.1039/F19878302647>.
- [239] R.A. Osawa, B.T. Barrocas, O.C. Monteiro, M. Conceição Oliveira, M.H. Florêncio, Photocatalytic degradation of amitriptyline, trazodone and venlafaxine using modified cobalt-titanate nanowires under UV–Vis radiation: Transformation products and in silico toxicity, *Chemical Engineering Journal* 373 (2019) 1338–1347. <https://doi.org/https://doi.org/10.1016/j.cej.2019.05.137>.
- [240] L. Ismail, A. Rifai, C. Ferronato, L. Fine, F. Jaber, J.-M. Chovelon, Towards a better understanding of the reactive species involved in the photocatalytic degradation of sulfaclozine, *Appl Catal B* 185 (2016) 88–99. <https://doi.org/https://doi.org/10.1016/j.apcatb.2015.12.008>.
- [241] K.-S. Kim, S.K. Kam, Y.S. Mok, Elucidation of the degradation pathways of sulfonamide antibiotics in a dielectric barrier discharge plasma system, *Chemical Engineering Journal* 271 (2015) 31–42. <https://doi.org/https://doi.org/10.1016/j.cej.2015.02.073>.
- [242] A. Dirany, I. Sirés, N. Oturan, A. Özcan, M.A. Oturan, Electrochemical Treatment of the Antibiotic Sulfachloropyridazine: Kinetics, Reaction Pathways, and Toxicity Evolution, *Environ Sci Technol* 46 (2012) 4074–4082. <https://doi.org/10.1021/es204621q>.

- [243] A. Fabiańska, A. Białk-Bielińska, P. Stepnowski, S. Stolte, E.M. Siedlecka, Electrochemical degradation of sulfonamides at BDD electrode: Kinetics, reaction pathway and eco-toxicity evaluation, *J Hazard Mater* 280 (2014) 579–587. <https://doi.org/https://doi.org/10.1016/j.jhazmat.2014.08.050>.